OSCILLATING WATER COLUMN WAVE ENERGY CONVERTERS INTEGRATED IN VERY LARGE FLOATING STRUCTURES

Dissertation

submitted to and approved by the

Department of Architecture, Civil Engineering and Environmental Sciences
University of Braunschweig – Institute of Technology

and the

Department of Civil and Environmental Engineering
University of Florence

in candidacy for the degree of a

Doktor-Ingenieurin (Dr.-Ing.) /

Dottore di Ricerca in Civil and Environmental Engineering[*)]

by

Ilaria Crema
born 07.07.1979
from Brindisi, Italy

Submitted on	28.02.2017
Oral examination on	08.05.2017
Professorial advisors	Prof. Hocine Oumeraci Prof. Lorenzo Cappietti

2018

*) Either the German or the Italian form of the title may be used.

Abstract

The increasing population density and the industrial expansion significantly affect the availability of land. In this context, the high modularity of Very Large Floating Structures (VLFSs) may indeed represent a promising alternative for multipurpose use. Furthermore, the interest for the sea as a source of renewable marine energy, particularly for wave energy, has tremendously increased in the last decade and years. Among the large diversity of Wave Energy Converters (WECs), the Oscillating Water Column (OWC) is one of the most promising concept. Moreover, when an OWC is incorporated in a VLFS, its efficiency in terms of wave energy absorption is not only increased, but also it has additionally the benefit of attenuating the heave motion of the floating structure. Hence, there is a growing interest in the development of an innovative VLFS equipped with OWC devices. In this scope, the mitigating effect of the OWC on the heave motion of the VLFS can be combined with an increased efficiency of the OWC, thus better contributing to supply energy for the facilities located on the floating system.

The main goal of this PhD research is the investigation of a VLFS-OWC System conceived for a hypothetical installation in a Mediterranean area, characterized by a moderate wave climate. For this purpose, small-scale experiments have been carried out in the wave-current flume of the Maritime Engineering Laboratory (LABIMA) of Florence University.

The laboratory tests focused on the effect of:

(i) the OWC design parameters (i.e., OWC geometry);
(ii) the incident wave conditions (i.e., regular and irregular wave trains);
(iii) the damping induced by a non-linear air turbine (i.e., a self-rectifying impulse turbine) idealised by vents with different diameters in the OWC chamber roof;
(iv) the length and the heave motion of the VLFS

on the performance of the OWC, including the attenuating effect of the incorporated OWC on the heave motion of the VLFS-OWC system.

The design of the fixed OWC, VLFS and VLFS-OWC models as well as the testing programme and laboratory procedures, are based on an extensive literature review of the available numerical and physical models on OWC devices and VLFS technologies.

The main findings of this study may be summarized as follows:

- the most dominant parameters affecting the performance of a fixed OWC are the chamber width (in wave propagation direction), the front wall draught and the damping induced by the air turbine;
- the additional parameters affecting the efficiency of an OWC integrated in a VLFS are the length of the structure and the heave motion;
- formulae are developed for predicting the heave motion of the VLFS-OWC system respectively, for regular waves and irregular waves;
- formulae are developed for improving the prediction of the performance of a fixed OWC for a floating OWC (integrated in a VLFS) respectively, for regular irregular waves.

These findings have contributed to improve the understanding of the functioning of the OWC device and the relative importance of the aforementioned parameters affecting the device under moderate wave climate.

Abstrakt

Die zunehmende Bevölkerungsdichte und die industrielle Expansion beeinflussen erheblich die Verfügbarkeit von Land. In diesem Zusammenhang könnte die hohe Modularität von sehr großen schwimmenden Bauwerken „Very Large Floating Structures“ (VLFSs) mit vielfältigen Einsatzmöglichkeiten eine viel versprechende Alternative darstellen. Außerdem hat in den letzten zehn Jahren das Interesse für das Meer als Quelle erneuerbarer Energie, vor allem im Bereich der Wellenenergie, stark zugenommen. Unter der großen Vielfalt von Wellenenergiekonvertern „Wave Energy Converter“ (WECs) ist die oszillierende Wassersäule „Oscillating Water Column“ (OWC) eines der vielversprechendsten Konzepte. Wenn ein OWC-System in ein VLFS eingebaut wird ist erstens die Wellenenergieabsorption erhöht und zweitens wird die Hubbewegung des schwimmenden Bauwerks gedämpft. Daher besteht ein wachsendes Interesse an der Entwicklung eines innovativen VLFS mit integrierten OWC-WEC. Der Dämpfungseffekt der OWC auf die Hubbewegung der VLFS steht in Beziehung zu einem höhten Wirkungsgrad des OWC-Systems, welcher zu einer höheren Energiegewinnung und -versorgung des schwimmenden Bauwerks führt.

Das Hauptziel dieser Doktorarbeit ist die Erforschung eines VLFS-OWC-Systems, das für eine hypothetische Installation in einem mediterranen Gebiet mit einem gemäßigten Wellenklima konzipiert wurde. Zu diesem Zweck wurden kleine Experimente im Wellenkanal des Maritime Engineering Laboratory (LABIMA) der Universität Florenz durchgeführt.

Die Labortests konzentrierten sich auf die Wirkung von:

(i) den OWC-Entwurfsparameter (d. h. OWC-Geometrie);
(ii) den einfallenden Wellenbedingungen (d. h. regelmäßiger und unregelmäßiger Wellengang);
(iii) der Dämpfung, welche durch eine nichtlineare Luftturbine (d. h. eine selbstgleichrichtende Impulsturbine) induziert wird, die durch Öffnungen mit unterschiedlichen Durchmessern in dem OWC-Kammerdach idealisiert ist;
(iv) der Länge und der Hubbewegung des VLFS

auf die Leistung des OWC-Systems, einschließlich der Dämpfungswirkung des eingebauten OWC auf die Hubbewegung des VLFS-OWC-Systems.

Das Design der festen OWC-, VLFS- und VLFS-OWC-Modelle, sowie das Testprogramm und die Laborverfahren basieren auf einer umfassenden Literaturrecherche über die verfügbaren numerischen und physikalischen Modelle für OWC-Geräte und VLFS-Technologien.

Die wichtigsten Ergebnisse dieser Doktorarbeit können wie folgt zusammengefasst werden:

- Die dominierenden Parameter, die die Leistung eines festen OWC-Systems beeinflussen, sind die Kammerbreite (in Wellenausbreitungsrichtung), der Frontwandzug und die induzierte Dämpfung der Luftturbine;
- Die zusätzlichen Parameter, die die Effizienz eines in einem VLFS integrierten OWCs beeinflussen, sind die Länge der Struktur und die Hubbewegung;
- Formeln zur Vorhersage der Hubbewegung des VLFS-OWC-Systems für regelmäßige und unregelmäßige Wellen wurden entwickelt;
- Formeln zur Verbesserung der Leistungsvorhersage eines festen OWC integriert in eine VLFS wurden für regelmäßige und unregelmäßige Wellen entwickelt.

Diese Ergebnisse haben dazu beigetragen, das Verständnis der Funktionsweise des OWC-Systems und die relative Bedeutung der oben genannten Parameter, bei moderatem Wellenklima, zu verbessern.

Acknowledgment

I would like to express my deepest gratitude to Prof. Cappietti and Prof. Oumeraci for their constant encouragement, patience, support and guidance without which this study would not have been possible.

I gratefully thank Prof. Aminti for his availability and my laboratory colleagues and friends Andrea and Yanis for their help and for the best moments spent during the hard work of the experiments. It was great to collaborate with them.

A special thank goes to Irene S. and Valentina for their precious help and for sharing with me joys, dramas, travels and their knowledge.

I would also like to thank all my PhD colleagues, I am very glad that we shared a great time in Braunschweig and in Florence.

Thanks to all the colleagues of Braunschweig and in particular to Mrs Gabi, I am very grateful for her great patient and care during my staying in LWI.

My special thanks go to Serena, Irene F., Pina and Sanaz, for all the help and for the best moments spent together, you were like sisters for me during all my staying in Braunschweig.

Finally, I would like to dedicate my PhD research to my beloved mother and father for their endless love and to my sister Giuliana for her everlasting support.

Table of Contents

List of Figures iv
List of Tables ix
List of Notations x

1 INTRODUCTION 1
1.1 Objectives 2
1.2 Methodology 2
2 CURRENT KNOWLEDGE ON VERY LARGE FLOATING STRUCTURES (VLFSS) AND OSCILLATING WATER COLUMN DEVICES (OWCS) 3
2.1 Very Large Floating Structures (VLFSs) 4
2.1.1 Definition, classification and processes 4
2.1.2 Design criteria 7
2.1.3 Past, present and future applications 9
2.1.4 Numerical and experimental studies on VLFS 11
2.1.5 Summary and implications for the present study 12
2.2 Oscillating Water Column Devices (OWCs) 13
2.2.1 Wave Energy Basics 13
2.2.2 Wave energy conversion technologies (WECs): a synthesis 15
2.2.3 OWC technology: classification and processes 15
2.2.4 Numerical and experimental studies on OWC devices 18
2.2.5 Summary and implications for the present study 24
2.3 Specification, objectives and methodology 25
3 CONCEPTUAL DESIGN OF A VLFS-OWC SYSTEM 27
3.1 Conceptual design of a VLFS 28
3.1.1 Selection of a hypothetical installation site 28
3.1.2 Sizing and Design 29
3.2 Conceptual design of an OWC 33
3.2.1 Selection of the suitable WEC technology 33
3.2.2 Sizing and Design 34
3.3 Conceptual design of the VLFS-OWC System 36
3.4 Summary and implications 37
4 LABORATORY TESTS IN WAVE FLUME 39
4.1 Testing facility, testing phases and methodology 40
4.1.1 Wave-current flume and model design 40
4.1.2 Measuring/observation techniques and calibration 42
4.1.3 Hydrodynamic test conditions 47
4.1.4 Testing phases and methodology 48

4.2 Phase I: Fixed OWC model 50

4.2.1 OWC model design and construction 50
4.2.2 Preliminary tests and implications for the main tests 53
4.2.3 OWC Model Setup for the main tests 55
4.2.4 Testing programme for Phase I 56
4.2.5 Preliminary data analysis and results of the phase I tests 58
4.2.6 Summary of key results and implications for the detailed analysis 65

4.3 Phase II: VLFS model without OWC devices 66

4.3.1 VLFS model design and construction 66
4.3.2 Preliminary tests and implications for the main tests 67
4.3.3 VLFS Model setup for main tests 69
4.3.4 Testing programme for Phase II 71
4.3.5 Preliminary data analysis and results 72
4.3.6 Summary of key results and implications for the detailed analysis 75

4.4 Phase III: VLFS-OWC Model 75

4.4.1 VLFS-OWC model design and construction 75
4.4.2 Preliminary tests and implications for the main tests 77
4.4.3 VLFS-OWC Model setup for the main tests 78
4.4.4 Testing programme for Phase III 79
4.4.5 Preliminary data analysis and results 80
4.4.6 Summary of key results and implications for the detailed analysis 85

4.5 Summary and implications 85

5 EMPIRICAL MODELS PREDICTING THE HEAVE MOTION OF VLFS-OWC SYSTEM AND THE PERFORMANCE OF OWC INTEGRATED IN A VLFS 87

5.1 Relative Capture Width of fixed OWC 88

5.1.1 Relative Capture Width of fixed OWC in regular waves 89
5.1.2 Relative Capture Width of Fixed OWC in irregular waves 90

5.2 Relative heave motion of a VLFS-OWC System 91

5.2.1 Relative heave motion of VLFS-OWC System in regular waves 92
5.2.2 Relative heave motion of VLFS-OWC System in irregular waves 93

5.3 Relative Capture Width of floating OWCs (integrated in a VLFS) 93

5.3.1 Relative Capture Width of floating OWC in regular waves 94
5.3.2 Relative Capture Width of floating OWC in irregular waves 96

5.4 Comparative analysis of fixed OWC vs floating OWC (integrated in VLFS) under regular waves 98

5.5 Comparative analysis of fixed OWC vs floating OWC (integrated in VLFS) under irregular waves 101

5.6 Empirical formulae for the heave motion of the VLFS-OWC System 103

5.6.1 Empirical formula predicting the heave motion of the VLFS-OWC System in regular waves 103
5.6.2 Empirical formula predicting the relative heave motion of the VLFS-OWC System in irregular waves 104

5.7 Empirical formula for the performance of floating OWCs (integrated in VLFS) under regular waves 105

5.7.1 Incompressible Simonetti's Multi Regression Model for Relative Capture Width of fixed OWC in regular waves 105

5.7.2 Empirical formula predicting the performance of OWC integrated in VLFS under regular waves 107

5.8 Empirical formulae for the performance of fixed OWC and floating OWCs (integrated in VLFS) under irregular waves 109

5.8.1 Empirical formula predicting the performance of fixed OWC in irregular waves 109

5.8.2 Empirical formula predicting the performance of OWC incorporated in a VLFS under irregular waves 112

5.9 Summary and discussion 114

6 CONCLUDING REMARKS AND OUTLOOKS 117

6.1 General summary of the thesis 117

6.2 Summary and discussion of key results 118

6.3 Outlooks 121

REFERENCES 122

Annex A: Calibration curves for each pressure transducer 128

Annex B: Calibration curves for each hot wire anemometer 130

List of Figures

Fig. 2.1 - Organisation structure of *Chapter 2*. 3
Fig. 2.2 - a) Pontoon-type VLFS (the floating airport Mega Float in Tokyo Bay, Japan) and b) Semi-submersible type VLFS (the floating city Aquapolis in Okinawa, Japan) 5
Fig. 2.3 - Components of a pontoon type VLFSs (Watanabe et al., 2004). 5
Fig. 2.4 - Realization process of a pontoon type VLFS (Suzuki, 2005). 6
Fig. 2.5 - Various Types of Mooring Systems (Watanabe et al., 2004). 7
Fig. 2.6 - Vertical motion of an air-cushion supported structure and compression of the cushion (modified from van Kessel, 2010). 9
Fig. 2.7 - Some of the several applications and project of VLFSs. 10
Fig. 2.8 – Classification of the Wave Energy Converters (WECs) proposed by Falcão, (2010), taking into account the main working principle (from Aqua-RET Project ©, 2012). 15
Fig. 2.9 - Different types of OWCs: (a) fixed (Pico plant); (b and c) floating, (respectively Backward Bent Duct Buoy (BBDB) and Spar-buoy OWC), (Falcão & Henriques, 2014). 16
Fig. 2.10 - Outline of oscillating water column (OWC) device (Takao & Setoguchi 2012). 16
Fig. 2.11 - Some OWC devices, which reach the prototype stage (Webb et al., 2005). 17
Fig. 2.12 - Two basic approaches to theoretical OWC modelling: (a) weightless piston and (b) uniform air pressure model (Falcão et al., 2014). 18
Fig. 2.13 - Schematic representation of the balance required for liquid and gas properties at two scales (Braeunig et al., 2009). 23
Fig. 2.14 - Methodology adopted in the PhD thesis. 26
Fig. 3.1 - Organisation structure of *Chapter 3*. 27
Fig. 3.2 - Annual Energy [kWh/m] and Scatter matrix [MWh/m] extracted at -25 m SWL referred to the hypothetical installation site selected for the VLFS-OWC System in the Mediterranean Sea (Central Tuscany), (Vannucchi, 2012). 28
Fig. 3.3 - Tuscany area: analysis of the non-technical barriers (Vannucchi, 2012). 29
Fig. 3.4 - a) (on the left) Concrete caissons pier of Enel Thermal Power Plant at Torrevaldaliga (RM), b) (on the right) the Spanish company DRACE. 30
Fig. 3.5 - Structural characteristic of each watertight hollow caisson of the VLFS: a) 3D view and b) cross section view. 30
Fig. 3.6 - Multi-module construction method, assembling stage and VLFS assembled. 31
Fig. 3.7 - Schematic representation of the stabilization and overturning of floating body. (CG = centre of gravity, CB = centre of buoyancy, M = metacentre). 32
Fig. 3.8 - Trend of the caisson unit stability varying the freeboard. 32
Fig. 3.9 - Schematic representation of the geometrical characteristics of the OWC device preliminary designed for the integration in the VLFS. 34
Fig. 3.10 - Wave energy variation within the water column assessed for the range of waves H_{m0}=2.0m, 10< T_e<6.0s and h=25m. 35
Fig. 3.11 - Self-rectifying impulse turbine (Falcão, 2004). 35
Fig. 3.12 - 3D view of the conceptual design of the VLFS-OWC system. 36
Fig. 4.1 - Organisation structure of *Chapter 4*. 39
Fig. 4.2 - a) LABIMA wave-current flume and b) Piston-type wave maker. 40
Fig. 4.3 - Entire VLFS-OWC System and model segment tested. 41
Fig. 4.4 - Ultrasonic distance sensors series 943-M18 F4-2D-1C0-330E by HONEYWELL. 42
Fig. 4.5 - Pressure transducers series 46 X, by KELLER. 43
Fig. 4.6 - a) Measurement station developed by LABIMA for the calibration of the pressure transducers in the air; b) Hydrometric rod for the acquisition of the water level in the pipe. 43

Fig. 4.7 - CTA Hot wire anemometer series R11-R20-X by DANTEC. a) Particular of the probe body and of b) the probe support. 44
Fig. 4.8 - a) Measurement station developed at LABIMA for the calibration of the hot wire anemometer; b) Support for sensor built on the separating chamber. 44
Fig. 4.9 - Load Cells Series 54-100-C3 by CELMI. 46
Fig. 4.10 - Picture captured during the video recording of the W1D2V2% under the wave H02. The picture shows the different phase observed between incoming wave and water column oscillations inside the OWC (indicated by the red arrow). 46
Fig. 4.11 - Organization structure and phases of the experiments. 49
Fig. 4.12 - Example of OWC geometry (W1D2V0.5%) tested in Phase I. 50
Fig. 4.13 - 3D view of the three chamber widths W1, W2 and W3 tested in the laboratory experiments (model scale 1:50). 51
Fig. 4.14 - 2D view of the three front wall draughts D tested for each chamber width W (model scale 1:50). 52
Fig. 4.15 - Fixed OWC model setup for the preliminary tests and tested conditions (Table 4-8). 53
Fig. 4.16 - Setup of ultrasonic wave probe and pressure transducer on the OWC device in the preliminary tests of Phase I. 54
Fig. 4.17 - Fixed OWC model setup for the main tests for Phase I and tested conditions (Table 4-8). 55
Fig. 4.18 - Setup of WG, PT and HW on and inside the OWC, during the tests of Phase I. 56
Fig. 4.19 - Time series of water level oscillations inside the OWC chamber for resonance test (a) and Fourier transform spectra of the induced water surface oscillations (b), exemplarily for the OWC models W1D2V1%, W2D1V1% and W2D1V2%. 58
Fig. 4.20 - Natural resonance frequency characterizing the OWC alternatives tested with V2%. 59
Fig. 4.21 - Resonance condition for the geometry W2D1V2% and relative water depth kh=2.07. 59
Fig. 4.22 - Effect of chamber width W, on: a) water surface elevation $\eta_{OWC}(t)$, compared with the $\eta(t)$, recorded at the same location in the same test without any model, b) air pressure $P_{OWC}(t)$ and c) airflow velocity $U_{OWC}(t)$, for relative water depth kh=2.07 (Time series recorded at the centre of the OWC, exemplarily for regular wave tests (H=0.04m, kh=2.07 & h=0.50m). 60
Fig. 4.23 - Time series acquired at the centre of the OWC. Effect of D on: a) $\eta_{OWC}(t)$, compared with the $\eta(t)$, recorded at the same location in the same test without any model, b) $P_{OWC}(t)$ and c) $U_{OWC}(t)$, for regular wave tests H02 (H=0.04m, kh=2.07 & h=0.50m). 61
Fig. 4.24 - Air volume flux Q_{OWC} vs. air chamber pressure P_{OWC} for the nine vent diameters V with the associated damping coefficients K used in the parameter study. 62
Fig. 4.25 - Effect of damping coefficients K on: (a) Air pressure oscillation amplitude ΔP_{OWC}, (b) water surface oscillations $\Delta\eta_{OWC}$ at the centre of the OWC chamber and on: (c) maximum air volume flux Q_{max} in the pipe for regular wave tests (H=0.04m, kh=1.22-3.15 & h=0.50m) 62
Fig. 4.26 – Scatter plot between the incident wave recorded at WG5 in absence of the OWC model and the same incident waves calculated by the reflection analysis for: a) W1D1V0.5%, b) W2D1V0.5% and c) W3D1V0.5% under the irregular waves tested. 64
Fig. 4.27 - *Capture width CW* versus damping K: (a) regular wave tests H02 (H=0.04m, T=1.0s, kh=2.07) and (b) irregular wave tests H5 (H_{m0}=0.06m, T_p=1.1s, kh=1.85). 65
Fig. 4.28 - VLFS model (a) Methacrylate box units composing the VLFS; (b) Side view of one semi-submerged box unit; (c) Valve equipping each box unit for buoyancy control. 66
Fig. 4.29 - VLFS assembled in laboratory for the tests of Phase II. 67
Fig. 4.30 - VLFS model setup of the preliminary tests and tested conditions (Table 4-14). 67
Fig. 4.31 - VLFS model setup of the main tests for Phase II and tested conditions (Table 4-14). 69
Fig. 4.32 - Deployed sensors (DM: displacement meters, PT: pressure transducer and LC: load cells) on and inside the VLFS model for tests in Phase II. 70

Fig. 4.33 - Longitudinal distributions of the heave motion amplitudes he_m, recorded for the two VLFS models: a) model with L_{VLFS}=2.60m and b) model with L_{VLFS}=5.60m, subject to regular waves (H= 0.04 -0.06m & kh=1.02 -3.15 in water depth h=0.50m). 72
Fig. 4.34 - Relative heave amplitude he^* versus relative VLFS length L^*. Heave measured at two points located at 0.10m and 1.30m from the leading edge of both VLFS models with L_{VLFS}=2.6 & 5.6m subject to regular waves (H=0.04 -0.06m & kh=1.02 -3.15 in water depth h=0.50m). 73
Fig. 4.35 - Relative tension $N^*= N_e/\rho g \cdot B \cdot G \cdot L_{VLFS}$ versus relative water depth kh, exemplarily for the two upper cables holding the units of both tested VLFS model lengths L_{VLFS}=2.6 & 5.6m under regular wave tests (0.04 ≤H≤ 0.06m & 1.02 ≤kh≤ 3.15). 74
Fig. 4.36 - Relative air pressure $P^*=Pi/\rho \cdot g \cdot L_{VLFS}$, versus relative water depth kh, exemplarily for the first VLFS unit (i.e. the leading edge) of both tested VLFS model lengths L_{VLFS}=2.6 & 5.6m under regular wave tests (0.04≤H≤0.06m & 1.02≤kh≤3.15). 74
Fig. 4.37 - Example of VLFS-OWC geometry (M0L_{VLFS}2-W2D1V2%) tested in Phase III (Table 4-18). 76
Fig. 4.38 - VLFS-OWC model setup for the preliminary tests and tested conditions (Table 4-18). 77
Fig. 4.39 - Support of the hot-wire anemometer used during the tests of Phase III. 77
Fig. 4.40 - VLFS-OWC model setup of the main tests for Phase III (Table 4-18). 79
Fig. 4.41 - OWC integrated in the VLFS (M0L_{VLFS}1): Effect of OWC chamber width W, on: (a) inner water surface oscillations $\eta_{OWC}(t)$, compared with the $\eta(t)$, recorded at the same location in the same test without any model, b) inner air pressure $P_{OWC}(t)$ and c) inner airflow velocity $U_{OWC}(t)$, for regular wave tests (H=0.04m and kh=2.07). 81
Fig. 4.42 - Effect of the damping coefficients K on (a) Air pressure oscillation amplitude ΔP_{OWC}, (b) water surface oscillations $\Delta\eta_{OWC}$ at the centre of the OWC chamber and on (c) maximum air volume flux Q_{max} in the pipe, for the OWC integrated in the shorter VLFS model (L_{VLFS}=2.60m) subject to regular wave tests (H=0.04m & 1.22<kh<3.15). 82
Fig. 4.43 - a) Air pressure oscillation amplitude ΔP_{OWC} and b) water surface oscillations $\Delta\eta_{OWC}$ at the centre of the OWC chamber, c) maximum airflow velocity U_{max} in the pipe, related to the chamber width W=0.30m and damping coefficients K=1473kg$^{1/2}$m$^{-7/2}$, for the OWC integrated in both VLFS model lengths (L_{VLFS}=2.60 & 5.60m) subject to regular wave tests (0.02≤H≤0.06m & 1.85≤kh≤2.68). 83
Fig. 4.44 - Capture width CW versus damping K for OWC models integrated in VLFS models with L_{VLFS}= 2.60 & 5.60m subject to a) regular waves H02 (H=0.04m, T=1.0s) and b) irregular waves H5 (H_{m0}=0.06m, T_p=1.1s). 84
Fig. 5.1 - Organisation structure of Chapter 5. 87
Fig. 5.2 - Relative Capture Width, $CW^*_{fixed,reg}$, versus relative chamber width W*=W/λ, for each fixed OWC model subject to regular waves (H=0.04m & kh=1.22-3.15, with $k=2\pi/\lambda$) 89
Fig. 5.3 - Relative Capture Width, $CW^*_{fixed,reg}$, versus relative front wall draught, D^*, for each fixed OWC model subject to regular waves (H=0.04m & kh=1.22-3.15, with $k=2\pi/\lambda$) 90
Fig. 5.4 - Relative Capture Width, $CW^*_{fixed,irr}$, versus relative chamber width $W^*=W/\lambda_p$, for each fixed OWC model subject to irregular waves (H_{m0}=0.02-0.04m & kh=1.85-2.68, with $k=2\pi/\lambda_p$). 90
Fig. 5.5 - Relative Capture Width, $CW^*_{fixed,irr}$, versus relative front wall draught, D^*, for each fixed OWC model subject to irregular waves (H_{m0}=0.02-0.04m & kh=1.85-2.68, with $k=2\pi/\lambda_p$). 91
Fig. 5.6 - Relative heave motion, he^*, versus relative VLFS length $L^*=L_{VLFS}/\lambda$. Heave is measured at the leading edge, where the OWC is integrated. Results are related to the VLFS-OWC model subject to regular waves (H=0.04-0.06m & kh=1.02-3.15, with $k=2\pi/\lambda$). 92
Fig. 5.7 - Relative heave motion, he^*, versus relative VLFS length L^*. Heave measured at the leading edge, where the OWC is integrated. Results related to the VLFS-OWC model subject to irregular waves (H_{m0}=0.02-0.06m & kh=1.85-2.68., with k=2π/λ_p). 93

Fig. 5.8 - Relative Capture Width, $CW^*_{float,reg}$, versus relative chamber width W*= W/λ, for each OWC model integrated in the VLFS (LVLFS=2.60m & 5.60m) subject to regular waves (H=0.04m & kh=1.22-3.15, with k=2π/λ). 94
Fig. 5.9 - Relative Capture Width, $CW^*_{float,reg}$, versus relative VLFS length $L^*=L_{VLFS}/\lambda$, for each OWC model integrated in the VLFS subject to regular waves (H=0.04m & kh=1.22-3.15, with k=2π/λ). 95
Fig. 5.10 - Relative Capture Width, $CW^*_{float,reg}$, versus relative heave motion $he^*=he/a_w$ (with a_w=0.5H) for each OWC model integrated in the VLFS subject to regular waves (H=0.04m & kh=1.22-3.15 with k=2π/λ). 95
Fig. 5.11 - Relative Capture Width, $CW^*_{float,irr}$, versus relative chamber width $W^*= W/\lambda_p$, for each OWC model integrated in the VLFS (L_{VLFS}=2.60m & 5.60m) subject to irregular waves (H_{m0}=0.02-0.04m & kh=1.85-2.68, with k=2π/λ_p). 96
Fig. 5.12 - Relative Capture Width, $CW^*_{float,irr}$, versus relative VLFS length $L^*=L_{VLFS}/\lambda_p$, for each OWC model integrated in the VLFS subject to irregular waves (H_{m0}=0.02-0.04m & kh=1.85-2.68, with k=2π/λ_p). 97
Fig. 5.13 - Relative Capture Width $CW^*_{float,irr}$ versus relative heave motion $he^*=he/aw$ for each OWC model integrated in the VLFS subject to irregular waves (H_{m0}=0.02-0.04m & kh=1.85-2.68, with $k=2\pi/\lambda_p$). 97
Fig. 5.14 - Comparison between $CW^*_{float,reg}$ and $CW^*_{fixed,reg}$ versus relative heave motion he^* for all the design alternatives tested for fixed OWC and VLFS-OWC models subject to regular waves (H=0.04m & kh=1.22-3.15, with $k=2\pi/\lambda$). 98
Fig. 5.15 - Comparison between $CW^*_{float,reg}$ and $CW^*_{fixed,reg}$ versus relative VLFS length L^* for all design alternatives tested for fixed OWC and VLFS-OWC models subject to regular waves (H=0.04m & kh=1.22-3.15, with k=2π/λ). 99
Fig. 5.16 - Comparison between $CW^*_{float,reg}$ and $CW^*_{fixed,reg}$ versus the relative chamber width W^* for all the design alternatives tested for fixed OWC and VLFS-OWC models subject to regular waves (H=0.04m & kh=1.22-3.15 with k=2π/λ). 99
Fig. 5.17 - Comparison of $CW^*_{float,reg}$ and $CW^*_{fixed,reg}$ versus relative front wall draught D^* for all design alternatives tested for fixed OWC and VLFS-OWC models subject to regular waves (H=0.04m & kh=1.22-3.15, with $k=2\pi/\lambda$). 100
Fig. 5.18 - Comparison of capture width ratio $CW^*_{float,irr}$ and $CW^*_{fixed,irr}$ versus relative heave motion he^* for all design alternatives tested for fixed OWC and VLFS-OWC models subject to irregular waves (h^*=1.85-2.68). 101
Fig. 5.19 - Comparison of $CW^*_{float,irr}$ and $CW^*_{fixed,irr}$ versus relative VLFS length L^* for all design alternatives tested for fixed OWC and VLFS-OWC models subject to irregular waves (H_{m0}=0.02-0.04m & kh=1.85-2.68, with $k=2\pi/\lambda_p$). 102
Fig. 5.20 - Comparison of $CW^*_{float,irr}$ and $CW^*_{fixed,irr}$ versus relative chamber width W^* for all design alternatives tested for fixed OWC and VLFS-OWC models subject to irregular waves (H_{m0}=0.02-0.04m & kh=1.85-2.68, with $k=2\pi/\lambda_p$). 102
Fig. 5.21 - Comparison of $CW^*_{float,irr}$ and $CW^*_{fixed,irr}$ versus relative front wall draught D^* for all design alternatives tested for fixed OWC and VLFS-OWC models subject to irregular waves (H_{m0}=0.02-0.04m & kh=1.85-2.68, with $k=2\pi/\lambda_p$). 103
Fig. 5.22 - Relative heave motion $he^*=he/0.5H$ of the VLFS-OWC models subject to regular waves (h^*=1.22 -3.15). 104
Fig. 5.23 - Empirical model for relative heave motion he^*_{irr} of VLFS-OWC models subject to irregular waves (h^*=1.85 -2.68). 104
Fig. 5.24 - Scatter plot between the *incompressible MRM* prediction model and laboratory data (Phase I) of $CW^*_{fixed,reg}$ (named ε_{OWC} in figure) for different ranges of the non-dimensional parameters W^*, D^* and h^* (Simonetti et al., 2016). 105
Fig. 5.25 - Relation between relative capture width ratio CW^*_{float} / CW^*_{fixed} and input parameter Γ, defined by Eq. 5.24. 107

Fig. 5.26 - Scatter plot between $CW^*_{float,reg}$ predicted by Eq. 5.23 and $CW^*_{float,reg}$ obtained from laboratory data (Phase III) for different ranges of the dimensionless parameters W^*, D^*, K^* and L^* under regular waves (h^*=1.22-3.15). 108
Fig. 5.27 - Scatter plot between calculated capture width $CW^*_{float,reg}$ using Eq. 5.26 and laboratory data (Phase III) of $CW^*_{float,reg}$ for different ranges of the dimensionless parameters W^*, D^*, K^* and L^* in regular waves (h^*=1.22-3.15). 108
Fig. 5.28 - Procedure for the application of the proposed correction factor, $CF_{float,reg}$ to extend Simonetti's *incompressible MRM model* (Eq. 5.13) in order to obtain a prediction formula of the *relative Capture Width* $CW^*_{float,reg}$, for a floating OWC (integrated in a VLFS) in regular waves. 109
Fig. 5.29 - Capture width CW^*_{fixed} of a fixed OWC obtained from laboratory experiments with irregular waves (Phase I) and CW^*_{MRM} predicted by Simonetti's *MRM model* (Eq. 5.20) for the same fixed OWC under regular waves with equivalent energy density of the irregular waves tested, as a function of parameter Φ defined by Eq. 5.31 111
Fig. 5.30 - Procedure for the application of the proposed correction factor $CF_{fixed,irr}$ to the capture width CW^*_{MRM} from the *incompressible Simonetti's MRM model* (Eq. 5.20) for fixed OWC in regular waves in order to obtain the new formula to predict capture width $CW^*_{fixed,irr}$, for a fixed OWC in irregular waves 111
Fig. 5.31 - Scatter plot between the formula predicted by applying the Correction Factor, $CF_{fixed,irr}$ to the Simonetti's *MRM model* (Eq. 5.28) and laboratory data (Phase I) of $CW^*_{fixed,irr}$ for different ranges of the dimensionless parameters W^*, D^*, K^*, L^* and M^* in regular waves (h^*=1.85-2.23) 112
Fig. 5.32 - Empirical formula for capture width ratio $CW^*_{float,irr}/CW^*_{fixed,irr}$ as a function of parameter Ω, defined by Eq. 5.35 112
Fig. 5.33 - Scatter plot between relative capture width calculate $CW^*_{float,irr}$ using Eq. 5.34 with Ω according to Eq. 5.35 and CW^*_{float} obtained from laboratory data (Phase III) for different ranges of the dimensionless parameters W^*, D^*, K^* and L^* under irregular waves (h^*=1.85-2.68). 113
Fig. 5.34 - Procedure for the application of the proposed correction factors, $CF_{fixed,irr}$ and $CF_{float,irr}$ to *capture width* CW^*_{MRM} from the *incompressible* Simonetti's *MRM model in regular waves* (Eq. 5.20), in order to obtain the new formula (Eq. 5.37) to predict the *relative capture width* of floating OWC (integrated in a VLFS) in irregular waves, $CW^*_{float,irr}$. 113
Fig. 5.35 - Scatter plot between the formula predicted by applying the correction factors, $CF_{fixed,irr}$ and $CF_{float,irr}$ to Simonetti's *incompressible MRM model* and laboratory data (Phase III) of $CW^*_{float,irr}$ for different ranges of the dimensionless parameters W^*, D^*, K^*, L^* and M^* under irregular waves (h^*=1.85-2.68) 114

List of Tables

Table 3-1: Target waves representative of the hypothetical installation site selected, located in the Central Tuscany at a water depth of -25m SWL. 29
Table 4-1: Scale relations, according to Froude similarity. 41
Table 4-2: Wave trains representative of the hypothetical installation site selected for a VLFS-OWC System and dimensionless water depth kh (model scale 1:50). 47
Table 4-3: Time windows selected for the data analysis. 47
Table 4-4: Characteristic incident wave parameters obtained from time domain analysis of regular wave tests in the flume without any model (W0D0V0). 48
Table 4-5: Characteristic incident wave parameters obtained from frequency and time domain analysis of irregular wave tests in the flume without any model (W0D0V0). 48
Table 4-6: Fixed design parameters of the OWC model (scale 1:50). 51
Table 4-7: Sizes of the vents, mimicking the damping induced by the air turbine for each OWC geometry (model scale 1:50). 52
Table 4-8: Varied design parameters in the OWC model (scale 1:50). 53
Table 4-9: Location of the sensors for the preliminary tests for Phase I. 54
Table 4-10: Location of the sensors for the tests of Phase I. 56
Table 4-11: Testing programme for Phase I. 57
Table 4-12: Natural frequency of the OWC models considered in the RES tests. 59
Table 4-13: Damping coefficient K, calculated for each vent tested. 61
Table 4-14: Design characteristics of the VLFS model (scale 1:50). 67
Table 4-15: Location of the sensors for the preliminary tests for Phase II. 68
Table 4-16: Location of the sensors for the tests in Phase II. 71
Table 4-17: Testing programme for Phase II. 72
Table 4-18: Design characteristics of the VLFS model (scale 1:50). 76
Table 4-19: Location of the sensors for the tests of Phase III. 78
Table 4-21: Testing programme for Phase III. 79
Table 4-22: Testing programme for the additional tests performed in Phase III. 80
Table 5-1: Range of non-dimensional parameters considered for the comparison between relative capture width assessed for fixed OWC and floating OWC in regular waves (H, T). 98
Table 5-2: Range of non-dimensional parameters considered for the comparison between relative capture width assessed for fixed OWC and floating OWC in irregular waves (H_{m0}, T_p). 101
Table 5-3: Range of non-dimensional parameters in which Simonetti et al. 2016 declared the validity of the *incompressible MRM model* predicting the *relative Capture Width* for fixed OWC (CW^*_{MRM}), in regular waves (H, T). 106
Table 5-4: Correction Factors (CF_{50}) proposed by Simonetti et al., (2016) for the air pressure oscillation amplitude within the OWC chamber, Δp_{OWC}, the volume air flow oscillation amplitude, Δp_{OWC} and the relative Capture Width, $CW^*_{fixed,reg}$ for model scale 1:50. 107
Table 5-5: Irregular waves simulated in the laboratory experiments and equivalent regular wave trains having the same incident wave power. 110

List of Notations

Roman notations:

a_w	wave amplitude [m]
B	OWC chamber length (perpendicular to wave propagation direction) [m]
B_{VLFS}	VLFS width [m]
CW	capture width [m]
CW^*	relative capture width [-]
$CW^*_{fixed,irr}$	relative capture width of fixed OWC in irregular waves [-]
$CW^*_{fixed,reg}$	relative capture width of fixed OWC in regular waves [-]
$CW^*_{float,irr}$	relative capture width of floating OWC in irregular waves [-]
$CW^*_{float,reg}$	relative capture width of floating OWC in regular waves [-]
D	OWC front wall draught [m]
D^*	dimensionless OWC front wall draught [-]
D_c	vertical distance of the free surface within the aircushion [m]
E	tension [Volt]
E_0	tension acquired without airflow [Volt]
EI	flexural rigidity per unit length [kg·m^3/s^2 or N·m^2]
E_k	kinetic energy [J/m]
Ep	potential energy [J/m]
F_c	Freeboard [m]
f_{OWC}	OWC natural frequency [Hz]
g	gravitational acceleration [m/s^2]
G	OWC back wall length [m]
g^*	dimensionless gravitational acceleration [-]
G_{VLFS}	VLFS draft [m]
H	incident wave height [m]
h	water depth [m]
h^*	dimensionless water depth [-]
h_c	height of the air-cushion underneath the structure [m]
he	heave floating motion [m]
he^*	dimensionless heave motion [-]
he_m	average heave motion amplitude [m]
H	mean wave height [m]
H_{m0}	significant wave height [m]
H_{rms}	root mean square wave height [m]
i^*	impulsiveness parameter [-]
k	wavenumber of the incident wave [1/m]
K	turbine damping coefficient [kg$^{1/2}$m$^{-7/2}$]
K^*	dimensionless turbine damping [-]

K_{opt}	optimal damping K for a given OWC geometry [$kg^{1/2}m^{7/2}$]
L^*	dimensionless VLFS length [-]
L_{VLFS}	VLFS length [m]
M_{VLFS}	VLFS mass [kg]
$M_{VLFS\text{-}OWC}$	VLFS-OWC mass [kg]
M^*	relative VLFS-OWC mass [-]
N_e	tension at the horizontal cables holding together the VLFS units [N]
N_e^*	relative tension [-]
P^*	relative ait pressure in the VLFS unit [-]
Pi	air pressure in the VLFS unit [Pa]
P_{OWC}	relative ait pressure in the OWC air chamber [Pa]
pr	vertical distribution of the wave energy amount [-]
Q_{OWCmax}	average value of the maximum air volume flux in the OWC [m^3/s]
Q_{OWC}	air volume flux through the OWC top cover pipe [m^3/s]
$S_{TopCover}$	OWC top cover surface [m^2]
T	incident wave period [s]
T_e	wave energy period or wave spectral period $T_{m\text{-}10}$ [s]
th_{fbt}	OWC front, back and top cover wall thickness [m]
th_s	side wall thickness [m]
T_{OWC}	average OWC inner oscillation period [s]
T_p	peak period [s]
T_{test}	length of the analysis windows [s]
U_m	average air velocity along the pipe cross section [m/s]
U_{max}	maximum airflow velocity [m/s]
U_y	vertical component of air velocity in the OWC top cover pipe [m/s]
V	diameter of the vent on the OWC top cover [m]
W	OWC chamber width in wave propagation direction [m]
W^*	dimensionless OWC chamber width in wave propagation direction [-]

Greek notations:

ΔP_{OWC}	OWC pressure oscillation amplitude in the average T_{OWC} [kg/ms^2]
$\Delta\eta_{OWC}$	water surface displacement in the average T_{OWC} [m]
η_{OWC}	water level at the centre of the OWC chamber [m]
Θ	gas law index [-]
λ	wavelength obtained from the wave period T [m]
λ_p	wavelength obtained from the peak period T_p [m]
λ_c	characteristic length of a VLFS [m]
Π_{abs}	period average pneumatic power absorbed by the OWC [W]
Π_{wave}	period averaged incident wave power per unit width [W/m]
Π^*	non-dimensional pressure parameter [-]
ρ_a	air density [kg/m^3]
ρ_w	water density [kg/m^3]

ρ_w*	relative water density [-]
Υ	compressibility factor of the aircushion [-]
ω	incident wave frequency [Hz]
Ω	compressibility factor of the aircushion [-]

Abbreviations:

CB	Centre of buoyancy
CFD	Computational Fluid Dynamics
$CF_{fixed,reg}$	Correction Factor for the prediction of fixed OWC in irregular waves from MRM
$CF_{float,irr}$	Correction Factor for the prediction of floating OWC in irregular waves from MRM
$CF_{float,reg}$	Correction Factor for the prediction of floating OWC in regular waves from MRM
CF_{50}	Correction Factor for the air compressibility scale effects
CG	Centre of gravity
DM	Displacement Meters
FFT	Fast Fourier Transform
HW	Hot Wire anemometer
LC	Load Cell
MRM	Incompressible Multiple Regression Model
RMSE	Root Mean Square Error
OTD	Overtopping Device
OWC	Oscillating Water Column
PT	Pressure Transducer
PTO	Power Take Off
SWL	Still Water Level
VLFS	Very Large Floating Structure
WAB	Wave Activate Body
WEC	Wave Energy Converter
WG	Wave Gauge

1 Introduction

The Earth's land surface measures 148,300,000km^2, while the total area of the Earth's surface is 510,083,000km^2. Thus, the water surface area takes up 70% of the Earth's total surface area, while the land only 30%, (i.e., less than one third of the entire surface).

In the beginning of the third millennium, humanity ran into a new problem: the lack of land, which is becoming crucial with the fast growth of the Earth's population and corresponding expansion of industrial development and urban agglomerations. Countries such as Korea (693ab./km^2), Netherlands (394ab./km^2), Belgium (338ab./km^2), Japan (337ab./km^2), Italy (197ab./km^2) and China (137ab./km^2), have a very high population density. Numerous other countries in Europe and Asia are approaching the same density (Demographia, 2012).

Moreover, several developed countries have been successfully reclaiming land from the sea, in order to create new space and to reduce their overloaded land space. For instance, Netherlands, Japan, Singapore, Dubai and other countries have expanded their areas significantly through land reclamation (Kolman, 2012). Such works are, however subject to constraints, such as the negative environmental impact on the coastlines of the country and neighbouring countries and marine ecological system, as well as huge economic costs in reclaiming land from deep coastal waters, especially when the sand for reclamation has to be bought from other countries. In addition, land reclamation is a good solution only for rather shallow waters (i.e., depth less than 20m).

In response to the needs and issues mentioned above, the researchers and engineers have proposed an interesting and attractive solution, such as the construction of Very Large Floating Structures (VLFSs) (Watanabe et al., 2004).

The VLFSs can be located near the shore as well as rather far into the open sea and can be have a multipurpose use (e.g., power plant, storage facilities, bridges, rescue bases, entertainment facilities, airports, habitations, etc.).

At the same time the use of renewable energy is stimulated for the growing fossil fuels depletion and pollution, then the VLFS design cannot ignore the offshore renewable energy, which could arise for example from, wind, waves, current and thermal gradients.

Since the present study focuses on the harvesting of the wave energy using one of the several existents Wave Energy Converter technologies (WECs), it is motivated the development of a suitable and environmentally friendly VLFS-WEC System, in which the WECs integrated could contribute to supply energy for part of the activities and/or for some services and facilities located on the floating platform.

1.1 Objectives

Based on the aforementioned considerations and motivations, the main objectives of this research, which will be specified more precisely at the end of *Chapter 2*, are:

1) the preliminary sizing and design of a Very Large Floating Structure equipped with Oscillating Water Column devices (i.e., namely VLFS-OWC System), taking into account its reliability and feasibility in a site selected in the Mediterranean Sea and characterized by a moderate wave climate (mean annual wave power of 3kW/m).
2) the study of the effect of the mutual interactions between VLFS and OWC technologies on the performance of the integrated OWC devices in terms of wave energy absorption.
3) the development of empirical models for the prediction of the performance of floating OWCs (integrated in a VLFS), in order to support the engineers in the preliminary design stage of the OWC devices, starting from the knowledge of the characteristics wave parameters of the site selected for the installation.

1.2 Methodology

To achieve the aforementioned objectives, a methodology essentially based on small-scale physical modelling is adopted. The entire study is organized in the following stages, which as for the objectives will be specified more precisely in the last section of *Chapter 2*, based on the implications drawn from the results of the review and analysis of the current knowledge:

- review and analysis of the state of the art of the VLFS and the OWC technologies with the purpose of identifying the knowledge gaps and the implications for the selection and sizing of the geometry of the VLFS and the OWC device to be integrated, including the most relevant approaches to be used in this study;
- conceptual design of the VLFS-OWC System, based on the selection a hypothetical installation site located in the Mediterranean Sea and characterization of the representative sea state to be used in the experiments;
- small-scale physical models aimed at providing a preliminary analysis of the effect of different design parameters on the complex interactions between the VLFS and the integrated OWC and the performance of the OWC device. To address these objectives, the experiments are carried adopting a tiered approach: (i) Phase I: OWC models in fixed condition; (ii) Phase II: VLFS models without the OWCs and (iii) Phase III: VLFS equipped with OWCs models. Preliminary scale model tests, using a very simplified condition allows the optimization of the model setup and programme of each test phase.
- dimensional analysis and development of empirical models for the prediction of the floating response (i.e., heave motion) of the VLFS-OWC System and for the performance of floating OWC (integrated in a VLFS), based on the results achieved in the laboratory tests.

Both objectives and methodology are specified more precisely in the last section of *Chapter 2* (see *section 2.3*) based on the implications drawn from the results of the review and analysis of the current knowledge.

2 Current knowledge on Very Large Floating Structures (VLFSs) and Oscillating Water Column devices (OWCs)

In this chapter, the current knowledge on Very Large Floating Structures (VLFSs) and Oscillating Water Column devices (OWCs) is reviewed and analysed, in order to identify the justifications and the implications for the selection of the suitable VLFS geometry and the proper OWC devices to be integrated in the VLFS (*Chapter 3*).

The available approaches related to numerical and physical modelling of VLFS and OWC devices are also reviewed and analysed. As a result, the knowledge gaps and the open issues are identified, so as to plan and find the relevant requirements for the small-scale model tests aimed at providing the basic understanding for the development of a new empirical model predicting the performance of the OWC integrated in VLFS in a moderate wave climate. The organization structure and procedure adopted in *Chapter 2* are briefly summarized in Fig. 2.1.

As a final result of this review, the tentative objectives and methodologies, introduced in *Chapter 1*, will be specified more precisely at the end of this chapter.

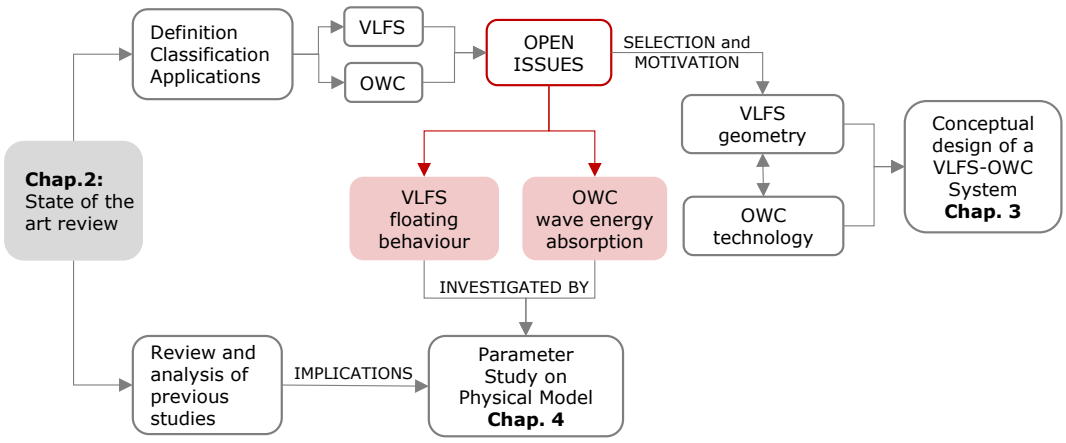

Fig. 2.1 - Organisation structure of *Chapter 2*.

2.1 Very Large Floating Structures (VLFSs)

Very Large Floating Structure (VLFS) is an exciting new solution for land creation from the sea. This technology has several advantages over the conventional land reclamation approach, due to its environmentally friendliness to the marine ecosystem, its cost effectiveness in larger water depths, and its insulation from seismic shocks, since it is inherently base isolated (Wang et al., 2008). Furthermore, a VLFS can be used for various applications such as floating airports, floating bridges, floating oil storage, floating energy plants, floating piers and floating hotels. Given its broad applications, VLFS represents the key technology for mankind to colonize the oceans for space, food, and energy.

To select the proper VLFS to be developed (see *Chapter 3*) and investigated by means of small-scale laboratory experiments (see *Chapter 4*), the current knowledge on VLFSs, including a general definition and classification as well as previous experimental and numerical modelling approaches, is critically reviewed and analysed in the following sections.

2.1.1 Definition, classification and processes

Suzuki and Yoshida (1996) proposed that for a floating structure to be classified as "*very large*", its length must be greater than the incident wavelength, λ, and larger than the characteristic length, λ_c, defined by its flexural rigidity and the fluid density.

Therefore, since the elastic response is dominant, as rational measure to distinguish VLFS from the conventional floating offshore structures, in terms of global response, the characteristic length λ_c was proposed, modelling the floating structure as a uniform beam and the hydrostatic restoring force as an elastic foundation:

$$\lambda_c = 2\pi \left(\frac{EI}{\rho g}\right)^{\frac{1}{4}} \tag{2.1}$$

where, EI [kg·m^3/s^2 or N·m^2] is the flexural rigidity per unit length; ρ [kg/m^3] is the fluid density and g [m/s^2] is the gravitational acceleration.

If the length of the structure is less than the characteristic length, λ_c, the response is dominated by rigid body motion, else by elastic deformations (Suzuki et al., 2006).

In terms of the construction method, VLFSs are classified in two wide categories:

- *Single-module type* method, in which the VLFS is built in one piece;
- *Multi-module type* method performed assembling several smaller modules together.

In terms of their geometry, Watanabe et al., 2004 classified VLFSs in:

- *Pontoon-type* (or Mega-Float) (Fig. 2.2a): is also known in the literature as mat-like VLFS for its small draft related to the length dimension. It is a simple flat structure floating on the sea level, characterized by high stability, low manufacturing costs and easy maintenance and repair. However, due to their structural characteristics, the pontoon type VLFSs are subjected to significant hydro-elastic responses when interacting with the waves and are suitable for very calm seas.

- *Semi-submersible type* (Fig. 2.2b): is a structure raised above the sea level using column tubes, piles or other bracing systems to minimize the effects of waves while maintaining a constant buoyant force then are usually used in open sea. When the semi-submersible VLFSs are attached to the seabed using vertical tethers with high pretension, they are referred to as tension-leg platforms.

a) Pontoon-type VLFS b) Semi-submersible type VLFS

Fig. 2.2 - a) Pontoon-type VLFS (the floating airport Mega Float in Tokyo Bay, Japan) and b) Semi-submersible type VLFS (the floating city Aquapolis in Okinawa, Japan)

Apart from alleviating pressure on land demand and the easy and fast construction, relocation, transportation and enlargement, pontoon type VLFSs are suitable for use in sites characterized by not exceptionally energetic sea states and behave hydro-elastically under wave action (Shuku, et al., 2001).

In general, a pontoon-type VLFS consists of five main components (Fig. 2.3):

1) a main floating body;
2) an access bridge or a floating road, for the connection with the coast;
3) a mooring facility or station keeping the structure in a specific place;
4) a breakwater for reducing the impact of wave forces on the floating structure (usually needed if the wave height is greater than 4.0m);
5) structures, facilities and communications located on a VLFS.

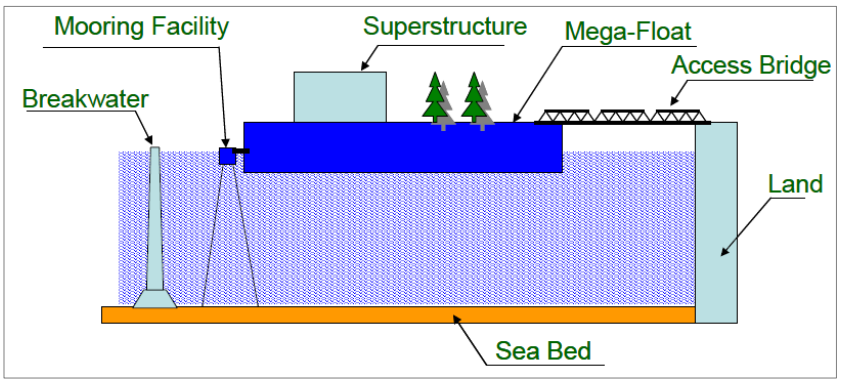

Fig. 2.3 - Components of a pontoon type VLFSs (Watanabe et al., 2004).

The construction process of a pontoon-type VLFS, can be summarized as in Fig. 2.3 and in the steps described below (Suzuki, 2005):

- Analysis of the floating motion and the effect of horizontal forces due to waves, which in VLFSs are balanced by catenary chains or tension legs, depending of the mooring system.
- Evaluation and approval of the design by the authority. In this contest, the environmental issues play an important role, so related project implications need to be carefully taken into consideration just since the phase of the conceptual design.
- Fabrication and towing of each unit of the VLFS.
- Installation of the VLFS performed by joining the structure units at sea, taking into account the influence of both wave conditions and unit joining sequences on the responses of structure and performance.
- Maintenance plan of the VLFS for at least 100 years, which requires environmental impact studies and regular inspection procedures.

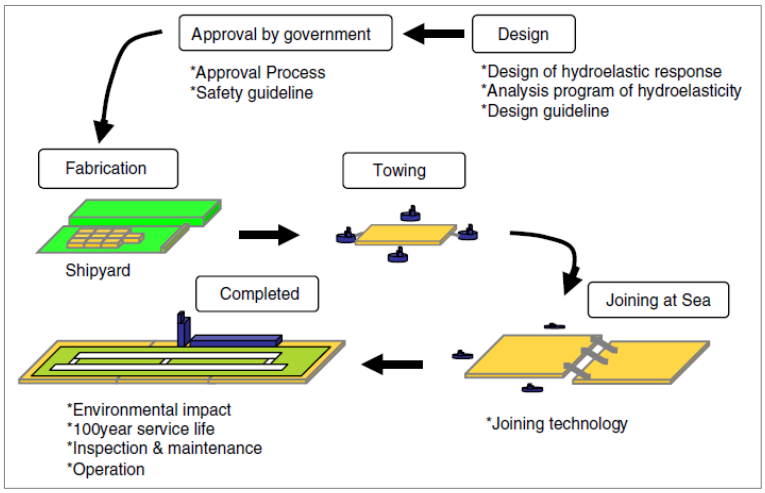

Fig. 2.4 - Realization process of a pontoon type VLFS (Suzuki, 2005).

Hydro-elastic response of a VLFS

Generally, the design methods of ships or ocean structures are based on the rigid body assumption. However, VLFS, which is much bigger than conventional ships cannot be considered as rigid bodies, therefore, the comprehension of its hydro-elastic behaviour, considering the VLFS structural flexibility is essential.

The fundamental concept of hydro-elastic analysis was proposed in 1980s and the development of effective tools of hydro-elastic analysis was a challenge for many researchers in the last two decades (Kim et al., 2011).

The hydro-elastic response of a VLFS under regular waves can be analytically described, considering the structure like a long uniform floating plate. The equation of vertical displacement of a thin beam is given as (Ohmatsu, 2005):

$$m\frac{\partial^2\zeta}{\partial t^2} + EI\frac{\partial^4\zeta}{\partial x^4} + \rho g\zeta = -i\omega\rho\phi \tag{2.2}$$

where, ζ(x, t) is the vertical displacement; m is the mass of the plate and EI is the flexural rigidity. From Eq.2.2 and the body boundary condition:

$$\frac{\partial\phi}{\partial z} = \frac{\partial\zeta}{\partial t} \quad at\ \ z = 0 \tag{2.3}$$

Then it is possible to derive the following relation, named "*modified free surface condition*":

$$\left(1 - \frac{m\omega^2}{\rho g} + \frac{EI}{\rho g}\Delta^2\right)\frac{\partial\phi}{\partial z} = \frac{\omega^2}{g}\phi = K\phi \tag{2.4}$$

If m and EI are equal to 0, the result becomes a free surface condition of the water surface. By the same argument, from this modified free surface condition it is possible to derive the "*modified dispersion relation*":

$$\left[1 - \left(\frac{\omega}{\omega_0}\right)^2 + \left(\frac{k}{k_p}\right)^4\right] k\tanh kh = \frac{\omega^2}{g} \equiv K \tag{2.5}$$

in which: $\omega_0=\rho g/m$ corresponds to heave mode natural frequency, and $k_p^4= \rho g/EI$ to the characteristic wave number. When the wave number k becomes very small, the phase velocity of elastic waves becomes the same as that of water waves (Ohmatsu, 2005).

Ohmatsu, (2005) stated that for usual VLFS, and for practical periodic waves, the phase velocity of elastic waves is bigger than that of water waves except in the case of periodic extremely long wave. Moreover, to assess the VLFS structural responses he categorized the various calculation methods in two main representative categories of elastic deformation:

I. *Mode-expansion method*: in which the elastic motion is represented by a summation of many modes of motion.
II. *Mesh method*: in which the elastic motion of a thin plate is represented by the succession of vertical displacement of these substructures.

2.1.2 Design criteria

Since the design life of a VLFS is typically from 50 to 100 years, the design criteria are substantially greater than those adopted for conventional ships and offshore structures. Special criteria are indicated not only for structural design but also for inspection and maintenance, considering that normal dry-docking for maintenance and repair is generally not possible (Suzuki et al., 2006).

a) VLFS shape

The selection of the proper VLFS shape depends on its purpose, the sea currents, the wave behaviour on a site, etc. Recent studies show that the hydro-elastic response of a VLFS could be significantly reduced by altering its shape, in particular the leading edge and the aft end (Wang et al., 2010). The elliptical and the triangular fore-end shapes were found to be the most effectives in mitigating the hydro-elastic response, because the incident wave energy is easily scattered away due to the elliptic shape of the floating structure. However, Tay et al., (2012) found that the effectiveness of the elliptical and polygonal fore-ends diminishes when the incident wavelength increases, as compared to the rectangular shape, because the response is dominated by inertia forces, and as a consequence the rectangular shape response, with a larger mass is the smallest.

b) Connectors

The VLFSs, due to their massive sizes, are usually built by connecting several modules (i.e., the VLFS units), which are fabricated in shipyard and connected on site by welding or by using rigid connectors.

Fu et al., (2007) and Wang et al., (2010b) proposed the use of hinge or semi-rigid connectors since the non-rigid connectors are more effective in reducing the hydro-elastic response as compared with the rigid connectors. However, to date there is still work to be done on developing a robust and economical connection system for VLFS units.

c) Mooring Systems

The mooring system is used to ensure that the VLFS is kept in position so that the facilities installed on the floating structure can be reliably operated as well as to prevent the structure from drifting away under critical sea conditions and storms. A freely drifting VLFS may lead to not only damage to the surrounding facilities but also to the loss of human life if it collides with ships.

The existent mooring systems may be divided into many methods (Fig. 2.5): i) the *dolphin-frame guide*, ii) the mooring by *cable* and *chain*; iii) the *tension leg* and iv) the *pier/quay wall* method. Operating conditions and environmental factors such as waves, wind forces and depth determine the type of mooring system to be chosen.

After the selection of the suitable method, the design procedure for the mooring system may take into account the shock absorbing material, the quantity and layout of devices to meet the environmental conditions and the operating conditions and requirements (Watanabe et al., 2004).

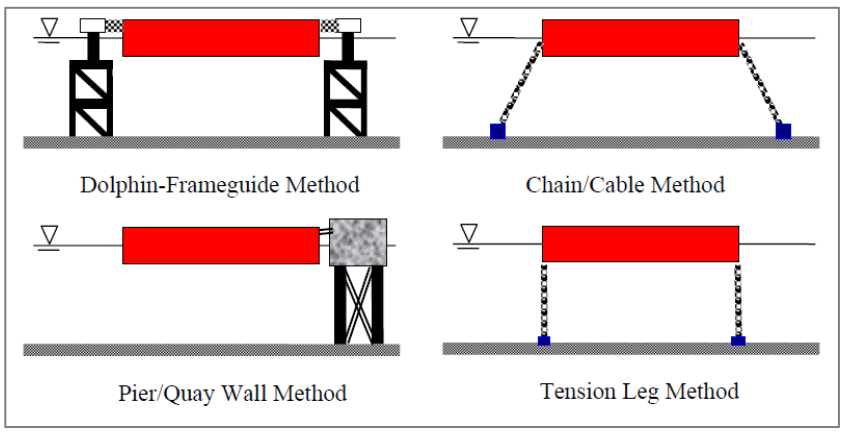

Fig. 2.5 - Various Types of Mooring Systems (Watanabe et al., 2004).

Since due to their large surface areas and relatively small depths, VLFSs behave elastically under wave action, several methods were proposed by engineers to mitigate the VLFS responses for applications that demands stringent serviceability requirements (Wang et al., 2010).

d) Bottom-founded and floating box-like breakwaters

Bottom-founded breakwaters close to the VLFS represent one of the earliest methods. At the state of the art, a general rule of thumb is to have a breakwater if the significant wave height is greater than 4m (Watanabe et al., 2004).

Utsunomiya et al. (2001) and Ohmatsu (1999) showed that the bottom founded breakwater is very effective in reducing the hydro-elastic response as well as the drift forces. However, such type of breakwaters still has some issues, such as: massive construction material requirements, difficulty in construction occupying precious sea space, not environmentally friendly and coastal erosion due to the reflected waves from the breakwater.

Floating box-like breakwaters moored with mooring lines are proposed as an alternative to the conventional bottom-founded, since they can be easily removed in case of a hypothetical relocation of the VLFS.

e) Anti-motion devices

Anti-motion devices can be conceived as bodies attached to an edge of the VLFS, so they do not need mooring system like floating breakwaters, reducing the time needed for the construction. The first form of anti-motion device was a submerged horizontal or vertical plate attached to the fore-end of the VLFS. Analysis investigating the hydro-elastic response with the submerged vertical plate (Ohta et al., 1999; Watanabe et al., 2003), highlighted an increasing of the reduction in the deflection with increasing the depth of the device and decreasing wavelength. Box-shaped anti-motion devices were experimentally investigated by Takagi et al., (2000), who found that this kind of devices can reduce not only the deformation but also the shearing force and moment of the platform, reducing the motion of VLFS in both beam-sea and oblique sea. The use of a curtain wall with slits and the inverted-L type anti motion devices, was also proposed by Masanobu et al., (2003), in order to mitigate the hydro-elastic response by generating eddies, dissipating wave energy and attenuating the steady drift forces.

Oscillating Water Column (OWC) devices, attached to the fore-end of the VLFS, represent an innovative solution to reduce the floating motion under wave action and were proposed by several researchers (Maeda et al., 2000; Ikoma et al., 2003; Hong et al., 2006; Hong et al., 2007; Kyoung et al., 2008; Hong et al., 2009). Respect to the aforementioned anti-motion devices, the OWCs can achieve more reduction in the floating response due to the capability of the air chamber of the device in absorbing wave energy. Hong et. al, (2007) also proposed the use of an OWC floating breakwater connected to the VLFS by a pin-connector system, demonstrating that a long submerged horizontal plate length minimizes the responses of the fore-end of the VLFS most effectively.

The effect of three-continuous OWCs attached at the VLFS leading edge, with different submerged vertical plate shapes, was investigated. In particular, the wave energy absorbed by synchronizing the wave period with the natural period of the OWC device was studied, proving the effectiveness of the L-shape in reducing the hydro-elastic response (Shigemitsu et al., 2001).

f) Air-cushion System

Pressurized air-cushion system is a concept used in supporting semi-submersibles and concrete gravity structures, in order to stabilize the structure, thus resulting in a reduction of the VLFS displacements, drift forces and mooring loads (Thiagarajan & Morris-Thomas 2006).

The units of VLFS are raised above the water surface (Fig. 2.6), reducing the hull resistance against waves and current flow as well as the surface interference and the water drag. The entrapped air is compressed and this creates an air-cushion, which eliminates the friction between the bottom hull and the water surface (Pinkster, 1997; Lee et al., 2000).

Chenu et al., (2004) performed laboratory tests on 1:100 models in order to study the effect of the air-cushion on the stability and dynamics of Concrete Gravity Structures (CGS). Their study focused on the assessment of the effect of the air-cushion on: i) the metacentric height; ii) the added mass and iii) the natural frequency in heave and pitch of the model. They found that the water depth affects the heave natural frequency and the heave added mass.

Van Kessel (2010) studied the effect of the cushion pressure on the dynamic behaviour of a large air-cushion supported mega-floaters in waves and highlighted the relevant effect of air compressibility. When the structure moves slowly in vertical direction, the free water surface inside the air-chambers moves in the same direction. However, due to the air compressibility, the displacement of the free water surface within the chambers is smaller than the vertical motion of the structure.

The compressibility of the air-cushion mainly depends on the height of the air chamber underneath the structure, h_c, implying a polytrophic process, which can be described as (Van Kessel, 2010):

$$\left(\frac{P(t)}{P_0}\right)^{1/\theta} h_c = constant \tag{2.6}$$

where, θ is the gas law index (generally 1.4 for air); P_0 is the initial pressure inside the air-cushion and $P(t)$ is the pressure inside the air-cushion at the instant t, as in Eq. 2.7:

$$P(t) = P_{atm}\rho g D_c(t) \tag{2.7}$$

In which $D_c(t)$ is the vertical distance between mean sea level and the free surface within the aircushion. If the structure moves Δx downward and the compressibility of air is defined as a small non-dimensional parameter ϒ, then the aircushion is compressed by ϒΔx, (Fig. 2.6). From Eq. 2.6 and Eq. 2.7 and considering the compressibility of air (Van Kessel, 2010):

$$\left(1+\frac{\rho g}{P_{atm}}D_c(t)\right)^{\frac{1}{\theta}} h_c(t) = \left(1+\frac{\rho g}{P_{atm}}\{D_c(t)+(1-\Upsilon)\Delta x\}\right)^{\frac{1}{\theta}} \cdot (h_c(t) - \Upsilon \cdot \Delta x) \tag{2.8}$$

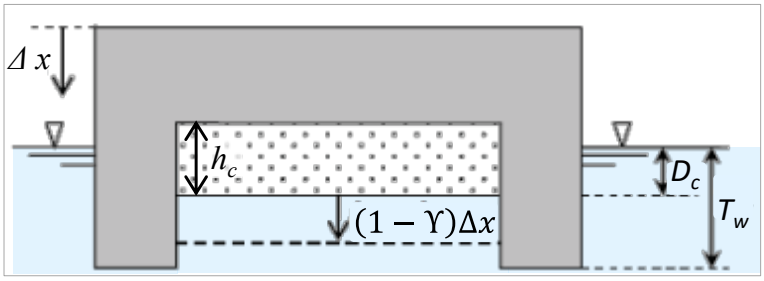

Fig. 2.6 - Vertical motion of an air-cushion supported structure and compression of the cushion (modified from van Kessel, 2010).

If the right hand side of this equation is rewritten by a Taylor expansion around Δx=0, the following compressibility factor of the aircushion is obtained as follows (Van Kessel, 2010):

$$\Upsilon = \frac{\rho g h_c}{\theta \cdot P(t) + \rho g h_c} \tag{2.9}$$

Among the several anti-motion methods, OWC devices were proposed as a cost-effective solution. However, the OWC anti-motion effect need to be improved optimizing its design, in order to maximize its combined effect of wave energy absorber and VLFS floating attenuator.
The air-cushion system represents an effective solution for the construction of each VLFS unit, due to its capability to stabilize the VLFS with less mooring loads.
However, Van Kessel (2010) suggests that the air compressibility at full scale has a relevant effect at full-scale, which may influence the VLFS floating behaviour. Hence, since generally at model scale air is compressed by small pressures behaving as incompressible, it is necessary to take into account that the experimental tests could not reproduce accurately the VLFS floating behaviour.

2.1.3 Past, present and future applications

Due to their many advantages as compared to the other marine structures, the VLFSs can be suitable for a variety of purposes (Fig. 2.7).

Japan, the world's leader in constructing VLFSs, built in 1998 in the Tokyo bay the Mega-Float, the first sizeable floating runway (1km long). Some other applications of VLFS in Japan are the

floating fuel storage bases at the Shirashima Island and Kamigoto Island, and floating ferry piers at Ujina port, Hiroshima. VLFS also finds application as floating bridges, allowing an economical solution when the water depth is large or the riverbed/seabed is very soft.

Floating docks have been constructed in the USA and other countries. In 2003 a floating pier was built in the Port Hercule de la Condamine, in Monaco. It is a floating caisson 350m long, 28m wide and weighing 167000t, and was built in Algeciras Bay and towed by sea to its destination Monaco.

Mega-Float, Tokyo Bay, Japan.

Emergency Rescue Base, Tokyo Bay, Japan.

Floating performance stage, Marina Bay, Singapore.

Floating pier, Port Hercule de la Condamine, Monaco.

Sustainable engineering science barge at Hudson River, Manhattan, USA.

Lilypad floating ecopolis (www.vincent.callebaut.org).

Fig. 2.7 - Some of the several applications and projects of VLFSs.

Since the VLFS are well isolated from earthquakes and can be moved, they are ideal for applications as floating emergency rescue bases. Three Floating Disaster Prevention Bases were completed in Yokohama, Osaka and Nagoya Bay. All of them has mooring facilities, a heliport, interior storage spaces for cargo and a track crane. Two famous very large floating bridges are the 2km long Lacey V. Murrow Bridge and the Third Washington Bridge over Lake Washington in

Seattle. The world's largest floating performance stage was built at the Marina Bay in Singapore and also South Korea has initiated a number of VLFS projects.

The application of VLFS as floating farms in urban cities may also emerge as an innovative solution to provide arable land in supplying food to the increasing growth of human population while maintaining the integrity of the ecosystem.

The sustainable engineering science barge constructed by the New York Sun Works Centre on the Hudson River in Manhattan demonstrates that urban agriculture on floating structure is possible without causing damage to the environment. In salmon producing countries such as Norway, USA, Canada and Chile, marine salmon farms are constructed to ensure continuous supply of fresh fish.

VLFS technology has also made possible future large human habitation on the ocean surface. The Lilypad Floating Ecopolis, proposed by the Belgium architect Vincent Callebaut, is an example of a visionary proposition to house the city population on a huge floating lily-shaped island. Pernice (2009) gives more concepts of floating cities in a recent paper.

Since more than half of the Netherlands's land area is below sea level, the Dutch have also proposed the concept of a floating town comprising greenhouses, commercial centre and residential area (Wang & Wang 2015).

2.1.4 Numerical and experimental studies on VLFS

In order to assess the reliability of the numerical models and to understand the physical phenomena, the appropriate approach is to perform experimental studies, which provide a setting where the wave forcing and the measurements can be controlled accurately. In particular, for a VLFS that has never been built, even if the reliability of the theoretical analysis is very high, it is crucial to validate the theoretical analysis against laboratory tests (Wang et al., 2008).

Generally, the tests are conducted in wave flume or basin equipped with a wave generator, that controls the wave forcing on the structure and a wave absorption system (e.g., a beach), which is usually located at the far end of the flume, maximizing the dissipation of incident wave energy, to limit reflection phenomena.

The Society of Naval Architects of Japan (SNAJ, 1997) suggested the following four main objectives in conducting model experiments on floating structures:

1) to validate the result of the theoretical analysis, performing experiments on the oscillating response of the VLFS in regular waves of small wave amplitude.
2) to study issues that are difficult to estimate theoretically, such as: i) fluid forces due to the fluid viscosity or; ii) non-linear effects of wave heights due to the VLFS behaviour in large amplitude waves.
3) to investigate the overall performance of a VLFS in a realistic situation by simulating the VLFS under irregular waves.
4) to study the joining operation of multi-floating modules, simulating the construction and the connections of the VLFS units by model experiments.

However, two main significant issues can affect model experiments on VLFS as follows:

- Adopting an extraordinarily small-scale model can lead to problem in the accuracy of the generated waves (i.e. short waves) and of measuring the behaviour of the model.
- Reproducing at model scale the VLFS hydro-elastic response needs to make the rigidity of the model similar to the rigidity of the VLFS at full scale, which is hardly possible in small-scale models.

Endo & Yago, (1999) carried out laboratory experiments (model scale 1:30) of the elastic response of a pontoon type VLFS to dynamic loads. The VLFS model (9.75m long, 1.9m wide and 0.55m high) was tested under impulsive load and moving load, to assess the elastic response of a VLFS to the take-off and landing loads of aircrafts. The tests were manly aimed at verifying the validity of the analysis method for solving the elastic-response problems in time domain (Ohmatsu, 1998; Endo, 2000).

Ohkawa, (2000) performed laboratory tests (model scale 1:100) to validate the theoretical elastic-response analyses of a VLFS (10m long, 2m wide and 0.70m high) under: i)the mutual effect of a VLFS and a breakwater; ii)a rectangular VLFS of non-uniform rigidity and iii)non-rectangular VLFS of uniform rigidity.

Ohta et al., (2002) carried out model tests by using an elastic model with additional structures attached, to assess their effects on the attenuation of the floating motion. However, they found a new problem, enhancement of horizontal motion, due to the additional structures. The anti-wave performance of offshore Mega-Floats was doubled as result of their new designs.

Li et al., (2003) studied the dynamic response of box-typed VLFS in waves and validated the three-dimensional linear hydro-elastic theory by means of small-scale physical models (1:100) performed in the State Key Laboratory of Ocean Engineering at Shanghai Jiao Tong University (50m long, 30m wide and with a depth 6m).

Since the high cost of the laboratory tests, Kagemoto et al., (1999), and Takagi et al., (2007) studied the hydro-elastic response at mini-scale in very small water tanks. Using this scale factor, they confirmed that it is difficult to measure accurately the VLFS displacement and that effects as surface tension and frictional at the bottom of the tank can be significant.

Given the increasing interest on the pontoon type VLFSs, due to their simplicity, the effort of the research is mainly focused on the assessment of the floating response of the VLFSs at sea, several theoretical and numerical studies are performed to predict the effect of waves on the dynamic response of the structure and to support their design.
However, the validation of the numerical results requires, beside field observations, more reliable laboratory tests, aimed at assessing the floating behaviour of a VLFS in regular and irregular waves, to take into account the viscosity and the non-linear effects as well as to simulate the construction method and the connections of the VLFS units. In this contest, it is important to select properly the scale factor in order to avoid accuracy problem in measuring the behaviour of the model as well as to take into account the difficult representation at small scale of the VLFS hydro-elastic response.

2.1.5 Summary and implications for the present study

The following specific implications to account for the development of a reliable and feasible VLFS with incorporated OWC devices, might be drawn from the review and analysis of the current knowledge on VLFSs:

- To fulfil serviceability and safety requirements, most studies on VLFS were focused on the VLFS floating behaviour in waves. Among the several anti-motion methods proposed in the literature review and, considering that an efficient incident wave absorption can result in a better floating attenuation, the OWC device is selected as the most appropriate technology for the integration in the VLFS (VLFS-OWC System). Moreover, OWC belongs to the simplest and most robust WEC systems.
- The pontoon type is the geometry selected for the conceptual design of the VLFS, due to its low manufacturing costs, easy portability, maintenance and repair. Moreover, since the pontoon-type geometry is suitable for use in not exceptionally energetic sites, it could be a suitable solution for the hypothetical installation in a site located in the Mediterranean Sea and characterized by a moderated wave climate.
- The multi-module manufacturing method for floating platform, performed by joining several VLFS units together, is the most appropriate, since it allows an easy construction and transportation as well as possible future enlargements, modifications, decommissioning and reuse of the structure.
- The floating motion of the VLFS can be improved by supporting each VLFS unit with a pressurized air-cushion system. However, it is important to consider that the compressibility within the air-cushion might have a relevant beneficial effect on the behaviour of the VLFS in waves and might also affect the efficiency of the integrated OWC devices.
- Physical models represent a crucial step for the validation of the numerical models and for the study of the non-linear effects, generally neglected in the theoretical models. Moreover, to avoid surface tension effects and frictional effects at the bottom of the wave flume it is important to select a proper model scale factor. It should be stressed that a proper representation of the VLFS hydro-elastic response can hardly be achieved.
- To maximize the dissipation of the incident wave energy as well as to limit reflection phenomena, it is necessary to equip the far end of the wave flume with a wave absorption system (e.g. a beach).

2.2 Oscillating Water Column Devices (OWCs)

The aim of this section is to provide a general definition and classification of OWC wave energy converters as well as to review and analyze the previous numerical and physical models on OWC devices, in order to identify the gaps of knowledge and the specific issues to be considered during the modelling approach. Before analyzing the current knowledge on OWC wave energy converters, the basics of wave energy and the commonly used indicator for evaluating the performance of the OWC, in terms of wave energy extraction capability, are briefly reported.

2.2.1 Wave Energy Basics

a) Energy density for regular and irregular waves

The total mechanical energy of a wave system is the sum of its kinetic energy and its potential energy. The kinetic energy, E_k, is that part of the total energy due to water particle velocities associated with wave motion. While, potential energy, E_p, is the energy resulting from part of the fluid mass being e.g. above the trough: the wave crest.

The *total energy* in one wavelength λ per unit wave crest width [J/m] is:

$$E = E_k + E_p = \int_x^{x+\lambda} \int_{-d}^{\eta} \rho \frac{u^2 + w^2}{2} dz\, dx + \int_x^{x+\lambda} \rho g \left[\frac{(\eta + h)^2}{2} - \frac{h^2}{2} \right] dx \tag{2.10}$$

where, ρ [kg/m^3] is the density of sea water; h [m] is the water depth; u [m/s] is the fluid velocity in x-direction; w [m/s] is the fluid velocity in z-direction; η is the water surface elevation and h the water depth.

According to the Airy linear wave theory, if the potential energy is determined relative to S.W.L., and all waves are propagated in the same direction, potential and kinetic energy components are equal and the total wave energy in one wavelength per unit crest width is given by:

$$E = E_k + E_p = \frac{\rho g H^2 \lambda}{16} + \frac{\rho g H^2 \lambda}{16} = \frac{\rho g H^2 \lambda}{8} \tag{2.11}$$

The total average wave energy per unit surface area is called *specific energy* or *energy density* ($\bar{E}$), that for regular waves is given by Eq. 2.11 as [J/m^2]:

$$\bar{E} = \frac{E}{\lambda} = \frac{\rho g H^2}{8} \tag{2.12}$$

As for a real sea state, the waves are irregular and the random signal can be exactly reproduced as the sum of a large (theoretically infinite) number of harmonic wave components (a Fourier series) with a *variance density spectrum* [m^2/Hz] defined as:

$$S_f(f) = \lim_{\Delta f \to 0} \frac{1}{\Delta f} \frac{1}{2} \overline{a_i^{\,2}} \tag{2.13}$$

where: a_i is the wave amplitude of each spectral wave component i and Δf is the frequency interval. Then, the specific energy or energy density spectrum for irregular waves ($E_f(f)$) is given by multiplying the density spectrum, $S_f(f)$ by ρg as:

$$E_f(f) = \frac{1}{2} \rho g \lim_{\Delta f \to 0} \frac{1}{\Delta f} \overline{a_i^{\,2}} \tag{2.14}$$

b) Wave Power for regular and irregular waves

Wave energy flux is the rate at which energy is transmitted in the direction of wave propagation over the entire water column across a vertical plane perpendicular to wave direction. Assuming linear wave theory for pressure p and velocity u, Eq. 2.15 describes the energy flux averaged over wave period T per unit wave crest width, transmitted across a vertical plane perpendicular to the wave direction [W/m]:

$$\bar{\Pi} = \frac{1}{T} \int_t^{t+r} \int_{-h}^{\eta} pudzdt \tag{2.15}$$

where, p [kg·m^{-1}·s^{-2}] is the relative pressure; t [s] is the start time; r [s] is the end time.
Integration of Eq. 2.15 simplifies to:

$$\overline{\Pi} = \bar{E}nC = \bar{E}\ C_g \tag{2.16}$$

The rate at which wave energy propagates is directly dependent on the group velocity of the wave (C_g), which is given by:

$$C_g = nC \tag{2.17}$$

where, C [m/s] is the wave celerity and n is a constant as determined by:

$$n = \frac{1}{2}\left[1 + \frac{4\pi h\ /\ \lambda}{\sinh\ (4\pi h\ /\ \lambda)}\right] \tag{2.18}$$

In deep water, Eq. 2.17 simplifies to n=0.5 and C_{g0}=0.5·C_0 or $C_{g0} = gT/4\pi$ and the wave energy density is transmitted in the zone from the surface to $\lambda_0/2$ below SWL.

Wave energy flux, is also called *Wave Power* [W/m]. Eqs 2.15-2.17 indicate that wave power $\overline{\Pi}$ generally depends on wave height H, wave period T and water depth h.

For deep water (n=0.5) however, Eq. 2.17 is obtained, showing that $\overline{\Pi}$ is only dependent on wave height and wave period:

$$\overline{\Pi}_{w,reg} = \bar{E}\mathrm{nC} = \frac{\rho g H^2}{8} \cdot \frac{gT}{4\pi} = \frac{\rho g^2 H^2 T}{32\pi} \tag{2.19}$$

For irregular waves, the spectral parameters (i.e., the significant wave height, $H_{m0} = 4\sqrt{m_0}$ (with $m_0 = \int_0^\infty \mathrm{S}_f(f)df$) and the wave energy period T_e, (or.,$T_{m-10} = m_{-1}/m_0$) are used in Eq. 2.17 and the period averaged wave power per unit width is obtained as follows:

$$\overline{\Pi}_{w,irreg} = \frac{\rho g^2}{4\pi}\int_0^\infty \mathrm{S}_f(f)\frac{1}{f}df = \frac{\rho g^2}{4\pi}m_{-1} = \frac{\rho g^2 {H_{m0}}^2 T_{m-10}}{64\pi} \tag{2.20}$$

c) Performance of a Wave Energy Converter device

To assess the performance of wave energy converters (WECs), many studies referred to the *Capture Width*, *CW,* defined as the width of the wave front (assuming uni-directional waves) that contains the same amount of power as that absorbed by the device (Price et al., 2009).

The *Capture Width* is expressed by the ratio of the mean absorbed pneumatic power, Π_{abs}, [W] to the averaged wave power associated to the incident waves, Π_w, [W/m] (Eqs.2.17 and 2.18):

$$CW = \frac{\overline{\Pi_{abs}}}{\overline{\Pi_w}} \tag{2.21}$$

The averaged absorbed pneumatic power is estimated by integrating the product of inner air pressure (inside the OWC chamber), *p(t)*, and air flow rate, *Q(t)*, throughout the air turbine (Sarmento, 1993):

$$\overline{\Pi_{abs}} = \frac{1}{\mathrm{T}}\int_0^{\mathrm{T}} Q(t)p(t)dt \tag{2.22}$$

However, a commonly used index of the performance of a WEC is the *dimensionless Capture Width*, *CW**, obtained by normalizing the *Capture Width [m]* (Eq. 2.19) by the length of the device transversal to the wave direction (Evans & Porter 1995; Morris-Thomas et al. 2007; Zhang et al. 2012; Kamath et al. 2015)

*CW** reflects directly the fraction of the far field available wave power adsorbed by the device, taking into account its hydraulic and pneumatic conversion efficiency. Many researchers commonly used as far field incident waves to calculate the incident wave power when considering the assessment of the performance of a WEC. In this way, the local perturbation of the flow induced by the presence of the OWC device is considered in the index used to evaluate the performance, thus allowing the comparison among different design alternatives of the devices (Morris-Thomas et al., 2007).

2.2.2 Wave energy conversion technologies (WECs): a synthesis

The wide variety of wave energy technologies, resulting from the different ways in which energy can be absorbed from the waves and transformed into electrical form. Wave energy devices work because forces induced by the waves cause relative movement between different parts of the converter system. Therefore, the wave energy can be extracted using mechanical or electro-dynamic means. According to Falcão, (2010) and considering the basic principle of energy extraction, the WECs can be classified in the following three main categories (Fig. 2.8):

i. *Oscillating water column (OWC)*: devices with a partly submerged structure open below the water surface, inside which air is trapped above the water free surface. The oscillating motion of the internal free surface produced by the incident waves makes the air to flow through an air turbine that drives an electrical generator.

ii. *Wave Activated Bodies (WAB)*: constituted by moving elements directly activated by the cyclic oscillation of the waves. The power is extracted by converting the kinetic energy of these moving elements into electric current. These devices can be further categorized in sub-groups describing the energy extraction by the principle motion of the floating body: heave, pitch and roll (i.e., respectively the translation in the *z*-direction (up and down), the rotation about transverse *y*-axis and the rotation about longitudinal *x*-axis). The motions of surge, sway and yaw (i.e., respectively translation in the x-direction (forward and backward) and translation in the y-direction (side to side), requiring an external restoring force (mooring) in order to return to its original equilibrium position.

iii. *Overtopping Devices (OTD)*: equipped with reservoirs that are filled by incoming waves to levels above the average surrounding sea. The water is then released and gravity causes it to fall back toward the sea surface. The energy of the falling water is used to turn hydro turbines.

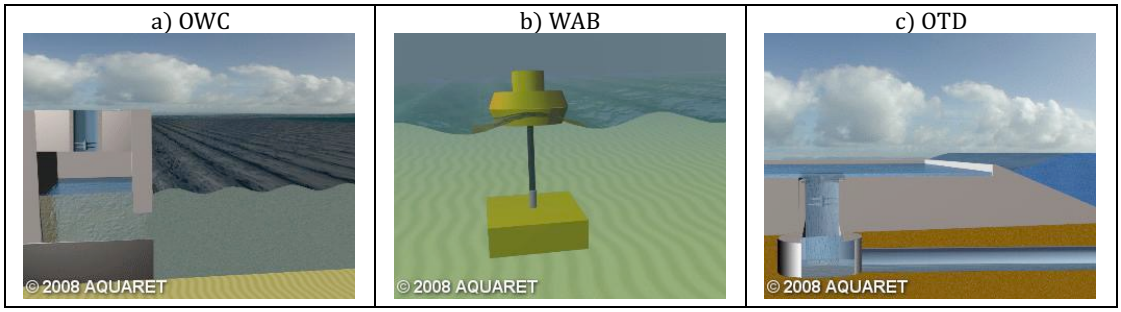

Fig. 2.8 – Classification of the Wave Energy Converters (WECs) proposed by Falcão, (2010), taking into account the main working principle (from Aqua-RET Project ©, 2012).

2.2.3 OWC technology: classification and processes

Oscillating Water Column (OWC) devices are a simple and non-disruptive class of WECs, in which the air turbine is never in contact with the seawater, allowing a long service life of the equipment.

In addition, the OWC is a more mature technology than the other types, because it is the most tested and a large part of WEC prototypes deployed so far into the sea are of OWC type (Falcão, 2010; Torre-Enciso et al., 2009; Heath et al., 2000).

An OWC device can be a fixed or an oscillating hollow structure open below the water surface, which traps air above the inner free surface (Fig. 2.9).

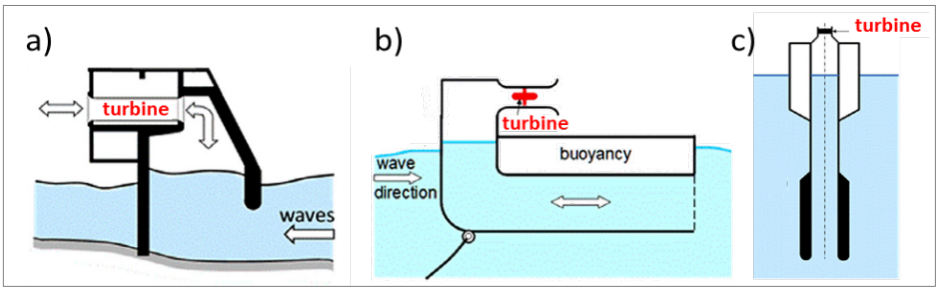

Fig. 2.9 - Different types of OWCs: (a) fixed (Pico plant); (b and c) floating, (respectively Backward Bent Duct Buoy (BBDB) and Spar-buoy OWC), (Falcão & Henriques, 2014).

When waves approach the device, alternately compress and decompress the trapped air, which forces air to flow through a turbine coupled to a generator. Unlike to a fixed OWC, in a floating OWC the structure oscillates, leading to radiation of waves and the relative motion between the device and the internal free surface provides the airflow.

Generally, OWCs utilize self-rectifying air turbines that can constantly spin in one direction regardless of airflow direction (e.g., the axial-flow Wells turbines or the axial and radial-flow Impulse turbines), allowing for optimal energy harvesting.

The OWC energy conversion chain consists of three main processes (Fig. 2.10):

i) *wave to air* chamber (hydraulic and pneumatic processes);
ii) *air turbine* (mechanical processes);
iii) *electrical generator* (electrical processes).

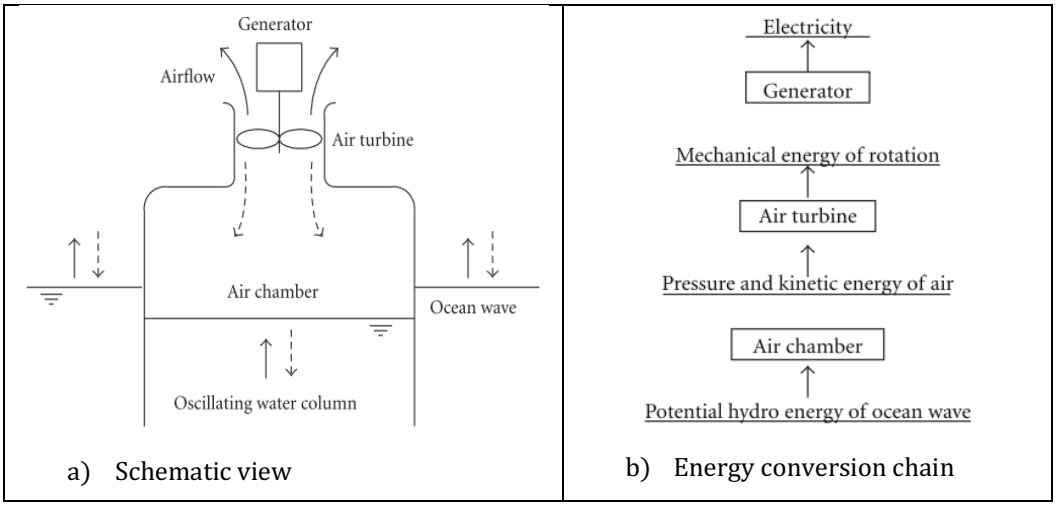

Fig. 2.10 - Outline of oscillating water column (OWC) device (Takao & Setoguchi 2012).

The wave-to-pneumatic energy conversion is the most critical element in the energy conversion chain ("wave to wire"). First, because it is, together with the air turbine, the major source of losses. Second, because it is difficult to model accurately, either by physical or by numerical modelling (Falcão, 2004).

However, as compared to the other WEC technologies, OWC devices present:

i) extremely simple and low cost construction;
ii) easy maintenance in the operating phase;
iii) possibility of sharing costs if installed in structures ensuring other functions such as floating or fixed breakwaters, large floating multi-purpose platforms etc.

Several OWC devices, which reached the prototype stage (Fig. 2.11), contributed to the current understanding of this technology, in particular to their working principle.

Limpet - 500 kW United Kingdom.

Pico Plant - 400kW Portugal.

OSPREY - 2MW North of Scotland.

Oceanlinx -330kW Port Kembla, Australia

Mutriku plant 16 OWCs 296kW, Spain

Backward Bent Duct Buoy (BBDB), Irland.

Fig. 2.11 - Some OWC devices, which reach the prototype stage (Webb et al., 2005).

2.2.4 Numerical and experimental studies on OWC devices

To assess the OWC performance at an early development stage, testing different configurations and optimizing the shape in order to maximize the power extraction (Gomes et al., 2012) by using theoretical and numerical models based on linear wave theory are an essential step, since they provide details and important information at moderate costs and in a relatively short time.

Principally, within the framework of potential flow theory, two basic theoretical approaches on the interaction between the OWC and the incoming waves may be adopted (Fig. 2.12):

I. *Rigid Piston Model*: in which the inner OWC free surface is modelled as a heaving weightless rigid piston (McCormick, 1981; Robinson, 1982; Watts et al., 1985; Maeda et al., 1985). This approach ignores the free surface deformation and implies an unrealistic non-uniform surface pressure distribution (the air pressure in the chamber is in fact very approximately spatially uniform). The rigid piston model may be acceptable if the OWC free-surface dimensions are much smaller than the wavelength and are small compared with the OWC length (i.e. when OWC the chamber is not affected by sloshing), (Evans, 1971; Ma, 1995);

II. *Uniform Pressure Model*: in which the inner OWC free surface is modelled as a uniform air pressure free surface (Evans, 1982). The governing equations are expressed in terms of pressure on the OWC free surface and flow rate displace by the OWC surface motion.

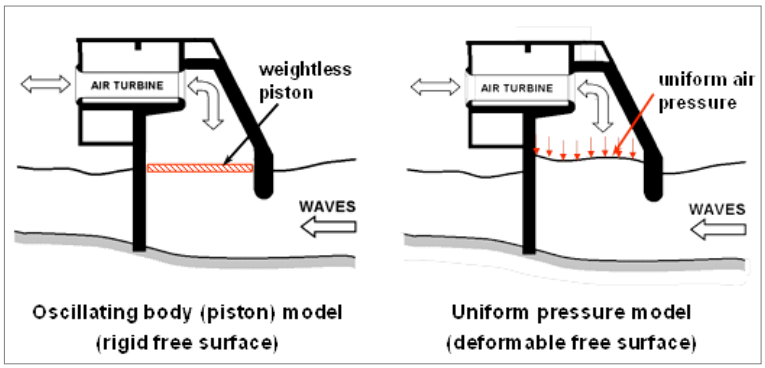

Fig. 2.12 - Two basic approaches to theoretical OWC modelling: (a) weightless piston and (b) uniform air pressure model (Falcão et al., 2014).

Both potential flow models can be solved either in the time domain or in the frequency domain and both require as input the OWC hydrodynamic coefficients (i.e., added mass and radiation damping), which depend on the OWC geometry and the water depth. The OWC hydrodynamic coefficients can be obtained numerically or analytically, determining velocity potential by solving diffraction and radiation problems for the OWC.

The analytical methods can be adopted only for relatively simple OWC geometries, (e.g. cylindrical axisymmetric OWC with negligible wall thickness) and are generally based on *eigenfunction expansion* or *matched eigenfunction expansions* methods (Yeung, 1981). In case of more complex OWC geometries, numerical models based on the potential theory are usually adopted and solved by means of Boundary Element Methods (BEM). However, the aforementioned approaches, based on potential flow theory, are not capable of representing the relevant non-linear effects, associated with:

i) large amplitude of the waves;
ii) large amplitude of the motion of the water column inside the device;
iii) wave breaking and
iv) real fluid effects due to viscosity, turbulence and vortex shedding.

To account for such non-linear effects, Computational Fluid Dynamics (CFD) codes (e.g. FLUENT© and OpenFOAM®), based on the numerical integration of the *Navier–Stokes* equations are adopted. However, CFD codes are computationally demanding and require experimental validation.

Therefore, physical models represent normally the next step and are usually performed with scales ranging from about 1:100 in small flumes to about 1:10 in larger wave basins (Falcão, 2013).

Moreover, the OWC concept was also studied at full-scale in the 1980s and 1990s, as in the cases of the Kværner multi-resonant OWC, in Norway (Malmo et al., 1986), the Pico plant in Azores, in Portugal (Falcão, 2000) and the LIMPET plant in Islay, Scotland (Heath et al., 2000).

To identify the most relevant parameters affecting the performance (i.e., the Capture Width see *subsection 2.2.1*) of: i) fixed OWC, ii) floating OWC and iii) OWC integrated in a floating structure, here the state of the art of the model studies (physical and numerical), is separately presented. Finally, the air compressibility effect is addressed.

a) Models on fixed OWC

Sarmento, (1993) performed a physical model (scale factor 1:35) on shoreline PICO-power plant, aimed at optimizing the OWC geometry, by means of a parameter study carried out using irregular waves representative of the wave climate of the installation site. In the laboratory experiments, several superimposed layers of filter made of synthetic carpet material simulated the damping induced by the linear PTO (Wells turbine). The OWC model was initially reproduced with a chamber width (in wave propagation direction) of 0.18m, a width (in direction normal to wave direction) of 0.23m and protruding harbour walls 0.22m long. The results showed that for the optimized size of the OWC chamber it is possible to find the optimum damping induced by the turbine, which allows the largest value of the capture width. Moreover, his study demonstrated that the OWC performance is significantly affected by the front wall draught, which was fixed at a level lower than the expected extreme wave trough.

Morris-Thomas et al., (2007) also studied the effect of the front wall geometry on the hydrodynamic efficiency of a shore based OWC physical model (scale factor 1:12.5) using regular waves. The tests focused on the effect of front wall draught and thickness: on the OWC efficiency for relative depth ranging from kh=0.298 to 3.705 and wave steepness from kA=0.010 to 0.218. The OWC model was characterized by a width in direction normal to wave direction of 1.37m, a chamber width of 0.64m in wave direction propagation. They reproduced the non-linear PTO by a square vent, of width 5 mm, situated in the roof of the chamber. To determine the incident wave energy, incident waves were generated with the OWC model removed from the wave tank. The free-surface displacements were recorded by a sensor located at the centre of the removed model position. Their results demonstrated that the hydrodynamic efficiency is not greatly influenced by the front wall thickness. However, they observed that, in case of short waves, when the front wall submergence decreases, the OWC efficiency increases (CW^*_{max} =0.70).

Sheng et al., (2012) investigated the relation between the OWC conversion efficiency and the water column by means of laboratory tests on a fixed cylindrical OWC model under regular waves (0.6s< T<2.6s). Moreover, a non-linear PTO (impulse turbine) was modelled by orifices with ratio (i.e., the orifice area to horizontal. area of the water column in the OWC chamber) between 0.5%-2.0%, for which the damping level in the scaled models provides an optimal power conversion efficiency of the OWC device. Their study confirmed the importance of the OWC sizes (draught and sectional area of the water column) concerning an appropriate wave energy extraction of the device, finding the following most relevant factors that must be taking into account:

(i) The draught of the water column strongly influences the resonance period of the interior water surface. For a bottom-fixed OWC, the response of the interior water surface is close to unit when the incoming wave period is larger than the resonance period of the water column.
(ii) The water column sectional area affects the maximum efficiency and the absorbed wave power. The study shows that with higher and longer waves a better effect is achieved with a larger device.

However, they highlighted important practical limitations in sizing the OWC device, suggesting that in order to avoid the sloshing motion, which leads to energy losses, the OWC chamber width (in wave direction) may not exceed the 1/4-1/5 wavelength.

Lopez et al., (2012); López & Iglesias, (2014) and López et al., (2015) also highlighted the importance of studying the coupling between the chamber and the air turbine of a breakwater-integrated OWC, to optimize the device performance by adapting the turbine specifications to the chamber geometry and wave climate. They calibrated and validated a 2D numerical model by laboratory tests in wave flume (scale factor 1:25). The OWC model was tested under both regular waves (0.02<H<0.10m, 1.4<T<2.6s) and irregular waves (0.04<H_{m0}<0.08m, 1.4<T_p<2.6s),

reproducing different damping coefficients induced by a non-linear PTO, by means of different orifices. Their results showed that one of the most relevant factors affecting the OWC performance is the induced turbine damping. In particular, they observed an increasing trend of flow velocity and vortices when the damping coefficient decreases. Moreover, for the OWC under irregular waves they observed that the performance of the device increases with increasing the wave steepness at low frequencies and decreases at high wave frequencies.

Iturrioz et al., (2014) and (2015) developed and validated a CFD model based on RANS-VOF using open source code (IHFOAM) with flume tank experiments, to study the hydrodynamics and pneumatics around a fixed detached OWC. The laboratory tests were performed adopting a geometric scale 1:30 and the OWC model was characterized by a width of 0.30m in wave propagation direction, a width of 0.68m and a freeboard of 0.15m. A set of regular and irregular waves (0.03m$<H<$0.08m, 1.1s$<T<$3.2s at a water depth of 0.60m) were tested with different orifices simulating a non-linear PTO.

More recently, Ning et al., (2016) performed laboratory tests on a fixed OWC, in order to assess the effects of: i) incident regular wave amplitude (0.02m$<A_i<$0.07m 0.95s$<T<$2.35s); ii) chamber width (0.55÷0.85m); iii) front wall draught (0.14÷0.20m), iv) non-linear turbine damping (with orifice diameters in the range 0.04÷0.08m) and (v) bottom slope in the chamber on the OWC performance. They found that the OWC performance increases as the wave amplitude A_i increases from 0.02m to 0.03m, and decreases as A_i increases from 0.03m to 0.04m. The maximum efficiency was achieved at A_i=0.03m (CW^*_{max}=0.83), for the fixed values of chamber width, front wall draught and orifice diameter, respectively of 0.55m, 0.14m and 0.06m. Moreover, they found that when the chamber width increases, the OWC performance increases for low-frequency waves, and it follows an opposite trend for high-frequency waves. As observed in previous studies the front wall draught and the induced damping strongly affect the device performance. Their study confirmed that longer front wall draughts lead to a lower efficiency and resonant frequency and that the optimal efficiency occurs for a given induced damping.

b) Models on Floating OWC

Whittaker et al., (1986) reported the first laboratory experiments on the hydrodynamic design of an axisymmetric floating OWC (i.e. a tail tube buoy) in a wave flume. They found that the capture width increases proportionally with the tube diameter for the buoy diameter ratios up to 75%, and that increasing the length of the tube leads to a wider frequency bandwidth response. Moreover, they confirmed the relevant effect of the applied damping on the performance of the device.

Sykes et al., (2009) performed experiments at selected frequencies and with increasing wave amplitude on a simple floating undamped OWC (i.e., a hollow vertical circular cylinder). They compared the numerical predictions, obtained from the linear hydrodynamic BEM code WAMIT, with the laboratory measurements. They provided a preliminary assessment of the validity of the use of BEM code for this particular geometry, confirming the limitations of numerical modelling based on linear water wave theory (e.g., highly non-linear pressure signals measured during the tests, suggested the presence of these physical effects, which are not accommodated by BEM code).

Gomes et al., (2012b) carried out small-scale tests (1:120) on an axisymmetric floating OWC (i.e., spar-buoy OWC) under regular waves, aimed at investigating the effect of the relative motion between the water column and the OWC device on its performance. They also compared the experimental results with numerical results based on linear wave theory, confirming smaller value of pressure and capture width than those predicted by the numerical models which not account for the viscous effects. Two OWC configurations were tested: one was constrained to heave motion; the other one was slack moored. Moreover, according to (Lewis et al., 2003; Forestier et al., 2007), they simulated different damping conditions, induced by a linear PTO (Wells turbine), using a porous membrane placed at the top of the air chamber. To assess the natural periods of each configuration they performed decay tests, achieving natural oscillation periods (e.g., 0.91s and 0.88s in heave, respectively for the model constrained in heave and the slack moored one). The results on the more realistic slack-mooring configuration showed a dynamic instability when the incoming wave frequency is near the heave resonance, showing a decreasing trend of the power extraction in proximity of that frequency, when compared with the configuration constrained in heave. In addition, the different damping, induced by the linear turbine, affected the OWC performance, showing a higher energy extraction when the damping coefficient decreases.

Martinelli et al., (2013) tested a multi-chamber floating OWC (i.e., the M-OWC SeaBreath) to provide a preliminary optimization of the chamber size, the ducts and the turbine, considering a possible application in the Adriatic Sea, with a 3kW turbine, and a capacity factor of 40%. The

laboratory tests were performed on fixed and floating OWC models, both 1.50m wide (in wave propagation direction), 0.30m wide and with a front wall draught of 0.125m. Each OWC model was composed by four chambers tested under regular waves ($0.02<H<0.06$m, $0.5<T<1.8$s) and irregular waves (H_{m0}=0.06m, $0.6<T_p<1.8$s). Their study showed that, due to the communication between the chambers and the external atmosphere, even for long waves, the device efficiency is similar to the maximum. They also observed a lower capture width under irregular waves than under regular waves (respectively CW^*_{reg}=0.13 and CW^*_{irreg}=0.06 for T=1.2s), confirming the importance of testing the device under real sea states. Moreover, the floating OWC model showed a maximum efficiency for a peak wavelength equal to the structure length, demonstrating that for very long waves, the device "rides" the waves, with lower water oscillations in the chambers.

Luo et al., (2014) analysed the performance of a heave-only axisymmetric floating OWC device with undamped mooring system by means of a CFD code validated against previous experimental, analytical and numerical results. Their results showed that incoming wave frequency and turbine damping coefficient have a significant effect on the efficiency of the device. Unlike the fixed OWC with one resonance frequency, the heave-only floating OWC present two resonance frequencies, one for the OWC and one for the water column oscillation inside the chamber. Moreover, they observed that the frequency bandwidth of high efficiency can be adjusted by turbine damping coefficient so as to improve the device performance with varied wave frequencies. For heave-free floating OWC the maximum efficiency (CW^*_{max}=0.83) was achieved when the OWC chamber width (in wave propagation direction) is 0.24 times the incoming wavelength.

c) Models on OWC integrated in floating structures

All of the abovementioned studies deal with the fixed OWC and floating OWC. To date, only few researches focused on the assessment of the performance of OWC integrated in floating structures.

He et al., (2012) and He et al., (2013) studied experimentally OWC devices integrated in slack-moored floating breakwaters, as a sustainable option for cost sharing between wave energy capturing devices and shore protection structures. They performed laboratory tests on a floating breakwater at first with symmetric OWC (He et al., 2012), then with asymmetric OWC (He et al., 2013) in order to improve the performance of the devices, increasing the amplitude of the air pressure oscillation inside the devices over a wide range of wave frequencies. The tests were carried out varying: i) the damping induced by a non-linear turbine (by different slot openings); ii) the front wall draught (0.29÷0.17m varied by means of extra ballasts); iii) the chamber width (0.20÷0.60m), and iv) tthe incoming regular waves (H=0.04m, $1.1\text{s}<T<1.7\text{s}$).

Their study showed that for both symmetric and asymmetric configurations, the integration of OWC devices leads to the reduction of the wave transmission and the motion the floating structure. However, the asymmetric OWCs leads to an increase of the heave responses and of the performance of the devices, increasing the inner air-pressures amplitude. Since the response of a floating structure to waves is affected by the total mass, the mass distribution in the structure and the mooring system, they observed the irrelevant effect of the front wall draught on the heave response. Moreover, they also observed that with very short waves, the heave response becomes small and the structure move out of phase with the waves. Therefore, the breakwater behaves like a fixed structure and the air-pressure fluctuation within the chamber is affected mainly by the OWC natural period. Instead, for very long wave, the breakwater moves in phase with waves, thus the air-pressure fluctuation decreases with increasing wave period beyond the natural period of the heave response.

Theoretical and numerical models based on linear wave theory are considered an essential step in the assessment of the OWC performance at an early stage of the analysis. However, these approaches cannot properly represent the non-linear effects, associated with: i) large amplitude of the waves; ii) large amplitude of the water column motion; iii) wave breaking and iv) real fluid effects. More advanced CFD codes can account for such effects, but require experimental validation. Therefore, physical models represent the crucial next step.
For fixed OWC, the state of the art revealed that three are the main design parameters affecting its performance: 1) the chamber width (in the direction of wave propagation); 2) the front wall draught and 3) the damping induced by the air turbine.
For floating OWC, in addition to the aforementioned design parameters, the relative motion between the water column and the OWC device has a relevant effect on its performance.
For integrated OWC, the performance of the device could be also affected by the floating motion of the structure (in which the device is integrated).

d) Air compressibility effects in air chamber

Although physical models represent an essential step for the calibration and validation of numerical models, as well as for a preliminary development of an OWC device, there are relevant scale effects to be taken into account, in particular those related to the air compressibility in the OWC air chamber.

In OWC devices the air in the chamber above the water column is subject to oscillating relative pressure and then the density of the air varies in time, according to some pressure-density relations. Considering that the OWC chamber volume should be large enough, to avoid green water from reaching the air turbine under energetic sea conditions, the spring-like effect of air compressibility has a relevant effect in full-sized OWC (Falcão & Henriques, 2014a).

The air chamber and the air turbine are open systems subject to the thermodynamic processes associated with compression and decompression. Since the amount of heat transferred across the walls of the system (i.e., chamber and turbine walls and air-water interface) is smaller than the amount of work done by the motion of the water column and by the rotor of the turbine, it is possible to consider the process as adiabatic. Moreover, assuming that the losses in the flow due to viscous effects are negligible, the process is reversible and the relation between air density and relative air pressure is isentropic (Falcão & Justino, 1999; Sheng et al., 2013; Falcão & Henriques, 2014). However, due to the viscous losses, important changes in specific entropy occur in the flow through the air turbine and can be related to its efficiency. Falcão & Justino, (1999) higligted relevant differences between the two main phases that take place in the air chamber:

1. *Enhalation phase* ($p_{OWC}<0$): the air is sucked inside the device by the turbine and mixes with the de-pressurized air in the chamber, which has a density and a temperature lower than those of the atmosphere. When the air flows from the atmosphere to the chamber, a highly turbolent mixing process takes place, while the airflow with specific entropy $s>s_a$ enters in the chamber.

2. *Exhalation phase* ($p_{OWC}>0$): the pressurized air leaves the device througth the turbine with a larger density than of atmosphere, in an isentropic process for the air remaining in the chamber, while a complex mixing process occurs outside.

Assuming the air as an ideal gas, Falcão & Henriques, (2014) proposed the following polytropic relation between the relative air pressure in the chamber, p_{OWC}, and the air chamber density, ρ_a:

$$\frac{p_{atm}-p}{\rho_a{}^{\theta}}=\frac{p_{atm}}{\rho_{atm}{}^{\theta}} \tag{2.23}$$

where ρ_{atm} is the atmospheric air density, p_{atm} is the atmospheric air pressure and θ is the polytropic exponent related to the effciency of the air turbine (for a perfectly efficient turbine θ=1.4). They also considered the spring-like effect due to air compressibility in the chamber, defining the mass flow rate of air through the air turbine as:

$$\frac{dm}{dt}=V\frac{d\rho_a}{dt}+\rho_a q \tag{2.24}$$

where $q=dV/dt$ is the volume flow rate displaced by the oscillation of the water column.

To respect the dynamic similarity and considering Eq. 2.21, the relation that should take equal values under corresponding conditions in model and full scale was defined as follows:

$$\Psi=\frac{V}{\theta q(p+p_{atm})}\frac{dp}{dt} \tag{2.25}$$

For a perfect Froude similarity, the scale ratio of the air chamber volume should be $V_m/V_p=\varepsilon^3$ (in which the subscript m and p denote the model and the prototype scale) and for a correct representation of air compressibility the realtion Ψ_m must be equal to Ψ_p, requiring equally efficient turbines at both scales ($\theta_m=\theta_p$). Then, assuming the same atmospheric pressure at both scales, the air chamber volume ratio becomes:

$$\frac{V_m}{V_p}=\frac{\theta_m}{\theta_p}\frac{\rho_p}{\rho_m}\varepsilon^2 \tag{2.26}$$

Falcão & Henriques, (2014) suggested that in model testing, at scales smaller than about 1:8th, the polytropic exponent is θ_m=1 and the water density ratio is ρ_m/ρ_p=0.97 (if the model is performed in a wave tank or flume filled with fresch water), then Eq. 2.26 becomes:

$$\frac{V_m}{V_p} = \frac{1}{\theta_p}\varepsilon^2 \tag{2.27}$$

Considering that at model scale air is compressed by small pressures and behaves essentially as incompressible (i.e. *Mach number, Ma*< 0.2-0.3), several options aimed at satisfying the scaling requirements of air compressibility, assuming fully geometric similarity in model testing of OWCs, could be taken into account:

- Adjustment of the material properties by the selection of an appropriate operational gas, even if it is a fundamental thermodynamic material requirement, that the isentropic exponent is always greater than unity.
- Alteration of the fluid density in order to influence the ratio of mass forces and compression forces. Indeed, as stated by Braeunig et al., (2009) and Braeunig et al., 2010) for the sloshing model tests on tanks of a membrane LNG vessel, keeping at model scale the same liquid and gas characteristics as at full scale, leads to an over-influence of compressibility effects (Fig. 2.13). However, considering the required high fluid densities, scaled reciprocal proportionally to the characteristic length, this option is impractical.

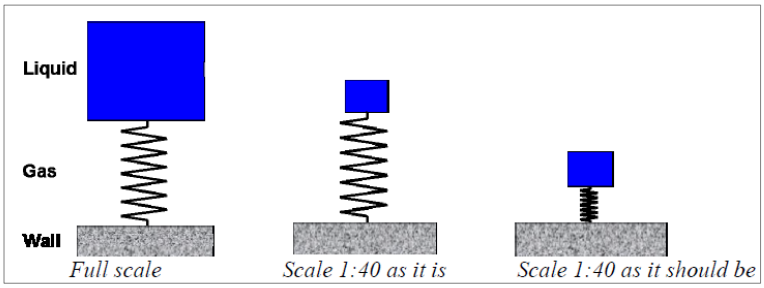

Fig. 2.13 - Schematic representation of the balance required for liquid and gas properties at two scales (Braeunig et al., 2009).

- Control of the ambient atmospheric pressure by adopting an ambient pressure ratio of model to prototype equal to that of the length ratio, which however implies relevant costs and efforts.
- A more practical solution is to connect the air chamber of the model to an additional rigid-walled reservoir of air with appropriate volume (Sarmento, 1993; Weber, 2007). However, even if this solution is feasible for fixed OWCs, in case of floating OWCs, it could introduce elastic, damping and inertia forces, influencing the static stability and the system dynamics.

The errors induced by neglecting the air compressibility effects, when modelling OWC devices at small-scale, was evaluated by Simonetti, (2016), who compared the results from OWC models performed by a compressible CFD model at full-scale (1:1) and at small scale (1:50). Simonetti, (2016), provided correction factors for the laboratory results, highlighting that the effect of neglecting the air compressibility may result in an overestimation of about 10% for relative air pressure p_{owc} and airflow volume q, but less than 10% for the performance of the device. Moreover, in order to evaluate the effect of the model scale on the air compressibility, Simonetti, (2016) simulated three smaller scales (1:5, 1:10 and 1:25), showing the relevant influence of the Mach number (*Ma*), which governs the compressibility of the airflow.

Since at full scale, large volumes of the air chamber are necessary to avoid green water from reaching the turbine, the air compressibility may have a relevant role in the processes involved within the OWC device.
At model scale, air is compressed by small pressures and behaves essentially as incompressible (i.e. Mach number, Ma< 0.2-0.3). Several options were suggested to satisfy the scaling requirements of air compressibility, for a fully geometric similarity. However a suitable simulation of the thermodynamic effects in the OWC chamber is usually a not practical solution. Moreover, in case of floating (or integrated) OWCs, some of the proposed solutions could introduce elastic, damping

and inertia forces, influencing the system dynamics.
Model experiments should take into account that, neglecting the air compressibility leads to an overestimation less than 10% of the OWC performance and that this overestimation is strongly influenced by the selection of the scale factor (hence by the Mach number), (Simonetti, 2016).

2.2.5 Summary and implications for the present study

Since the losses in the energy conversion chain are known to be relatively large and occur mostly in the conversion of wave to pneumatic energy and in the air turbine, the OWC design and construction are the most crucial issues affecting the costs of the produced energy. Hence, the hydrodynamics associated with wave energy absorption and the air turbine aerodynamics are both critical issues to take into account during the design stage (Falcão, 2004).

Although the hydrodynamics of wave energy conversion is already well understood, there is no established approach to structure conception, design and constructional method. This is due to the high complexity of the significant loads induced by waves breaking on structures. The uncertainty associated with the prediction of such wave loads commonly result either in large safety factors (too conservative design) or in an unsafe design. Moreover, the OWC design and construction procedures are strongly dependent on the construction site.

In this context, the integration of Oscillating Water Column devices (OWCs) into Very Large Floating Structures (VLFSs), as conceived in this study, might be beneficial as it presents many advantages, such as shared construction/maintenance costs implied by the multi-use of the VLFS and easy access for construction, operation and maintenance.

The review and analysis of the current knowledge on OWC-WECs pointed out the following specific implications to take into account for the selection and development of a suitable OWC device to be incorporated in the VLFS:

- Among the several WEC technologies, the OWC device has no moving elements directly activated by the waves and no contact of the air turbine with seawater, then it is robust, reliable and easy to maintain. Moreover, OWC is adaptable and therefore the most suitable device for the VLFS, since it can be integrated without altering the structure. Furthermore, the OWCs represent an innovative method in attenuating the VLFS floating behaviour. Then, if properly designed OWC may provide a double function: to attenuate the VLFS motion and to harvest and convert the incident wave energy.
- Theoretical and numerical models based on linear wave theory cannot represent the non-linear effects (due to large amplitude of the waves and the water column motion, wave breaking and real fluid effects). Although, CFD code can account for such effects, this approach requires the experimental validation. Therefore, physical models represent a crucial step in the assessment of the OWC performance at an early stage of development.
- A common index for the energy harvesting performance of WECs is the dimensionless Capture Width, CW*, obtained by normalizing the Capture Width [m] (Eq. 2.18) by the length of the device transversal to the wave direction (Evans & Porter, 1995; Morris-Thomas et al., 2007; Zhang et al., 2012; Kamath et al., 2015). The selection of CW* as a commonly used index allows the comparison with existent studies.
- To assess the performance of an OWC specific measurements are necessary in the small-scale tests, the relative air pressure variations in the air chamber, the ongoing/outgoing air fluxes and the water surface oscillations.
- The wave energy conversion of fixed OWCs is strongly affected by the chamber width (in the direction of wave propagation) and by the front wall draught. Therefore, a parameter study has to be performed in order to improve the knowledge of their effect on the OWC performance.
- The damping induced by the air turbine also plays a relevant role on the performance of the device and need to be investigated at small scale. The literature review suggests two main methodologies to reproduce at model scale the damping effect. Morris-Thomas et al., (2007), Sheng et al., (2012)and Ning et al., (2016) used an orifice to mimic the non-linear effect of self-rectifying impulse turbines. Lewis et al., (2003), Forestier et al., (2007) adopted a window equipped with a porous material to simulate the laminar effect induced by Wells turbines.
- The performance of floating OWC is mainly affected by the aforementioned design parameter and by the relative motion between the water column and the OWC.

- As for OWC integrated in a floating structure, to date few studies were performed on floating breakwaters equipped with OWCs. The results show that in addition to the design parameters observed for the fixed and floating OWC, the performance of the device may be also affected by the floating motion of the structure. In particular, it was observed that the structure moves in phase with very long waves, resulting in a decreasing of the air-pressure fluctuation inside the device with increasing the wave period beyond the natural period of the heaving response of the structure.
- Due to the remarkable influence of the OWC geometry on wave energy conversion, its sizing has to be performed according to the sea state characteristics of the hypothetical installation site. Then, to obtain results representative of a real sea state, irregular wave tests are crucial.
- Among the several scale effects affecting usually the physical models, the most relevant is the air compressibility, which has a significant influence at prototype scale. Although, the state of the art suggests several methods to reproduce properly the thermodynamic effects within the OWC chamber, most of them are not practicable in laboratory and could introduce additional effects on the system dynamics.
- Neglecting the air compressibility effects during the laboratory tests, leads to an overestimation of the OWC performance up to 10%. Then, the results achieved in the experiments should be corrected, according to Simonetti, (2016).

2.3 Specification, objectives and methodology

Based on the analysis and the results of the state of the art review, three are the main objectives of this PhD thesis as specified below:

i) Development of a conceptual design of a VLFS-OWC system, taking into account the suitability and feasibility in a hypothetical installation site located in the Mediterranean Sea and characterized by a moderate wave climate.
ii) Performance and analysis of systematic small-scale physical model tests in a wave flume to investigate the VLFS-OWC system. The physical model is performed adopting a tiered approach (fixed OWC, VLFS without OWCs, VLFS with incorporated OWCs) and is mainly aimed at assessing the combined effect of OWC design parameters (chamber width and front wall draught), air turbine induced damping, length of the VLFS and VLFS floating behaviour, on the performance of the integrated OWC under both regular and irregular wave tests in deep to intermediate water depths.
iii) Analysis of the experimental results to develop empirical formulae aimed at the prediction of: i) the heave motion of the VLFS-OWC System and, ii) the performance of OWC integrated in a VLFS. The empirical formulae might be adopted as a supporting tool for the preliminary design stage to determine the most appropriate geometrical parameters of the OWC chamber, the air turbine damping as a function of the incident wave parameters representative of the installation sea state.

The methodology adopted to achieve the aforementioned objectives is schematically summarized in Fig. 2.14, and described as follows:

In *Chapter 3*, the design and sizing of a VLFS-OWC system is reported, considering the reliability and feasibility in a hypothetical installation site of the Mediterranean Sea. The potential installation site is selected according to the results achieved in a previous study on the assessment of the wave energy potentials in the Mediterranean Sea (Vannucchi et al., 2012). Once selected the site, characterized by a moderate wave climate (mean annual wave power of 3kW/m), the representative sea state is defined, to perform a preliminary sizing of the VLFS-OWC system. Then, the VLFS is suitable designed, taking into account the building method, the construction materials and the feasibility in the Mediterranean dockyards. The sizing and design of the OWC are performed based on the outcomes of the review and analysis of the state of the art and on the characteristic wave parameters representative of the installation site. The integration of the OWC devices in the VLFS aims at combining efficiently the attenuation of VLFS motions and the improvement of the OWC performance, both aspects are addressed in the laboratory experiments.

In *Chapter 4,* a detailed description of the small-scale experiments on VLFS-OWC model, laboratory setup, methodology and measurements, is provided. The laboratory tests are carried out by means of a parameter study and a tiered approach consisting in three phases: (i) Fixed OWC

models (Phase I); (ii) VLFS models without the OWCs (Phase II) and (iii) VLFS equipped with OWCs (Phase III). The main aim of the experiments is the assessment of the parameters, which mainly affect the performance of fixed OWC, and the evaluation of the effect of the VLFS motions on the OWC performance, by comparing fixed OWC models with floating OWC models. The measurements acquired from the tests are preliminary analysed with the objective of providing a basis for a better understanding of the OWC wave energy conversion under fixed and floating conditions.

In Chapter 5, starting from the findings of the preliminary analysis and by means of dimensional analysis, empirical formulae for the prediction of the VLFS heave motion and of the performance of the integrated OWCs in regular and irregular waves are developed. The main purpose of the prediction formulae is to support the preliminary design and sizing of the integrated OWC device in a VLFS, giving as input the most relevant design parameters of the OWC device and of the VLFS as well as the wave characteristics of the site selected for the installation of the VLFS-OWC System.

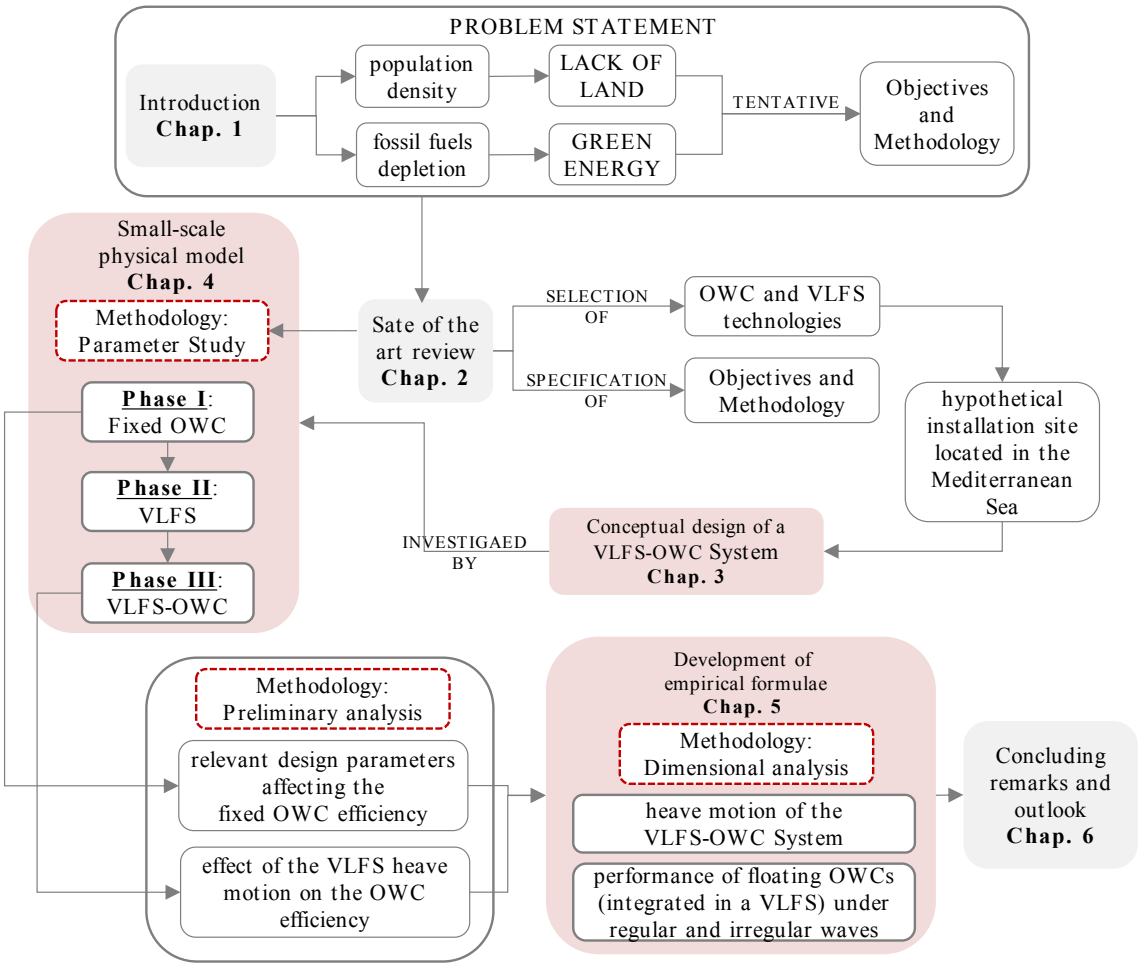

Fig. 2.14 - Methodology adopted in the PhD thesis.

3 Conceptual design of a VLFS-OWC System

The main aim of this chapter is to motivate the specific proposal of the VLFS-OWC System in terms of its sizing, building methodology and the preliminary conceptual design, taking into account its technical feasibility in a site selected in the Mediterranean Sea, characterized by a moderate wave climate (mean annual wave power of 3 kW/m).

The selection of the hypothetical installation site is performed according to a previous PhD work on the assessment of the wave energy potentials in the Mediterranean Sea and the analysis of the non-technical barriers (Vannucchi, 2012). Once the site is selected, construction materials and methodology are carefully chosen considering their feasibility and the representative sea state, to size the VLFS ensuring the safety conditions for possible operational staff and facilities.

Based on the review and analysis of the current knowledge (*Chapter 2*) and the design wave parameters of the selected site, the preliminary OWC design is performed, in order to be incorporated in the VLFS, combining efficiently the effect of the OWC on the attenuation of the VLFS motions and the wave energy conversion, both aspects being addressed in the laboratory experiments (*Chapter 4*). The outcomes of this chapter provide the basis for the design of the laboratory tests aimed to investigate the effect of changing design parameters of VLFS and OWC on the wave energy conversion.

The organization structure and procedure adopted in *Chapter 3* is summarized in (Fig. 3.1).

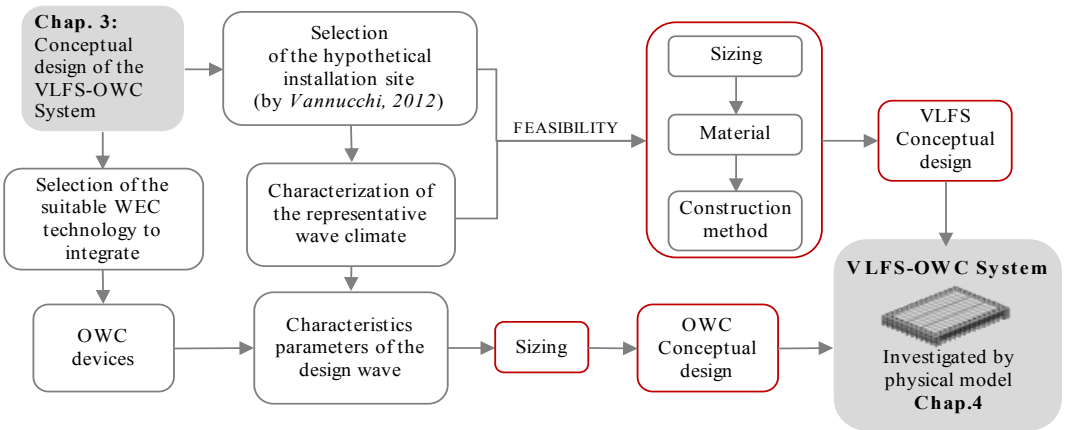

Fig. 3.1 - Organisation structure of *Chapter 3*.

3.1 Conceptual design of a VLFS

This section provides the preliminary conceptual design and sizing of a VLFS, taking into account its feasibility in a specific site proposed for a hypothetical installation. It begins with the selection of the installation site and the suitable VLFS geometry. Then, sizing, construction materials and manufacturing methodology are proposed, considering the technical feasibility as well as the main hazards for equipment, operational staff and facilities.

3.1.1 Selection of a hypothetical installation site

The installation site is selected according to the outcomes achieved by Vannucchi (2012) on the wave energy potential in the Mediterranean Sea and the identification of possible focus zones near the coastal areas and non-technical barriers.

The site considered refers to one of the most energetic Italian Mediterranean area located in the Central Tuscany at a water depth of -25m S.W.L and characterized by a mean annual wave power of about 3kW/m, (Fig. 3.2). This annual wave power is obtained with an occurrence frequency of about 4.2%, for sea states in the range 1.5m≤H_{m0}≤2.0m and 6.5s≤T_e ≤8.5s (where T_e is the wave energy period or wave spectral period T_{m-10}, (see *subsection 2.2.1*)). The mean annual energy value, above 1MWh/m, refers to a sea state with an occurrence frequency of about 16% and waves heights and period in the range: 1.0m≤H_{m0}≤3.0m and 5.0s≤T_e ≤8.0s.

Central Tuscany

lat. (UTM32): 4816119

long. (UTM32): 606514

Water depth:

-25m SWL

Annual Energy [kWh/m]

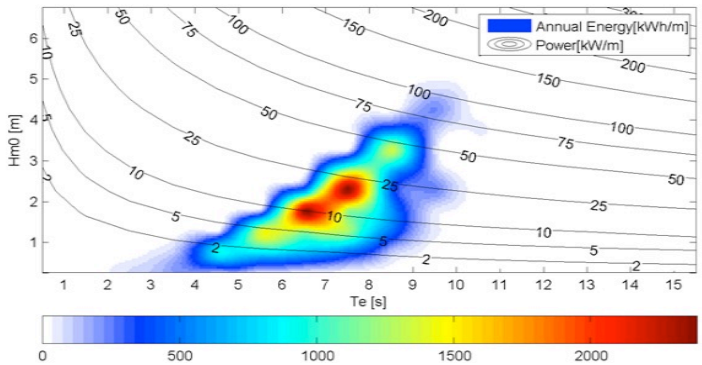

Scatter matrix of the annual energy [MWh/m] of H_{m0} and T_e

		H_{m0} [m]							
		<1	1	1,5	2	2,5	3	3,5	>3,5
Te [s]	<3	0,1	0,0						
	3	0,2	0,1						
	4	0,2	0,8	0,0	0,1				
	5	0,1	0,7	0,5	0,1				
	6	0,1	0,6	1,4	2,4	0,6			
	7	0,0	0,5	1,3	1,2	2,4	1,2	0,0	
	8	0,0	0,1	1,3	0,6	0,8	0,7	1,1	0,3
	>8	0,0	0,1	0,1	0,1	0,2	0,1	0,1	0,2

Fig. 3.2 - Annual Energy [kWh/m] and Scatter matrix [MWh/m] extracted at -25 m SWL referred to the hypothetical installation site selected for the VLFS-OWC System in the Mediterranean Sea (Central Tuscany), (Vannucchi, 2012).

To ensure the feasibility and reliability of the VLFS, in addition to the energy potentials characterizing the installation site, the analysis performed by Vannucchi (2012) on the non-technical barriers as the environmental, logistical and social constraints, is taken into account, (Fig. 3.3).

In particular, Vannucchi (2012) considered: i) the presence of marine protected area, ii) the distance from the coast and harbour facility and iii) the navigation routes.

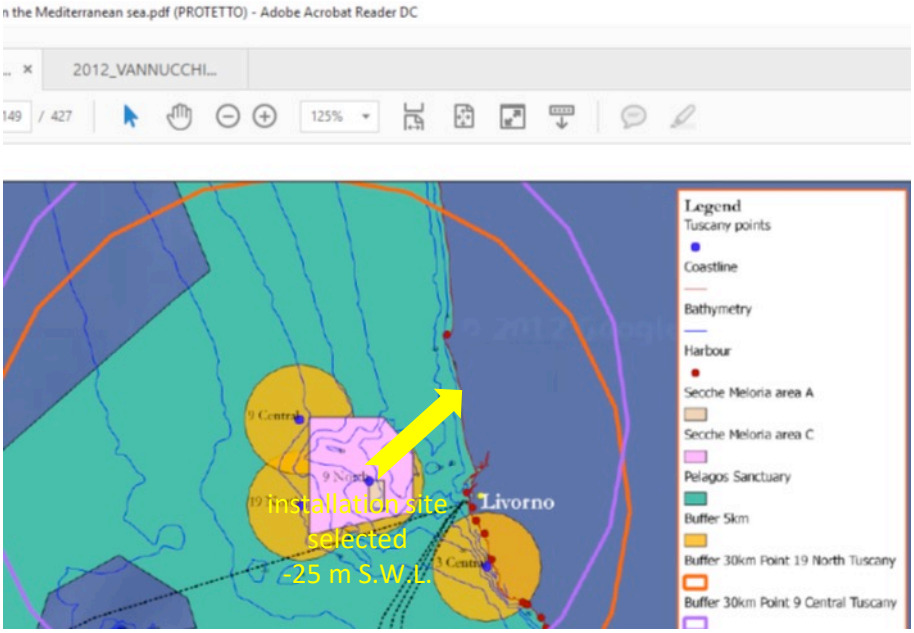

Fig. 3.3 - Tuscany area: analysis of the non-technical barriers (Vannucchi, 2012).

The installation site considered is far from two of the most important protected area of the Mediterranean Sea (i.e. the Secche della Meloria and the Pelagos Sanctuary) and is located in front of Livorno, which is a large population centre and a commercial harbour, also famous for the shipbuilding. Since the main navigation routes do not cover this area, it would result the most suitable solution site to install the VLFS-OWC System. Furthermore, the distance of 580m from the coast, could allow the cable installation and grid connection at relatively low cost.

According to the above considerations, seven target waves are selected as representative of the sea state characterizing the Central Tuscany site at a water depth of -25 m S.W.L. (Table 3-1).

Table 3-1: Target waves representative of the hypothetical installation site selected, located in the Central Tuscany at a water depth of -25m SWL.

	H_{m0} [m]	T_{m-10} [s]
Wave-1	1.0	6.5
Wave-2	1.0	7.0
Wave-3	2.0	6.0
Wave-4	2.0	7.0
Wave-5	2.0	10.0
Wave-6	2.0	8.0
Wave-7	3.0	8.0

3.1.2 Sizing and Design

From the analysis and review of the state of the art performed in *Chapter 2,* between the two main geometries of VLFS, that selected for this study is the pontoon type VLFS, which in addition to its ecological aspect, features many advantages, including low manufacturing cost as well as easy and fast construction. Moreover, the literature review suggests the use of the pontoon type VLFS in not exceptionally energetic sites (see *Chapter 2*), and then it is suitable for the moderate wave climate characterizing the site selected.

Concerning the preliminary sizing and design of the VLFS, the feasibility of its construction in the Mediterranean Sea, is taken into account, as reported in detail below.

a) Material and construction method proposed

The current knowledge on the VLFS technologies suggests that one of the most suitable material used for their construction is the concrete (e.g., Floating bridge in Dubai, Floating container

terminal in Valdez, Ujina's floating pier in Hiroshima etc.), which features also the following several advantages compared to other materials (VSL International LTD. 1992)

- low cost and suitability in marine environment;
- easy to make concrete structures buoyant in the construction stage as well as permanently and for towing;
- possibility to make the structures heavy enough for a safe permanent installation;
- possibility to provide storage space.

However, since water tightness of concrete is important, to avoid or limit corrosion of the reinforcement, either watertight concrete or offshore concrete should be used (Fujikubo & Suzuki, 2015).

The method proposed for the manufacturing of the VLFS is selected according to its feasibility in the existing Mediterranean dockyards, which are provided for the facilities specifically designed for the construction of the concrete caissons and towing (Fig. 3.4). Therefore, the multi-module construction method, performed by assembling at sea each watertight precast concrete module is the most appropriate.

Fig. 3.4 - a) (on the left) Concrete caissons pier of Enel Thermal Power Plant at Torrevaldaliga (RM), b) (on the right) the Spanish company DRACE.

It is important to note that the precast concrete modules could be repurposed to open up extra floor space, which can be re-modelled and utilised as car parks, offices and storage rooms[1]. The multi-module construction method is also the most suitable in case of future renovations or expansions of the structure as well as for maintenance and repair operations.

Each module, conceived for the construction of the VLFS is a concrete watertight hollow caisson (22.50m high, 30.0m wide and 0.10m long), obtained by assembling (Fig. 3.5):

- cover slab with a rectangular shape of 30x10m and thickness 0.25m;
- front wall 30m wide and 22.25m high, with a thickness 0.40m;
- side walls 10m wide and 22.25m high, with a thickness 0.40m.

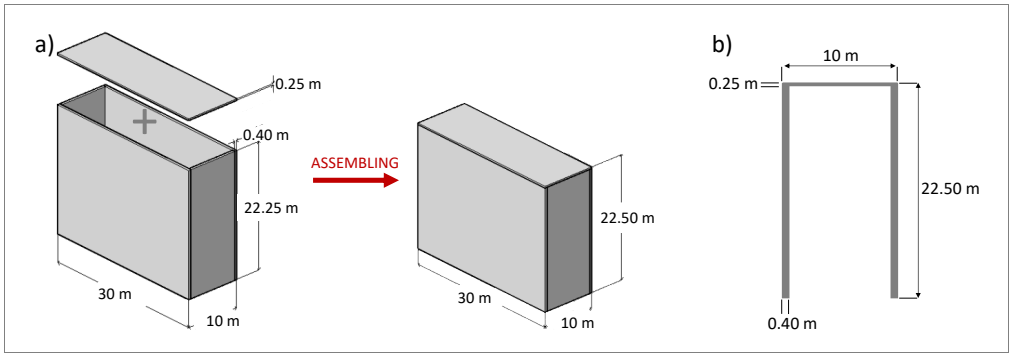

Fig. 3.5 - Structural characteristic of each watertight hollow caisson of the VLFS: a) 3D view and b) cross section view.

[1] The floating pier built at Port Hercule de la Condamine in Monaco, is a double-hulled precast structure, which houses a 380-lot car park and dry dock for recreational craft. This offers a significant advantage over land reclamation given the ease in ability to extend habitable space below the water line.

The VLFS proposed in this study is a rectangular shape platform, obtained joining watertight floating caisson units (Fig. 3.6).

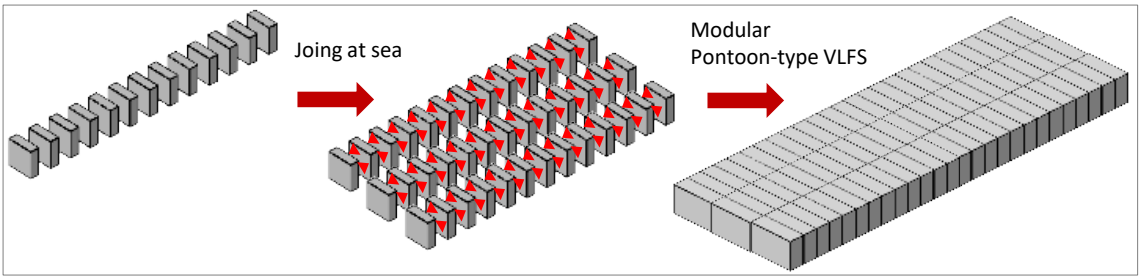

Fig. 3.6 - Multi-module construction method, assembling stage and VLFS assembled.

b) Selected freeboard

To establish the appropriate freeboard of the structure, a preliminary rough estimate of the maximum mean overtopping discharge, is performed. The wave parameters taken into account are those related to the toe of the structure, as obtained by the wave resource study for the site (see Table 3-1). Considering the height of the caisson unit, the relevant wave parameter has been calculated for the worst sea state available that is, the one associated to the wave with a recurrence interval of 50 years for the site selected (H_{m0}=7.0m T_p=7.8s), (Vannucchi, 2012).

According to the suggestions of the EurOtop Manual (Pullen et al., 2007), the mean overtopping discharge for vertical breakwaters depends on the interaction between waves and structure, expressed by a wave breaking or "impulsiveness" parameter given as follow:

$$i^* = 1.35\frac{h}{H_{m0}} \cdot \frac{2\pi h}{g{T_{m-1,0}}^2} \tag{3.1}$$

where h is the water depth at the toe of the VLFS (-25 m S.W.L.).

It has been proven that, for i^*>0.3 waves are pulsating (non-impulsive), whereas for $i^* \leq 0.3$, wave are impulsive. Considering that the overtopping phenomenon is substantially different in case of impulsive or non-impulsive waves, a different method is used for estimating the mean overtopping discharge.

In this study, the impact of the significant wave approaching the VLFS resulted to be non-impulsive (i^*>0.3). Hence, the mean overtopping discharge can be calculated through the deterministic design formula as follow:

$$\frac{q}{\sqrt{g{H_{m0}}^3}} = 0.04exp\left(-1.8\frac{F_c}{H_{m0}}\right) \tag{3.2}$$

in which, F_c is the crest freeboard. Since the freeboard designed for the VLFS is +8.0m S.W.L., the mean overtopping discharge results about 0.30l/s/m. Then, considering the main hazards for equipment, operational staff and facilities on or close to the VLFS, the freeboard selected found compliant with the tolerable discharges limits proposed by Pullen et al., (2007). However, it will be necessary to protect the instrumental equipment located back 5-10m from the edge of the structure.

c) Stability assessment of a VLFS unit

Taking into account the several construction stages of the VLFS, with particular respect to the towing and assembling at sea, a rough evaluation of the stability of the individual caisson unit is essential. As reported above, the caisson unit proposed is a watertight hollow retaining structure, characterized by a total concrete volume of about 773m^3 and a weight of about 2000t (with the reinforced concrete density equal to 2500Kg/m^3).

Although the caisson unit could achieve the buoyant equilibrium, such that the total force composed of gravity and buoyancy vanishes, it may still not present a complete mechanical equilibrium. Then, also the mechanical stability of the caisson unit is a significant element of safety to be evaluated.

The total moment of all the forces acting on the caisson unit must also vanish; otherwise when the caisson is stressed by an external force, it will necessarily start to rotate. The mechanical stability is the capacity of the caisson unit to oppose the tipping, which could occur during the towing stage of the caisson unit at the installation site.

Thus, in order to give a rough evaluation of the caisson unit stability, it is necessary to determine the location of the centre of gravity (CG) and the centre of buoyancy (CB). The latter is the centre of the volume of water, which the caisson unit displaces.

Considering the freeboard designed at +8.0m S.W.L. and a reference axis z, with origin at the centre of the top cover surface, the position of the centre of buoyancy (z_{CB}) is located at 14.25m, instead the position of the centre of gravity is given by:

$$z_{CG} = \frac{F_{top}z_{top} + F_{lat}z_{lat} + F_{iw}z_{iw}}{F_{top} + F_{lat} + F_{iw}} = 14.5m \tag{3.3}$$

in which:

- F_{top}, is the force applied at the top cover of the caisson unit:
- $F_{top} = \rho_{cls}V_{top}g = 1.84 \cdot 10^6 N$, at z_{top}= 0.125m
- F_{lat}, is the force applied at the lateral walls of the caisson unit:
- $F_{lat} = \rho_{cls}V_{lat}g = 17 \cdot 10^6 N$, at z_{lat}= 11.25m
- F_{iw}, is the force applied at the inner water volume of the caisson unit:
- $F_{iw} = \rho_w V_{iw} g = 25 \cdot 10^6 N$, at z_{iw}= 17.8m.

The stability condition requires that the canter of gravity (CG) lies below the Metacentre (M), which is defined as a fictive point usually placed on the vertical line through the equilibrium positions of the centre of buoyancy and gravity (Wang & Wang 2015), (Fig. 3.7).

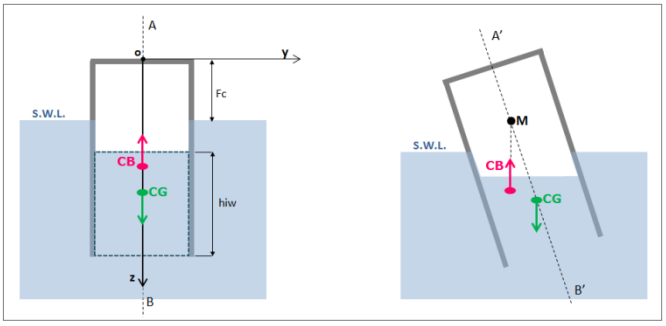

Fig. 3.7 - Schematic representation of the stabilization and overturning of floating body. (CG = centre of gravity, CB = centre of buoyancy, M = metacentre).

The evaluation of CB and CG position for the proposed caisson unit reveals that the centre of gravity is located just below the centre of buoyancy. Therefore, the equilibrium orientation of the caisson unit is less stable and under a small stress perturbation, it could flip over. A solution for the stability problem is to shift CG, applying a system of ballast at the end edge of the lateral caisson walls, or to design a different caisson layout, increasing the width with respect to the draft dimension (Fig. 3.8).

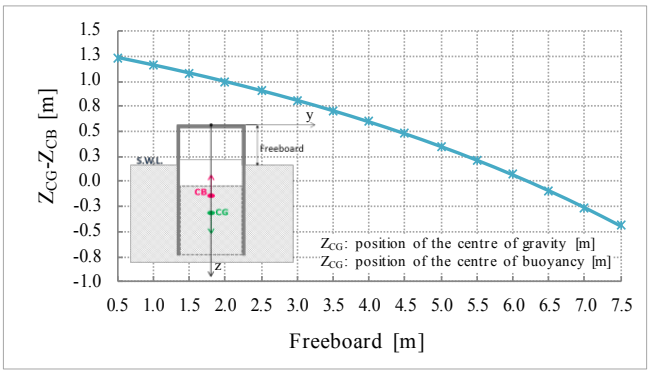

Fig. 3.8 - Trend of the caisson unit stability varying the freeboard.

However, to address the stability problem, the installation at the top of each unit of a specific system capable of changing the air volume and pressure inside the caisson and as consequence, the height of the inner water column, is proposed.

The air-controlled system, taking the air inside the caisson, could shift CG below CB, inducing the unit to a higher immersion and consequently to the increasing of the restoring moment. Moreover, this specific system could be applied during the towing stage, as well as before the assembling among the floating units. Once the units are joined at the installation site, the air-controlled blows the air inside each unit making the VLFS at the designed freeboard, then it could be applied also in order to control and to vary the freeboard according the requirements of the multipurpose VLFS.

d) Mooring System selected

As for the preliminary design of the mooring system, the catenary lines are proposed for the VLFS, since they are the most common mooring type employed for these structures (Shuku, 2001; Wang & Wang, 2015).

The catenary mooring system offer slackness in each line, which effectively allows mooring lines to behave as a spring. This provides the mooring line with the ability to extend with tension forces acting through it and can be used to attenuate and to restrain motions of the VLFS. Moreover, pretensions in the catenary lines are used to secure the desired position of the structure (Andrikopoulos, 2012).

The site selected for a hypothetical installation of the VLFS-OWC system is located in a Mediterranean area in front of Livorno coasts at a water depth of -25m S.W.L. This site has a mean annual wave power of about 3kW/m and is characterized by a sea state in the range $1.5 \leq H_{m0} \leq 2.0$*m and* $6.5 \leq T_e \leq 8.5$*s.*
The VLFS is preliminary sized and designed as a pontoon type modular platform, manufactured by joining concrete watertight hollow caissons, as building elements. Each caisson unit is equipped with a proper air-controlled system aimed at regulating the buoyancy and the stability during the towing stage at the installation site.
The VLFS freeboard of +8.0m S.W.L, in order to limit the overtopping discharges to tolerable values, as suggested by Pullen et al., (2007). A catenary mooring system is proposed to keep the VLFS in site

3.2 Conceptual design of an OWC

Since the use of renewable energies, such as offshore energies (e.g. from waves) is stimulated by the increasing shortage of fossil fuels and pollution, the VLFS conceived for this study is equipped with Wave Energy Converters (WECs), which can be used directly to supply part of the multipurpose activities based on the VLFS.

3.2.1 Selection of the suitable WEC technology

Considering the aforementioned VLFS structural characteristics, each of the main three technologies of WEC (see *Chapter 2*): i) Oscillating Water Column, (OWC), ii) Wave Activate Body (WAB) and iii) Overtopping Devices (OTD), could be integrated.

As for the WABs, it could be possible to conceive the whole VLFS as a heaving oscillating-body device, reacting against the sea bottom, driving four hydraulic systems aimed to convert energy from the large forces applied by the incoming waves. In this case, the four hydraulic systems could be located in correspondence of the four mooring lines, which keep the structure in site.

Moreover, Drew et al., (2009) suggested the use of this Power Take Off system, (PTO), when WEC size and weight are an issue, and the force created by these pressures are considerably greater than those from the best electrical machines. However, to maximize its efficiency, this technology implies a large movement of the VLFS, resulting not appropriate in ensuring the safety upon it.

Concerning the possible installation of Pitching devices (e.g., Pelamis or McCabe Wave Pump), in which the energy conversion is based on relative pitching motion between two bodies, they could be integrated among the units of the VLFS by means of hinged joints, and aligned with the wave direction. However, also this installation, due to the moving parts of the VLFS, is not adequately safe to guarantee the stability requirements.

As for OTDs floating (e.g. Wave Dragon), or fixed (e.g. Tapchan), their possible installation is not suitable, because of the large space needed for the deployment of the water reservoir, which would involve a drastic reduction of available VLFS surface for other facilities.

Since, to allow the usability of the VLFS, the preliminary design stage must take into account the stability requirement, ensuring the safety for operational staff and facilities, the state of the art suggests the use of OWC devices as an innovative and effective methodology, which also allow the integration without altering the structure (Maeda et al., 2000; Ikoma et al., 2003; Hong et al., 2006; Hong et al., 2007; Kyoung et al., 2008; Hong et al., 2009).

3.2.2 Sizing and Design

The OWC device conceived for the integration in the VLFS is a precast concrete watertight hollow caisson, characterized by a rectangular chamber, for an easy manufacturing stage as well as for sharing the costs with those needed for the VLFS construction.

To achieve an efficient wave energy absorption with an effective attenuation of the VLFS floating motion, the preliminary OWC sizing is performed considering the current knowledge on OWCs and the characteristics parameters of the wave which allows the highest annual energy (2.4MWh/m), in the hypothetical installation site selected (namely the *Design Wave* H_{m0}: 2.0m T_e: 6.0s).

Hence, the OWC is preliminary designed resulting in the geometrical characteristics reported in Fig. 3.9 and summarized as follows:

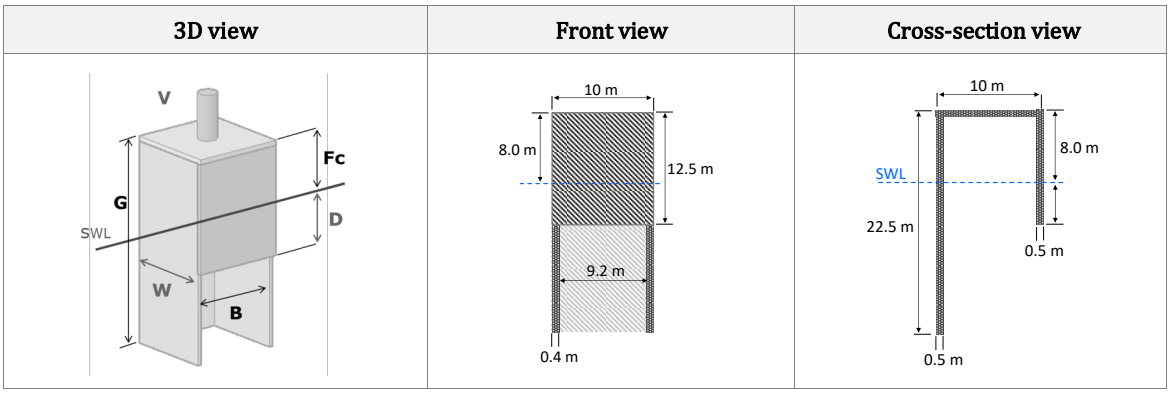

Fig. 3.9 - Schematic representation of the geometrical characteristics of the OWC device preliminary designed for the integration in the VLFS.

- Inner OWC chamber is sized with a rectangular-shaped section of 83m^2 and a chamber with a length (perpendicular to the wave direction) of B=10m, designed in order to avoid the formation of standing waves, to ensure a wave-sloshing period below 5s (Webb et al., 2005) and considering the sizes of existent OWCs (Limpet: 6m, Mutriku: 5-6m, Pico: 12m and Oceanlinx: 10m);
- Freeboard (Fc) is +8.0m S.W.L., according to the freeboard designed for the VLFS and the tolerable discharges limits proposed by Pullen et al., (2007);
- Back wall (G) is sized in order to maximize the reflected waves, amplifying the water column oscillation (Suroso, 2005) and account for the vertical distribution of the wave energy amount, *pr,* (i.e., the variation in the water column of the energy transported by the waves) evaluated for the range of waves H_{m0}: 2.0m, $10 < T_e < 6.0$s (see Table 3-1), as in Eq. 3.4 (Fig. 3.10):

$$pr = \frac{\overline{E(z*)}}{\overline{E_t(h)}} \tag{3.4}$$

in which: $E(z^*)$, is the wave energy (potential and kinetic) until the water depth z^*, (with values that vary in the range 0.5-50m with a step of 0.5m) and $E_t(h)$, is the total wave energy (potential and kinetic) on the whole water depth h.

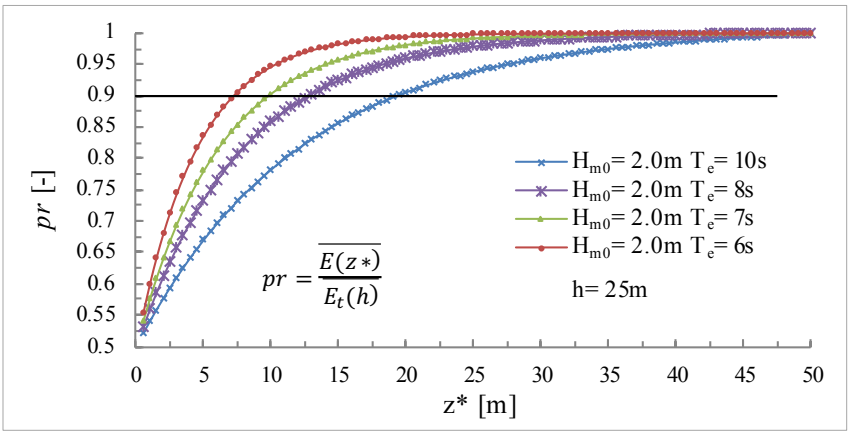

Fig. 3.10 - Wave energy variation within the water column assessed for the range of waves H_{m0}=2.0m, 10< T_e<6.0s and h=25m.

- Moreover, the same trend of pr was obtained considering the two waves characterized by a significant wave height equal to 1.0 and 3.0m (see Table 3-1), showing that the wave height doesn't influence significantly the pr values. Neglecting the 10% of the total wave energy, it is possible to note that, z^* converges to pr=0.9 faster for shorter wave periods (e.g. for T_e=6.0s the 90% is achieved with z^*=7.5m, instead for T=10s z^* is 22.5m). Hence, to capture the total wave power within the range of waves characterizing the installation site, the back wall is designed 22.5m long.
- Front wall is 12.5m long with a slope of 90°, to minimize the wave run up and maximize wave reflection, producing an amplification of the water column oscillation;
- Front, Top Cover and Back wall, are designed considering other prototype models and the current state of the art of reinforced concrete cellular caisson for marine structures.
- Lateral walls are 22.5m long as the back walls, with thickness of 0.4m and slope 90°.

The Power Take Off System (PTO)

Due the several disadvantages of the Wells Turbine such as: i) drop in power output due to aerodynamic losses at flow rates exceeding the stall-free critical value, iii) large diameter needed for its power[2] and iii) noise. (Falcão, 2004; Webb et al., 2005), the self-rectifying impulse turbine is selected as the suitable PTO for each OWC device embodied in the VLFS (Fig. 3.11).

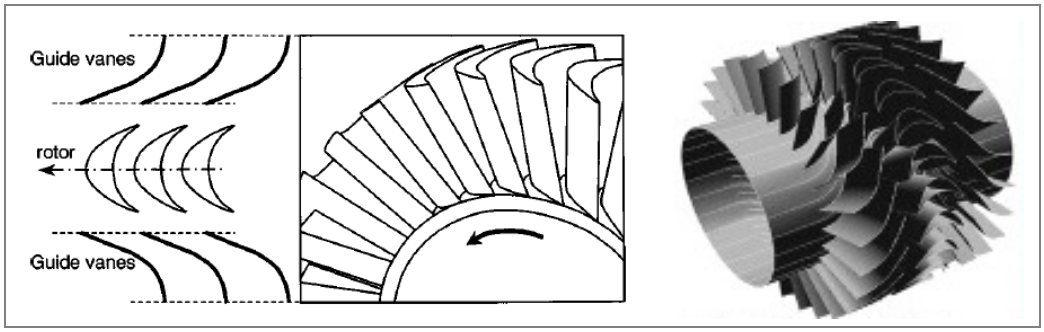

Fig. 3.11 - Self-rectifying impulse turbine (Falcão, 2004).

The self-rectifying impulse turbine is characterized by neighboring blades form channel for the passage of the air flow. The blade geometry is a modified version of the classical impulse steam turbine: the necessity of symmetry imposes in this case sharp edges and equal inlet and outlet blades angles.

[2] 2.3 m for the single rotor 400kW turbine of Pico plant, 2.6m for the counter rotating 500kW turbine of Islay II plant, 3.5m for OSPREY.

Unlike the Wells turbine, the impulse turbine has marked nonlinear characteristic (almost quadratic) and can have very good starting characteristics, lower operating speeds and a satisfactory efficiency over a wider range of flow rates (Falcão & Gato, 2012).

The WEC technology selected for the integration in the VLFS is the OWC, in order to allow, by means of its anti-motion effect, the usability of the structure. To share the manufacturing costs with the structure, each OWC is a precast concrete watertight hollow caisson, wuth a rectangular chamber (10x10x22.5m). The preliminary design of the OWC is performed considering the wave associated to the highest annual energy (2.4MWh/m with H_{m0}: 2.0m and T_e: 6.0s), with the main purpose of maximizing the incident power absorption, minimizing at the same time the VLFS floating motion. Each OWC is equipped with a self-rectifying impulse turbine PTO.

3.3 Conceptual design of the VLFS-OWC System

The VLFS-OWC is a modular rectangular-shaped pontoon type platform equipped with OWC devices (Fig. 3.12).

To reduce the dependence on the wave direction, the OWC devices are integrated along the perimeter of the VLFS and preliminary designed with the main purpose of: i) absorbing the incident wave-energy, protecting the VLFS from the wave loads and attenuating the VLFS floating motion; ii) converting the wave energy in a usable form, which can be used directly to supply part of the activities based on the VLFS-OWC System.

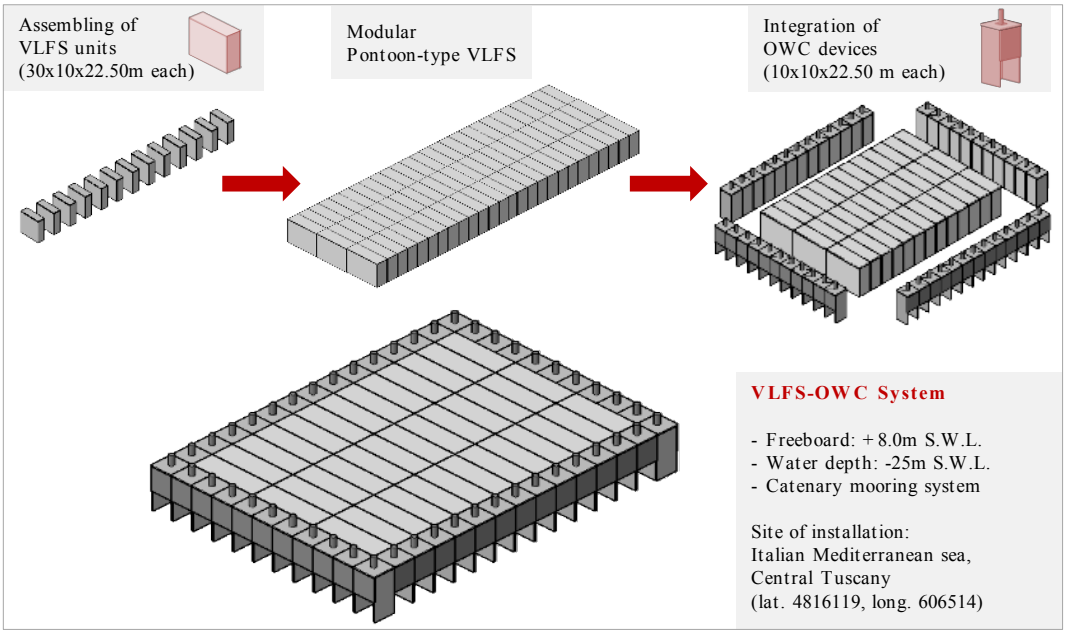

Fig. 3.12 - 3D view of the conceptual design of the VLFS-OWC system.

Each OWC device has a pneumatic chamber with rectangular-shaped section of 83m² and a large opening at the bottom, placed below the water level. The compression and decompression of the air volume, trapped above the inner water surface, due to the wave-induced water oscillation inside the chamber, produces an airflow through a duct, which drives a self-rectifying impulse turbine, located at the top of the device.

The VLFS-OWC System is kept in place by means of a catenary mooring system, which ensure the desired position of the structure, with a freeboard of +8.0m S.W.L. Moreover, the multi-module type construction method proposed for the VLFS-OWC system could allow future enlargement of the structure as well as easy maintenance and repair procedures.

3.4 Summary and implications

The pontoon-type VLFS-OWC System conceived for this study is preliminary designed considering the hypothetical site selected for its installation, located in a Mediterranean area at a depth of -25m S.W.L., and characterized by a moderate wave climate (about 3kW/m) with a sea state in the range 1.5m$\leq H_{m0} \leq$2.0m and 6.5s$\leq T_e \leq$8.5s.

The building procedure proposed for the VLFS is based on the multi-module-type method, performed by joining concrete watertight hollow caissons, equipped with an air-controlled system to ensure the stability during the towing stage. To share the manufacturing costs the OWC devices equipping the VLFS are precast concrete watertight hollow caissons, integrated along its perimeter, reducing the dependence of the VLFS-OWC System on the wave direction.

The conceptual design of the VLFS-OWC System and the design wave conditions of the installation site, are used for the laboratory tests planning, particularly: i) the VLFS and OWC scale-models construction; ii) the plan of tests on the sensitivity analysis to different design parameters, and iv) the specific laboratory technique adopted for the simulation of the air turbine-induced damping on the OWC device.

Since the OWCs integrated are mainly aimed at the improvement of the wave energy absorption and at the same time at the minimization of the VLFS-OWC floating motion, the implications for the experimental study presented in *Chapter 4,* may be summarized as follows:

- The size proposed for the VLFS-OWC and the 2D physical model approach allow to reproduce only the central section of the VLFS-OWC, providing results representative of an infinitely wide floating system. Moreover, as suggested in the literature review, the use of too small model scales must be avoided due to the surface tension effects and frictional effects at the bottom of the tank (Kagemoto et al., 1999; Takagi et al., 2007).
- Due to its relevant influence on the floating behaviour and then on the OWC performance, the preliminary designed length of the VLFS-OWC has to be experimentally investigated.
- For a suitable characterization of the VLFS-OWC behaviour, the physical model has to be performed, account for the connections between the VLFS units as well as the mooring system, aimed to keep the structure at the freeboard without affecting the floating motion during the tests.
- To provide additional data on the structural behaviour at sea, measurements of tensions necessary to hold together the units and pressures inside the units needed for the stability and buoyancy are necessary.
- Extensive scale model experiments are necessary in order to investigate and possibly to optimize the integrated OWC, achieving the best performance in a moderate wave climate. To address this objective, the laboratory tests have to be performed by means of a parameter study, investigating the effect of the most relevant design parameters affecting the performance of the device, which according with the state of the art review, are: i) the front wall draught; ii) the damping induced by the impulse air turbine, and iii) the chamber width (in the direction of propagation of the waves).
- Regarding the main objectives of this study (specified at the end of Chapter 2) for the assessment of the effect of the VLFS on the OWC performance, a tiered approach methodology has to be adopted, investigating at first the effect of the design parameters on the fixed OWC and on the VLFS without OWC, then on the VLFS-OWC system.

4 Laboratory tests in wave flume

In this chapter, the extensive scale-model experiments on a Very Large Floating Structure (VLFS), Oscillating Water Column (OWC) converters and on OWCs incorporated in VLFS, are described. A preliminary analysis of the results obtained for the different phases of tests, is performed. The experiments are mainly aimed at providing a better understanding of the effect of diverse parameters on the VLFS behaviour and the OWC performance.

Based on this understanding, prediction formulae, are derived. To address these objectives, the tests are carried out systematically in three phases: (i) Phase I: OWC models in fixed condition; (ii) Phase II: VLFS models without the OWCs and (iii) Phase III: VLFS equipped with OWCs. The effects of several design parameters on the OWC performance and the VLFS behaviour are preliminary analysed, including: (i) size of OWC chamber and front wall draught; (ii) pressure drop due to the air turbine and (iii) size and mass of the VLFS.

The parameter study is performed with irregular wave trains representative of the moderate wave climate of the hypothetical Mediterranean installation site. Regular wave tests are also conducted to facilitate the understanding of the involved processes and interactions, and also for numerical model validation. The preliminary analysis provides the implications for the final data analysis presented in *Chapter 5*, where formulae predicting the heave motion and the performance of floating OWC (integrated in VLFS), are developed. The organization structure and procedure adopted in Chapter 4 is briefly summarized in Fig. 4.1.

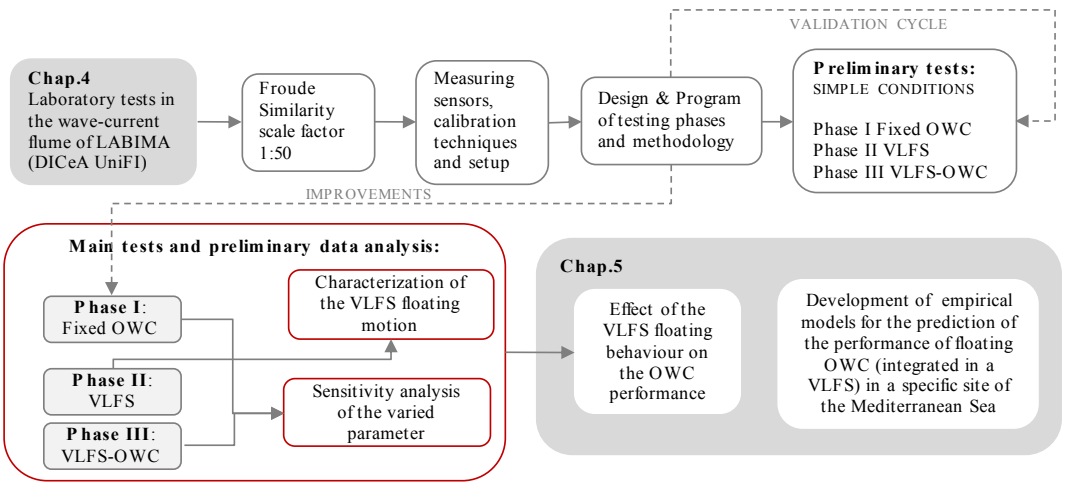

Fig. 4.1 - Organisation structure of *Chapter 4*.

4.1 Testing facility, testing phases and methodology

To provide data useful by a third part as well as to check the repeatability of the tests, in this section a detailed description of wave flume facility, model design, acquisition and calibration techniques and methodology, is reported.

4.1.1 Wave-current flume and model design

The experiments are conducted in the wave-current flume of the Maritime Engineering Laboratory (LABIMA) of the Civil and Environmental Department (DICeA) of Florence University (Fig. 4.2).

Fig. 4.2 - a) LABIMA wave-current flume and b) Piston-type wave maker.

The wave-current flume (37.30m long, 0.80m wide and 0.80m high) consists of 27 sectors, completely made of steel and glass and two basins, one behind the wave maker and the other located at the end of the flume. The basin behind the wave maker is fitted with a rubble mound breakwater, reducing the wave motions and the resonance along the wave flume during the tests.

A piston-type wave maker with a stroke of 1.6m, is driven by an electromechanical system with an extremely high accuracy (0.1mm in position). The wave maker motion is controlled by a latest generation electronics, with standard Fast EtherCAT communication. The electronics performs the control signals sent from a computer on which software for the generation, data acquisition and data analysis are installed. By means of a software developed by LABIMA and based on the technique called Deterministic Amplitudes and Random Phases (Hughes, 1993), the wave maker can generate a wave motion with specific spectral characteristics (maximum H_s=0.16m for T_p=1s in 0.50m of water depth). The signal is sent to the control system of wave maker and with the probes positioning along the flume, the wave motion acquisition is performed in real time. The system allows the generation of both sine waves, with height and period assigned, and sea states with random energy spectrum equal to the real waves (e.g. Jonswap, Pierson-Moskowitz, Scott Neuman, Bretschneider and Ochi-Hubble).

The random signal generated can be saved and repeated, allowing the generation of the same sea state. After the acquisition, the signal is analysed both in frequency domain (Spectral analysis) and time domain (Zero-Crossing analysis), to obtain all the characteristic wave parameters (e.g.: H_{m0}, $H_{1/3}$, $H_{1/10}$, H_{max}, H_{rms}, T_m, $T_{1/3}$, T_p, T_{m01}, T_{m-10}).

The wave-current flume is also equipped with a bidirectional recirculation system having a maximum flow rate of 25l/s (presently under renewal 100l/s). Butterfly valves are used to control the recirculation discharge that is measured using a magneto-electric flow meter with declared accuracy of 0.15%.

To reproduce properly the VLFS-OWC System, taking into account the predominance of gravitational forces among those related to the viscosity, the surface tension, the roughness, etc., the scale model is designed according to Froude similarity (Hughes, 1993). The model and the prototype must have the same Froude number, expressing the ratio between the square root of inertial forces F_i and gravitational forces F_g:

$$F_r = \sqrt{\frac{F_i}{F_g}} = \sqrt{\frac{\rho L^2 V^2}{\rho L^3 g}} = \frac{V}{\sqrt{gL}} \tag{4.1}$$

in which: ρ is the mass density [kg/m³]; g is the gravity acceleration [m/s²]; L is a characteristic length [m] and V is a characteristic velocity [m/s]. Froude similarity is given by the following assumption:

$$N_{Fr} = \frac{Fr_p}{Fr_m} = 1 \tag{4.2}$$

Hence, considering the following laboratory constrains related to the generation of the waves:

- maximum water level in front of the wave maker (0.50 – 0.60m);
- maximum significant wave height generated (H_s=0.15m, T_p=1-2s);

for the physical model object of this research, the following undistorted geometric scale is adopted:

$$N_L = \frac{L_m}{L_p} = \frac{1}{50} \tag{4.3}$$

in which: L_m is the model linear dimension and L_p is the prototype linear dimension.

Based on the dimensional analysis and assuming the validity of Froude similarity, the other parameters, involved in the investigation, are obtained. Table 4.1 shows the scale relations used to reduce the physical model.

Table 4-1: Scale relations, according to Froude similarity.

PARAMETER	FROUDE SCALE RELATION	PARAMETER	FROUDE SCALE RELATION
Length	N_L	Mass density	$N_\rho = 1$
Area	$N_A = N_L^2$	Mass	$N_m = N_L^3$
Volume	$N_V = N_L^3$	Force	$N_F = N_L^3$
Time	$N_T = N_L^{1/2}$	Pressure	$N_P = N_L$
Velocity	$N_V = N_L^{1/2}$	Flow rate	$N_q = N_L^{3/2}$
Acceleration	$N_a = 1$	Mass	$N_m = N_L^3$

Considering the size of the wave flume and the 2D modelling approach, the central segment of the whole VLFS-OWC System is reproduced, providing a data set representative of an infinitely wide floating system. The tested segment is made of six OWCs integrated respectively: three in the front edge and three in the rear edge of the VLFS section (Fig. 4.3).

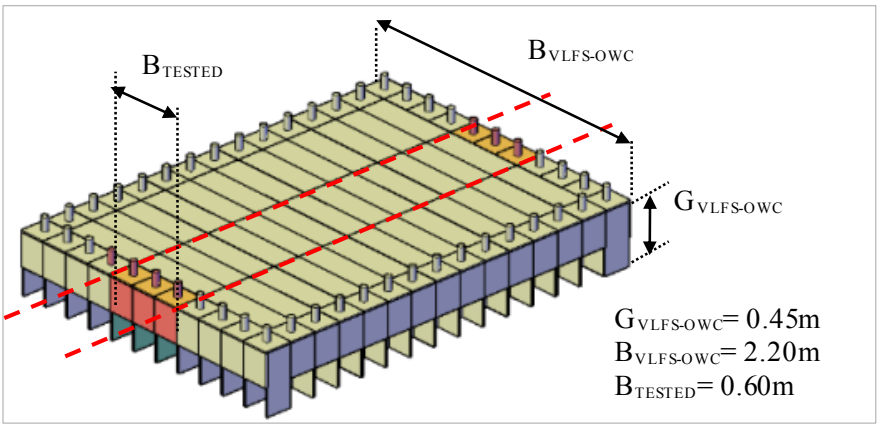

Fig. 4.3 - Entire VLFS-OWC System and model segment tested.

4.1.2 Measuring/observation techniques and calibration

The laboratory tests are performed equipping the model segment with different sensors, carefully selected according to a preliminary assessment of the expected ranges of air pressures (assessed at 0-20mbar) and air velocities (assessed at 0-20m/s), by means of a simplified frequency domain rigid piston model (Simonetti et al., 2015).

Overall, four different sensors are used to provide the following measurements:

a) Ultrasonic distance sensors (WG and DM)
   - incident, reflected and transmitted waves;
   - free surface oscillations within the OWC chamber;
   - vertical oscillations of VLFS;
b) Pressure transducers (PT)
   - air pressure within the OWC chamber;
   - air pressure inside the VLFS building elements;
c) Hot-wire anemometer (HW)
   - airflow velocity in the centre of the pipe, mimicking the air turbine;
d) Load cells (LC)
   - tensioning forces, needed to assemble the VLFS building elements;
   - horizontal mooring forces, needed to avoid horizontal movements of the VLFS.

a) Ultrasonic distance sensors (WG and DM)

The time histories of water surface elevation and vertical oscillations of the VLFS, are measured respectively by six ultrasonic distance sensors, (*WGs)* and five displacement meters *(DMs),* (Series 943-M18 F4V-2D-1C0-330E) developed by HONEYWELL and characterized by analogue output of 0-10Volt (Fig. 4.4).

The sensor is constituted by an epoxy resin material and is fixed in a vertical position above the free surface (i.e. water surface or VLFS surface), with the signal emission surface facing down. The operation mode consists on the measure time delays between emitted and echo pulses, determining the sensor-to-target distance. The instrument converts that measurement into an electronic signal, representative of the level. The level acquired has to be converted into a length by means of a preliminary calibration procedure.

Since an impulsive ultrasonic beam that expands in the conical form with an angle of 8 degrees characterizes the sensor, to set properly the instruments along the flume and on the model segment, this aspect was taken into account.

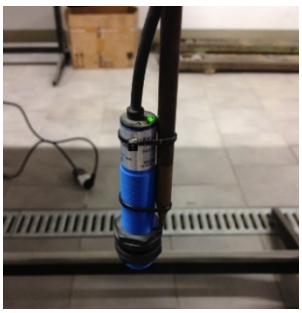

Specifications
▪ Signal output: 0-10Volt ▪ Max. sensing distance: 500mm ▪ Min. sensing distance: 60mm ▪ Switching frequency: 4.7Hz ▪ Repeatability: 0.2% or ± 1mm

Fig. 4.4 - Ultrasonic distance sensors series 943-M18 F4-2D-1C0-330E by HONEYWELL.

The calibration procedure consists of moving the sensor by means of a graduated bar with respect to a fixed flat surface and acquiring the output signal in Volt for several distances within the declared range of operability (60-500mm).

After the acquisition of the analog signal for each distance, *V(t)*, the linear regression is performed, so as to provide the corresponding measurement in cm, *η(t)*, valid for overall the ultrasonic distance sensors used:

$$\eta(t) = 44 * V(t) - 6 \tag{4.4}$$

b) Pressure transducers (PT)

Seven pressure transducers, (*PT-1* to *PT-7*), are used to measure the relative air pressure related to the atmospheric pressure: i) inside the VLFS building elements and ii) within the OWC chamber. The PT sensors are differential membrane pressure transducers, developed by KELLER (Series 46 X), (Fig. 4.5).

The physical deformation of the strain gauges connected to the membrane and to a Wheatstone bridge configuration allows the conversion of pressure into an electrical signal. The pressure applied to the sensor produces a deflection of the baffle, introducing strain to the gauges. The deformation gives a change of the electrical resistance proportional to the pressure.

Specifications
▪ Signal output: 4-20mA ▪ Max. sensing pressure: 500mbar ▪ Min. sensing pressure: 0mbar ▪ Operating Temperature 0-80°C ▪ Repeatability: 0.1% FS

Fig. 4.5 - Pressure transducers series 46 X, by KELLER.

Since, the pressure transducer developed by KELLER is a submersible capacitive transmitter, suitable for water level measurements, a different process allowing the calibration of the transducer in the air, is needed.

The calibration in the air is performed, converting the output signal of the sensor, expressed in 4-20mA, into a signal in 2-10Volt, by means of a resistance of 500Ω. The sensor provides measurements also in a range of 1.3-2Volt, allowing the acquisition of the negative pressure.

As for the calibration procedure, a suitable measurement station was developed (Fig. 4.6). The measurement station consists of two vertical pipes made of methacrylate and connected by two valves: A and B, which allow the water inlet/outlet from respectively the pipes.

The pressure transducer, connected to the acquisition system, is placed in the upper edge of the pipe on the left, through a suitable airtight system. A valve located in the pipe on the left (C) allows the inlet of the air, restoring the atmospheric pressure.

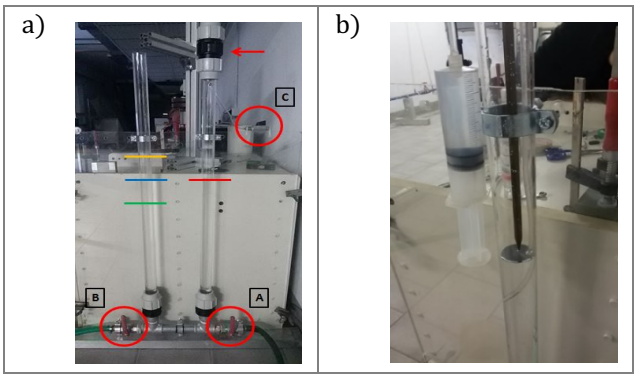

Fig. 4.6 - a) Measurement station developed by LABIMA for the calibration of the pressure transducers in the air; b) Hydrometric rod for the acquisition of the water level in the pipe.

The calibration procedure is carried out according to the following steps:

- first the valve C is open in order to establish the atmospheric pressure on the two water columns (red and blue lines in Fig. 4.6a);
- then, the calibration is performed for negative pressures (i.e. air decompression) and positive pressures (i.e. air decompression). Concerning the procedure adopted for negative pressures: after closing the valve C, the water level in the pipe on the left is reduced by opening the valve B with a step of 0.50cm until the minimum value of the calibration range (green line in Fig. 4.6a);

- as for the procedure adopted for positive pressures: after restoring the atmospheric pressure and closing the valve A, B and C, the water level in the pipe on the left is increased, injecting water, with a step of 0.50cm, by means of a graduate syringe.

For each step, the exacted value read on the hydrometric rod (Fig. 4.6b) and the corresponding analogue output of the sensor are collected. The calibration procedures, for negative and positive pressures, *P(t)*, were repeated several times obtaining, the following equation which provides the corresponding measurement in mbar:

$$P(t) = \alpha * V(t) - \beta \tag{4.5}$$

The calibration curve obtained for each PT used during the tests are reported in *Annex A.*

c) Hot-wire anemometer (HW)

The inflow and outflow air velocity from the OWC, is measured by constant temperature hot wire anemometer, *HW*, (CTA, series R11-R20-X by DANTEC), consisting in two main parts (Fig. 4.7):

- probe body, in which a short and thin tungsten wire is welded to two prongs (made of stainless steel or nickel). The entire length of the wire acts as a sensor.
- probe support, which has the function to provide the electrical connection between the probe body and the probe cable, as well as to provide a mechanical mount for the probe.

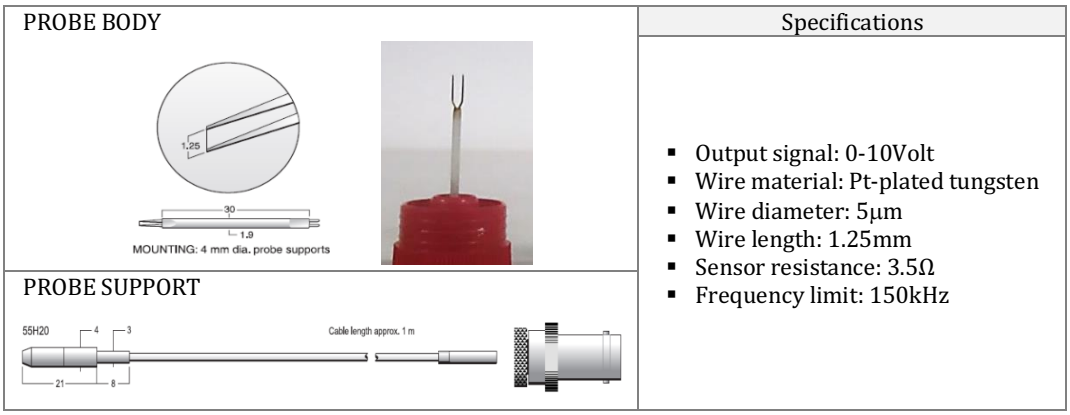

Fig. 4.7 - CTA Hot wire anemometer series R11-R20-X by DANTEC. a) Particular of the probe body and of b) the probe support.

The measurement technique is based on the heat transfer from a heated wire to the relatively cold surrounding fluid. The heat transfer is a function of the fluid velocity.

The relation between the fluid velocity and the electrical output of the system is established, by means of a proper calibration process, that was part of the fulfilment of a master thesis performed on the development of a LabVIEW application for calibration and data acquisition by hot-wire probes (Bellucci, 2014).

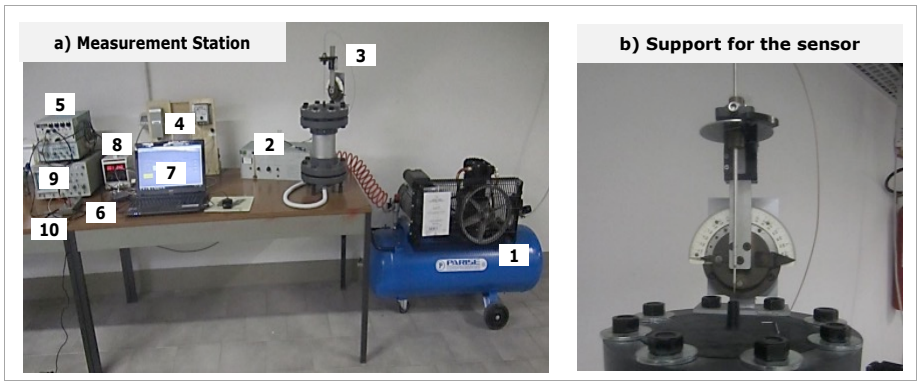

Fig. 4.8 - a) Measurement station developed at LABIMA for the calibration of the hot wire anemometer; b) Support for sensor built on the separating chamber.

The measurement station (Fig. 4.8), developed for the calibration of the sensor, consists on:

1) Compressor (P100CM model by Parisi);
2) Flow rate controller (DISA control unit type 55D44);
3) Separating chamber and probe support (made by a 3D printer);
4) Differential pressure transducers (PX274-0.1DI and PX655-02DI by Omega);
5) Wheatstone Bridge (55M05 power pack, 55M01 main unit and 55M10 CTA bridge standards, developed by DISA);
6) DAQ device (USB 6002 by National Instrument);
7) Computer;
8) Voltage generator for the pressure transducers;
9) Oscilloscope (dual trace oscilloscope 9012 by Wavetek);
10) Tester (E2373A by HP).

Overall, three hot-wire anemometers are used for the tests (named HW-1, HW-2 and HW-3). The calibration procedure adopted for each of them is performed, according to these main steps:

- First the hot-wire anemometer is located in the support, equipping the separating chamber (3). The body of the probe is fixed at a distance of 1cm from the orifice connecting the separating chamber outside.
- The ambient temperature, T_{cal},[3] is registered before starting the calibration.
- The sensor is connected to the Wheatstone bridge (5). A waiting time of 15 minutes is necessary, so as to achieve a constant temperature of the wire, before starting the acquisition.
- Then, the airflow, from the compressor (1) passes to the separating chamber (3), through a flow rate controller (2) and invests the body of the probe. Two differential pressure transducers (4) are used to monitor and measure the dynamic pressure within the separating chamber.
- To keep the hot wire at a constant temperature, the bridge varies the intensity of current through the wire, varying the voltage across the hot wire edges. The change of voltage across the hot wire edges is the analogue signal of the bridge output.
- The analogue signals are input to the data acquisition module DAQ (6), connected to a computer. The data uploaded in LabVIEW software are calibrated by the King's Law (Eq. 4.6) (Bruun, 1995).

$$E^2 = E_0^2 + B\, v^{\mathrm{n}} \tag{4.6}$$

in which: E is the tension value acquired during when invests the sensor [Volt]; E_0 is the tension value acquired when the airflow is 0, [Volt]; B and n are two calibration coefficients; and v is airflow velocity, [m/s]. The equation providing the corresponding measurement in m/s is obtained, for each HW, linearizing the King's Law as follows:

$$\ln(E^2 - E_0^2) = n\, \ln v + \ln B \tag{4.7}$$

Then, by means of the least squares method the coefficient B and n are calculated:

$$n = \frac{(\sum X\, Y) - \frac{(\sum X)\,(\sum Y)}{N}}{(\sum X^2) - \frac{(\sum X)^2}{N}} \tag{4.8}$$

$$\ln B = \frac{\sum Y}{N} - n\,\frac{\sum X}{N} \qquad B = e^{\ln \mathrm{B}} \tag{4.9}$$

in which, N is the number of points acquired during the calibration. The calibration curve adopted for overall the hot-wire anemometer used in the tests are reported in *Annex B.* To minimize the error, the calibrated signal is corrected by the correction factor (FC_{hw}) (Bearman, 1971), as follows:

[3] The thermal exchange caused by forced convection is directly proportional to the difference between the wire and the ambient temperature (respectively T_w and T_a). One of the most important sources of error in measuring velocity using hot-wire anemometry is the change in the hot-wire calibration due to changes in the ambient temperature (Cimbala & Park, 1994). Then, it is necessary to keep track of the flow temperature during calibration (T_{cal}) and experimental measures (T_a).

$$\frac{T_w - T_a}{T_w - T_{cal}} = FC_{hw} \tag{4.10}$$

where, the hot wire temperature, T_w is given by:

$$T_w = T_{cal} + \frac{OH}{\alpha} \tag{4.11}$$

in which, OH is the overheat ratio (OH=1.4) and α is the is the temperature coefficient of resistance (0.0044 for tungsten).

d) Load Cells (LC)

Eight Load Cells are used, (*LC-1* to *LC-8*), (series 54-100-C3, developed by CELMI) (Fig. 4.9), to measure the tensioning forces, needed to assemble the VLFS building elements and the horizontal mooring forces, aimed to avoid horizontal movements of the VLFS.

Specifications
▪ Signal output: 4-20mA ▪ Max. sensing load: 100Kg ▪ Min. sensing load: 0.1Kg ▪ Operating Temperature -40-80°C ▪ Repeatability: 1% FS

Fig. 4.9 - Load Cells Series 54-100-C3 by CELMI.

As regards the relation between the load, *Ld(t)* and the electrical output, *V(t)*, the following relation provided by the manufacturer CELMI was used for each LC used in the tests:

$$Load(t) = 50 * V(t) \tag{4.12}$$

e) Video records

Video records are performed by means of a digital camera (model PowerShot G9 by Canon) aimed at providing a qualitative knowledge of the hydrodynamic processes in front of the model (e.g. monitoring the incident waves) and inside the model (e.g. monitoring the free surface oscillations within the OWC chamber).

A qualitative and roughly quantitative measure of the water surface displacement from the S.W.L., is provided by means of a grid with a mesh of 5mm, drawn on the front and side wall of the OWC model (Fig. 4.10).

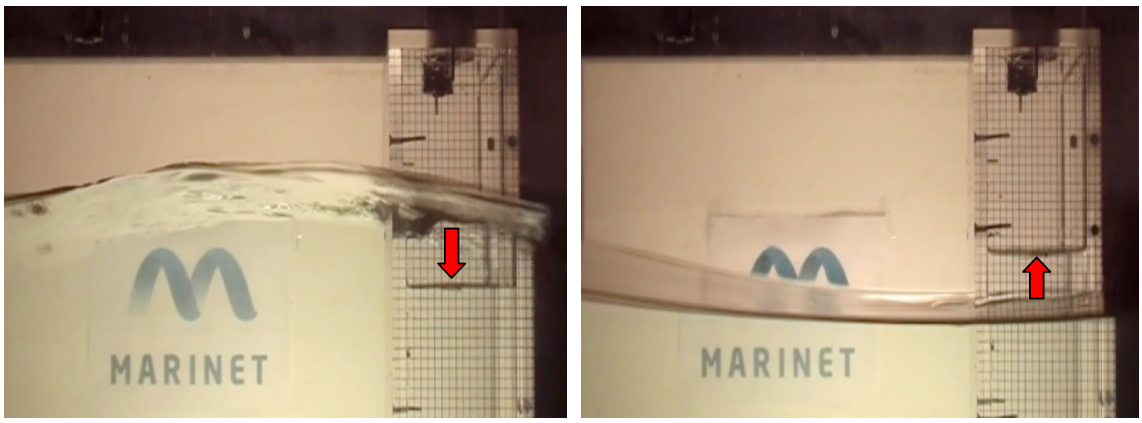

Fig. 4.10 - Picture captured during the video recording of the W1D2V2% under the wave H02. The picture shows the different phase observed between incoming wave and water column oscillations inside the OWC (indicated by the red arrow).

4.1.3 Hydrodynamic test conditions

As for the sea states reproduced during the experiments, eight scenarios are selected as representative of the hypothetical installation site in the Mediterranean sea (see *Chapter 3*), at a water depth -25m S.W.L. (0.50m at model scale), (Vannucchi, 2012).

In Table 4-2 the target characteristics of the waves simulated during the tests, are reported.

Table 4-2: Wave trains representative of the hypothetical installation site selected for a VLFS-OWC System and dimensionless water depth kh (model scale 1:50).

Notation	Wave Type	H [m]	T[s]	kh [-]	H/λ [-]	Duration [s][4]	Phase I	Phase II	Phase III
H01	Regular	0.04	0.8	3.15	0.040	70	✓	✓	✓
H02	Regular	0.04	1.0	2.07	0.025	70	✓	✓	✓
H03	Regular	0.04	1.4	1.22	0.013	70	✓	✓	✓
H04	Regular	0.04	1.2	1.53	0.018	70		✓	✓
H05	Regular	0.06	0.9	2.51	0.048	70		✓	✓
H06	Regular	0.06	1.6	1.02	0.015	70		✓	✓
Notation	**Wave Type**	H_{m0}[m]	T_p[s]	kh [-]	H/λ [-]	**Duration [s]**	**Phase I**	**Phase II**	**Phase III**
H1	Irregular	0.025	0.9	2.68	0.021	100	✓	✓	✓
H2	Irregular	0.027	1.0	2.28	0.019	100	✓	✓	✓
H3	Irregular	0.040	1.0	2.23	0.028	100	✓	✓	✓
H4	Irregular	0.042	1.1	1.88	0.024	100	✓	✓	✓
H5	Irregular	0.061	1.1	1.85	0.034	100	✓	✓	✓

Three regular waves (H01 to H03) are characterized by wave heights of 0.04m and wave periods in the range $0.8 \leq T \leq 1.4$s. To characterize the floating behaviour of the VLFS, three additional regular waves (H04, H05 and H06) are simulated only for Phase II and Phase III.

Five irregular waves are characterized by Jonswap wave spectrum (for fetch-limited waves) and significant wave heights in the range $0.02 \leq H_{m0} \leq 0.06$m and significant wave periods in the range $0.9 \leq T_p \leq 1.1$s. Concerning the data analysis, suitable time windows are selected for each wave simulated during the tests (Table 4-3).

Table 4-3: Time windows selected for the data analysis.

Notation	λ [m]	C[m/s]	Cg[m/s]	Pre-trigger [s]	First time lapse [s]	Last time lapse [s]	N° waves
H01	1.00	1.25	0.62	10	55	70	19
H02	1.56	1.56	0.78	10	45	65	20
H03	3.06	2.18	1.09	10	40	60	14
H04	2.25	1.87	0.94	10	40	70	25
H05	1.26	1.40	0.70	10	50	70	22
H06	3.99	2.49	1.25	10	30	70	13
H1	1.18	1.36	0.68	10	40	100	69
H2	1.41	1.48	0.74	10	40	100	63
H3	1.44	1.49	0.75	10	40	100	63
H4	1.75	1.65	0.83	10	40	100	57
H5	1.79	1.67	0.83	10	40	100	56

For the selection of the time windows, the distance of the model from the wave maker (fixed at 22m for each phase), the length of the wave-current flume (37m) and the characteristics of each wave motion, are taken into account as follows:

- The first frame is the instant in which the first wave reaches the model and is computed dividing the distance of the model from the wave maker to the wave group velocity (C_g).
- The last frame corresponds to the time necessary for waves to reach the end of the flume and the reflected waves to reach the model.

[4] Each signal acquired is related to the still water level, by means of the measurement of the water level during the pre-trigger time of 10 seconds before generating the waves.

The reference incident wave is assessed by generating the regular and irregular waves without any model in the flume (i.e. W0D0V0 tests) and acquiring the vertical free surface displacements through an ultrasonic wave probe (WG5) located at the centre of the removed model position.

Then, considering the aforementioned time windows properly selected for each wave simulated, the characteristics wave parameters are extracted by means of the time domain analysis for the regular waves as well as both time and frequency domain analysis for the irregular waves, (Table 4-4 and Table 4-5).

Table 4-4: Characteristic incident wave parameters obtained from time domain analysis of regular wave tests in the flume without any model (W0D0V0).

WAVE	$H_{1/3}$ [m]	H_{max} [m]	H_m [m]	$T_{1/3}$ [s]	T_m [s]	N° waves
H01	0.042	0.042	0.041	0.8	0.8	19
H02	0.043	0.045	0.041	1.0	1.0	20
H03	0.042	0.042	0.040	1.4	1.4	14
H04	0.038	0.038	0.036	1.2	1.2	25
H05	0.061	0.061	0.058	0.9	0.9	22
H06	0.059	0.062	0.055	1.6	1.6	12

Table 4-5: Characteristic incident wave parameters obtained from frequency and time domain analysis of irregular wave tests in the flume without any model (W0D0V0).

WAVE	H_{m0} [m]	T_p [s]	T_{m-10} [s]	T_{m01} [s]	$H_{1/3}$ [m]	H_{max} [m]	H_m [m]	$T_{1/3}$ [s]	T_m [s]	N° waves
H1	0.021	0.9	0.9	0.9	0.023	0.039	0.014	0.9	0.9	64
H2	0.021	1.0	1.0	0.9	0.023	0.033	0.014	1.0	1.0	62
H3	0.038	1.0	1.0	0.9	0.043	0.062	0.026	1.0	1.0	62
H4	0.040	1.1	1.0	1.0	0.038	0.057	0.024	1.1	1.0	161
H5	0.057	1.1	1.1	1.0	0.064	0.084	0.040	1.1	1.1	55

4.1.4 Testing phases and methodology

As shown in Fig. 4.11 and described in more detail in the next sections, the scale-model experiments are performed using a tiered approach in order to achieve the main objectives of this research. Before running each phase of the main tests, a preliminary investigation, based on simple conditions is performed, and a first level analysis is carried out, with the following objectives:

- verify the feasibility of the experimental activity and calibrate the physical model;
- become familiar with the laboratory procedures;
- check the quality of the acquired data;
- identify issues, finding improvements for the main tests.

As for the first step of the main tests, simulations without the model (W0D0V0) are carried out, so as to characterize each regular and irregular wave tested in the later phases (e.g. incident wave parameters).

Then, the parameter study, performed by changing the geometry of the OWC (i.e.: chamber width, in the direction of wave propagation, front wall draught and turbine damping), as well as those of the VLFS (i.e.: the length and the mass) is carried out, according to the following three phases:

1) ***Phase I - Fixed OWC model:*** assessing the effect of the varied design parameters on the OWC performance and providing results useful for the calibration of a Computational Fluid Dynamics code (CFD) in the OpenFOAM® framework, aimed to further optimization of the OWC (Simonetti et al., 2015). The results of Phase I, are used to select the OWC geometries to be tested in Phase III.
2) ***Phase II - VLFS model without OWCs:*** investigating the effect of varying the VLFS design parameters (i.e. two different lengths and masses) on the VLFS floating behaviour and providing useful data for the comparison with the results of Phase III in order to study the mitigating effect of the OWC on the VLFS floating behaviour. Due to time constraints, the data analysis of this aspect is not performed in this thesis.
3) ***Phase III -VLFS-OWC model:*** assessing the effect of varying the design parameters of OWC and VLFS on the performance of the OWC in floating conditions. The results coming from

Phase III are compared with those of Phase I, with the purpose of achieving the main objective of this research, which is the evaluation of the effect of the VLFS floating motions on the OWC performance in regular and irregular waves.

Additional tests are carried out during Phase II (1 additional test) and Phase III (71 additional tests), in order to provide a data set useful for future investigations, respectively on:

i) the effect of the mass on the floating behaviour of the VLFS without incorporated OWC devices;
ii) the mitigating effect of incorporated OWC devices on the VLFS floating motion (see *Subsections 4.3.4* and *4.4.4*).

However, since the additional tests are not directly to the objective of the present study, their analysis and the results are not included in this report.

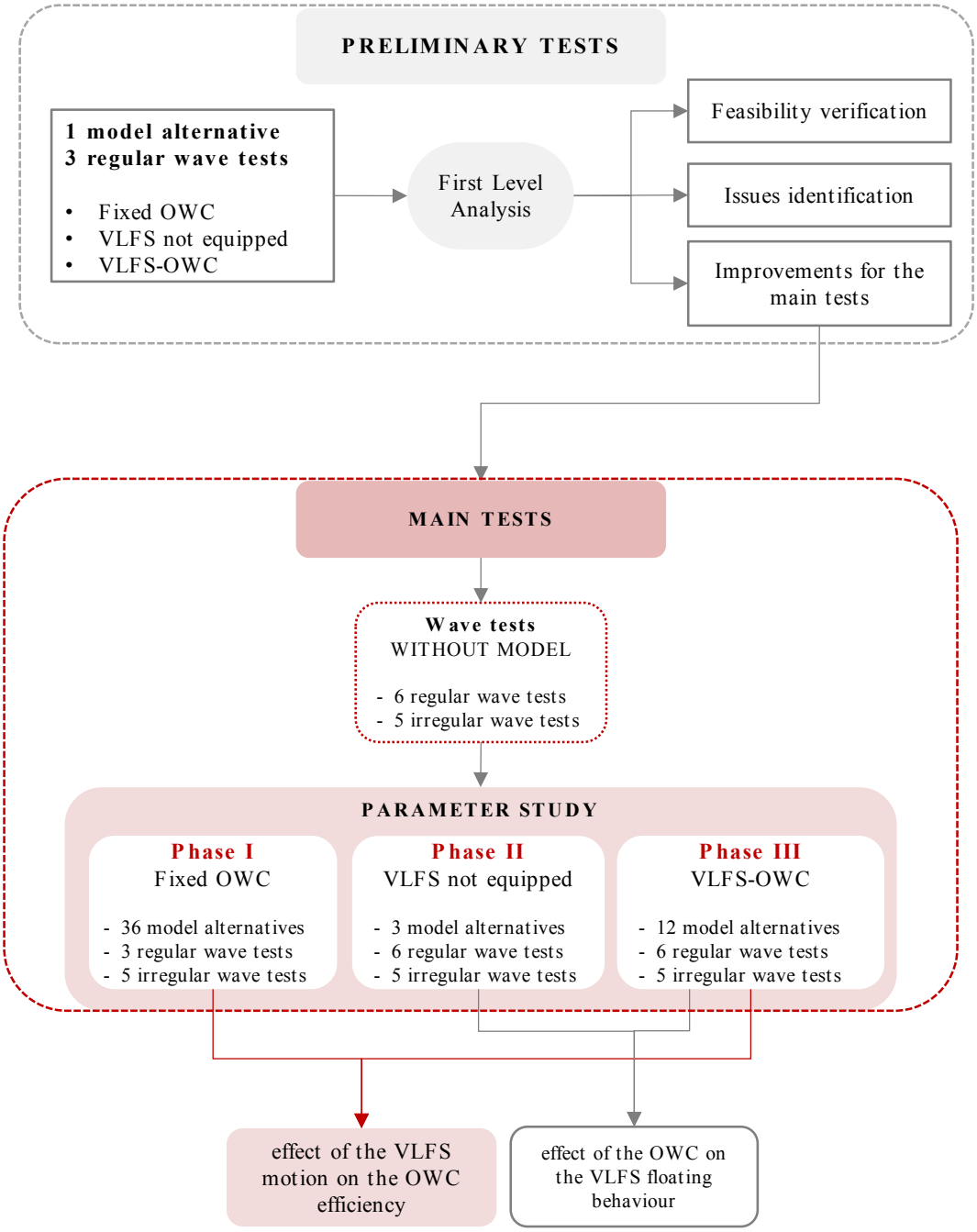

Fig. 4.11 - Organization structure and phases of the experiments.

4.2 Phase I: Fixed OWC model

A detailed description of the first phase of the small-scale tests on the rigidly fixed OWC device is provided in this section.

Different design parameters (i.e., chamber width, in the direction of the wave propagation, front wall draught and turbine damping) are investigated under regular and irregular wave trains, during the main tests of Phase I, in order to provide results mainly aimed at:

- evaluating the effect of the aforementioned OWC design parameters on the hydrodynamic processes inside the air chamber (i.e., air pressure variations, free surface oscillations of the water column and the variations outflow/inflow air volume flux);
- calibrating a Computational Fluid Dynamics code (CFD) in the OpenFOAM® framework aimed at further optimization of the performance of the fixed OWC (Simonetti et al., 2015);
- selecting the OWC geometries to achieve the best performance, restricting the range of OWC geometries to be tested in Phase III (VLFS-OWC models).

The results obtained for the fixed OWC models, provide the basis for a comparative analysis with the results achieved in Phase III (VLFS-OWC models), allowing the assessment of the effect of the VLFS floating motion on the OWC performance.

4.2.1 OWC model design and construction

The OWC model is built according to Froude similarity (scale factor 1:50), as a rectangular-shaped box made of methacrylate, given the advantages of this material (e.g., strength and transparency), thus allowing the observation of the processes inside the OWC chamber (Fig. 4.12).

Fig. 4.12 - Example of OWC geometry (W1D2V0.5%) tested in Phase I.

To avoid corrosion and losses in the air chamber, stainless steel screws are used for assembling the several components of the OWC and the OWC chamber is made water- and airtight by using silicone as sealing.

The representation of the Power-Take-Off mechanism (PTO) is another relevant aspect considered in modelling the OWC for this study. As stated in (Payne, 2008), scale modelling of PTO is not straightforward. Indeed, the technologies suitable for full-scale devices do not lend to the downscaling, because of the scaling factor of power in Froude similarity.

Since the OWC conceived to provide the VLFS is equipped with a self-rectifying impulse turbine, which is a non-linear PTO (Anand et al., 2007), the turbine is mimicked in the OWC scaled model by means of a vent located on the centre of the top cover, allowing a quadratic pressure drop relation.

To improve the knowledge of the OWC working principle, a parameter study is performed to identify the design characteristics which mainly affect the OWC performance. The design parameters of the OWC, which are kept constant are suitably selected according to the current knowledge on the OWC devices, as follows (Table 4-6):

- Chamber length perpendicular to the wave direction *(B)*, to minimize the formation of standing waves within the air chamber, ensuring a wave-sloshing period below 5s, which is in the range of the natural period of oscillation of practical OWC (Webb et al., 2005).
- Freeboard *(F_c)*, to consider the limits of the mean overtopping discharge in the site selected for the hypothetical installation (Pullen et al., 2007).
- Back Wall Length *(G)*, to maximize the reflected waves, amplifying the water column oscillation. According to the evaluation on the vertical propagation of the total incident wave energy, the back wall length is selected to capture the 85-90% of the wave power (see *section 3.1.2*). The back and sidewall lengths are designed longer than the front wall, to maximize the reflected waves, amplifying the water column oscillations (Suroso, 2005).
- Front Wall Slope (α=90°), to reduce the wave run up and maximize the wave reflection, amplifying the water column oscillation.
- Side Wall Slope (β=90°).

Table 4-6: Fixed design parameters of the OWC model (scale 1:50).

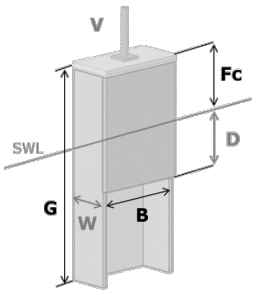	Notation	Description	[unit]	value
	B[5]	Chamber length	[m]	0.20
	G	Back wall length	[m]	0.45
	F_c	Freeboard	[m]	+0.16 S.W.L.
	th_{fbt}[6]	Front, back and top cover wall thickness	[m]	0.01
	th_s	Side walls thickness	[m]	0.008

Chamber width *W*, front wall draught *D* and turbine damping *V* are varied during the tests, owing to their key effects on the wave-to-pneumatic power conversion.

1) ***Chamber width in wave direction (W)***, because of its relevant influence on:

- resonance frequency of the OWC (Evans, 1978);
- air volume and air spring, which imply multiple resonance peaks (Lovas et al., 2010);
- wave sloshing period within the OWC chamber (Webb et al., 2005).

As stated in (Sheng et al., 2012), the wavelength may limit the size of the OWC, its chamber width, *W*, may not exceed 1/5 to1/4 of the wavelength (W/λ=0.20-0.25). Hence, considering the design wave parameters characterizing the installation site selected (H=2.0m, T=7.0s), parameter *W* must be less than 20–18m.

Three chamber widths are reproduced in the experiments by modifying the top cover and the sidewalls of the device, namely *W1*, *W2* and *W3* (see Fig. 4.13).

W1	W2	W3
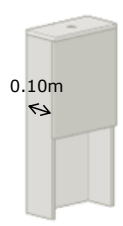	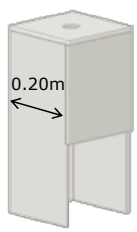	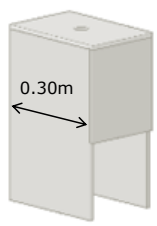

Fig. 4.13 - 3D view of the three chamber widths W1, W2 and W3 tested in the laboratory experiments (model scale 1:50).

[5] This value is also comparable with that of existent devices: Limpet: 6m, Mutriku: 5-6m, Pico: 12m and Oceanlinx: 10m.

[6] The front wall thickness is confirmed by the current state of the art of reinforced concrete cellular caisson design for marine structures (See *Chapter 2*).

2) ***Front wall draught (D)***, due to its significant influence on:

- resonance frequency of the OWC (Evans, 1978);
- formation of inlet broaching, that implies PTO losses (Webb et al., 2005);
- wave sloshing period within the air chamber (Sheng et al., 2012).

Three front wall draughts are reproduced by changing the front wall of the OWC model (*D1*, *D2* and *D3*), for each chamber width. The three front wall draughts are exemplarily reported for chamber width *W2* in Fig. 4.14.

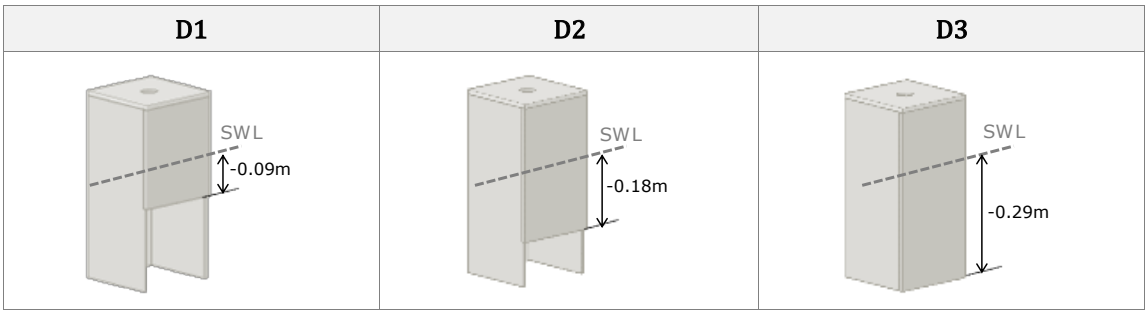

Fig. 4.14 - 2D view of the three front wall draughts D tested for each chamber width W (model scale 1:50).

3) ***Turbine damping (V)***, due to the pressure drop of the air turbine incorporated into the OWC device at prototype scale.

The non-linear PTO system, typical of impulse turbine (conceived to equip the OWC at prototype scale) is mimicked by using a vent located on the top cover of the OWC model as applied in (Sarmento, 1992; Sheng et al., 2012; Zhang et al., 2012; Iturrioz et al., 2014).

Different induced turbine damping are reproduced in the tests by changing the diameter of the vent. Each vent is equipped with a 0.10m long duct, to canalize the airflow and protect the sensor used to measure the airflow rate.

According to Sheng (2013), the diameters of the vents are selected with the following percentage of the top cover surface (STopCover): V0.5%, V1% and V2%.

During the tests, the maximum pressure within each OWC chamber is also collected, closing the vent (V0). Thus, according to the geometries of the OWC model tested, the different sizes of the vents reproduced in the laboratory are those reported in Table 4-7 and

Table 4-8.

Table 4-7: Sizes of the vents, mimicking the damping induced by the air turbine for each OWC geometry (model scale 1:50).

	NOTATION	Diameter [m]
W1	V0	closed
	V0.5%	0.008
	V1%	0.014
	V2%	0.020
W2	V0	closed
	V0.5%	0.016
	V1%	0.021
	V2%	0.030
W3	V0	closed
	V0.5%	0.018
	V1%	0.026
	V2%	0.036

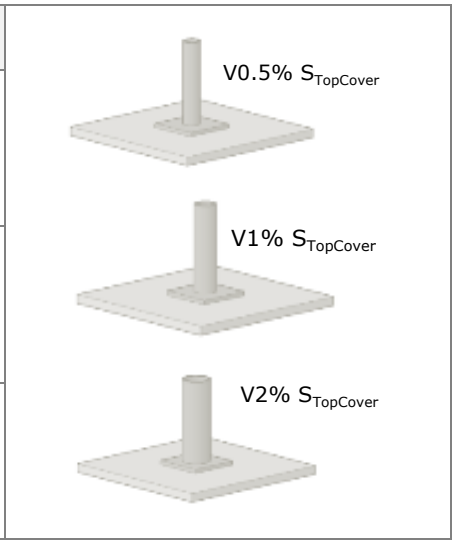

In

Table 4-8 the main design parameters varied for the parameter investigation on the OWC model, as well as the description of each notation used in the laboratory tests, are summarized.

Table 4-8: Varied design parameters in the OWC model (scale 1:50).

	Notation	Description	[unit]	value
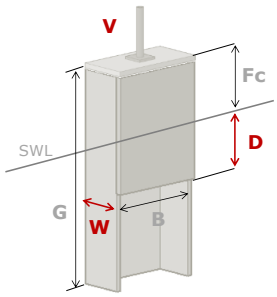	***W***	Chamber width	[m]	0.10 – 0.20 – 0.30
	D	Front wall draught	[m]	0.09 – 0.18 – 0.29
	V	Vent diameter	[m]	0.08 ÷ 0.036 [7]

4.2.2 Preliminary tests and implications for the main tests

The preliminary tests represent an important step of the procedure adopted for the laboratory tests and are mainly performed with the purpose of optimising the model set-up and the programme of the main tests (see *Subsection 4.1.4*). Together with the main tests of Phase I, these tests were also part of the MARINET[8] project, focusing on the generation of experimental data for the validation of Lattice Boltzmann numerical simulations on OWC (Thorimbert, 2014).

Based on simple conditions, the preliminary tests mainly aim at the identification of the issues to be improved in the main tests. One OWC geometry (W1D2), fixed to the wave flume walls, by means of steel bars, is tested, varying the induced pressure drop, under three regular waves H01, H02 and H03 (Fig. 4.15).

Setup of the preliminary tests for Phase I		
Geometry	**Test Conditions**	**Measurements**
W1=0.10m D2=-0.18m S.W.L. V0 (closed) V0.5% V1% V2%	3 Regular Wave tests (H=0.04m & T=0.8-1.4s) Water depth h=-0.50m S.W.L. Freeboard Fc=+0.16m S.W.L.	-Wave motion -Free surface oscillations inside the OWC -Relative air pressure inside the OWC

Fig. 4.15 - Fixed OWC model setup for the preliminary tests and tested conditions (Table 4-8).

For all tests, the water depth corresponding to the offshore conditions of the selected site is kept constant along the wave flume (h=0.5m) and the freeboard is fixed at +0.16m S.W.L.

The OWC model is located at a distance of 22m from the wave maker. The time histories of water surface elevation, in front, within and behind the model is measured by five ultrasonic distance sensors, *WG*, set at a sample frequency of 20Hz (Table 4-9).

In addition to the ultrasonic probe for the acquisition of the free surface level oscillations, the fixed OWC model is equipped with a pressure transducer, PT, connected to the device by means of a preformed opening on the top cover, which after the installation was properly waterproofed (Fig. 4.16 and Table 4-9).

A first level analysis of the data from the preliminary tests is performed so as to provide the starting basis for the main tests of Phase I (e.g. wave maker calibration, verification of the sensors, control of data set quality), and to achieve a better understanding of the following main aspects:

[7] Nine different sizes of vents V, and a condition of vent closed (V0), are tested as reported in Table 4-7.
[8] Marine Renewables Infrastructure Network http://www.fp7-marinet.eu/

- OWC response to the incident and reflected waves;
- pressure and free surface displacements of the water column inside the OWC chamber;
- intrinsic resonance conditions of the water column oscillations within the OWC;
- performance of the OWC model tested, including a preliminary assessment.

The following improvements are identified for the main tests of Phase I:

1) The rough assessment of the reflected waves pointed out a quite variable trend, demonstrating the relevant boundary effects on wave transmission and/or energy dissipation. To avoid these phenomena, a segment composed by three OWC chambers, (instead of one used in the preliminary tests) tightly joined, is performed for the main tests.
2) To minimize the standing wave phenomena, allowing also a longer duration of the tests and the acquisition of more data, a passive absorbing system is built for the main tests, on the opposite side of the flume, with respect of the wave maker.
3) A further important issue detected is related to the air losses. The manufacturing procedure of the model is improved, ensuring better water- and airtight conditions.
4) To understand the local interactions occurring inside the chamber, as well as to provide an improved assessment of the OWC performance, air flow measurements are needed for the main tests, by means of a hot-wire anemometer.
5) Due to its relevant sensitivity, the use of the hot wire anemometer implies to set the sampling frequency at 1kHz during the main tests of Phase I.
6) Finally, to improve the registrations of the time histories of water surface elevation, two more ultrasonic wave probes have to be deployed in the wave flume for the main tests, one 4m distant from the wave maker, to check the wave generated and the other one behind the model (25.29m distant from the wave maker for the transmission analysis.

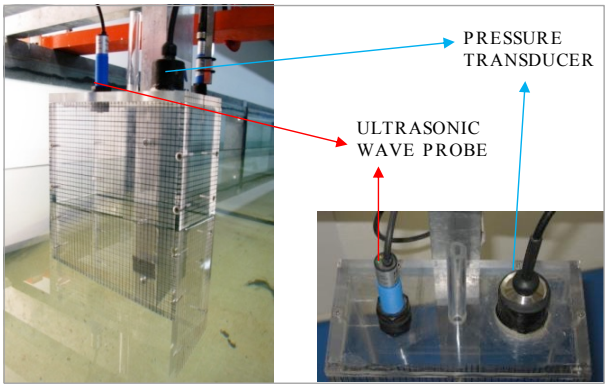

Fig. 4.16 - Setup of ultrasonic wave probe and pressure transducer on the OWC device in the preliminary tests of Phase I.

Table 4-9: Location of the sensors for the preliminary tests for Phase I.

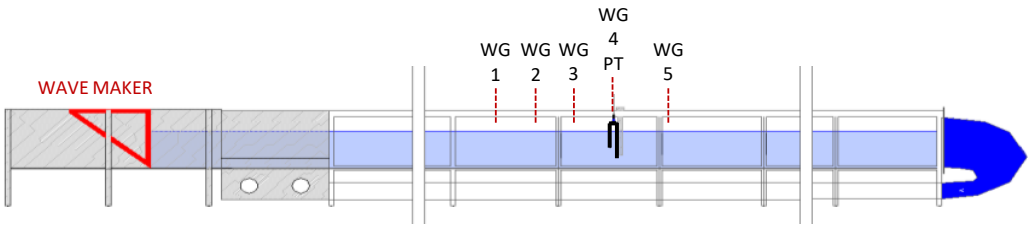

DESCRIPTION	NOTATION	MEASUREMENT	DISTANCE FROM THE WAVEMAKER [m]
Ultrasonic distance sensors	**WG1** **WG2** **WG3**	Incident and reflected wave	21.40 21.59 21.70
	WG4	Free surface oscillations inside the OWC	21.99

	WG5	Transmitted waves	24.99
Pressure Transducer	**PT**	Air pressure inside the OWC	21.99

4.2.3 OWC Model Setup for the main tests

Starting from the implications of the preliminary tests, three tightly joined OWC chambers compose the model segment tested during Phase I. The three chambers are firmly connected to a system of steel bars at the flume walls, keeping the model segment in a fixed position with respect to the bottom (Fig. 4.17).

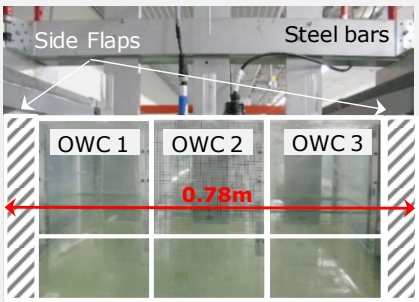

Setup of the main tests for Phase I		
Geometry	**Tests Conditions**	**Measurements**
36 model alternatives obtained varying: -3W -3 D -3 V -V	3 Regular Wave tests (H=0.04m & T=0.8-1.4s) 5 Irregular Wave tests (H_{m0}=0.02-0.06m & T_p=0.9-1.1s) Water depth h=-0.50m S.W.L. Freeboard Fc=+0.16m S.W.L.	-Wave motion -Free surface oscillations inside the OWC -Relative air pressure inside the OWC -Airflow velocity

Fig. 4.17 - Fixed OWC model setup for the main tests for Phase I and tested conditions (Table 4-8).

Moreover, to further reduce the boundary effects, two flaps (0.09m long), are connected at the model sides, achieving a total width of 0.78m, selected in order to facilitate the procedures adopted for the configuration change performed in the wave flume (the wave flume total width is 0.8m).

The vertical axis of the model is centred at the 17th sector of the wave flume, at a distance of 22m from the wave maker. As for the set-up, a 0.50m water depth is kept constant all along the flume and the freeboard of the OWC model is set at +0.16m S.W.

a) Setting of the sensors along the flume

To measure the time series of the wave motions along the flume, six ultrasonic wave probes, *WG*, are set as reported in Table 4-10 and described as follows:

- One in front of the wave maker to measure the generated waves (WG1);
- Three in front of the OWC model to acquire the incident and reflected waves (WG2, WG3 and WG4);
- Two behind the OWC model, to collect the transmitted waves (WG6, WG7).

The fixed distance of each wave probe from the OWC model and the wave maker, is selected according to the Goda & Suzuki method, adopted to separate incident and reflected waves and to determine their amplitude and phases (Goda & Suzuki 1995). The minimum distance between the model and the wave probes is equal of about one wavelength.

b) Setting of the sensors on and inside the fixed OWC model

To improve the understanding of the processes inside the device, the central OWC chamber of the model segment is equipped with three sensors (Fig. 4.18), located at a distance of 21.99m from the wave maker as reported in Table 4-10 and described as follows:

- an ultrasonic distance sensor (*WG5*), to measure water column oscillations;
- a pressure transducer (*PT),* to measure air pressure variations;
- a hot-wire anemometer (*HW)*, located in the pipe, to measure the airflow velocity.

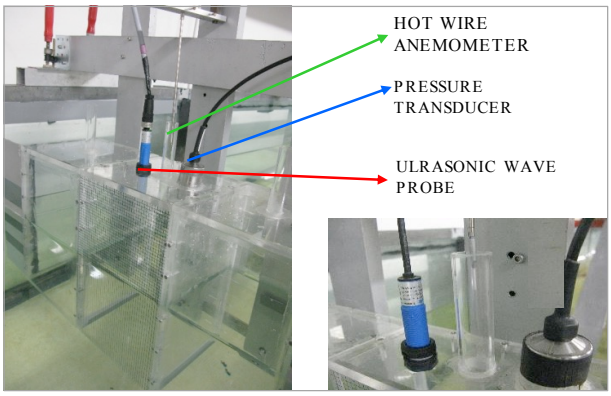

Fig. 4.18 - Setup of WG, PT and HW on and inside the OWC, during the tests of Phase I.

The location of the sensors for the tests of Phase I, as well as the description of each notation and the measurements performed in the laboratory tests are summarized in Table 4-10.

Table 4-10: Location of the sensors for the tests of Phase I.

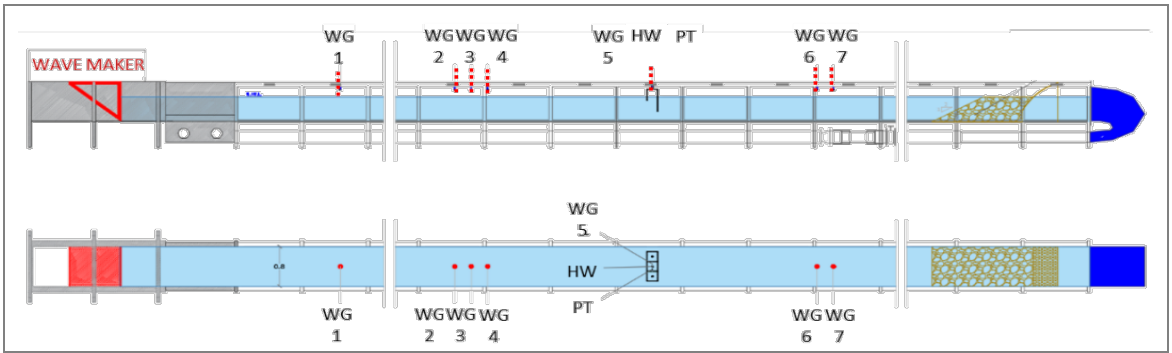

DESCRIPTION	NOTATION	MEASUREMENT	DISTANCE FROM THE WAVEMAKER [m]
Ultrasonic distance sensors	**WG1**	Generated Wave	4.00
	WG2 **WG3** **WG4**	Incident and reflected wave	18.39 18.69 18.99
	WG5	Free surface oscillations inside the OWC	21.99
	WG6 **WG7**	Transmitted wave	24.99 25.29
Pressure Transducer	**PT**	Air pressure inside the OWC	21.99
Hot-wire anemometer	**HW**	Outflow/inflow air velocity	21.99

4.2.4 Testing programme for Phase I

A total of 36 geometries are tested under regular (H01 to H03) and irregular (H1 to H5) wave trains, characterized by heights between 0.02 and 0.06m and periods between 0.8 and 1.4s (see Table 4-4 and Table 4-5).

Before starting with the main tests, a set of experiments are performed in absence of the model (W0D0V0 tests), in order to characterize the wave generated in each test, thus providing useful reference data for further comparisons with the tests including the OWC models.

Since the performance of the OWC, in terms of wave energy harvesting, may be improved by tuning the device to the frequency of the incident wave (associated with the highest annual energy in a particular location), additional tests on the OWC natural frequency are performed (RES tests).

The main aim of the RES tests is to investigate the effect of multiple design parameters, (i.e. geometry, air chamber volume, turbine damping) on the characteristic resonance frequency of each OWC geometry tested. RES tests are carried out in the absence of waves by elevating the free surface (+0.05m S.W.L.) in the chamber of the OWC through suction of the air from the duct located

on the roof of the OWC model. The duration of the air suction process is about 2 seconds, after which the water column oscillations start.

Overall, a total 366 tests on 36 OWC model alternatives, including regular wave tests (108 tests), irregular wave tests (180 tests and 3 for the tests without any model W0D0V0) and RES tests (30 tests), are performed for Phase I which took 45 working days (Table 4-11).

Table 4-11: Testing programme for Phase I.

Water depth: h=-0.50m S.W.L.				**Freeboard:** Fc=+0.16m S.W.L.					
Type of test	**Regular Waves** H01 (H=0.04m T=0.8s) H02 (H=0.04m T=1.0s) H03 (H=0.04m T=1.4s)			**Irregular Waves** H1 (H_{m0}=0.02m T_p=0.9s) H2 (H_{m0}=0.02m T_p=1.0s) H3 (H_{m0}=0.04m T_p=1.0s) H4 (H_{m0}=0.04m T_p=1.1s) H5 (H_{m0}=0.06m T_p=1.1s)					**Natural Frequency Tests**
CODE	**H01**	**H02**	**H03**	**H1**	**H2**	**H3**	**H4**	**H5**	**RES**
W0D0V0	✓	✓	✓	✓	✓	✓	✓	✓	
W1D1V0	✓	✓	✓	✓	✓	✓	✓	✓	
W1D1V0.5%	✓	✓	✓	✓	✓	✓	✓	✓	✓
W1D1V1%	✓	✓	✓	✓	✓	✓	✓	✓	✓
W1D1V2%	✓	✓	✓	✓	✓	✓	✓	✓	✓
W1D2V0	✓	✓	✓	✓	✓	✓	✓	✓	✓
W1D2V0.5%	✓	✓	✓	✓	✓	✓	✓	✓	✓
W1D2V1%	✓	✓	✓	✓	✓	✓	✓	✓	✓
W1D2V2%	✓	✓	✓	✓	✓	✓	✓	✓	✓
W1D3V0	✓	✓	✓	✓	✓	✓	✓	✓	✓
W1D3V0.5%	✓	✓	✓	✓	✓	✓	✓	✓	✓
W1D3V1%	✓	✓	✓	✓	✓	✓	✓	✓	✓
W1D3V2%	✓	✓	✓	✓	✓	✓	✓	✓	✓
W2D1V0	✓	✓	✓	✓	✓	✓	✓	✓	
W2D1V0.5%	✓	✓	✓	✓	✓	✓	✓	✓	✓
W2D1V1%	✓	✓	✓	✓	✓	✓	✓	✓	✓
W2D1V2%	✓	✓	✓	✓	✓	✓	✓	✓	✓
W2D2V0	✓	✓	✓	✓	✓	✓	✓	✓	✓
W2D2V0.5%	✓	✓	✓	✓	✓	✓	✓	✓	✓
W2D2V1%	✓	✓	✓	✓	✓	✓	✓	✓	✓
W2D2V2%	✓	✓	✓	✓	✓	✓	✓	✓	✓
W2D3V0	✓	✓	✓	✓	✓	✓	✓	✓	
W2D3V0.5%	✓	✓	✓	✓	✓	✓	✓	✓	✓
W2D3V1%	✓	✓	✓	✓	✓	✓	✓	✓	✓
W2D3V2%	✓	✓	✓	✓	✓	✓	✓	✓	✓
W3D1V0	✓	✓	✓	✓	✓	✓	✓	✓	
W3D1V0.5%	✓	✓	✓	✓	✓	✓	✓	✓	✓
W3D1V1%	✓	✓	✓	✓	✓	✓	✓	✓	✓
W3D1V2%	✓	✓	✓	✓	✓	✓	✓	✓	✓
W3D2V0	✓	✓	✓	✓	✓	✓	✓	✓	
W3D2V0.5%	✓	✓	✓	✓	✓	✓	✓	✓	✓
W3D2V1%	✓	✓	✓	✓	✓	✓	✓	✓	✓
W3D2V2%	✓	✓	✓	✓	✓	✓	✓	✓	✓
W3D3V0	✓	✓	✓	✓	✓	✓	✓	✓	
W3D3V0.5%	✓	✓	✓	✓	✓	✓	✓	✓	✓
W3D3V1%	✓	✓	✓	✓	✓	✓	✓	✓	✓
W3D3V2%	✓	✓	✓	✓	✓	✓	✓	✓	✓

4.2.5 Preliminary data analysis and results of the phase I tests

The sensitivity of the physical processes related to the OWC performance (i.e., free surface oscillations of the water column, relative air pressure in and outside (atmosphere) the chamber, and outflow/inflow air velocity) to the variation of the OWC design parameters (i.e., W, D and V), is performed.

The outcomes of the preliminary analysis are provided by evaluating at first the natural frequency of each OWC geometry tested in absence of waves (RES tests). Then, the effect of the variation of each parameter is analysed by comparing the time series acquired from each test.

The data analysis is particularly aimed at assessing the performance of each OWC geometry, in terms of *Capture Width,* with a focus on the most relevant design parameters.

The results of Phase I will also be compared with those of Phase III, providing the starting base for the development of empirical models predicting the performance of the OWC in *Chapter 5*. Moreover, as implied from the state of the art review (see *Chapter 2*), it is important to account for scale effects due to air compressibility in scale-model tests, so that an appropriate corrector factor for the experimental results might be required.

a) Natural frequency of the OWC

The natural frequency of the OWC (f_{OWC}) is assessed by a frequency domain analysis of the water column oscillations, $\eta_{OWC}(t)$, recorded during the RES tests.

The results obtained by sucking an initial inner water level 0.05m higher than the S.W.L. are reported exemplarily in Fig. 4.19a for the OWC models W1D2V1%, W2D1V1% and W2D1V2%.

A Fast Fourier Transform (FFT) is applied on the water surface elevation data to obtain f_{OWC}, for each OWC geometry (Fig. 4.19b).

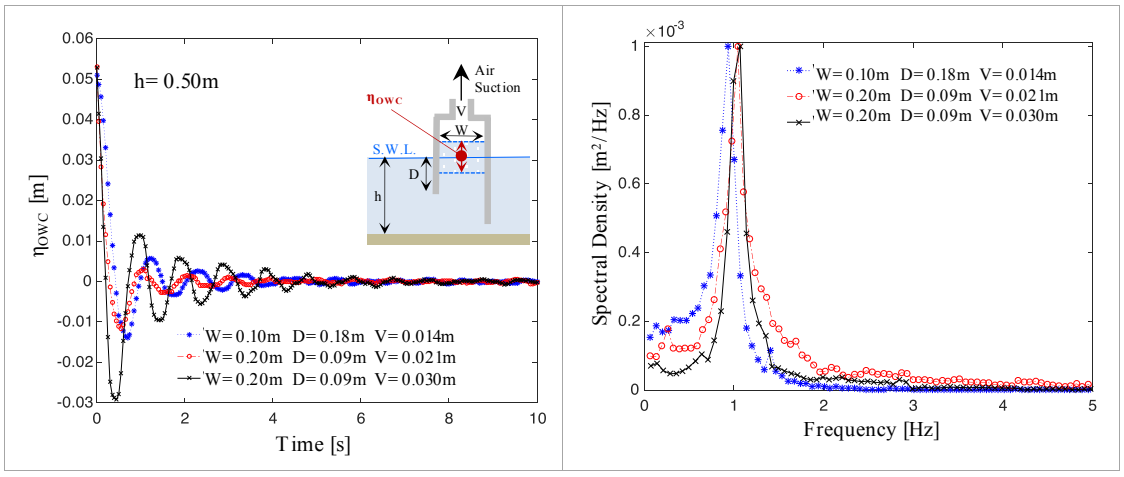

Fig. 4.19 - Time series of water level oscillations inside the OWC chamber for resonance test (a) and Fourier transform spectra of the induced water surface oscillations (b), exemplarily for the OWC models W1D2V1%, W2D1V1% and W2D1V2%.

The natural frequency (f_{OWC}) characteristic of each OWC model, shows values in the range 0.6Hz - 1.0Hz (Table 4-12).

The RES tests analysis highlights that the effect of front wall draught D on the natural resonance frequency of the OWC is the most relevant among all the other varied design parameters in this study. For each OWC geometry investigated a decrease of the resonance with increasing the submergence of the front wall, is observed. In Fig. 4.20 is exemplarily reported the decreasing trend of OWC frequency (from 1.0Hz to 0.8Hz) for a given chamber width W2=0.20m and vent V1% the OWC with different front wall draught (from D1=0.09m to D3=0.29m).

Table 4-12: Natural frequency of the OWC models considered in the RES tests.

OWC model	*fowc* [Hz]	*Towc* [s]	OWC model	*fowc* [Hz]	*Towc* [s]	OWC model	*fowc* [Hz]	*Towc* [s]
W1D1V0.5%	- [9]	-	W2D1V0.5%	-	-	W3D1V0.5%	-	-
W1D2V0.5%	-	-	W2D2V0.5%	-	-	W3D2V0.5%	-	-
W1D3V0.5%	-	-	W2D3V0.5%	0.6	1.7	W3D3V0.5%	-	-
W1D1V1%	0.9	1.1	W2D1V1%	1.0	1.0	W3D1V1%	0.9	1.1
W1D2V1%	-	-	W2D2V1%	0.9	1.1	W3D2V1%	0.9	1.1
W1D3V1%	0.8	1.3	W2D3V1%	0.8	1.3	W3D3V1%	0.8	1.3
W1D1V2%	1.1	0.9	W2D1V2%	1.0	1.0	W3D1V2%	1.0	1.0
W1D2V2%	0.9	1.1	W2D2V2%	0.9	1.1	W3D2V2%	0.9	1.1
W1D3V2%	0.8	1.2	W2D3V2%	0.8	1.2	W3D3V2%	0.8	1.2

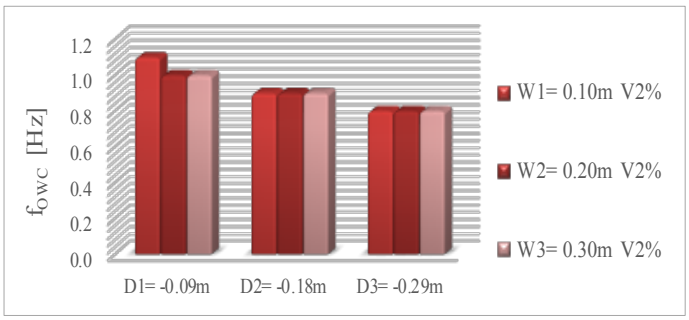

Fig. 4.20 - Natural resonance frequency characterizing the OWC alternatives tested with V2%.

This can be physically interpreted considering that, increasing *D* implies an increasing of the mass of water within the chamber leading to smaller resonance frequency. An exemplary case in which the incident wave frequency corresponds to the natural oscillation frequency of the device (W2D1V2% model) is reported Fig. 4.21.

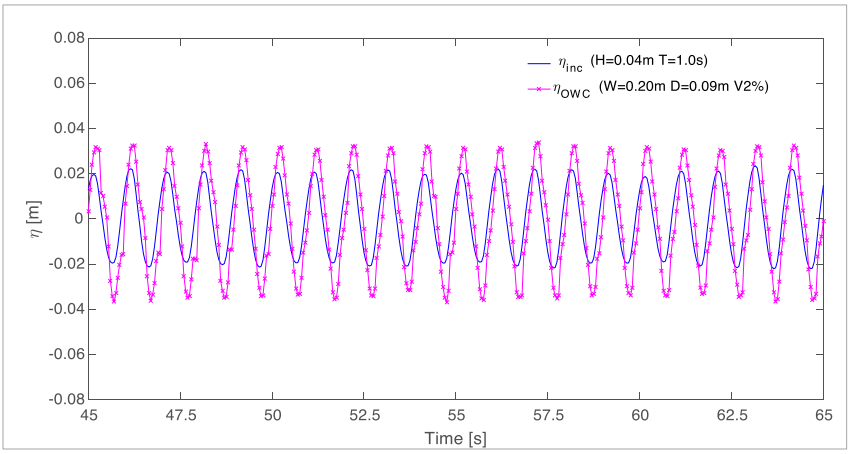

Fig. 4.21 - Resonance condition for the geometry W2D1V2% and relative water depth *kh*=2.07.

b) Effect of the chamber width on the processes inside the fixed OWC

As shown exemplarily for regular wave tests H02 (H=0.04m & kh=2.07) in Fig. 4.22, the effect of chamber width on the processes inside the OWC is analysed by comparing three OWC geometries characterized by different chamber width (W=0.10-0.30m) same percentage of the vent related to the top cover surface V1%=0.014 - 0.026m and same front wall draught (D1=-0.09m S.W.L.).

[9] For some OWC geometries, the equilibrium state is restored without any oscillation of the water level inside the chamber.

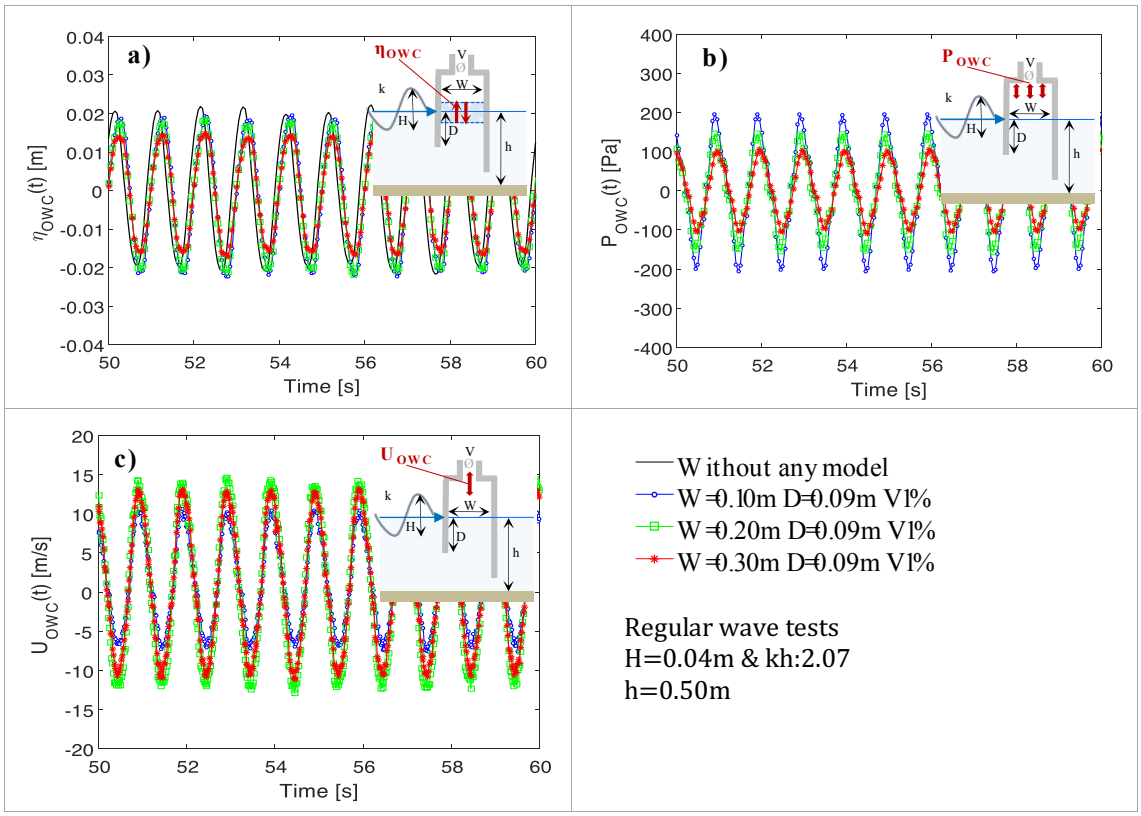

Fig. 4.22 - Effect of chamber width *W*, on: a) water surface elevation $\eta_{owc}(t)$, compared with the $\eta(t)$, recorded at the same location in the same test without any model, b) air pressure $P_{owc}(t)$ and c) airflow velocity $U_{owc}(t)$, for relative water depth *kh*=2.07 (Time series recorded at the centre of the OWC, exemplarily for regular wave tests (H=0.04m, kh=2.07 & h=0.50m).

Although the inner water level oscillations are not remarkably different among the three chamber widths, decreasing W leads to an increase of η_{owc} (Fig. 4.22a). This can be physically interpreted by considering that the same wave-induced pressure acts on a smaller section of water column, leading also to higher air pressure oscillations ΔP_{owc} for the same vent V (ΔP_{owc} = 399Pa for W1) (Fig. 4.22b).

The airflow velocity, generally presents an increasing trend with increasing *W*, however in the case exemplarily reported in Fig. 4.22c, the higher airflow velocity occurs in W2=0.20m (U_{max}=14.0m/s) instead of W3=0.30m, showing a strong dependence on the induced damping, that will be discussed in more detail below.

c) Effect of the front wall draught on the processes inside the fixed OWC

The front wall draught strongly influenced the hydrodynamic processes inside the OWC. All tests show that decreasing the submergence of the front wall draught leads to an increase of the water column oscillations $\eta_{owc}(t)$, air pressure $P_{owc}(t)$ and airflow velocity $U_{owc}(t)$. This is physically due to the wave-induced pressure which decreases exponentially with increasing depth below SWL and to the water volume within the chamber which increases by increasing the front wall draught D, leading to a lower natural frequency of the OWC.

As exemplarily reported in Fig. 4.23 for regular wave tests H02 (H=0.04m & kh=2.07) the comparison of time series for different *D* values, and for constant chamber width *W*=0.20 m, turbine damping condition V2% (V=0.030m) and relative water depth kh=2.07, illustrates remarkably the effect of the front wall draught on the processes inside the OWC chamber.

Generally, when D decreases, the average water surface oscillations $\Delta\eta_{owc}$, the air pressure oscillation amplitude ΔP_{owc} and the maximum air flow velocity U_{max} increase. The smallest front wall draught D1, leads respectively to $\Delta\eta_{owc}$ of 0.038m, ΔP_{owc} of 297 Pa and U_{max} of 14.0m/s.

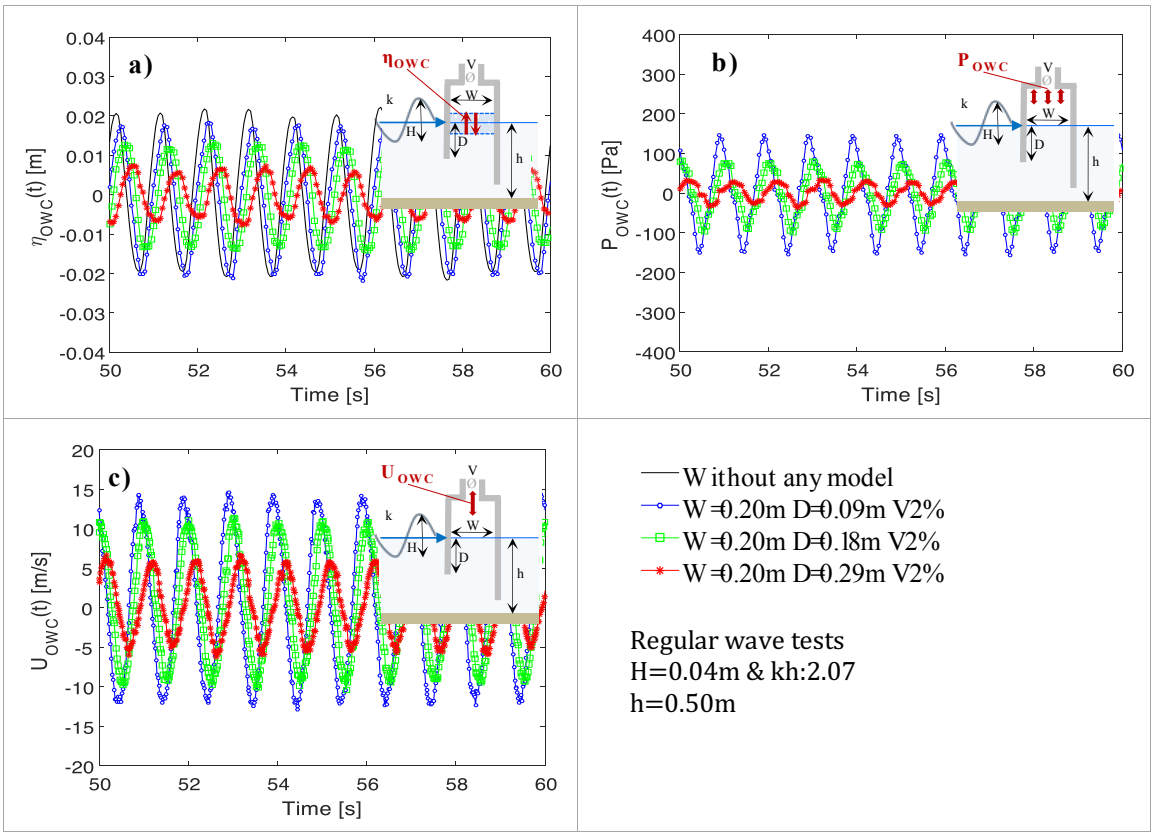

Fig. 4.23 - Time series acquired at the centre of the OWC. Effect of D on: a) $\eta_{OWC}(t)$, compared with the $\eta(t)$, recorded at the same location in the same test without any model, b) $P_{OWC}(t)$ and c) $U_{OWC}(t)$, for regular wave tests H02 (H=0.04m, kh=2.07 & h=0.50m).

d) Effect of the turbine damping on the physical processes inside the fixed OWC

The vents of different diameters V reproducing in laboratory the non-linear PTO system, allow an approximately quadratic relation between the airflow rate, Q_{OWC} and the relative air pressure P_{OWC}, that can be expressed, by means of the following parabolic expression, defining the damping coefficient K (López et al., 2015):

$$K = \frac{\sqrt{P_{OWC}}}{Q_{OWC}} \tag{4.14}$$

The values of K calculated from the instantaneous values of Q_{OWC} and P_{OWC} acquired during the tests for each vent diameters are reported in Table 4-13.

Table 4-13: Damping coefficient K, calculated for each vent tested.

NOTATION	VENT DIAMETER V [m]	DAMPING K [$kg^{1/2}m^{-7/2}$]	NOTATION
V0.5%	0.008	46904	K1
V1%	0.014	14491	K2
V2%	0.020	4785	K3
V0.5%	0.016	7416	K4
V1%	0.021	4472	K5
V2%	0.030	2074	K6
V0.5%	0.018	5138	K7
V1%	0.026	2746	K8
V2%	0.036	1473	K9

Value of K in the range 1473$kg^{1/2}m^{-7/2}$ - 46904$kg^{1/2}m^{-7/2}$ are obtained and the quadratic relation between P_{OWC} and Q_{OWC} is confirmed by means of a parabolic fitting with a determination coefficient R^2 higher than 0.9 for the nine vent diameters used in the parameter study (Fig. 4.24).

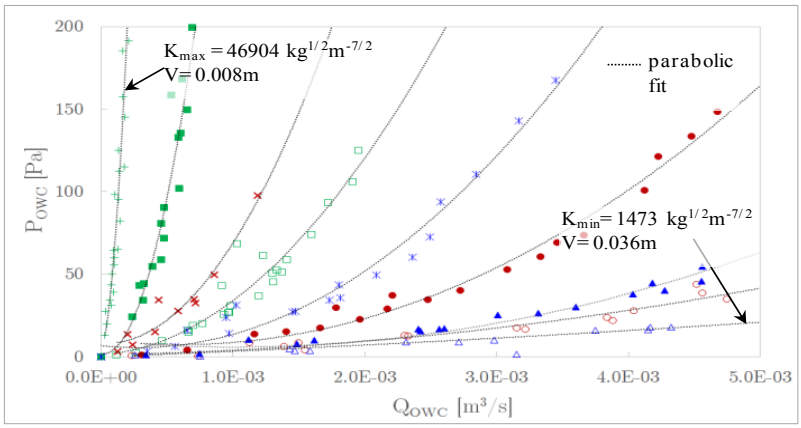

Fig. 4.24 - Air volume flux Q_{OWC} vs. air chamber pressure P_{OWC} for the nine vent diameters V with the associated damping coefficients K used in the parameter study.

In all the OWC models tested under regular wave tests (H=0.04m & kh=3.15, 2.07 & 1.22), damping coefficient K shows a significant effect on the processes inside the OWC chamber (Fig. 4.25).

The results obtained for the medium chamber width W2 (0.20m) tested with different D and V are exemplarily reported in Fig. 4.25. Generally, the inner air pressure oscillations ΔP_{OWC} increases with increasing damping coefficient K (Fig. 4.25a): ΔP_{OWC}=2-190Pa for the smallest damping value K=2074kg$^{1/2}$m$^{-7/2}$and ΔP_{OWC}=8-345Pa for the highest damping value K=7416kg$^{1/2}$m$^{-7/2}$. In contrast, inner water surface oscillations $\Delta\eta_{OWC}$ and maximum air volume flux Q_{OWCmax} in the pipe decrease with increasing K, respectively from 0.002-0.07m to 0.001-0.03m and from $3\cdot10^{-4}$-$4\cdot10^{-3}$m^3/s to $3\cdot10^{-4}$-$1\cdot10^{-3}$m^3/s, increasing K from 2074 to 7416kg$^{1/2}$m$^{-7/2}$(Fig. 4.25b and Fig. 4.25c).

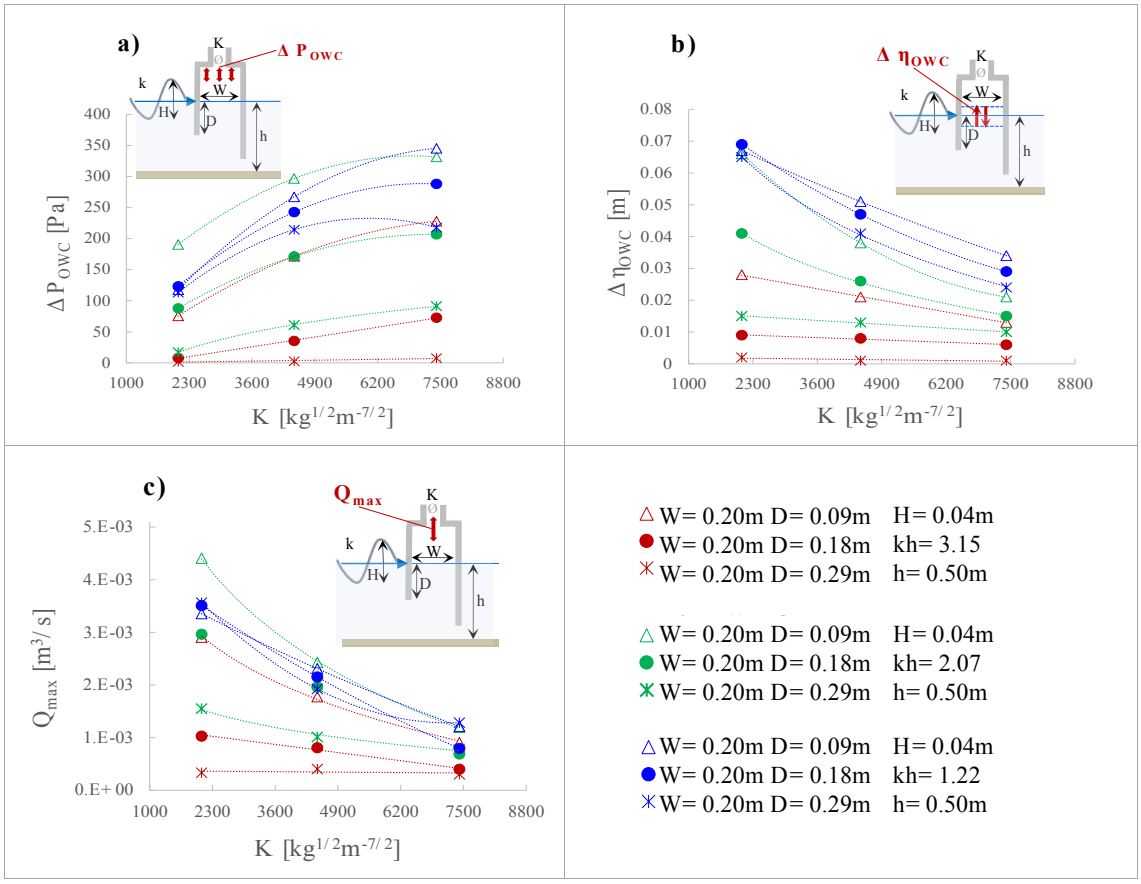

Fig. 4.25 - Effect of damping coefficients K on: (a) Air pressure oscillation amplitude ΔP_{OWC}, (b) water surface oscillations $\Delta\eta_{OWC}$ at the centre of the OWC chamber and on: (c) maximum air volume flux Q_{max} in the pipe for regular wave tests (H=0.04m, kh=1.22-3.15 & h=0.50m).

For fixed values of K, it is also confirmed that generally a decrease of the submergence D leads to higher ΔP_{OWC} and $\Delta\eta_{OWC}$. The same effect of D is observed for the maximum air volume flux, Q_{OWCmax}, except for the longest incident wave tests H03.

The incident waves remarkably affect the OWC hydrodynamics, leading to an increasing of air pressure, water surface oscillations and air volume flux, with increasing the wavelength. However, for the longest incident wave (kh=1.22) and the smallest induced damping K (2074kg$^{1/2}$m$^{-7/2}$), lower variation of ΔP_{OWC}, $\Delta\eta_{OWC}$ and Q_{OWCmax} occurs by varying the submergence D.

This is due to the relevant influence of D on the natural resonance frequency of the OWC (see Table 4-12).

e) Preliminary assessment of fixed OWC performance

Aimed at providing the basis for the comparative analysis with the results of Phase III tests and in order to restrict the range of OWC geometries to be integrated in the VLFS model of Phase III, the performance of each fixed OWC model tested in Phase I is preliminarily assessed.

A commonly used indicator for the performance of the OWC (and Wave Energy Converters in general) is the *Capture Width*, *CW* [m], defined as the width of the wave front (assuming uni-directional waves) that contains the same amount of power as that absorbed by the device (Price et al., 2009). The capture width is therefore described as the ratio of the mean absorbed pneumatic power, Π_{OWC}, [W] to the averaged wave power associated the incident waves, Π_{wave}, [W/m] (Eq.4.13):

$$CW = \frac{\overline{\Pi_{OWC}}}{\overline{\Pi_w}} \tag{4.13}$$

The mean absorbed pneumatic power is obtained through integration over the test duration T_{test} of the product of air pressure p(t)measured inside the OWC chamber and airflow rate Q(t) through the pipe, (Sarmento, 1993) (Eq.4.14):

$$\overline{\Pi_{OWC}} = \frac{1}{T_{test}}\int_0^{T_{test}} Q(t)p(t)dt \tag{4.14}$$

where, the air flow rate $Q_{OWC}(t)$ is derived from the time series of airflow velocity $U_{max}(t)$ sampled at the centre of the pipe located on the OWC cover. For this purpose, the average air velocity along the pipe cross section $U_m(t)$ is calculated depending on the flow regime described by Reynolds number, *Re*. For *Re*<2400, a laminar pipe flow (parabolic velocity distribution $U(r)$ over pipe cross-section) is assumed, hence $U_m(t)= U_{max}(t)/2$. For *Re*>2400, the flow inside the pipe is assumed to be turbulent and a one-seventh power law (Eq. 4.15) is used to calculate $U_m(t)$ from the velocity profile $U(r)$ along the pipe radius R.

$$\frac{U_{(r)}}{U_{max}} = \left(1 - \frac{r}{R}\right)^{\frac{1}{7}} \tag{4.15}$$

where, r is the distance from the pipe axis.

The period averaged wave power is evaluated for both incident regular and irregular wave trains.

For regular waves, the period-averaged wave power for a specific water depth h, is defined according to linear wave theory by Eq. 4.16 (Cornett, 2008):

$$\overline{\Pi_{wave\ reg}} = \frac{1}{16}\rho g H^2 \frac{\omega}{k}\left(1 + \frac{2kh}{\sinh(2kh)}\right) \tag{4.16}$$

in which, ρ is the water density, H is the regular wave height, ω is the wave frequency and k is the wave number.

For irregular waves, the period-averaged wave power is calculated as follows (Cornett, 2008):

$$\overline{\Pi_{wave\ irr}} = \rho g \sum_i c_{g,i} S_i\, \Delta f_i \tag{4.17}$$

where S_i is the frequency spectrum recorded in the laboratory tests, Δf_i is the frequency resolution and $c_{g,i}$ is the wave group celerity for each spectral wave component i, obtained by solving the linear dispersion relation for the specific water depth h (Eq. 4.18).

$$c_{g,i} = \frac{1}{2}\left(1 + \frac{2k_i h}{\sinh(2k_i h)}\right)\frac{g}{\omega_i}\tanh(k_i h) \tag{4.18}$$

in which, k_i is the wave number for component i and ω_i is the angular wave frequency for component i.

Π_{wave} is computed by the acquisitions of the ultrasonic wave probe (WG5) located at the centre of the removed model position (i.e. W0D0V0 tests see *section 4.1.3*).

The aforementioned approach is verified by performing the reflection analysis on the records acquired at the ultrasonic wave probes located in front of the OWC model (i.e., WG2, WG3 and WG4), (see Table 4-10). In Fig. 4.26, are exemplary reported the incident waves, calculated by Goda & Suzuki method (Goda & Suzuki, 1995) for three OWC alternatives (i.e., W1D1V0.5%, W1D1V0.5%, W1D1V0.5%) under the irregular waves tested (see Table 4-2), versus the incident waves acquired at WG5 during W0D0V0 tests.

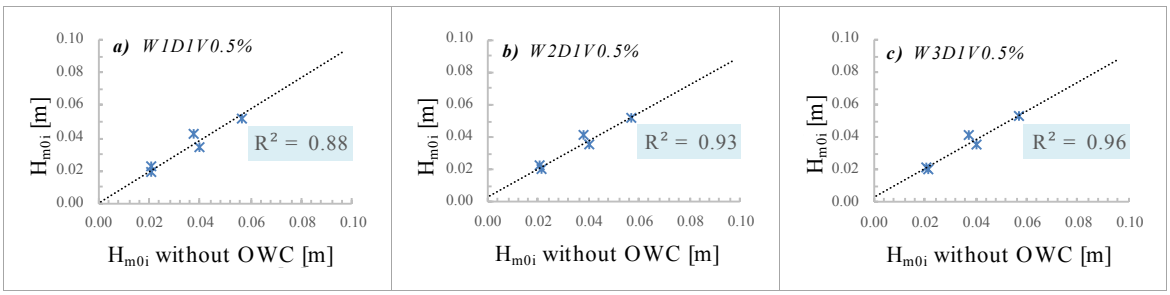

Fig. 4.26 – Scatter plot between the incident wave recorded at WG5 in absence of the OWC model and the same incident waves calculated by the reflection analysis for: a) W1D1V0.5%, b) W2D1V0.5% and c) W3D1V0.5% under the irregular waves tested.

Concerning the irregular wave tests, five of the overall 135 tests reached a *CW* slightly larger than the OWC width (i.e. with a maximum deviation less than 10%):

- W2D1V1% under the irregular wave H1 (H_{m0}=0.02m, T_p=0.9s);
- W2D1V1% and W2D1V2% under the irregular wave H2 (H_{m0}=0.02m, T_p=1.0s);
- W3D1V1% and W3D1V2% under the irregular wave H2 (H_{m0}=0.02m, T_p=1.0s).

Since due to the energy balance, *CW* cannot be higher than the OWC width (B=0.20m), the larger values of *CW* are due to experimental inaccuracy.

The sensitivity of the error was investigated by varying the spectrum data analysis parameters (as one of the possible source of inaccuracy) and proved that, as expected, this discrepancy is fully justify by such experimental approximations. Therefore, just for these four cases *CW* is approximated to 0.20m. As exemplarily illustrated in Fig. 4.27 for fixed regular wave conditions (H=0.04m, T=1.0s, kh=2.07, h=0.5m), for different chamber widths *W* and front wall draughts *D*, the capture width *CW* is significantly affected by draught *D* and damping *K*.

For each OWC geometry tested it is possible to identify an optimal value of the damping, K_{opt}, (for the vent sizes V1% and V2%), which allows to achieve the peak *CW* for a given incident wave frequency. For a given *D*, *W* and *K*, the comparison between the *CW* extracted for regular waves (H=0.04m, T=1.0s) with that calculated for irregular waves (H_{m0}=0.06m, T=1.1s), (Fig. 4.27a and b), shows that the *CW* values obtained for the latter (i.e. CW_{max}=0.15m) are always higher than for regular waves (i.e. CW_{max}=0.14m).

The reason of this difference between regular and irregular waves might be that as observed in the RES tests[10], the resonance of the OWC, is mostly influenced by the incident wave frequency. Since for regular waves, the energy is concentrated in a single frequency (i.e. monochromatic

[10] The simulated OWC chambers show the resonance for the incident waves characterized by a frequency of about 1Hz (see Table 4-12).

condition) whereas irregular wave spectrum consists of different frequency components, the resonance condition for the OWC in an irregular wave is more likely for a given size of the chamber.

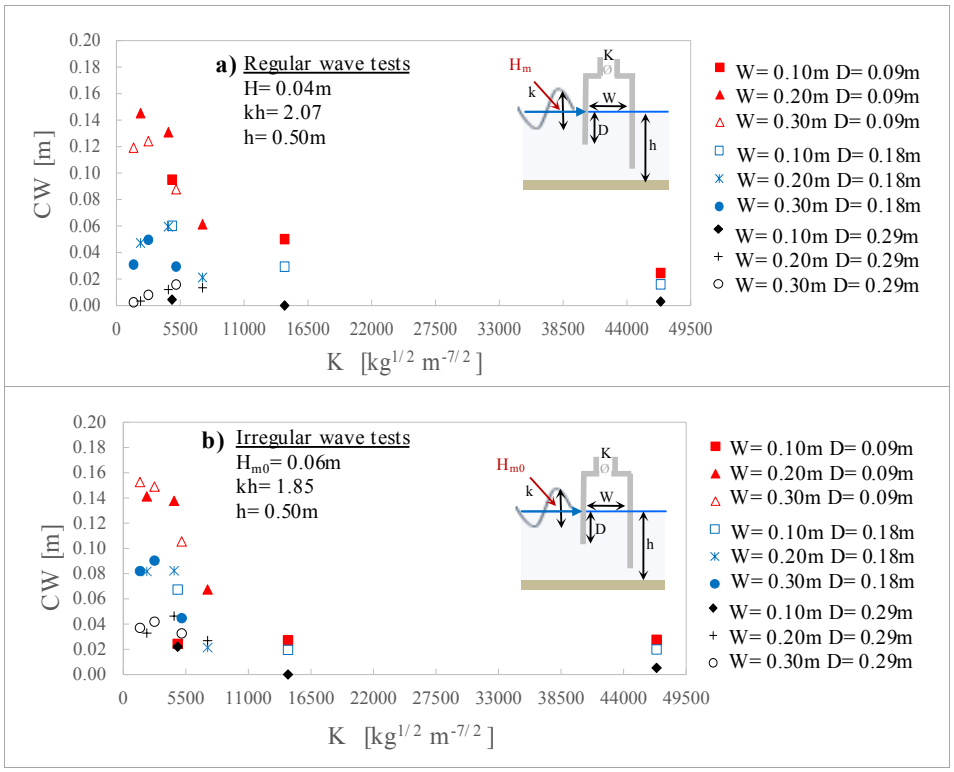

Fig. 4.27 - *Capture width CW* versus damping *K*: (a) regular wave tests H02 (H=0.04m, T=1.0s, kh=2.07) and (b) irregular wave tests H5 (H_{m0}=0.06m, T_p=1.1s, kh=1.85).

For each chamber width (W) and vent diameter (V) tested, the natural resonance frequency decreases with increasing the front wall draught (D).
The chamber width W has a relevant effect on the relative air pressure (ΔP_{OWC}), which increases with decreasing W. The higher averaged airflow velocity occurs with the medium chamber width tested (W2=0.20m), showing a strong dependence on the turbine damping (V).
The front wall draught D strongly affects the OWC chamber processes, showing an increasing trend of water column oscillations ($\Delta\eta_{OWC}$), air pressure (ΔP_{OWC}) and airflow velocity (Q_{OWC}), when D decreases.
The experiments also confirmed the significant influence of the damping coefficient K. Increasing K results in the increase of inner air pressure variations, but in a decrease of airflow velocity and inner water surface oscillations.
The incident wavelength (described in dispersion parameter kh with h=0.50m) strongly affects the response of the OWC, showing an increase of ΔP_{OWC}, $\Delta\eta_{OWC}$ and Q_{OWC} with increasing the wavelength (i.e. with decreasing kh-values).
According with Simonetti (2016), the experimental results might require the use of an appropriate correction factor, to account for air compressibility scale effects.

4.2.6 Summary of key results and implications for the detailed analysis

The preliminary analysis performed on the tests of Phase I is mainly focused on the investigation of the most relevant design parameters (i.e. chamber width *W*, front wall draught *D* and vent area simulating the turbine damping V) affecting the performance of the OWC. The key results and the implications for the detailed analysis in *Chapter 5* may be summarised as follows:

- The natural frequency f_{OWC} acquired for each OWC model is in the range f_{OWC}=0.6-1.0Hz. Among the varied OWC parameters, the front wall draught *D* has a significant effect on the natural frequency (f_{OWC} increases with increasing *D*).
- The damping coefficient *K* associated with each vent diameter *V* confirms the quadratic relation between airflow rate Q_{OWC} and air pressure P_{OWC}, with *K*= 1473 - 46904kg$^{1/2}$m$^{-7/2}$

for V=0.036-0.008m. Higher K results in higher inner air pressure P_{OWC}, but in lower inner water surface oscillations η_{OWC}, and airflow rate Q_{OWC}.

- The front wall draught D has a significant effect on the processes in the OWC chamber: decreasing D always implies an increase of η_{OWC}, P_{OWC} and Q_{OWC}.
- For a given D and K, a decrease of W results in an increase of inner air pressure P_{OWC}.
- The incident wave parameters, particularly the wavelength λ, strongly affect the OWC performance, showing that P_{OWC} and Q_{OWC} increase for longer waves.
- Higher OWC performance (*Capture Width)* are observed under the irregular wave tests. This might be tentatively explained by the different response of a given OWC chamber to the wave components of different frequencies. In contrast to a regular wave, an irregular wave consists of several different frequency components, so that OWC resonance conditions in irregular waves is more likely for a given chamber size

The implications for *Section 4.4* (Phase III tests on VLFS-OWC models) may be summarised as follows:

- Laboratory tests show higher values of CW for the smallest front wall draught (D1) and vents (simulating the turbine damping) in a range between 1% and 2% of the top cover area (V1% and V2%). To restrict the number of tests for Phase III, the following OWC geometries are selected for the integration in VLFS: W1D1V1%, W1D1V2%, W2D1V1%, W2D1V2%, W3D1V1% and W3D1V2%.

4.3 Phase II: VLFS model without OWC devices

The tests of Phase II are performed on the central segment of the VLFS-OWC model without the OWC devices. Two lengths of the VLFS under regular and irregular wave trains (see *subsection 4.1.3*) are tested, in order to:

- characterize the VLFS behaviour, in terms of displacements, pre-tensioning necessary to hold together the VLFS units and air pressure within the VLFS structure;
- assess the effect of the VLFS length on the floating behaviour.

The results achieved in Phase II could be used for a comparison with the results of Phase III (VLFS-OWC models), allowing to evaluate the mitigating effect of the OWCs on the VLFS motion. However, due to time constraints, this analysis is not performed in this thesis, so the obtained data related to this aspect will be analysed later.

4.3.1 VLFS model design and construction

To reproduce properly at model scale the building block procedure as conceived for the hypothetical installation of the VLFS-OWC System under prototype conditions at sea, the VLFS model is manufactured by assembling several methacrylate boxes with an open bottom, mimicking precast concrete VLFS units at prototype scale (Fig. 4.28).

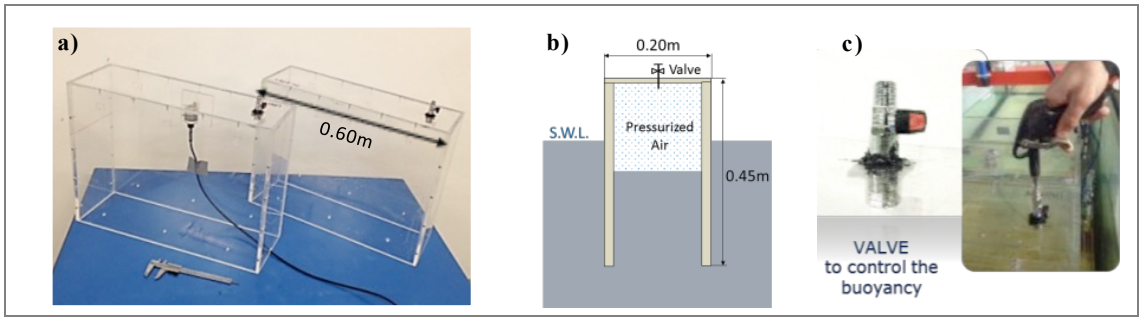

Fig. 4.28 - VLFS model (a) Methacrylate box units composing the VLFS; (b) Side view of one semi-submerged box unit; (c) Valve equipping each box unit for buoyancy control.

Stainless steel screws are used for assembling the components of each box and silicone is used for sealing to avoid air losses. Each box is 0.60m wide, 0.45m high and 0.20m deep (in the direction of the wave propagation). The sidewalls, the front and back walls have a thickness of 0.008m, whereas the top cover is 0.005m thick. A valve is installed on the roof of each box, allowing the

control and the modulation of the buoyancy by means of an external compressed air pump. Two stainless steel wire ropes (diameter of 0.0015m) are properly pre-tensioned and fixed at the two edge boxes of each side of the VLFS model, to hold together the units (Fig. 4.29).

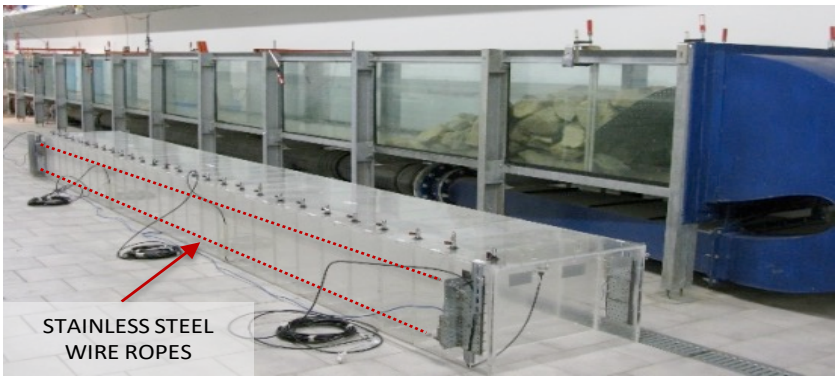

Fig. 4.29 - VLFS assembled in laboratory for the tests of Phase II.

The parameter study is performed, varying the length (L_{VLFS}) of the VLFS, respectively: $L_{VLFS}1$=2.60m, obtained by joining 13 box units and $L_{VLFS}2$=5.60m (2.15* $L_{VLFS}1$), obtained by joining 28 box units. In Table 4-14, the main design parameters of the VLFS model, as well as the description of each notation used in the laboratory tests, are summarized.

Table 4-14: Design characteristics of the VLFS model (scale 1:50).

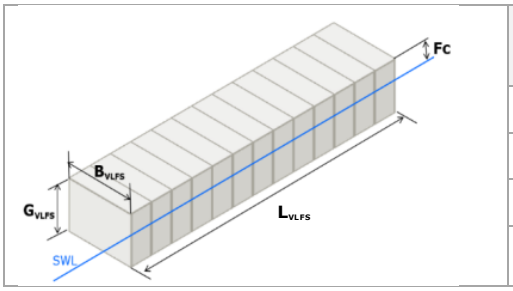

Notation	Description	[unit]	value
L_{VLFS}	VLFS length	[m]	2.60 and 5.60
B_{VLFS}	VLFS width	[m]	0.60
G_{VLFS}	VLFS height	[m]	0.45
M_{VLFS}	VLFS mass	[kg]	98 - 210

4.3.2 Preliminary tests and implications for the main tests

The preliminary tests, as a preparatory phase for the main tests in Phase II, are performed by deploying only the model with the shortest VLFS length L_{VLFS}=2.60m subject to regular wave tests with H=0.04 -0.06m and T=0.9-1.6s in a constant water depth h=0.50m (Fig. 4.30). The freeboard is fixed at +0.16m S.W.L.

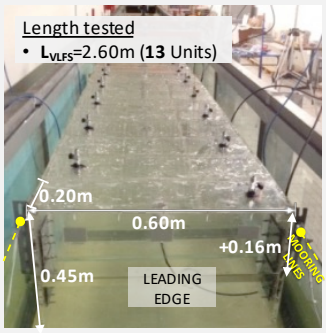

Setup of the preliminary tests for Phase II		
Geometry	**Tests Conditions**	**Measurements**
L_{VLFS}=2.60m	3 Regular Wave tests (H=0.04-0.06m & T=0.9-1.6s) Water depth h=-0.50m S.W.L. Freeboard Fc=+0.16m S.W.L.	-Wave motion -VLFS heave motion

Fig. 4.30 - VLFS model setup of the preliminary tests and tested conditions (Table 4-14).

The VLFS model is placed 22m far from the wave maker and is kept on site by means of four horizontal mooring cables: two connected to the leading edge and two to the rear edge, to limit the VLFS displacement at the heave motion.

The mooring cables are made of a thin and high stiffness cotton rope and are 5m long, to avoid the vertical forces acting on the VLFS during the tests.

Ten ultrasonic distance sensors are deployed along the wave flume using a sampling frequency of 1 kHz, as wave gauges (WG) and as displacement meters (DM) to record the vertical motions of the VLFS model (Table 4-15):

- WG1 is located in front of the wavemaker for the generated waves;
- WG2 -WG4 are set in front the model for the incident and reflected waves and WG11 behind the model for the trasmitted waves.
- DM6 -DM10 are located at a distance of 0.16m above the model deck to measure heave motions of the VLFS.

Table 4-15: Location of the sensors for the preliminary tests for Phase II.

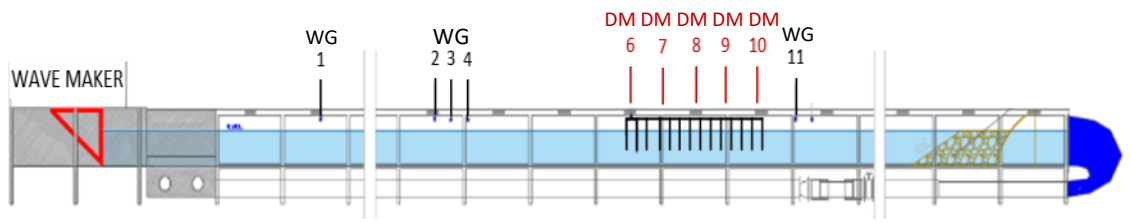

DESCRIPTION	NOTATION	MEASUREMENT	DISTANCE FROM THE WAVEMAKER [m]
Ultrasonic distance sensors	**WG1**	Generated Wave	4.00
	WG2	Incident and reflected wave	18.39
	WG3		18.69
	WG4		18.99
	DM6	Displacements at the leading edge	22.19
	DM7	Displacements at the centre of the front segment	22.79
	DM8	Displacements at the VLFS centre	23.39
	DM9	Displacements at the centre of the rear segment	23.99
	DM10	Displacements at the back edge of VLFS	24.59
	WG11	Transmitted wave	27.79

A first level analysis of the data from the preliminary tests is carried out to check the quality of the recorded data as well as the laboratory procedures related to the buoyancy, the setup of the freeboard and the mooring system adopted to limit the heave motion of the VLFS.

Although the sensors and the applied calibration procedures (see *Section 4.1*) provide a good quality of the acquired data and though the adopted horizontal mooring system allows the constriction in the heave motion thus avoiding vertical forces on the VLFS, the following crucial issues need to be improved for the main tests in Phase II:

1) *Avoiding air losses in the VLFS units*: The manufacturing procedure of the unit is improved, ensuring better water- and airtight conditions for the main tests. A procedure is introduced to check the water- and airtight conditions of each unit in a dedicated tank before assembling all units to a VLFS.
2) *Modelling the floating behaviour of the VLFS at small-scale*: a control of the tensions at the ropes holding the units and of the air pressure inside the VLFS, is required. Hence, for the main tests of Phase II, in addition to the ultrasonic distance sensors, load cells and pressure transducers are set on and inside the model, allowing to control the buoyancy and to record the processes inside the structure.
3) *Ensuring a proper buoyancy of the VLFS in the wave flume*: once the water- and airtight conditions is verified for each unit, all units are assembled and the VLFS model is setup in the wave flume, a systematic and improved procedure to ensure a proper buoyancy of the VLFS in the wave flume is introduced. Before starting each test, the settings of pressure inside the VLFS and tension of the cables holding the units are kept constant.

4.3.3 VLFS Model setup for main tests

A similar model setup as in the preliminary tests is also adopted for the main tests in Phase II, whereas the differences can be seen from Fig. 4.30 and Fig. 4.31.

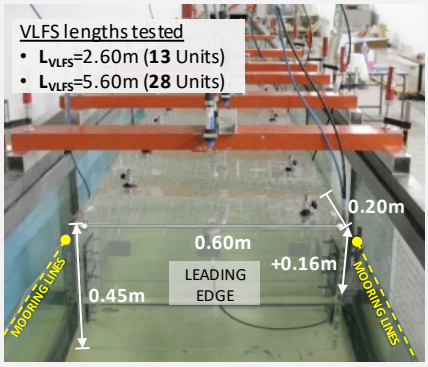

Setup of the main tests for Phase II		
Geometry	**Tests Conditions**	**Measurements**
2 VLFS model alternatives obtained varying: $L_{VLFS}1$=2.60m $L_{VLFS}2$=5.60m	6 Regular Wave tests (H=0.04-0.06m & T=0.8-1.6s) 5 Irregular Wave tests (H_{m0}=0.02-0.06m & T_p=0.9-1.1s) Water depth h=-0.50m S.W.L. Freeboard Fc=+0.16m S.W.L.	-Wave motion -VLFS heave motion -Relative air pressure inside some units of the VLFS -Tension at the cables connecting the first and last units

Fig. 4.31 - VLFS model setup of the main tests for Phase II and tested conditions (Table 4-14).

Setting of the sensors along the flume

To measure the wave motions along the flume and the heave motions of the VLFS model, the same deployment set of sensors as for the preliminary tests is adopted (Table 4-16).

Setting of the sensors on and inside the VLFS model

To improve the understanding of the floating behaviour of the VLFS, the two models in the tested in Phase II are additionally equipped with several sensors (Fig. 4.32), (Table 4-16).

- Four pressure transducers (PT1 to PT4) are installed in the internal wall of four units of the VLFS model, with the sensitive membrane upwards, to measure the relative inner air pressure during the tests. Once the model is floating and before staring each test, the air pressure inside each VLFS unit is set at 600Pa.
- Four load cells (LC1 to LC4) are installed on the four cables (two for each side), connecting the first and last units, in order to hold all the units. Once the model is on the flume bottom and before adding water to bring it floating, each cable is properly pre-tensioned at 19.5Kg. Such pre-tensioning resulted satisfactory, assuring a safe floating behaviour of the VLFS model during tests.

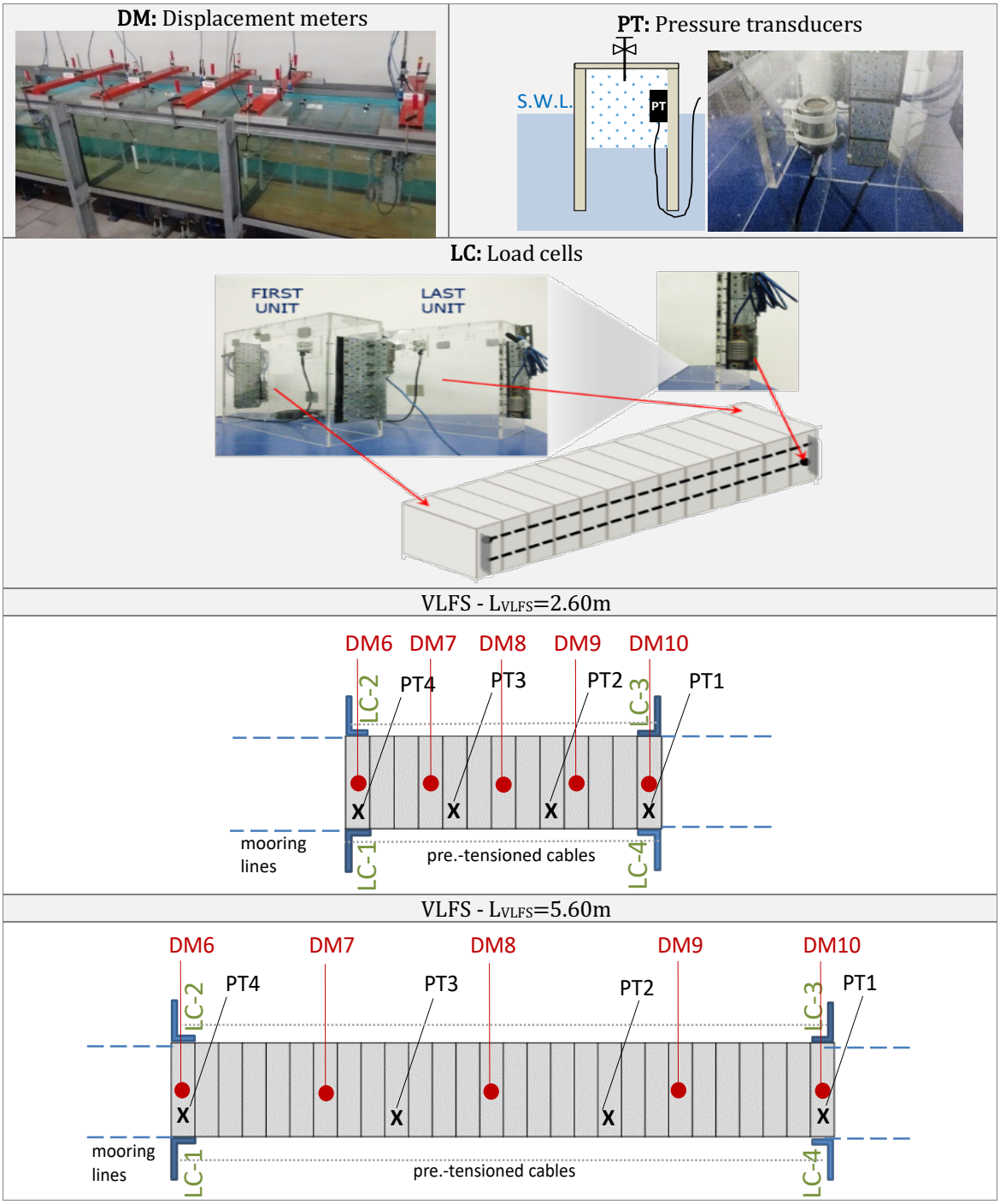

Fig. 4.32 - Deployed sensors (DM: displacement meters, PT: pressure transducer and LC: load cells) on and inside the VLFS model for tests in Phase II.

In Table 4-16 the location of the sensors for the tests of Phase II as well as the description of each notation and the measurements performed in the laboratory tests are summarized.

Table 4-16: Location of the sensors for the tests in Phase II.

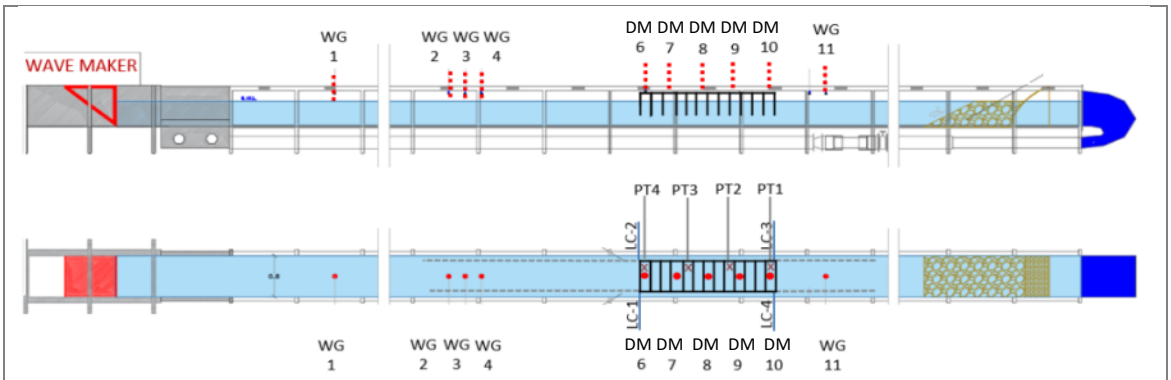

DESCRIPTION	NOTATION	MEASUREMENT	DISTANCE FROM THE WAVEMAKER [m]	
			F1	F2
Ultrasonic distance sensors	WG1	Generated Wave	4.00	4.00
	WG2	Incident and reflected wave	18.39	18.39
	WG3		18.69	18.69
	WG4		18.99	18.99
	DM6	Displacements at the leading edge of VLFS	22.19	22.19
	DM7	Displacements at the centre of the front segment of VLFS	22.79	23.39
	DM8	Displacements at the VLFS centre	23.39	24.79
	DM9	Displacements at the centre of the rear segment of VLFS	23.99	26.19
	DM10	Displacements at the back edge of VLFS	24.59	27.59
	WG11	Transmitted wave	27.79	30.79
Pressure transducers	PT4	Air pressure inside the first unit	22.26	22.26
	PT3	Air pressure at the centre of the first section of VLFS	23.06	24.06
	PT3	Air pressure at the centre of the last section of VLFS	23.86	25.86
	PT4	Air pressure inside the last unit	24.56	27.53
Load cells	LC1	Tension at the left side of the VLFS	22.09	22.09
	LC4		24.69	27.69
	LC2	Tension at the right side of the VLFS	22.09	22.09
	LC3		24.69	27.69

4.3.4 Testing programme for Phase II

Two lengths of the VLFS (F1 and F2) are tested under regular wave tests (H01 to H06) and irregular wave tests (H1 to H5), with heights between 0.02 and 0.06m and periods between 0.8 and 1.6s.

A supplementary test is carried out considering the effect of an additional mass of 20Kg equally distributed on the VLFS model 2.60m long (VLFS-M1F1). This test is not directly relevant for the objective of this study and is thus mainly directed towards providing data sets useful for further investigations on the effect of the mass on the floating behaviour of the VLFS without incorporated OWC devices.

Overall, 23 tests are performed for Phase II which took 4 working days (Table 4-17).

Table 4-17: Testing programme for Phase II.

Water depth: h=-0.50m S.W.L.						**Freeboard:** F_c=+0.16m S.W.L.					
Type of test	**Regular Waves** H01 (H=0.04m T=0.8s) H02 (H=0.04m T=1.0s) H03 (H=0.04m T=1.4s) H04 (H=0.04m T=1.2s) H05 (H=0.06m T=0.9s) H06 (H=0.06m T=1.6s)						**Irregular Waves** H1 (H_{m0}=0.02m T_p=0.9s) H2 (H_{m0}=0.02m T_p=1.0s) H3 (H_{m0}=0.04m T_p=1.0s) H4 (H_{m0}=0.04m T_p=1.1s) H5 (H_{m0}=0.06m T_p=1.1s)				
CODE	**H01**	**H02**	**H03**	**H04**	**H05**	**H06**	**H1**	**H2**	**H3**	**H4**	**H5**
VLFS- L_{VLFS}1	✓	✓	✓	✓	✓	✓	✓	✓	✓	✓	✓
VLFS-M1 L_{VLFS}1		✓									
VLFS- L_{VLFS}2	✓	✓	✓	✓	✓	✓	✓	✓	✓	✓	✓

4.3.5 Preliminary data analysis and results

The effect of the VLFS length on the floating behaviour is determined by means of a comparative analysis of the data recorded for each test focusing on the evaluation of the heave motion at five points along the VLFS (see Table 4-16). A comparative analysis is also performed, to characterize the structural behaviour for the two VLFS lengths (L_{VLFS}=2.60&5.60m) under incident waves, by assessing the variations of the tensions needed to hold together the units of the VLFS and the variations of the air pressure inside the VLFS. The average values of the heave motion amplitude, tension and pressure variations are extracted by means of the frequency domain analysis of the data acquired at each measurement point for the regular and irregular waves tested.

To facilitate the understanding of the interactions between the structure and the incident waves as well as its floating behaviour, the preliminary analysis performed on the regular wave tests is presented below.

a) Heave motion of the VLFS

The influence of the VLFS length on the floating behaviour is assessed by comparing the average heave motion amplitude[11], he_m, extracted at each measuring point x_{dm}, referred to the leading edge of the VLFS, for the two tested model lengths (Fig. 4.33a and b).

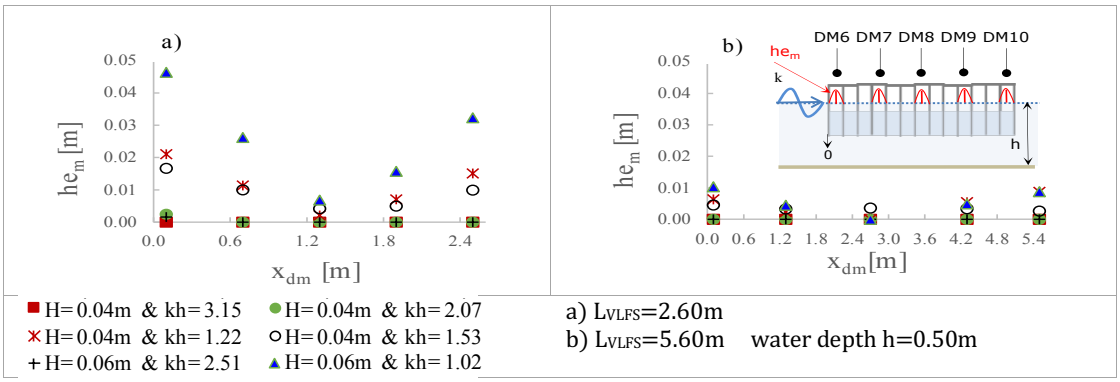

Fig. 4.33 - Longitudinal distributions of the heave motion amplitudes he_m, recorded for the two VLFS models: a) model with L_{VLFS}=2.60m and b) model with L_{VLFS}=5.60m, subject to regular waves (H= 0.04 -0.06m & kh=1.02 -3.15 in water depth h=0.50m).

The results show that, for both tested VLFS lengths, the maximum heave motion (he_m) occurs always in the leading edge (DM6), which is the most stressed point by the incident waves. However, for fixed wave heights, the heave motion amplitude generally increases with increasing wavelength. Comparing the two tested VLFS lengths it is shown that L_{VLFS} has also a relevant effect on the heave floating motion.

[11] The *heave motion amplitude, he_m*, is defined as the value of the maximum displacement from the zero value during one period of an oscillation.

For the shorter VLFS (Fig. 4.33a), maximum he_m=0.046m occurs at the leading edge for relative water depth kh=1.02, whereas for the longer VLFS under the same wave conditions, maximum he_m=0.01m (Fig. 4.33b).

The maximum heave motion (hem) occurs always in the leading edge and increases with increasing wavelength for both tested VLFS model lengths.
As observed for the wavelength, also the VLFS length shows a significant effect on the heave motion. Within the range of regular incident waves tested, increasing the VLFS length leads to a damping effect on hem

The significant effect of the wavelength and of the VLFS length on the heave motion is also confirmed by analysing the relative heave amplitude, normalized by the incident wave amplitude $he^*=he_m/a_w$, as a function of the VLFS length normalized by the incident wave $L^*=L_{VLFS}/\lambda$. The comparative analysis between the data acquired at two points, respectively located at 0.10m and 1.30m from the leading edge of both tested VLFS model lengths, highlights the decrease of the heave motion with decreasing $L^*$for a given wave height(Fig. 4.34).

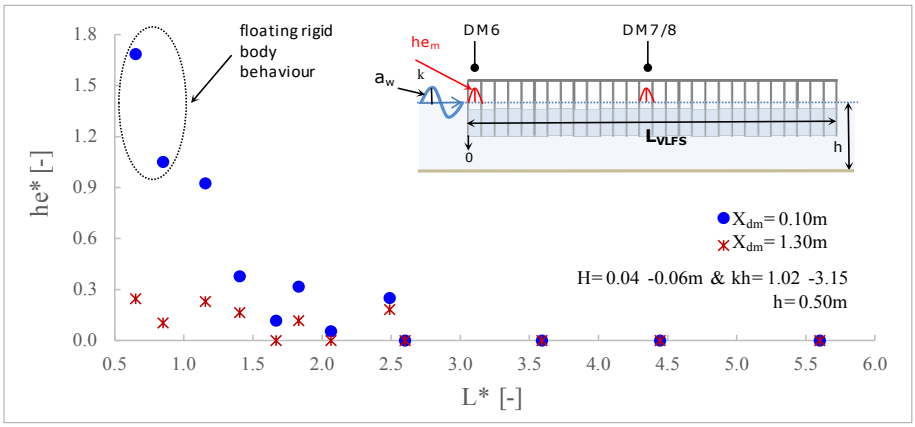

Fig. 4.34 - Relative heave amplitude he^* versus relative VLFS length L^*. Heave measured at two points located at 0.10m and 1.30m from the leading edge of both VLFS models with L_{VLFS}=2.6 & 5.6m subject to regular waves (H=0.04 -0.06m & kh=1.02 -3.15 in water depth h=0.50m).

Though the heave motion at the point closer to the leading edge is always larger within the range of waves tested, the maximum heave amplitude occurs for L^*=0.65 for both measuring points. Moreover, when L^*>2.5, the heave amplitude is totally damped, showing the same trend for both measuring points. The results confirm that for L_{VLFS} = 0.7-0.9 λ, the structure behaves as a floating rigid body and it is passively driven by the waves, without any effect on the wave attenuation, but with large heave amplitude motion (Tsubogo, 1997; Grotmaack, 2003).

For given incident wave height, the relative heave motion, $he^*=he_m/a_w$, decreases with increasing relative VLFS length $L^*=L_{VLFS}/\lambda$.
Generally, the heave amplitude is maximum for L^*=0.65, is totally damped for L^*>2.5 and the structure behaves like a floating rigid body for L_{VLFS} = 0.7-0.9λ.

b) Variation of the tensions holding the VLFS units together

The assessment of the average tension N_e [N] of the horizontal cables holding together the units for both tested VLFS model lengths is performed by relating the relative tension $N_e^*=N_e/\rho g \cdot B \cdot G \cdot L_{VLFS}$ (where B and G are the width and the height of the VLFS model, respectively) to the relative water depth *kh*. This is exemplarily shown in Fig. 4.35 for the two upper cables under regular waves (0.04 ≤H≤ 0.06m & 1.02 ≤kh≤ 3.15).

Within the range of tested wave conditions, the relative tension decreases with decreasing wavelength. The results show that $N_e^*_{max}=4\cdot10^{-3}$ for *kh* =1. However, the tension needed to hold together the VLFS units, is strongly affected by the length of the structure, L_{VLFS}.

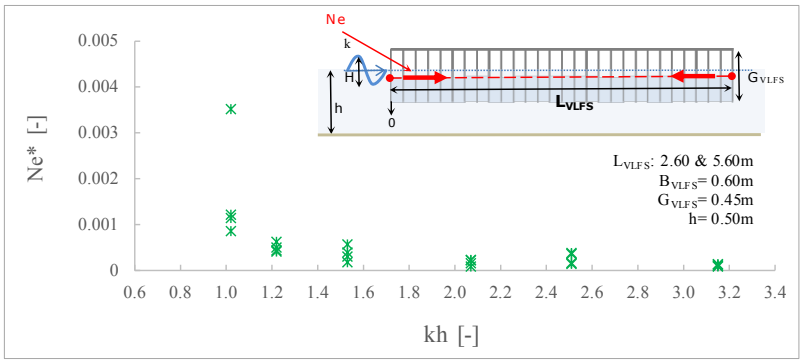

Fig. 4.35 - Relative tension $N^*= N_e/\rho g \cdot B \cdot G \cdot L_{VLFS}$ versus relative water depth kh, exemplarily for the two upper cables holding the units of both tested VLFS model lengths L_{VLFS}=2.6 & 5.6m under regular wave tests (0.04 ≤H≤ 0.06m & 1.02 ≤kh≤ 3.15).

Within the range of tested wave conditions, the relative tension $Ne^*= Ne/\rho g \cdot B \cdot G \cdot L_{VLFS}$ in the mooring cables decreases with decreasing wavelength (i.e. with increasing relative depth kh): $N_e{}^*_{max}=4 \cdot 10^{-3}$ is reached for kh=1.

c) Air pressure variations inside the VLFS

Since the pressure on the floating body changes in accordance with Bernoulli's equation, the pressure variation affects the motion of the floating structures and vice versa: This is referred to as a fluid-structure interaction (Wang et.al, 2008).

The effect of the pressure of the fluid acting below the VLFS model is evaluated by relating the relative air pressure $P^*=Pi/\rho \cdot g \cdot L_{VLFS}$, (in which Pi is the inner air pressure related to atmospheric pressure recorded at the four measuring points x_{pt}, located inside four VLFS units) to relative water depth kh for both the lengths tested under regular wave tests (0.04 ≤H≤ 0.06m & 1.02 ≤kh≤ 3.15), (Fig. 4.36).

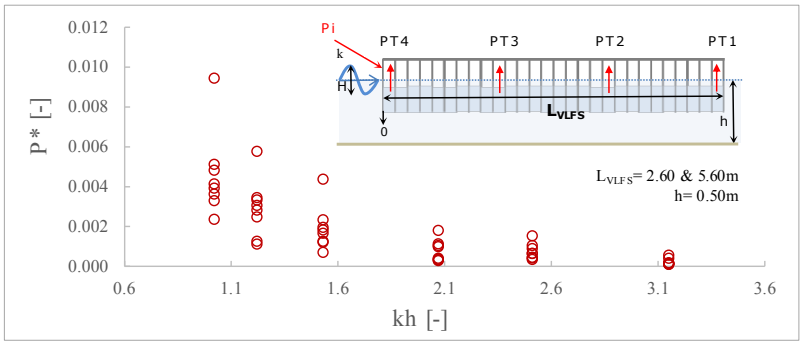

Fig. 4.36 - Relative air pressure $P^*=Pi/\rho \cdot g \cdot L_{VLFS}$, versus relative water depth kh, exemplarily for the first VLFS unit (i.e. the leading edge) of both tested VLFS model lengths L_{VLFS}=2.6 & 5.6m under regular wave tests (0.04≤H≤0.06m & 1.02≤kh≤3.15).

Within the range of tested wave conditions, the relative air pressure, recorded inside the VLFS units, decreases with decreasing wavelength (i.e. increasing the relative water depth kh).

Moreover, the laboratory tests show that the relative air pressure reaches the maximum ($P^*_{max}=9 \cdot 10^{-3}$) *for kh=1.02*. For a given relative water depth kh, it is also possible to note the relevant effect of the VLFS length, L_{VLFS} on the air pressure, which generally decreases whit increasing L_{VLFS} (from 2.60 to 5.60m).

Generally, the relative air pressure recorded inside the VLFS units, P decreases with decreasing wavelength (i.e. with increasing relative depth kh): $P^*=9 \cdot 10^{-3}$ is reached for kh=1.02. The relation between the relative air pressure P*, shows a strong dependency on the length of the structure L_{VLFS}. For fixed incoming wavelength, the pressure variation decreases when the VLFS length increases.*

4.3.6 Summary of key results and implications for the detailed analysis

The preliminary analysis of the Phase II tests is performed with the main purpose of characterizing the VLFS floating behaviour without any incorporated OWC.

To facilitate the comprehension of the effect of the VLFS length on the heave motion, a comparative analysis of the data recorded for two VLFS models with different lengths (L_{VLFS}=2.60m & 5.60m) is exemplary reported for the regular wave tests. Then, the variations of the tensions needed to hold together the units of the VLFS and the variations of the air pressure inside the VLFS are analysed. The key results and the implications for the detailed analysis in *Chapter 5* may be summarised as follows:

- The floating behaviour of the VLFS is dominated by the relative VLFS length, $L^*=L_{VLFS}/\lambda$.
- For both the tested VLFS lengths, the maximum heave motion (he_m) occurs at the leading edge and it is strongly affected by the incoming wavelength, showing an increasing trend with increasing wavelength. Moreover, the relative heave amplitude $he^*=he_m/a_w$, decreases with increasing L^*, reaching a maximum value for L^*=0.65 and showing a totally damped behaviour for L^*>2.5.
- The laboratory tests confirmed that the structure behaves as a floating rigid body for L_{VLFS} = 0.7-0.9 λ, without inducing any effect on the wave attenuation and reacting with large heave amplitude motion as reported by Tsubogo (1997) and Grotmaack (2003).
- Within the range of tested waves (0.04 ≤H_m≤ 0.06m & 1.02 ≤kh≤ 3.15) also the tension N_e, needed to hold together the VLFS units, is strongly affected by the incoming wavelength, showing a decreasing trend when wavelength decreases. Furthermore, the relative tension $N_e^*=N_e/\rho g\cdot B\cdot G\cdot L_{VLFS}$ decreases with increasing relative depth kh and reaches the maximum ($Ne^*_{max}=4\cdot 10^{-3}$) for kh=1.07.
- As for the heave motion and the tension, the air pressure, recorded inside the VLFS units Pi, decreases with decreasing wavelength. For a given incoming wave, the relative air pressure $P^*=Pi/\rho\cdot g\cdot L_{VLFS}$, shows also a decreasing trend with increasing the VLFS length.
- The assessment of the VLFS heave motions provides a reference case for the behaviour of the structure not equipped with OWC devices, for the comparison with the results achieved in Phase III (VLFS-OWC model) and those of the detailed data analysis in *Chapter 5*.
- Further results on the VLFS behaviour, in terms of pre-tensioning necessary to hold together the VLFS units and air pressure within the structure could be used in future analyses, on the mitigating effect of the OWCs on the VLFS motion, not performed in this thesis.

4.4 Phase III: VLFS-OWC Model

For the tests in Phase III, twelve VLFS-OWC geometries are tested under regular and irregular waves. The parameter study is carried out combining:

- one length of the OWC front wall draught (D);
- three sizes of the chamber width (W);
- six vent diameter V corresponding to six values of damping (K);
- two lengths of the VLFS model (L_{VLFS}).

The objective of the following preliminary data analysis is to evaluate the effect of the varied design parameters on the processes inside the floating OWC (incorporated in the VLFS).

The results will be used in the detailed analysis in *Chapter 5* to assess the effect of the VLFS heave motions on the OWC performance and to develop of an empirical model for the prediction of the performance of floating OWCs incorporated in a VLFS.

4.4.1 VLFS-OWC model design and construction

For the construction of the VLFS-OWC model, six OWC chambers are integrated in the VLFS[12]: three in the leading edge and three in the back edge, by means of stainless steel screw connections, suitably made water- and airtight after the assembling (Fig. 4.37).

[12] For a detailed description of the OWC and VLFS model construction, see respectively *subsection* 0 and *subsection* 4.3.1.

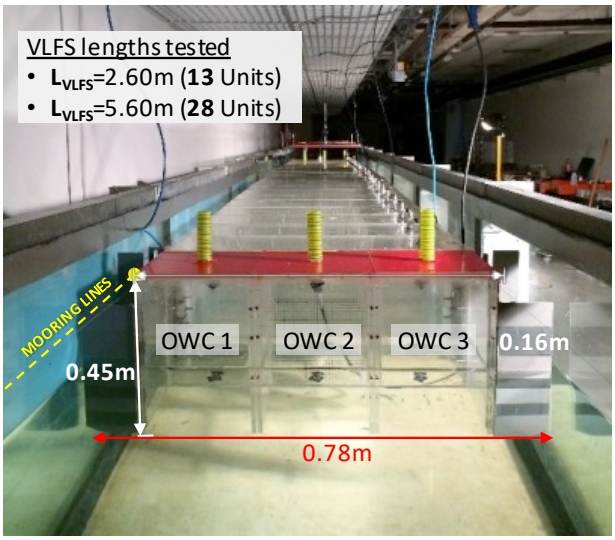

Fig. 4.37 - Example of VLFS-OWC geometry (M0L_{VLFS}2-W2D1V2%) tested in Phase III (Table 4-18).

The six most performant OWC models among all the OWC geometries tested in Phase I under fixed conditions (see *Section 4.2*) are selected for incorporation in the two lengths of the VLFS models with length L_{VLFS}=2.60 & 5.60m.

All selected OWC models have the same front wall draught (D1=-0.09m S.W.L.), but different chamber widths (W1=0.10m, W2=0.20m and W3=0.30m) and different vent areas simulating turbine damping K (V1% and V2% of the top cover surface).

In Table 4-18 the main design parameters of the VLFS-OWC model, as well as the description of each notation used in the laboratory tests, are summarized.

Table 4-18: Design characteristics of the VLFS model (scale 1:50).

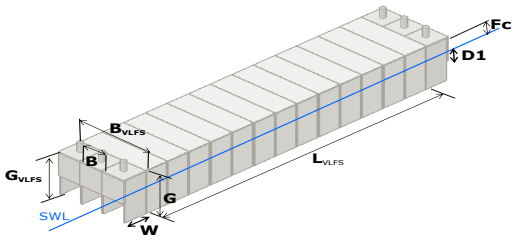

Notation	Description	[unit]	value
L_{VLFS}	VLFS length	[m]	2.60 - 5.60
B_{VLFS}	VLFS width	[m]	0.60
G_{VLFS}	VLFS height	[m]	0.45
W	OWC chamber width (in wave direction)	[m]	0.10 - 0.20 - 0.30
D	OWC front lip draught	[m]	0.09
V	Vent diameter	[m]	0.014 ÷ 0.036[13]
B	OWC width	[m]	0.20
G	OWC back wall length	[m]	0.45
$M_{VLFS\text{-}OWC}$	VLFS-OWC System mass	[kg]	115 - 227 (for VLFS-W1D1) 121 - 233 (for VLFS-W2D1) 128 - 240 (for VLFS-W3D1)

[13] Six different sizes of vents V are tested (see Table 4-7).

4.4.2 Preliminary tests and implications for the main tests

The preliminary tests are performed only for the shorter VLFS model (L_{VLFS}=2.60m) equipped with OWC model W2D1V1% under regular wave tests H02 (H=0.04m T=1.0s), (Fig. 4.38).

As in Phase I and Phase II, the VLFS-OWC model is placed 22m far from the wave maker. The water depth (h=0.50m) and the freeboard (+0.16m S.W.L) are kept constant and a passive wave absorbing system is built at the end of the flume.

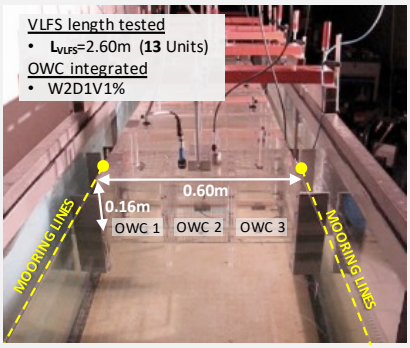

Setup of the preliminary tests for Phase III		
Geometry	**Tests Conditions**	**Measurements**
W1=0.10m D1=-0.09m S.W.L. V1% L_{VLFS}=2.60m	Regular Wave tests (H=0.04m & T=1.0s) Water depth h=-0.50m S.W.L. Freeboard Fc=+0.16m S.W.L	-Wave motion -VLFS heave motion -Relative air pressure inside the VLFS -Tension at the cables connecting the units -Free surface oscillations inside the OWC -Relative air pressure inside the OWC -Airflow velocity

Fig. 4.38 - VLFS-OWC model setup for the preliminary tests and tested conditions (Table 4-18).

As in Phase II, four horizontal cables are used to limit the VLFS motions (particularly heave motions). Unlike the model set up in Phase I, a suitable support for the setup of the hot-wire anemometer (HW sensor), is built, to equip the top cover of each OWC model (Fig. 4.39). Light aluminium section bars make the support rigidly coupled to the OWC chamber, thus ensuring a fixed setup of the HW sensor, avoiding interferences with the floating motion of the VLFS-OWC model during the tests.

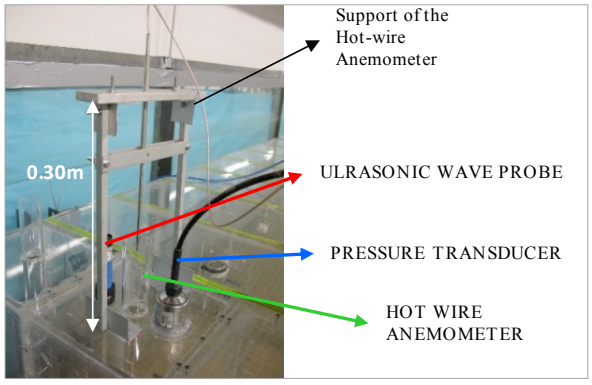

Fig. 4.39 - Support of the hot-wire anemometer used during the tests of Phase III.

In

Table 4-19 the deployment of overall the sensors (sampling frequency of 1kHz) along the wave flume, on and inside the VLFS-OWC model, combining the setup described for Phase I (see *subsection 4.2.3*) with that of Phase II (see *subsection 4.3.3*), is reported.

As for the previous test phases, a first level analysis of the data from the preliminary tests is carried out in order to identify possible improvements for the main tests of Phase III.

The first level analysis provides the following observations and implications for the main tests:

1) the calibration procedures of each sensor provide a good quality of the acquired data;
2) the procedures adopted for the buoyancy and the setup of the freeboard are the same as those in the tests performed in Phase II (see *section 4.3*);

3) the support built for the setup of the hot-wire anemometer shows a good resistance during the tests, fixing correctly the sensor without interfering with the floating motion of the VLFS-OWC model during the tests.

Table 4-19: Location of the sensors for the tests of Phase III.

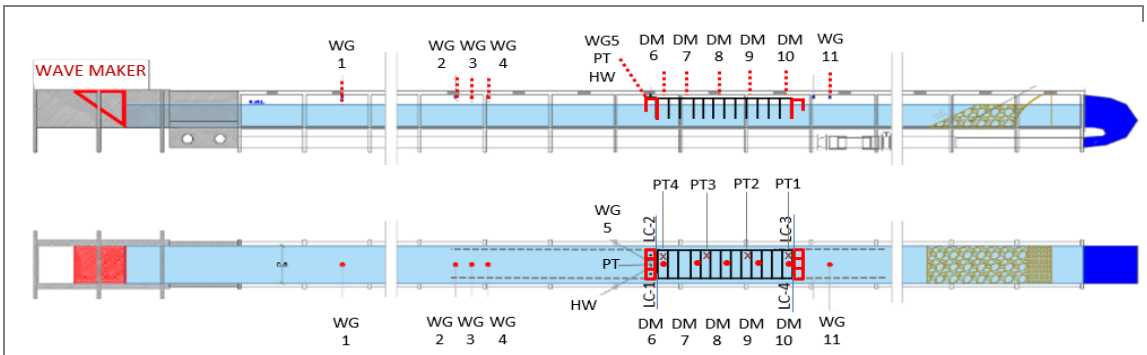

DESCRIPTION	NOTATION	MEASUREMENT	DISTANCE FROM THE WAVEMAKER [m]	
			13 VLFS Units	28 VLFS Units
Ultrasonic distance sensors	WG1	Generated Wave	4.00	4.00
	WG2	Incident and reflected wave	18.39	18.39
	WG3		18.69	18.69
	WG4		18.99	18.99
	WG5	Free surface oscillations inside the OWC	21.99	21.99
	DM6	Displacements at the leading edge of VLFS	22.19	22.19
	DM7	Displacements at the centre of the front segment of VLFS	22.79	23.39
	DM8	Displacements at the VLFS centre	23.39	24.79
	DM9	Displacements at the centre of the rear segment of VLFS	23.99	26.19
	DM10	Displacements at the back edge of VLFS	24.59	27.59
	WG11	Transmitted wave	27.79	30.79
Pressure transducers	PT4	Air pressure inside the first unit	22.26	22.26
	PT3	Air pressure at the centre of the first section of VLFS	23.06	24.06
	PT3	Air pressure at the centre of the last section of VLFS	23.86	25.86
	PT4	Air pressure inside the last unit	24.56	27.53
Hot-wire anemometer	HW	Outflow/inflow air velocity	21.99	21.99
Load cells	LC1	Tension at the left side of the VLFS	22.09	22.09
	LC4		24.69	27.69
	LC2	Tension at the right side of the VLFS	22.09	22.09
	LC3		24.69	27.69

4.4.3 VLFS-OWC Model setup for the main tests

The deployment of the sensors, the location of the VLFS-OWC model (
Table 4-19) and the tests procedures for the setting of buoyancy and freeboard are the same as in the preliminary tests.

A similar model setup as in the preliminary tests is also adopted for the main tests in Phase III, whereas the differences can be seen from Fig. 4.38 and Fig. 4.40.

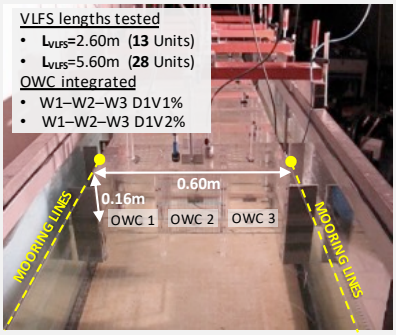

Setup of the main tests for Phase III		
Geometry	**Tests Conditions**	**Measurements**
12 model alternatives varying: -3 W -1 D -2 V -2 L_{VLFS}	6 Regular Wave tests (H=0.04-0.06m & T=0.8-1.6s) 5 Irregular Wave tests (H_{m0}=0.02-0.06m & T_p=0.9-1.1s) Water depth h=-0.50m S.W.L. Freeboard Fc=+0.16m S.W.L	-Wave motion -VLFS heave motion -Relative air pressure inside the VLFS units -Tension at the cables connecting the units -Free surface oscillations inside the OWC -Relative air pressure inside the OWC -Airflow velocity

Fig. 4.40 - VLFS-OWC model setup of the main tests for Phase III (Table 4-18).

4.4.4 Testing programme for Phase III

Overall, 12 VLFS-OWC models (six OWC models and two VLFS models) are tested, under regular waves (H01 to H06) and irregular wave trains (H1 to H5), with heights between 0.02 and 0.06m and periods between 0.8 and 1.6s in a constant water depth h=0.50m (Table 4-20).

Table 4-20: Testing programme for Phase III.

Water depth h=-0.50m S.W.L.	**Freeboard** F_c=+0.16m S.W.L.										
Type of test	**Regular Waves** H01 (H=0.04m T=0.8s) H02 (H=0.04m T=1.0s) H03 (H=0.04m T=1.4s) H04 (H=0.04m T=1.2s) H05 (H=0.06m T=0.9s) H06 (H=0.06m T=1.6s)						**Irregular Waves** H1 (H_{m0}=0.02m T_p=0.9s) H2 (H_{m0}=0.02m T_p=1.0s) H3 (H_{m0}=0.04m T_p=1.0s) H4 (H_{m0}=0.04m T_p=1.1s) H5 (H_{m0}=0.06m T_p=1.1s)				
CODE	**H01**	**H02**	**H03**	**H04**	**H05**	**H06**	**H1**	**H2**	**H3**	**H4**	**H5**
L_{VLFS}1- W1D1V1%	✓	✓	✓	✓	✓	✓	✓	✓	✓	✓	✓
L_{VLFS}1- W1D1V2%	✓	✓	✓	✓	✓	✓	✓	✓	✓	✓	✓
L_{VLFS}1- W2D1V1%	✓	✓	✓	✓	✓	✓	✓	✓	✓	✓	✓
L_{VLFS}1- W2D1V2%	✓	✓	✓	✓	✓	✓	✓	✓	✓	✓	✓
L_{VLFS}1- W3D1V1%	✓	✓	✓	✓	✓	✓	✓	✓	✓	✓	✓
L_{VLFS}1- W3D1V2%	✓	✓	✓	✓	✓	✓	✓	✓	✓	✓	✓
L_{VLFS}2- W1D1V1%	✓	✓	✓	✓	✓	✓	✓	✓	✓	✓	✓
L_{VLFS}2- W1D1V2%	✓	✓	✓	✓	✓	✓	✓	✓	✓	✓	✓
L_{VLFS}2- W2D1V1%	✓	✓	✓	✓	✓	✓	✓	✓	✓	✓	✓
L_{VLFS}2- W2D1V2%	✓	✓	✓	✓	✓	✓	✓	✓	✓	✓	✓
L_{VLFS}2- W3D1V1%	✓	✓	✓	✓	✓	✓	✓	✓	✓	✓	✓
L_{VLFS}2- W3D1V2%	✓	✓	✓	✓	✓	✓	✓	✓	✓	✓	✓

To provide a data set useful for future investigations on the motion of the VLFS-OWC system as well as on the mitigating effect of the OWC integrated, the following 71 additional tests are performed in Phase III (Table 4-21):

1) M1: tests with an additional mass of 20Kg equally distributed on the VLFS-OWC model 2.60m long, aimed at assessing the effect of the additional mass on the floating motion of the VLFS with incorporated OWC as well as on the energy harvesting performance.

2) B0: measurements performed on the OWC alternative W2D1V1% integrated in the back edge of the VLFS-OWC model, to provide data for the comparison of the performance with the same OWC alternative integrated in the leading edge.
3) B1: tests on the OWC alternative W2D1V1% integrated in the back edge of the VLFS with an additional mass of 20Kg equally distributed on the surface of the VLFS-OWC model 2.60m long, to investigate the effect of the additional mass on the performance of the OWC.
4) T0: measurements of the strengths on the vertical mooring lines performed on the longest VLFS equipped with the OWC alternative W2D1V1%, aimed to assess the strength of the lines needed to avoid vertical movements of the VLFS-OWC model.
5) T1: tests on the horizontal mooring lines connecting the leading edge of the VLFS-OWC model, equipped with the OWC aternative W2D1V1%.

However, the preliminary analysis concerning the aforementioned supplementary tests is not reported since they are not directly related to the objective of the present thesis.

Overall, 204 tests are performed for Phase III which took 21 working days (Table 4-20 and Table 4-21).

Table 4-21: Testing programme for the additional tests performed in Phase III.

Water depth h=-0.50m S.W.L.				**Freeboard** F_c=+0.16m S.W.L.							
Type of test	**Regular Waves** H01 (H_m=0.04m T=0.8s) H02 (H_m=0.04m T=1.0s) H03 (H_m=0.04m T=1.4s) H04 (H_m=0.04m T=1.2s) H05 (H_m=0.06m T=0.9s) H06 (H_m=0.06m T=1.6s)						**Irregular Waves** H1 (H_{m0}=0.04m T_p=0.8s) H2 (H_{m0}=0.04m T_p=0.8s) H3 (H_{m0}=0.04m T_p=0.8s) H4 (H_{m0}=0.04m T_p=0.8s) H5 (H_{m0}=0.04m T_p=0.8s)				
CODE	**H01**	**H02**	**H03**	**H04**	**H05**	**H06**	**H1**	**H2**	**H3**	**H4**	**H5**
M1L_{VLFS}1-W1D1V1%		✓									
M1L_{VLFS}1-W1D1V2%		✓									
M1L_{VLFS}1-W2D1V1%	✓	✓	✓	✓	✓	✓	✓	✓	✓	✓	✓
M1L_{VLFS}1-W2D1V2%		✓									
M1L_{VLFS}1-W3D1V2%		✓									
M1L_{VLFS}1-W3D1V1%		✓									
B0L_{VLFS}1-W2D1V1%	✓	✓	✓	✓	✓	✓	✓	✓	✓	✓	✓
B1L_{VLFS}1-W2D1V1%		✓									
T1L_{VLFS}1-W2D1V2%	✓	✓	✓	✓	✓	✓	✓	✓	✓	✓	✓
B0L_{VLFS}2-W2D1V1%	✓	✓	✓	✓	✓	✓	✓	✓	✓	✓	✓
T0L_{VLFS}2-W2D1V1%	✓	✓	✓	✓	✓	✓	✓	✓	✓	✓	✓
T1L_{VLFS}2-W2D1V1%	✓	✓	✓	✓	✓	✓	✓	✓	✓	✓	✓

4.4.5 Preliminary data analysis and results

As for the fixed OWC, the preliminary analysis of the sensitivity of the processes inside the floating OWC (i.e. free surface oscillations of the water column, differential air pressure between the chamber interior and the exterior atmosphere and outflow/inflow air velocity) to the varied VLFS-OWC design parameters (i.e. *W*, *V* and *F*) is performed.

Taking into account the implications drawn from the previous two phases, the preliminary analysis provides a useful starting base for the assessment of the effect of the VLFS motions on the OWC performance and for the development of an empirical model for the prediction of the performance of floating OWCs incorporated in a VLFS (see *Chapter 5*).

a) Effect of the chamber width on the processes inside the floating OWC

For given vent area (V1% of the top cover surface) to reproduce turbine damping K, a given VLFS model length (L_{VLFS}=2.60m) and given incident wave conditions H02 (H=0.04m & kh=2.07), the effect of the chamber width W, on the processes inside the OWC chamber is exemplarily reported in Fig. 4.41.

As observed for the fixed OWC (Fig. 4.22a, b and c in in *subsection 0*), the inner water surface oscillations, $\eta_{OWC}(t)$ are not remarkably different among the three chamber width (Fig. 4.41a), showing a slight increasing when W decreases. Concerning the inner air pressure, $P_{OWC}(t)$ increases with decreasing W (Fig. 4.41b). However, the inner airflow velocity $U_{OWC}(t)$ shows a different trend from that observed for the fixed OWC, namely a decrease of the chamber width, W, leads to an increase of $U_{OWC}(t)$ (Fig. 4.41c).

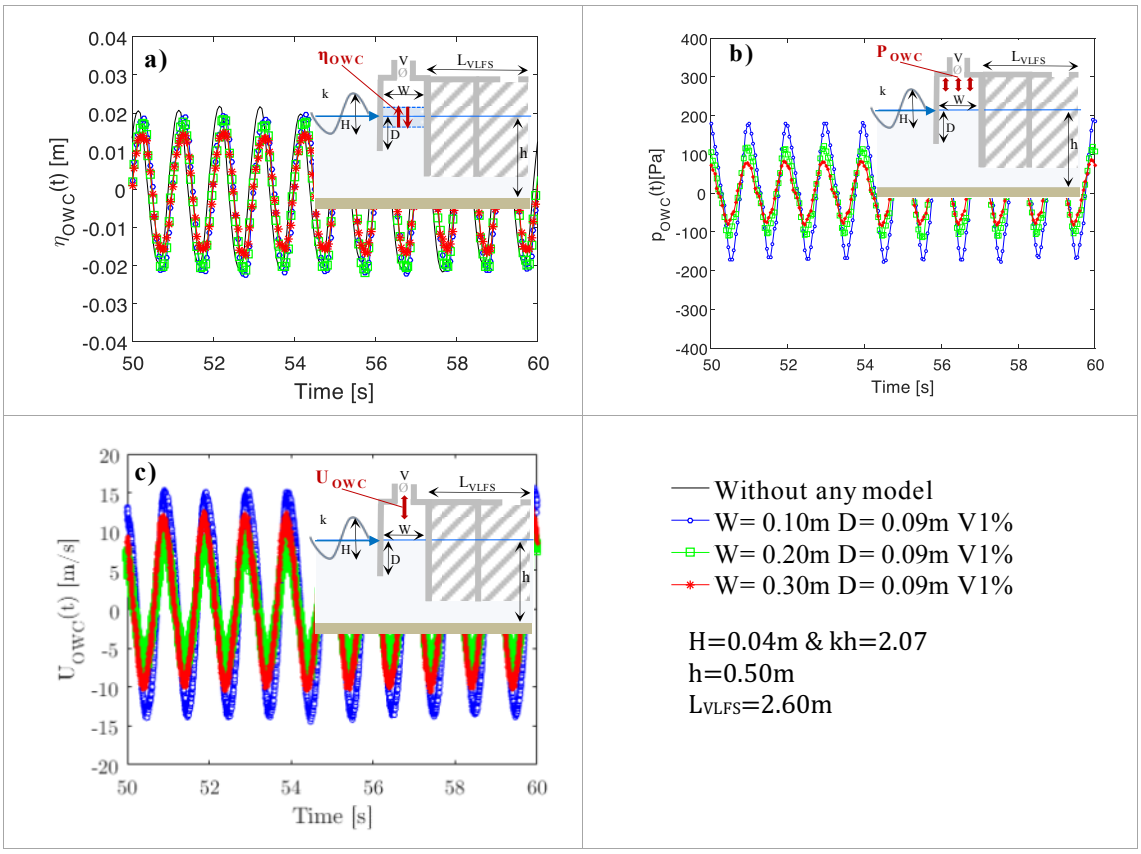

Fig. 4.41 - OWC integrated in the VLFS (M0L$_{VLFS}$1): Effect of OWC chamber width W, on: (a) inner water surface oscillations $\eta_{OWC}(t)$, compared with the $\eta(t)$, recorded at the same location in the same test without any model, b) inner air pressure $P_{OWC}(t)$ and c) inner airflow velocity $U_{OWC}(t)$, for regular wave tests (H=0.04m and kh=2.07).

The OWC chamber width W clearly affects the air pressure $P_{OWC}(t)$ and the water surface elevation $\eta_{OWC}(t)$ in the OWC chamber: like for a fixed OWC both P_{OWC} and η_{OWC} increase with decreasing W. However, in contrast to the results for the fixed OWC, airflow velocity $U_{OWC}(t)$ increases with decreasing W.

b) Effect of the turbine damping on the processes inside the floating OWC

The effect of the turbine damping K is reported in Fig. 4.42 exemplarily for the medium chamber width (W2=0.20m), integrated in the smallest VLFS (F1=2.60m) subject to regular waves (H=0.04m & 1.22<*kh*<3.15).

Generally, increasing K results in the increase of the inner air pressure oscillation amplitude, with values of ΔP_{OWC} in the range 58-174 Pa for the lowest damping K= 2074 kg$^{1/2}$m$^{-7/2}$ and in the range 100-329 Pa for the highest damping K=4472 kg$^{1/2}$m$^{-7/2}$ (Fig. 4.42a).

In contrast, $\Delta\eta_{OWC}$ and Q_{OWCmax}, (Fig. 4.42b and Fig. 4.42c) decrease with increasing K, respectively from 0.03-0.08 m to 0.02-0.05 m and from 1.4·10^{-4}-3·10^{-3} m^3/s to 8·10^{-4}-2·10^{-3} m^3/s for increasing K from 2074 to 4472 kg$^{1/2}$m$^{-7/2}$.

The relative water depth kh has a significant effect on the hydrodynamic and pneumatic processes in the OWC chamber, showing an increase of ΔP_{OWC}, $\Delta\eta_{OWC}$ and Q_{OWCmax} with longer waves (see Fig. 4.42 for kh=1.22, 2.07 and 3.15).

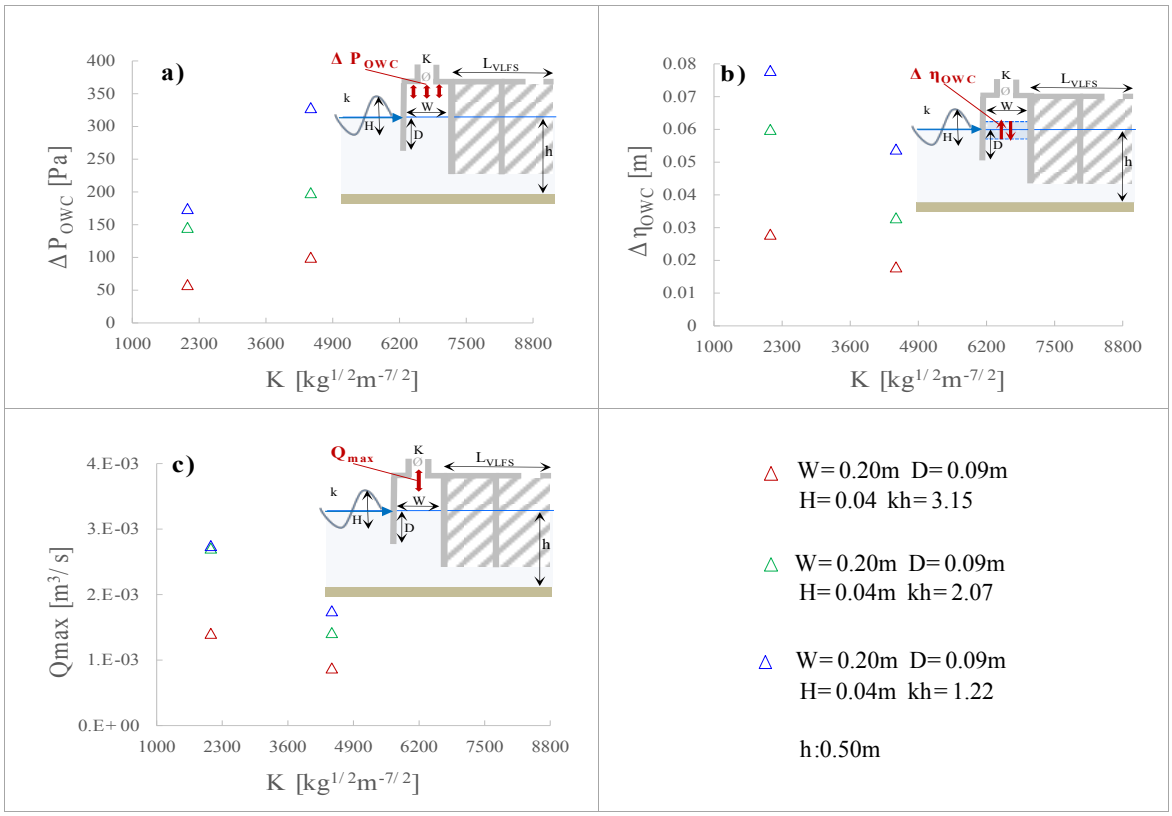

Fig. 4.42 - Effect of the damping coefficients *K* on (a) Air pressure oscillation amplitude ΔP_{OWC}, (b) water surface oscillations $\Delta\eta_{OWC}$ at the centre of the OWC chamber and on (c) maximum air volume flux Q_{max} in the pipe, for the OWC integrated in the shorter VLFS model (L_{VLFS}=2.60m) subject to regular wave tests (H=0.04m & 1.22<kh<3.15).

As observed for a fixed OWC in Fig. 4.25, also for the floating OWC device, the processes inside the chamber are significantly affected by the turbine induced damping: air pressure ΔP_{OWC} increases and both inner water level oscillations $\Delta\eta_{OWC}$ and air volume flux Q_{max} decrease, when damping coefficient K increases.

c) Effect of the VLFS length on the processes inside the floating OWC

The results highlight the significant effect of the VLFS length, L_{VLFS}, on the processes inside the OWC chamber.

As exemplarily illustrated in Fig. 4.43, for the floating OWC geometry W3D1V2% characterized by a damping coefficient K=1473kg$^{1/2}$m$^{-7/2}$ and subject to regular waves (0.02 ≤H≤ 0.06m & 1.85≤kh≤2.68), an important effect of L_{VLFS}, is observed.

Generally, increasing the wavelength λ induces an increase of all the processes inside the OWC. For the case in Fig. 4.43, it is seen that for λ>3.0m, the shorter VLFS (L_{VLFS}=2.60 m) leads to an increase of ΔP_{OWC}, $\Delta\eta_{OWC}$ and U_{max}, respectively of 70%, 40% and 20%.

However, for λ<3.0m the effect of L_{VLFS} is negligible, showing almost the same values for both VLFS model lengths tested.

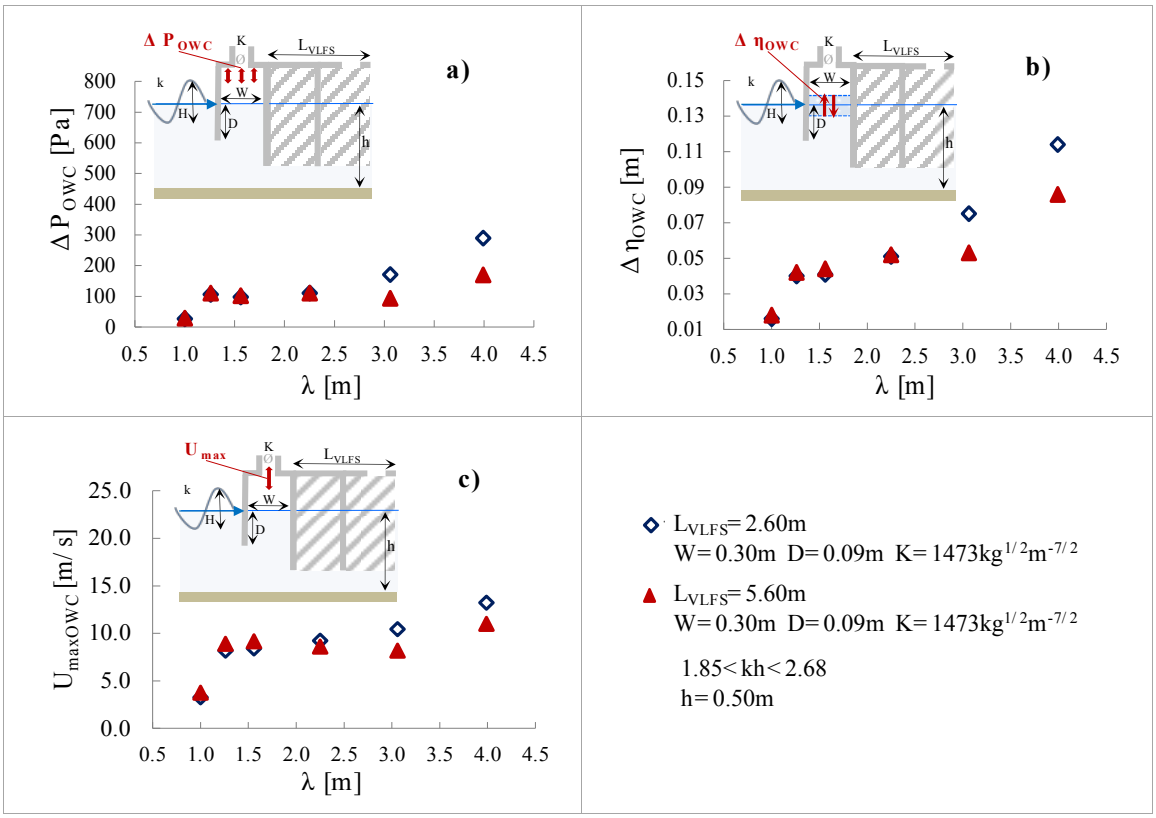

Fig. 4.43 - a) Air pressure oscillation amplitude ΔP_{OWC} and b) water surface oscillations $\Delta\eta_{OWC}$ at the centre of the OWC chamber, c) maximum airflow velocity U_{max} in the pipe, related to the chamber width W=0.30m and damping coefficients K=1473kg$^{1/2}$m$^{-7/2}$, for the OWC integrated in both VLFS model lengths (L_{VLFS}=2.60 & 5.60m) subject to regular wave tests (0.02≤H≤0.06m & 1.85≤kh≤2.68).

For the two VLFS lengths tested, (L_{VLFS}= 2.60 & 5.60m) only a slight effect of L_{VLFS} on the hydrodynamic and pneumatic processes inside the floating OWC are observed, depending on the incident wave length λ. For the OWC geometry W3D1V2% tested under regular wave tests, the effect of L_{VLFS} on air pressure ΔP_{OWC}, inner water level oscillations $\Delta\eta_{OWC}$ and air flow velocity Umax is negligible for λ<3.0m while for λ>3.0m, ΔP_{OWC}, $\Delta\eta_{OWC}$ and U_{max} increase with smaller L_{VLFS}. This effect increases for longer incident waves.

d) Floating OWC performance

As for the fixed OWC (see Fig. 4.27a and b), the effect of damping coefficient *K* on the floating OWC *Capture Width*, *CW*, is exemplarily shown for the OWC alternatives integrated in the two VLFS models with lengths L_{VLFS}=2.60 & 5.60m, subject to regular wave tests (Fig. 4.44a) and to irregular wave tests (Fig. 4.44b).

Also for the floating OWC, for a given chamber width W and incident wave frequency it is possible to identify an optimal damping K_{opt} associated with the maximum *CW* value.

For both, regular waves (H=0.04m & kh=2.07) and irregular waves (H_{m0}= 0.06m & kh=1.85), exemplarily reported in Fig. 4.44, the maximum CW occurs with damping K=2074kg$^{1/2}$m$^{-7/2}$, OWC chamber width W=0.20m and VLFS length L_{VLFS}=5.60m.

However, as observed for fixed OWC models, also the Capture Width of floating OWC shows higher values for the irregular waves (CW_{max}=0.14m), than for the regular waves (CW_{max}=0.13m).

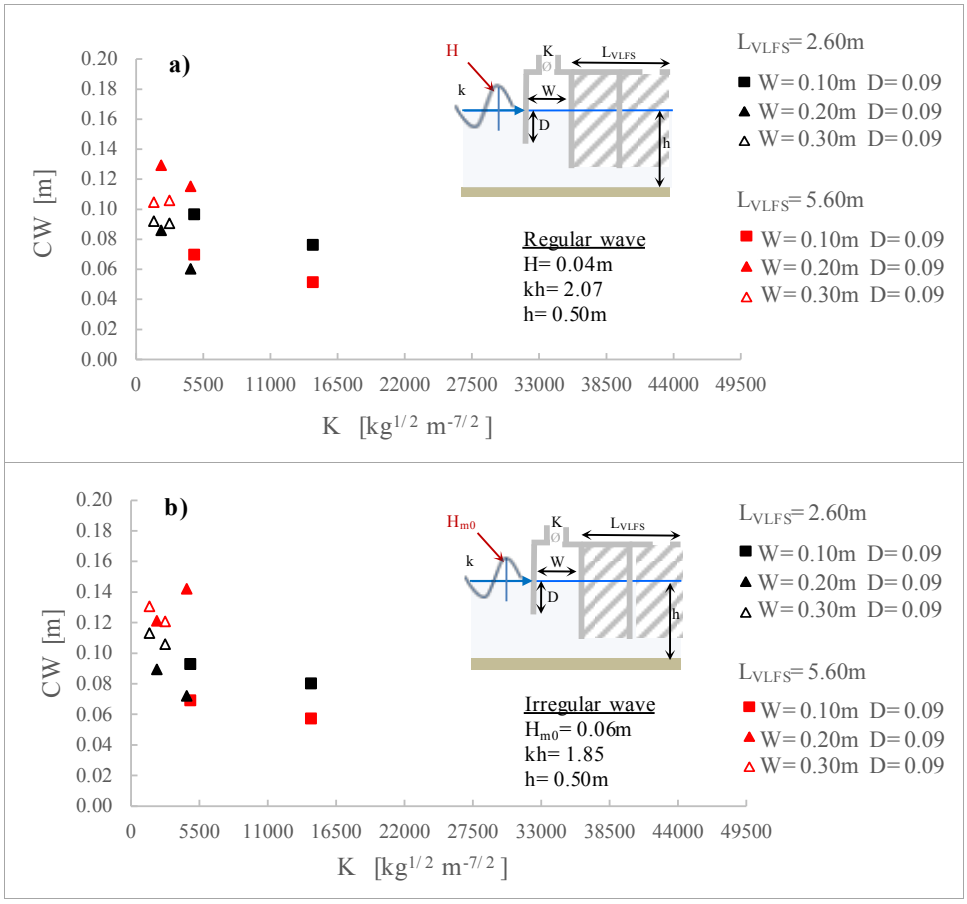

Fig. 4.44 - Capture width *CW* versus damping *K* for OWC models integrated in VLFS models with L_{VLFS}= 2.60 & 5.60m subject to a) regular waves H02 (H=0.04m, T=1.0s) and b) irregular waves H5 (H_{m0}=0.06m, T_p=1.1s).

Each OWC geometry integrated in the two VLFS lengths tested, shows a maximum value of the Capture Width for an optimal value of damping coefficient K_{opt}.
As observed for fixed OWC models also the CW obtained for floating OWC shows higher values for the irregular waves than for the regular waves.

4.4.6 Summary of key results and implications for the detailed analysis

The preliminary analysis performed on the tests of Phase III is mainly focused on the assessment of the effect of the varied parameters of the OWC-VLFS system (i.e. chamber width, *W*, diameter of the vent, *V* and VLFS length, L_{VLFS}), on the performance of the floating OWC (integrated in the VLFS).

The key results and the implications for the detailed analysis in *Chapter 5* may be summarised as follows:

- For given vent area V (i.e. turbine damping K) when chamber width W decreases the inner air pressure P_{OWC} (t) increases, as for the fixed OWC (respectively Fig. 4.41 and Fig. 4.22) However, unlike the fixed OWC, airflow velocity $U_{OWC}(t)$ increases with decreasing W.
- As observed for the OWC model with the medium chamber width (W2=0.20m) integrated in the shorter VLFS (L_{VLFS}=2.60m) subject to regular waves (H=0.04m & kh=1.22-3.15), when damping coefficient K decreases the inner air pressure P_{OWC} generally increases while the decrease of inner water surface oscillations ηOWC and air flow rate Q_{OWC} decrease.
- The VLFS length L_{VLFS} and the wave length λ strongly affect the processes inside the floating OWC. As exemplary reported for OWC model W3D1V2% (with W3=0.30 m) tested under regular waves, the effect of L_{VLFS} on P_{OWC}, η_{OWC} and inner air flow velocity *Umax*.is negligible for λ<3.0m while for λ>3.0m an increase of 70% for P_{OWC}, 40% for η_{OWC} and 20% for *Umax* is obtained a when L_{VLFS} is decreased from 5.60m to2.60m. This effect increases with increasing wave length λ.
- As for the fixed OWC, for each OWC geometry tested the Capture Width reaches the maximum for an optimal value of damping coefficient K_{opt}. Moreover, also in the case of floating OWC, the CW shows higher values for the irregular waves than for the regular waves.
- In order to assess the effect of the VLFS floating motion on the performance of the OWC, the identification of the most relevant parameters affecting the performance of the floating OWC provides useful data for the comparison with the results achieved in Phase I for the fixed OWC as well as in Phase II for the VLFS without any OWC incorporated.
- The comparative analysis of the results for fixed OWC and floating OWC incorporated in the two tested VLFS models (with lengths L_{VLFS}=2.60 & 5.60m) has to be performed on the six geometries selected from the results achieved for the fixed OWC: W1D1V1%, W1D1V2%, W2D1V1%, W2D1V2%, W3D1V1% and W3D1V2% under regular wave tests (H=0.04m & 1.22≤kh≤3.15) and irregular wave tests (0.02≤H_{m0}≤ 0.06m & 1.85 ≤kh≤ 2.68).

4.5 Summary and implications

The preliminary analysis of small-scale laboratory tests is performed for each of the following three phases: fixed OWC models (Phase I), VLFS models without incorporated OWC devices (Phase II) and floating OWC devices incorporated in VLFS models (Phase III) subject to regular and irregular waves in a constant water depth (h=0.50m).

The results achieved for each phase are used for the assessment of the effect of the motions of the VLFS on the OWC performance, providing the basis for the final data analysis in *Chapter 5.* Therefore, the key results and their implications for the final data analysis presented in *Chapter 5* are summarized as follows:

- From the tests of Phase I on fixed OWC models:
  - The front lip draught D significantly affects the natural frequency of each tested OWC model, i.e. the natural frequency decreases with larger draught D.
  - Within the range of tested wave conditions (kh=1.22-3.15 and H/L=0.013- 0.04), lip draught *D* significantly affects the processes inside the OWC chamber: decreasing *D* always implies an increase of η_{OWC}, P_{OWC} and Q_{OWC}.
  - For a given OWC geometry (i.e. for fixed values of front wall draught *D* and chamber width *W*) and for a relative water depth *kh*, it is possible to identify an optimal value of

the induced damping K_{opt} which maximizes the performance of the device, in terms of *Capture Width, CW*.

- For fixed D and K, a decrease of chamber width W leads to an increase of inner air pressure P_{OWC}.
- The relative water depth, kh, strongly affect the OWC performance, showing that P_{OWC} and Q_{OWC} increase for longer waves.
- Within the OWC geometries and wave conditions tested, higher CW values are observed for the irregular waves (CW_{max}=0.18m) than for regular waves (CW_{max}=0.15m).
- Laboratory tests show higher values of CW for the smallest front wall draught (D1) and vents (simulating the turbine damping) in a range between 1% and 2% of the top cover area (V1% and V2%). To restrict the number of tests for Phase III, the following OWC geometries are selected for the integration in VLFS: W1D1V1%, W1D1V2%, W2D1V1%, W2D1V2%, W3D1V1% and W3D1V2%.

- From the tests of Phase II on the VLFS models without OWC devices:
  - The relative VLFS length, $L^*=L_{VLFS}/\lambda$ has a significant on the floating behaviour of the VLFS.
  - The maximum heave motion (he_m) occurs always at the leading edge and shows a relevant dependence on the relative water depth, kh: decreasing kh (i.e. increasing wavelength) leads to increase the heave floating motion. Moreover, the relative heave amplitude $he^*= he_m/a_w$, is also affected by L^*, reaching a maximum value for L^*=0.65 and showing a totally damped behaviour for L^*>2.5.
  - The assessment of the VLFS behaviour, (i.e. heave motions) provides a reference case for the comparison with the results achieved in Phase III (VLFS-OWC model).

- From the tests of Phase III on the VLFS-OWC models:
  - As observed for the tests on fixed OWC also for the floating OWC (integrated in VLFS) it is possible to find an optimal value of K_{opt} which allow to reach the maximum CW for a particular OWC geometry.
  - The VLFS length and the relative water depth kh strongly affect the floating OWC *Capture Width*, *CW*. Within the range of tested waves and OWC geometry alternatives, an increase of the VLFS length L_{VLFS} induces an increasing of CW.

5 Empirical models predicting the heave motion of VLFS-OWC System and the performance of OWC integrated in a VLFS

This Chapter presents the dimensional analysis adopted to develop at first a formula predicting the floating behaviour (i.e. heave motion) of a VLFS-OWC System given: i) the wave parameters (T, H & h); ii) the OWC design parameters (chamber width, W and front wall draught, D); iii) the turbine damping (K) and iv) the length of the VLFS (L_{VLFS}).

Then a correction factor, *CF*, is proposed, to extend the incompressible Multi Regression Model of Simonetti et al. (2016) for the performance of fixed OWC in regular waves. As a result, a new formula for the prediction of the performance of floating OWC (integrated in VLFS) in real sea state, is obtained. Both prediction formulae might be used for the preliminary design and sizing of a VLFS-OWC System. These formulae allow the assessment of the heave motion of the VLFS-OWC System as well as the selection of the optimal OWC geometry, which ensure the best possible performance in a given installation site located in a moderated wave climate. The organization structure of *Chapter 5* is briefly summarized in Fig. 5.1.

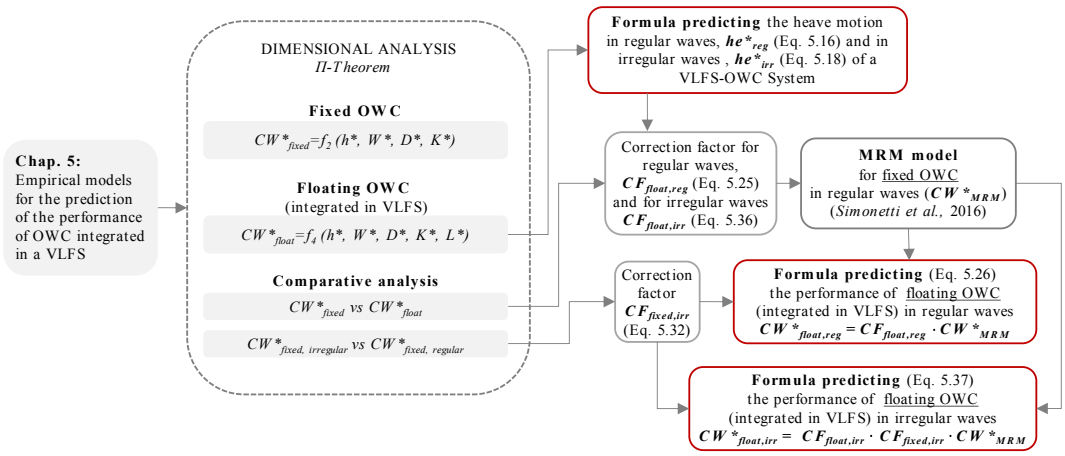

Fig. 5.1 - Organisation structure of Chapter 5.

5.1 Relative Capture Width of fixed OWC

The preliminary analysis on fixed OWC models in regular and irregular waves (see *section 4.2*) highlighted that, the pneumatic power output of the device, $\Pi_{OWCfixed}$, is remarkably influenced by the following independent dimensional variables:

- Sea state conditions:
  - incident wave height, H [m] or H_{m0} [m] (respectively for regular and irregular waves);
  - wave period, T [s] or T_p [s] (respectively for regular and irregular waves);
  - water depth, h [m].
- Design parameters of the OWC device:
  - chamber width, W [m];
  - front wall draught, D [m];
  - turbine damping coefficient, K [$kg^{1/2} \cdot m^{-7/2}$].
- Fluid properties:
  - water density, ρ_w [$kg \cdot m^{-3}$];
  - air density, ρ_a [$kg \cdot m^{-3}$].
- Gravitational acceleration:
  - g [$m \cdot s^{-2}$]

As a result, the pneumatic power output, $\Pi_{OWCfixed}$, can be described as a function of the aforementioned parameters as follows:

$$\Pi_{OWCfixed} = f_1(H, T, h, W, D, K, \rho_w, \rho_a, g) \tag{5.1}$$

To reduce the number of independent variables and to identify the length scales involved in the OWC performance, the *Π-theorem* is applied.

The independent characteristic wave parameters H, T (or H_{m0}, T_p) and ρ_a are selected as length scales (length, time and mass). As performed by (Simonetti 2016) for the numerical study of a fixed OWC in regular waves, the resulting six dimensionless parameters, as independent variables, are defined as follows:

(i) relative water depth, h^*:

$$h^* = k \cdot h \tag{5.2}$$

in which k and λ are obtained by the dispersion relation, with $k=2\pi/\lambda$ for regular waves and $k=2\pi/\lambda_p$ for irregular waves.

(ii) relative chamber width, W^*:

$$W^* = W/\lambda \quad (\text{or } W^* = W/\lambda_p) \tag{5.3}$$

with λ for regular waves and λ_p for irregular waves. The definition of W^* accounts for the strong effect of the wavelength and the chamber width on the OWC performance (particularly on the inner air pressure and the airflow rate).

(iii) relative front wall draught, D^*:

$$D^* = D\Big/\left(H \cdot \frac{\cosh k(h-D)}{\cosh(kh)}\right) \quad \left(\text{or } D^* = D\Big/\left(H_{m0} \cdot \frac{\cosh k(h-D)}{\cosh(kh)}\right)\right) \tag{5.4}$$

with H for regular waves and H_{m0} for irregular waves. The definition of D* accounts for the effect of incident wave H (or H_{m0}) and the attenuation of the wave-induced pressure at depth $h=D$ beneath S.W.L., according to Airy wave theory.

(iv) relative damping induced by the air turbine, K^*:

$$K^* = K \cdot B \cdot W/{\rho_a}^{1/2} \tag{5.5}$$

including the effect of chamber width W for a given chamber length B, transversal to wave direction, (with B=0.20m for the model tests in this study) and air density ρ_a, on the OWC response to different induced damping, K.

(v) relative water density, ρ_w*:

$$\rho_w{}^* = \rho_w/\rho_a \tag{5.6}$$

(vi) relative gravitational acceleration, g*:

$$g^* = g \cdot T^2/H \ \ (\text{or} \ \ g^* = g \cdot T_p{}^2/H_{m0}) \tag{5.7}$$

with H and T for regular waves and H_{m0} and T_p for irregular waves.

The *Relative Capture Width*, CW^*, is obtained by normalizing the *Capture Width* CW (as defined in Eq. 4.13) by the OWC chamber length, B:

$$CW^* = CW/B \tag{5.8}$$

The sensitivity of CW^* to $\rho_w{}^*$ and g^*, is assumed to be negligible with respect to the other aforementioned parameters, since the small range of variation in practical applications.

Based on the dimensionless parameters defined in Eqs. 5.2-5.7, the *relative Capture Width* for fixed OWC, CW^*_{fixed}, can be expressed as follows:

$$CW^*{}_{fixed} = f_2(h^*, W^*, D^*, K^*) \tag{5.9}$$

5.1.1 Relative Capture Width of fixed OWC in regular waves

The relation between relative chamber width $W^*=W/\lambda$ and *relative Capture Width* of fixed OWC in regular waves, $CW^*_{fixed,reg}$ (H=0.04m & kh=1.22-3.15), confirmed that the front wall draught, D has a significant influence on the OWC performance (Fig. 5.2).

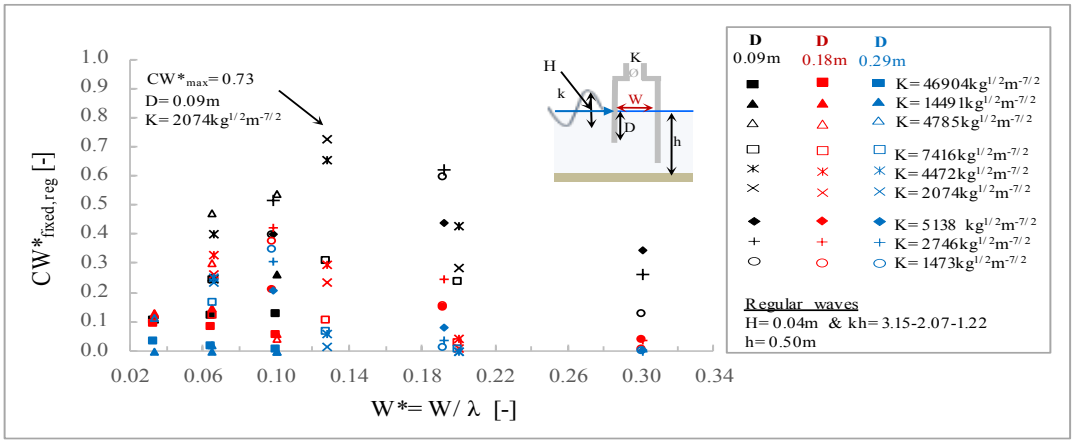

Fig. 5.2 - Relative Capture Width, $CW^*_{fixed,reg}$, versus relative chamber width W*=W/λ, for each fixed OWC model subject to regular waves (H=0.04m & kh=1.22-3.15, with $k=2\pi/\lambda$).

For given values of chamber width W and damping coefficient K, generally the smallest front wall draught ($D1$=0.09m) leads to the highest values of $CW^*_{fixed,reg}$ for all tested regular waves. However, it is worth to note that both K and W/λ also play an important role on OWC. The maximum performance of the OWC, CW^*_{max}=0.73, is rather achieved with the lower damping coefficient, K=2074kg$^{1/2}$m$^{-7/2}$ and relative chamber width, W^*=0.13 (OWC geometry W2D1V2%). For the medium and the longest front wall draught, respectively $D2$=0.18m and $D3$=0.29m, the maximum performance of the OWC is much lower than for D1 (CW^*_{max}=0.42 for $D2$, and CW^*_{max}=0.34 for $D3$) and is obtained for W^*=0.10.

Within the range of waves tested (H=0.04m & kh=1.22-3.15), $CW^*_{fixed,reg}$ decreases with increasing the relative front wall draught, D^*. The maximum performance, CW^*_{max}=0.73, is achieved when D^*=3.21, W=0.20m, K=2074kg$^{1/2}$m$^{-7/2}$ and the wave has H=0.04m and T=1.0s (kh=2.07) (Fig. 5.3). Moreover, it is possible to confirm that, for given values of $D^*$the performance

of the OWC device, $CW^*_{fixed,reg}$ is strongly influenced by the turbine damping, K and the frequency of the incident wave.

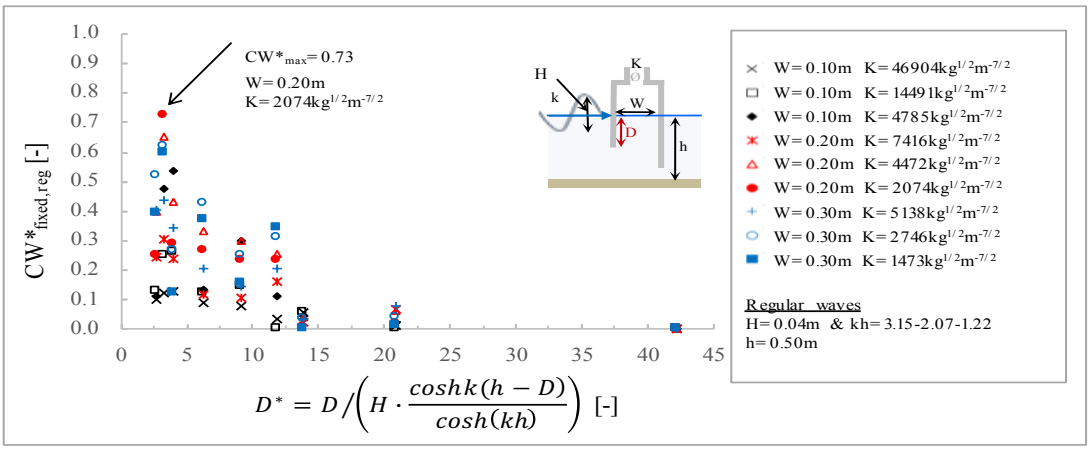

Fig. 5.3 - Relative Capture Width, $CW^*_{fixed,reg}$, versus relative front wall draught, D^*, for each fixed OWC model subject to regular waves (H=0.04m & kh=1.22-3.15, with $k=2\pi/\lambda$).

5.1.2 Relative Capture Width of Fixed OWC in irregular waves

As for regular wave tests (Fig. 5.2), for given chamber width W and damping coefficient K, also in irregular waves (H_{m0}=0.02-0.04m & kh=1.85-2.68) the highest performance of fixed OWC, $CW^*_{fixed,irr}$, is achieved with the smallest front wall draught ($D1$=0.09m) (Fig. 5.4).

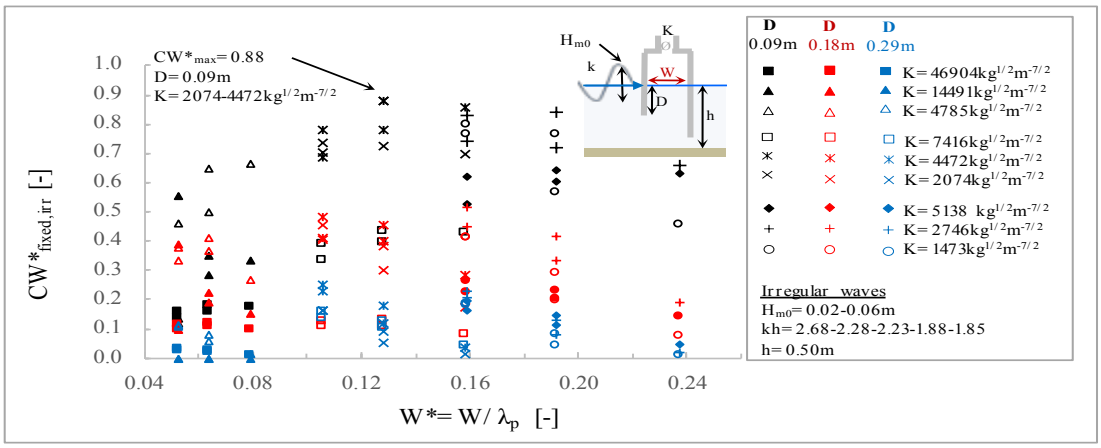

Fig. 5.4 - Relative Capture Width, $CW^*_{fixed,irr}$, versus relative chamber width $W^*=W/\lambda_p$, for each fixed OWC model subject to irregular waves (H_{m0}=0.02-0.04m & kh=1.85-2.68, with $k=2\pi/\lambda_p$).

The maximum relative capture width of fixed OWC in irregular waves, CW^*_{max}=0.88, (CW^*_{max}=0.73 in regular waves), is achieved for relative chamber width W^*=0.13 and damping coefficients K=2074 & 4472kg$^{1/2}$·m$^{-7/2}$, (OWC geometries W2D1V1% & W2D1V2%).

The medium and longest front wall draughts, $D2$=0.18m and $D3$=0.29m, result in much lower performance of the OWC converter (CW^*_{max}=0.52 for $D2$ and W^*=0.16, CW^*_{max}=0.25 for $D3$ and W^*=0.11).

The decreasing trend of $CW^*_{fixed,irr}$ with increasing relative front wall draught, D^*, is confirmed within the range of irregular waves tested (H_{m0}=0.02-0.04m & kh=1.85-2.68) (Fig. 5.5), with CW^*_{max} achieved when D^*=3.49, W=0.20m, damping coefficients K=2074 & 4472kg$^{1/2}$m$^{-7/2}$ and for incident waves having H_{m0}=0.04m and T_p=1.0s (kh=2.23).

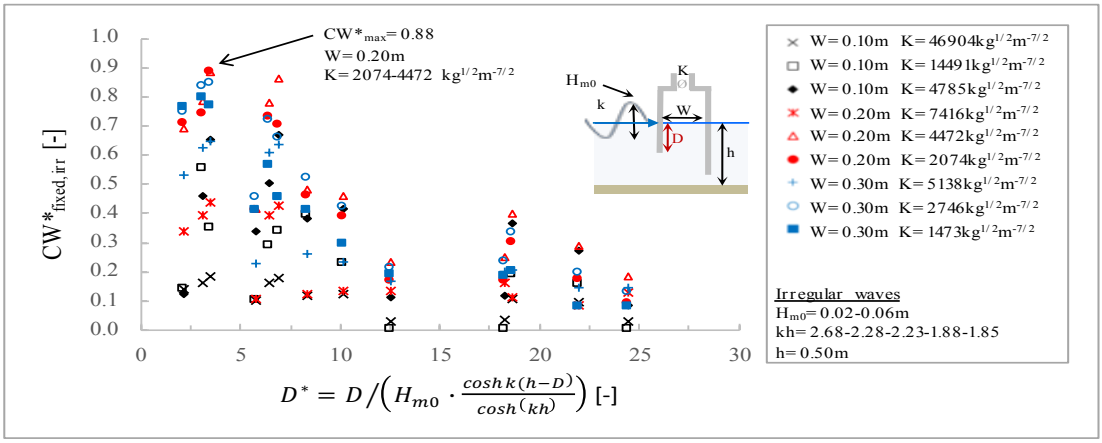

Fig. 5.5 - Relative Capture Width, $CW^*_{fixed,irr}$, versus relative front wall draught, D^*, for each fixed OWC model subject to irregular waves (H_{m0}=0.02-0.04m & kh=1.85-2.68, with $k=2\pi/\lambda_p$).

For given chamber width W and damping coefficient K, the highest performance of fixed OWC (CW^*_{fixed}) are obtained with the smallest front wall draught (D1=0.09m) in both wave conditions tested, regular and irregular.
For the regular wave tests, the performance of the OWC device reaches its maximum, CW^*_{max}=0.73, with lower damping coefficient K=2074kg$^{1/2}$m$^{7/2}$, relative chamber width W=0.13 and relative front wall D*=3.21 (OWC model W2D1V2% with H=0.04m T=1.0s). Based on the experimental results, Simonetti, (2016) performed a numerical model investigating an higher resolution of OWC design parameters (i.e., W, D and K with values closer to those that achieved CW^*_{max} during the tests), demonstrating that a proper design of the device could give performance 10% higher (CW^*_{max}=0.83).*
As for the irregular wave tests, CW^*_{max}=0.88 is achieved for damping coefficients K=2074 & 4472kg$^{1/2}$m$^{-7/2}$, for relative chamber width W=0.13 and relative front wall draught D*=3.49 (OWC models W2D1V1% & W2D1V2% subject to H_{m0}=0.04m and T_p=1.0s).*
The different performance achieved in regular and irregular waves, might be interpreted considering that the same OWC geometry is subject to a not comparable incident wave power, Π_w, [W/m], respectively for regular and irregular waves. As described in more detail in subsection 5.8.1, the compare have wave trains energetically, it is necessary to replace the irregular waves by single sinusoidal waves with height $H=H_{rms}$ and period $T=T_e$ obtained from the wave energy spectrum. Moreover, as the natural resonance of the OWC is mostly influenced by the incident wave frequency, it is worth to note that due to the different concentration of energy: i) in a single frequency for regular waves, and ii) in many different frequency components for irregular waves, the OWC resonance under irregular waves could be reached more easily.

5.2 Relative heave motion of a VLFS-OWC System

The preliminary analysis on VLFS models (Phase II of tests) and VLFS-OWC models (Phase III of tests) in regular and irregular waves (see *sections 4.3 and 4.4*) highlighted that, the floating motion in heave direction of the VLFS-OWC System is strongly influenced by the following independent dimensional variables:

- Sea state conditions:

- incident wave height, H [m] or H_{m0} [m] (respectively for regular and irregular waves);
- wave period, T [s] or T_p [s] (respectively for regular and irregular waves);
- water depth, h [m].

- Design parameters of the OWC device:

- chamber width, W [m];
- front wall draught, D [m];
- turbine damping coefficient, K [kg$^{1/2}$·m$^{-7/2}$].

- Design parameters of the VLFS:
  - length, L_{VLFS} [m];
- Fluid properties:
  - water density, ρ_w [kg·m^{-3}];
  - air density, ρ_a [kg·m^{-3}].
- Gravitational acceleration:
  - g [m·s^{-2}].

As a result, the heave motion amplitude, he can be defined as a function of the aforementioned parameters as follows:

$$he = f_2(H, T, h, W, D, K, L_{VLFS}, \rho_w, \rho_a, g) \tag{5.10}$$

By means of the *Π-theorem*, the number of independent variables is reduced and the length scales involved in the heave motion of the floating system, are identified.

As for the dimensional analysis performed for the performance of fixed OWC, (*see section 5.1*) the independent characteristic wave parameters H, T (or H_{m0}, T_p) are selected as length scales (length and time). In addition to the resulting dimensionless parameters seen before (i.e. relative water depth, h^*, relative chamber width, W^*, relative front wall draught, D* and relative turbine damping, K^*), the relative VLFS length is defined as:

$$L^* = L_{VLFS}/\lambda \quad (\text{or } L^* = L_{VLFS}/\lambda_p) \tag{5.11}$$

with λ for regular waves and λ_p for irregular waves.

The *relative heave motion*, he^*, is obtained by normalizing the heave motion amplitude, he by the amplitude of the incident wave, a_w:

$$he^* = he/a_w \tag{5.12}$$

where a_w=0.5H, is the amplitude of the regular incident wave and a_w=0.5H_{m0} is the amplitude of the irregular incident wave.

Based on the dimensionless parameters, defined in Eqs. 5.2-5.11, the *relative heave motion he**, can be expressed as follows:

$$he^* = f_3(h^*, W^*, D^*, K^*, L^*) \tag{5.13}$$

5.2.1 Relative heave motion of VLFS-OWC System in regular waves

As observed for the VLFS model without OWC devices (Phase II), the relative VLFS length, L^*, strongly affects the relative heave motion, he^* (see *subsection 4.3.5*). Concerning the tests on the VLFS-OWC models (Phase III), it is possible to note that an increase of L^*, generally leads to a decrease of the relative heave motion, he^* (Fig. 5.6).

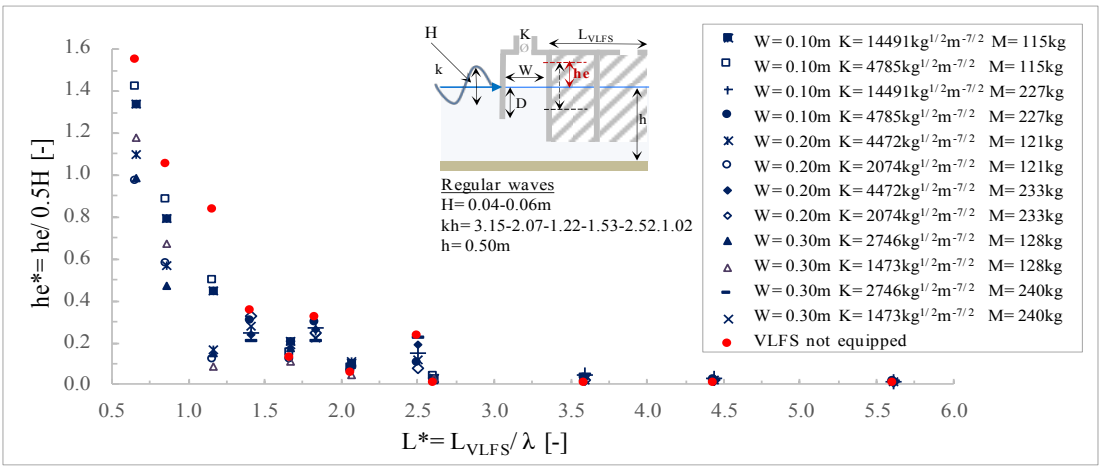

Fig. 5.6 - Relative heave motion, he^*, versus relative VLFS length $L^*=L_{VLFS}/\lambda$. Heave is measured at the leading edge, where the OWC is integrated. Results are related to the VLFS-OWC model subject to regular waves (H=0.04-0.06m & kh=1.02-3.15, with $k=2\pi/\lambda$).

Within the tested range of design parameters of the VLFS-OWC system (W, D, K and L_{VLFS}) in regular waves (H=0.04-0.06m & kh=1.02-3.15), the relative heave motion reaches the maximum, he^*_{max}=1.4 (he^*_{max}=1.6 for VLFS models without OWCs) for L^*=0.65 and is totally damped for L^*>2.5.

However, the relation between he^* and L^* indicates an important variation of the heave motion for lower values of L^* (0.65<L^*<2.5), within the range of variation of the design parameters of the integrated OWC (i.e. W=0.10-0.30m & K=1473-14491kg$^{1/2}$m$^{-7/2}$) and therefore within the range of variation of the inertia of the VLFS-OWC (i.e. $M_{VLFS\text{-}OWC}$=115-240kg).

In particular, for a given L^* in the range 0.65<L^*<2.5, it is possible to observe generally that an increase of induced damping, K, and chamber width, W, which in turn imply an increase of the inertia of the floating system leads to a decrease of he^*.

5.2.2 Relative heave motion of VLFS-OWC System in irregular waves

The relative heave motion he^* in irregular waves, could be considered approximately damped, with a maximum value he^*_{max}=0.25 (i.e., $he=a_w/4$) when $L^*=1.38$. As observed for the regular waves (Fig. 5.6), the decreasing trend of he^* with increasing L^*, is confirmed (Fig. 5.7).

Moreover, for fixed L^*, the dimensionless heave motion he^* shows a high variation, mainly due to the different inertia of the OWC-VLFS (i.e., different masses resulting from the different OWC geometries integrated).

Unlike in the regular wave tests (Fig. 5.6), the integration of OWC in the VLFS results in a slight increase of he^* as compared to that achieved for VLFS models without OWCs (he^*_{max}=0.11 for VLFS models without OWCs).

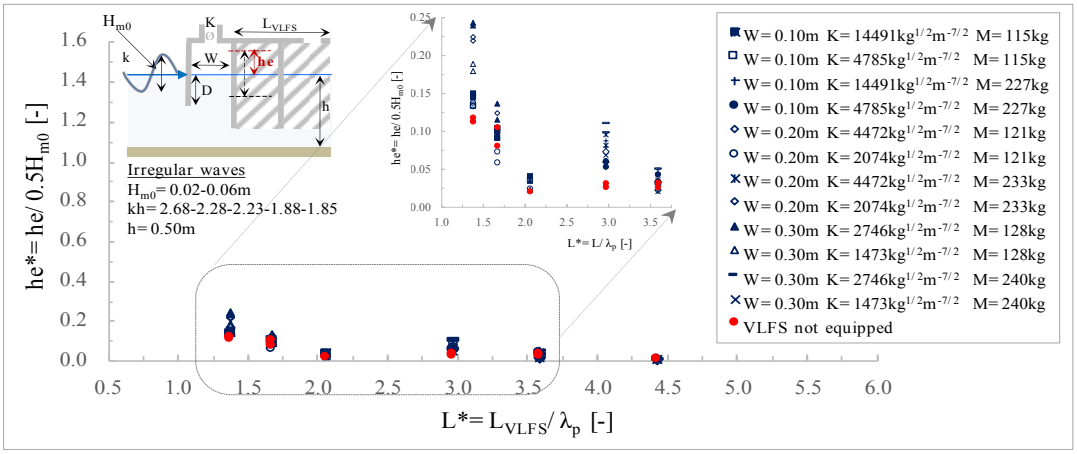

Fig. 5.7 - Relative heave motion, he^*, versus relative VLFS length L^*. Heave measured at the leading edge, where the OWC is integrated. Results related to the VLFS-OWC model subject to irregular waves (H_{m0}=0.02-0.06m & kh=1.85-2.68., with k=2π/λ_p).

Within the range of regular waves (H=0.04m & kh=1.22-3.15), he shows its maximum, he^*_{max}=1.4 for L*=0.65 and is totally damped for L*>2.5. Although, for the range of irregular waves (H_{m0}=0.02-0.04m & kh=1.85-2.68), he* is always lower than 0.25, it is worth to note that as observed for the regular waves, increasing L* leads to a decrease of he*.*

5.3 Relative Capture Width of floating OWCs (integrated in a VLFS)

The results achieved in the preliminary analysis on floating OWC models (integrated in a VLFS), (see *section 4.4*), highlighted that, in addition to independent dimensional variables presented before for fixed OWC (see *section 5.1*), the pneumatic power output, $\Pi_{OWC\text{-}float}$ is strongly influenced by the length of the Very Large Floating Structure, L_{VLFS} [m].

As a result, the pneumatic power output $\Pi_{OWCfloat}$, can be described as:

$$\Pi_{OWCfloat} = f_4(H, T, h, W, D, K, L_{VLFS}, \rho_w, \rho_a, g, \ldots^{14}) \quad (5.14)$$

Concerning the relevant sensitivity on the *relative Capture Width* for floating OWC, CW^*_{float} and applying the *Π-theorem*, and the dimensionless parameters defined in Eqs. 5.2 - 5.11, the *relative Capture Width* of floating OWC (integrated in a VLFS), CW^*_{float}, can be expressed as:

$$CW^*_{float} = f_5(h^*, W^*, D^*, K^*, L^*) \quad (5.15)$$

5.3.1 Relative Capture Width of floating OWC in regular waves

As for fixed OWC in regular waves and irregular waves (Fig. 5.2 and Fig. 5.4), $CW^*_{float,reg}$ is analyzed as a function of relative chamber width $W^*=W/\lambda$ for the six most performant OWC alternatives selected from Phase I for integration in both tested VLFS lengths L_{VLFS}= 2.60m & 5.60m and subject to the same regular waves (H=0.04m & kh=1.22-3.15) (Fig. 5.8).

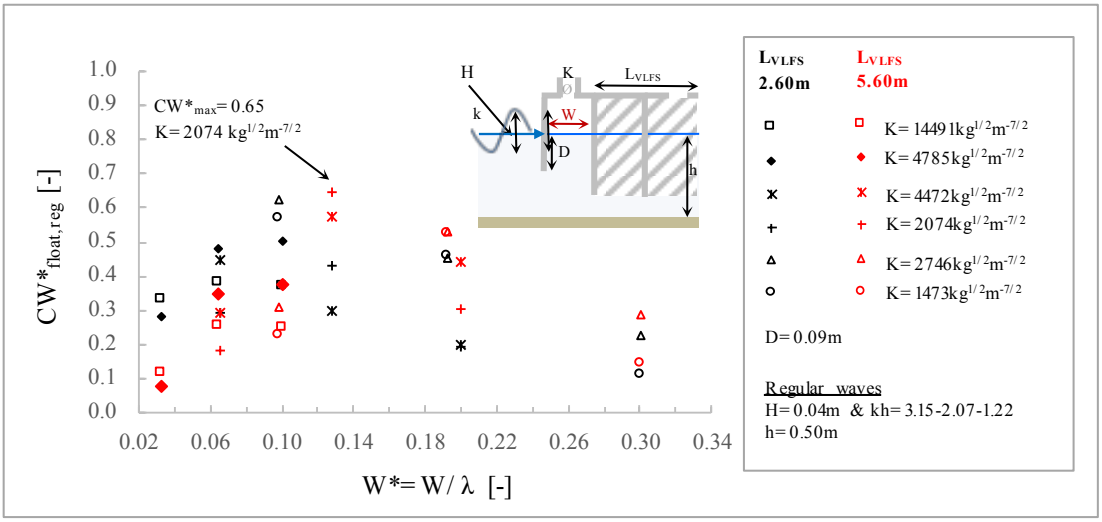

Fig. 5.8 - Relative Capture Width, $CW^*_{float,reg}$, versus relative chamber width W*= W/λ, for each OWC model integrated in the VLFS (LVLFS=2.60m & 5.60m) subject to regular waves (H=0.04m & kh=1.22-3.15, with k=2π/λ).

In particular, the six OWC models selected for the VLFS have the same front wall draught (i.e., the smallest $D1$=0.09m), different chamber widths (W=0.10m-0.30m) and different vent areas simulating different damping coefficients, K ($V1\%$ and $V2\%$).

The comparative analysis aimed to highlight the significant effects of VLFS length L_{VLFS}, damping coefficient K and relative chamber width W^* on $CW^*_{float,reg}$.

Within the range of regular waves tested, $CW^*_{float,reg}$ shows higher values for the shorter VLFS when W/λ=0.03-0.10 (i.e., black markers in Fig. 5.8). However, for W/λ>0.10 an increase of L_{VLFS} leads to higher $CW^*_{float,reg}$ (i.e., red markers in Fig. 5.8). The maximum $CW^*_{float,reg}$ occurs when W/λ=0.13 ($CW^*_{float,reg\,max}$=0.65 for H=0.04m & kh=2.07 and OWC model W2D1V2%).

The relation between $CW^*_{float,reg}$ versus relative VLFS length $L^*=L_{VLFS}/\lambda$ confirms the effect of the VLFS length, for each OWC geometry and induced damping, K (Fig. 5.9).

[14] It is worth to note that, the pneumatic power output of OWCs integrated in VLFS, could be influenced by other independent dimensional variables, such as the mass of the VLFS or the geometry of each VLFS unit (i.e. the height). However, for this study the parameter which plays a relevant role in the wave energy conversion is just the length of the VLFS.

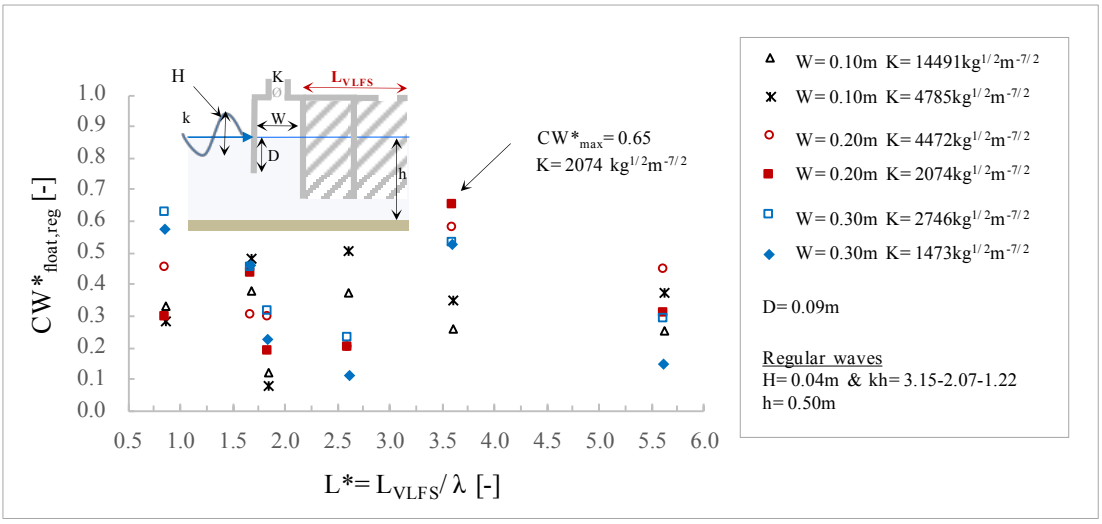

Fig. 5.9 - Relative Capture Width, $CW^*_{float,reg}$, versus relative VLFS length $L^*=L_{VLFS}/\lambda$, for each OWC model integrated in the VLFS subject to regular waves (H=0.04m & kh=1.22-3.15, with k=2π/λ).

Within the range of regular waves tested (H=0.04m & kh=1.22-3.15), the maximum performance ($CW^*_{float,reg\ max}$=0.65) occurs when, L^*=3.6 for a damping coefficient K=2746kg$^{1/2}$m$^{-7/2}$ and for chamber width W=0.20m. Moreover, for given L^*, the high variation of $CW^*_{float,reg}$ is due to the significant effect of K and W.

Analysing $CW^*_{float,reg}$ versus the relative heave motion evaluated at the point closer to the leading edge (i.e. where the OWC is integrated) and normalized by the incident wave amplitude, $he^*=he/a_w$, it is possible to highlight its relevant effect on the performance of the OWC integrated (Fig. 5.10).

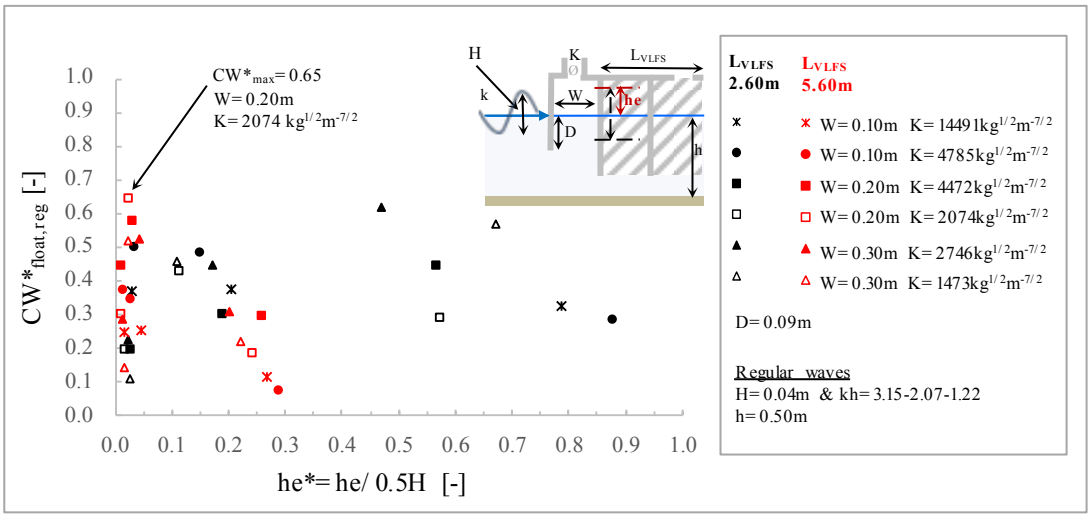

Fig. 5.10 - Relative Capture Width, $CW^*_{float,reg}$, versus relative heave motion $he^*=he/a_w$ (with a_w=0.5H) for each OWC model integrated in the VLFS subject to regular waves (H=0.04m & kh=1.22-3.15 with k=2π/λ).

For all tested alternatives integrated in the longer VLFS (red markers in Fig. 5.10) $CW^*_{float,reg}$ shows an increase for he^*=0.01 to 0.023 where the maximum value $CW^*_{float,reg\ max}$=0.65 is reached for the OWC chamber width W=0.20m and damping coefficient K=2074kg$^{1/2}$m$^{-7/2}$. For higher values, he^*>0.023, $CW^*_{float,reg}$ decreases to $CW^*_{float,reg\ min}$=0.08 for chamber width W=0.10m and damping coefficient K=4785kg$^{1/2}$m$^{-7/2}$.

Also for the shorter VLFS (black markers in Fig. 5.10) $CW^*_{float,reg}$ increases for lower values he^*<0.023, whereas for he^*=0.023 to 0.2, $CW^*_{float,reg}$ has a lower rate of decrease, than that observed for the longer VLFS.

Moreover, for the shorter VLFS, when he^*>0.2, it is possible to note that $CW^*_{float,reg}$ is strongly influenced by W and K. In particular, $CW^*_{float,reg}$ increases for W=0.20m & K=4472kg$^{1/2}$m$^{-7/2}$ and W=0.30m & K=1473-2746kg$^{1/2}$m$^{-7/2}$ and decreases for W=0.10m & K=4785kg$^{1/2}$m$^{-7/2}$ and W=0.20m & K=2074kg$^{1/2}$m$^{-7/2}$.

For given values of he^*, the influence of chamber width W and damping coefficient K on relative capture width $CW^*_{float,reg}$ is confirmed.

It has to be noted that, the integration of different OWC geometries in the two VLFS lengths imply a different mass of the OWC-VLFS model and therefore a different inertia, which significantly affect the floating response of the overall the system (i.e. the heave motion amplitude, *he*).

5.3.2 Relative Capture Width of floating OWC in irregular waves

Concerning the irregular waves (H_{m0}=0.02-0.04m & kh=1.85-2.68, with $k=2\pi/\lambda_p$), the relative capture width of floating OWC, $CW^*_{float,irr}$, obtained for all the OWC alternatives integrated in the VLFS model with both lengths L_{VLFS}= 2.60m & 5.60m, highlights the important effect of relative VLFS length L^* and damping coefficient K (Fig. 5.11).

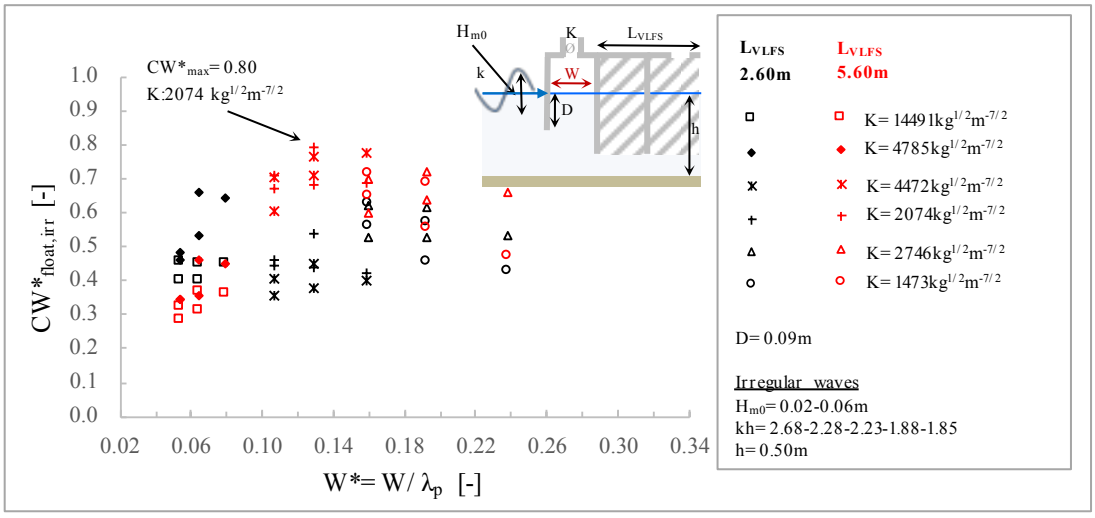

Fig. 5.11 - Relative Capture Width, $CW^*_{float,irr}$, versus relative chamber width $W^*= W/\lambda_p$, for each OWC model integrated in the VLFS (L_{VLFS}=2.60m & 5.60m) subject to irregular waves (H_{m0}=0.02-0.04m & kh=1.85-2.68, with k=2π/λ_p).

Considering the shorter VLFS (i.e., black markers in Fig. 5.11), the relative capture width reaches its maximum $CW^*_{float,irr\ max}=0.66$ for W/λ=0.06. For comparison, under regular waves (i.e., black markers in Fig. 5.8), the OWC in the shorter VLFS reaches its maximum performance, $CW^*_{float,reg\ max}=0.62$ for W/λ=0.10).

However, for W/λ>0.10 an increase of the VLFS length L_{VLFS} from 2.60m to 5.60m leads to an increase of the performance of the integrated OWC (i.e., red markers in Fig. 5.11), which reaches its maximum, $CW^*_{float,irr\ max}$=0.80 for W^*=0.13 of the integrated W2D1V2% under irregular waves with H_{m0}=0.04m & kh=2.23. For the same OWC-VLFS model under regular waves with H=0.04m & kh=2.07(i.e., red markers in Fig. 5.8), $CW^*_{float,reg\ max}$=0.65.

Within the range of irregular waves tested (H_{m0}=0.02-0.04m & kh=1.85-2.68), the maximum performance of the OWC integrated ($CW^*_{float,irr\ max}$=0.80) occurs when L^*=3.6, the chamber width W=0.20m and the damping coefficient K=2074kg$^{1/2}$m$^{-7/2}$ (Fig. 5.12).

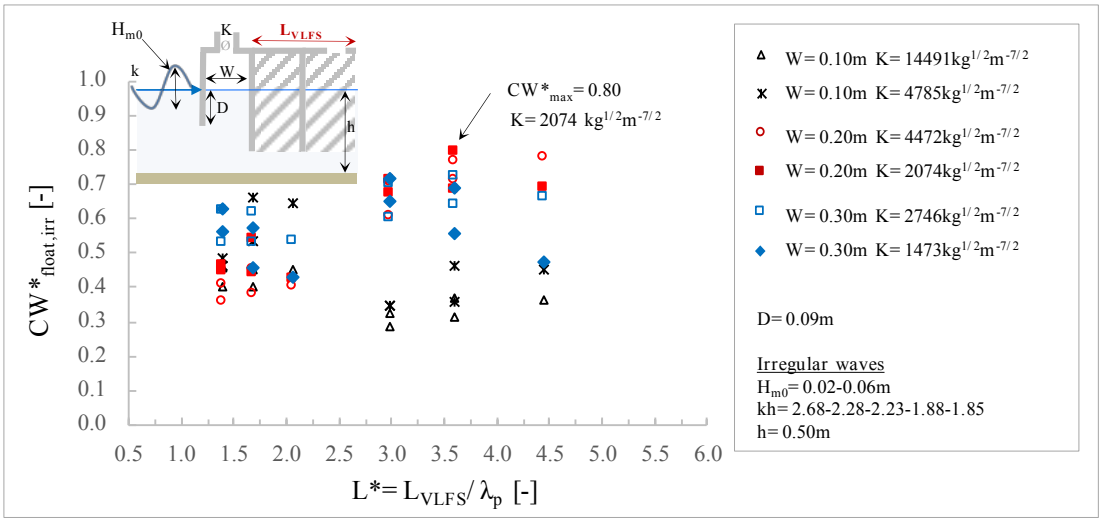

Fig. 5.12 - Relative Capture Width, $CW^*_{float,irr}$, versus relative VLFS length $L^*=L_{VLFS}/\lambda_p$, for each OWC model integrated in the VLFS subject to irregular waves (H_{m0}=0.02-0.04m & kh=1.85-2.68, with $k=2\pi/\lambda_p$).

Concerning the effect of the relative heave motion he^* obtained for each VLFS-OWC model under irregular waves (H_{m0}=0.02-0.04m & kh=1.85-2.68), a slight influence on the relative capture width $CW^*_{float,irr}$ of the OWC integrated in the VLFS models for both lengths L_{VLFS}= 2.60m & 5.60m is observed in Fig. 5.13.

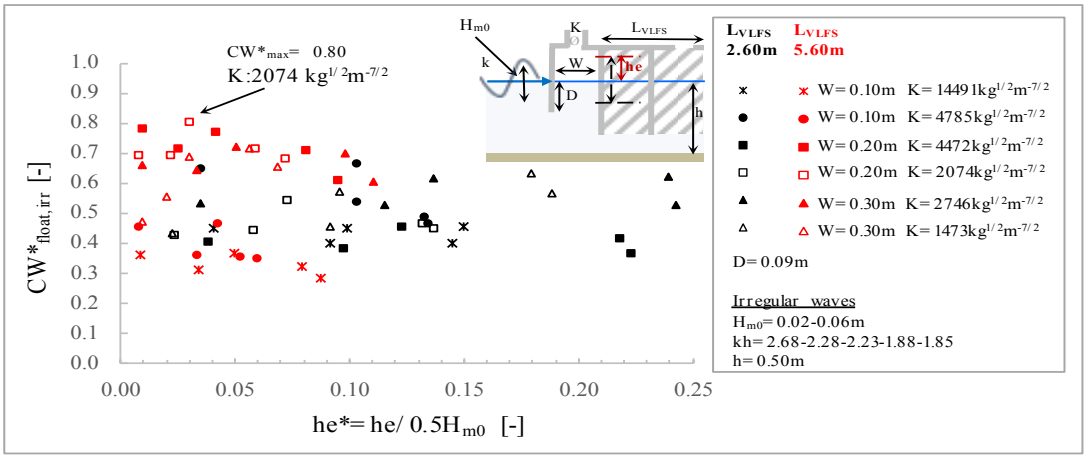

Fig. 5.13 - Relative Capture Width $CW^*_{float,irr}$ versus relative heave motion $he^*=he/aw$ for each OWC model integrated in the VLFS subject to irregular waves (H_{m0}=0.02-0.04m & kh=1.85-2.68, with $k=2\pi/\lambda_p$).

The longer VLFS (red markers in Fig. 5.13) with a given geometry of OWC integrated, results in a slow variation of $CW^*_{float,irr}$ with increasing he^*, except for the OWC geometries W2D1V1% (W=0.20m & K=4472kg$^{1/2}$m$^{-7/2}$) and W1D1V2% (W=0.10m & K=4785kg$^{1/2}$m$^{-7/2}$), which show a decrease of $CW^*_{float,irr}$ of about 20% when he^* increases from 0.01 to 0.10 for W2D1V1% and from 0.01 to 0.07 for W1D1V2%.

The shorter VLFS (black markers in Fig. 5.13) shows a lower rate of decrease of $CW^*_{float,irr}$ with increasing he^*, except for the OWC geometry W1D1V2% (K=4785kg$^{1/2}$m$^{-7/2}$ & W=0.10m), in which $CW^*_{float,irr}$ decreases by about 20% for he^*=0.04 to 0.14. However, among the OWC alternatives, only the geometry W3D1V2% (W=0.30m & K=1473kg$^{1/2}$m$^{-7/2}$), shows an increase of $CW^*_{float,irr}$ of about 20% with increasing he^* from 0.02 to 0.19.

For the regular or irregular waves tested, the performance of floating OWC (integrated in a VLFS), CW^*_{float}, is significantly affected by the damping coefficient, K, the chamber width, W and the VLFS length, L_{VLFS} (which in turn influenced the heave motion, he).
Within the range of tested regular waves, $CW^*_{float,reg}$ reaches the maximum value $CW^*_{float,reg\ max}$=0.65 when L=3.6, K=2746kg$^{1/2}$m$^{-7/2}$, W=0.20m and he*=0.02 (with H=0.04m & kh=2.07 for the OWC alternativeW2D1V2%). For the tested irregular waves, $CW^*_{float,irr}$ reaches its maximum, $CW^*_{float,irr\ max}$=0.80 when L*=3.6, K=2074kg$^{1/2}$m$^{-7/2}$, W*=0.13 and he*=0.03 (with H_{m0}=0.04m & kh=2.23 for the OWC alternative W2D1V2%).*
As for fixed OWC also the integrated OWC models show a different response (in terms of Capture Width), in regular and irregular incident waves. However, as stated for fixed OWC, this different performance is due to the incident wave power of the two types of wave trains which are not comparable (see Table 4-2 and Table 5-5).
Comparing the maximum performance of fixed and floating OWC under the same regular waves ($CW^*_{fixed,reg\ max}$=0.73 & $CW^*_{float,reg\ max}$=0.65) and irregular waves ($CW^*_{fixed,irr\ max}$=0.88 & $CW^*_{float,irr\ max}$=0.80), it is possible to note that the integration in VLFS leads to a decrease of about 8% of the maximum performance. This decrease of CW^*_{max}, could be physically interpreted, considering that the frequency of the heave motion of the VLFS-OWC could interact with the natural resonance frequency of the OWC integrated (in this case W2D1V2%).

5.4 Comparative analysis of fixed OWC vs floating OWC (integrated in VLFS) under regular waves

The relative capture width assessed for fixed OWC in regular waves ($CW^*_{fixed,reg}$) and the same OWC incorporated in a VLFS ($CW^*_{float,reg}$), are analysed by comparing the results achieved in the small-scale tests, respectively in Phase I (*subsection 4.2.5*) and Phase III (*subsection 4.4.5*) and by evaluating the ratio $CW^*_{float}/CW^*_{fixed}$. Both models are analysed within the range of dimensionless parameters considered for regular wave conditions, OWC, VLFS and VLFS-OWC System, reported in Table 5-1.

Table 5-1: Range of non-dimensional parameters considered for the comparison between relative capture width assessed for fixed OWC and floating OWC in regular waves (H, T).

DESCRIPTION	DEFINITION	RANGE
Relative water depth	$h^* = k \cdot h$ (with k=2π/λ)	1.22<h^*<3.15
Relative OWC chamber width	$W^* = W/\lambda$	0.03<W^*<0.30
Relative OWC front wall draught	$D^* = D/\left(H \cdot \frac{\cosh k(h-D)}{\cosh(kh)}\right)$ (with k=2π/λ)	3.01<D^*<3.98
Relative turbine damping	$K^* = K \cdot B \cdot W/\rho_a{}^{1/2}$	82.95<K^*<289.83
Relative VLFS length	$L^* = L_{VLFS}/\lambda$	0.85<L^*<5.60

Despite the relatively low determination coefficient (R^2=0.70), the experimental results demonstrate the effect of the relative heave motion *he** on the ratio $CW^*_{float,reg}/CW^*_{fixed,reg}$ (Fig. 5.14).

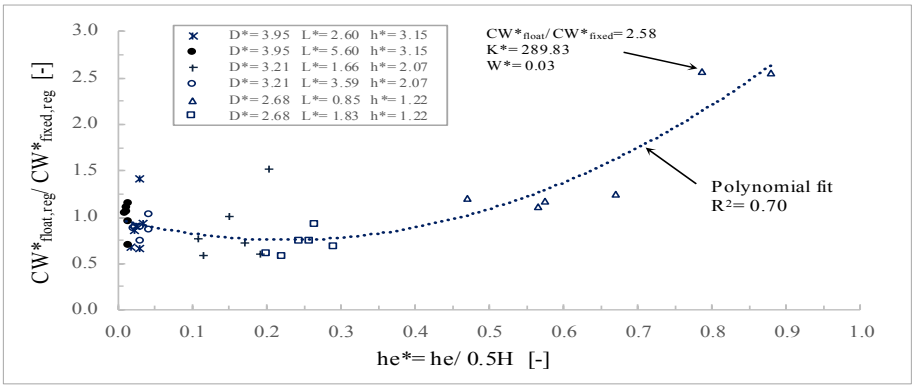

Fig. 5.14 - Comparison between $CW^*_{float,reg}$ and $CW^*_{fixed,reg}$ versus relative heave motion *he** for all the design alternatives tested for fixed OWC and VLFS-OWC models subject to regular waves (H=0.04m & kh=1.22-3.15, with $k=2\pi/\lambda$).

As expected, $CW^*_{float,reg}/CW^*_{fixed,reg}=1$ for a relative heave $he^*=0$, which corresponds to the same OWC under fixed conditions (Fig. 5.14). Moreover, $CW^*_{float,reg}/CW^*_{fixed,reg}$ slightly decreases for $0<he^*<0.3$, and then increases at a growing rate for larger heave motion $he^*>0.3$, reaching values of more than 2.5 for heave motions in the order of incident wave amplitude a_w (i.e. for $he^*=0.79$). However, the relatively low determination coefficient ($R^2=0.70$) for the relation between performance ratio $CW^*_{float,reg}/CW^*_{fixed,reg}$ and relative heave motion he^* in Fig. 5.14 suggests that relative heave $he^*$is not the sole parameter affecting the ratio $CW^*_{float,reg}/CW^*_{fixed,reg}$.

Analysing $CW^*_{float,reg}/CW^*_{fixed,reg}$ versus L^* for all design alternatives tested in both Phase I (fixed OWC) and Phase III (OWC integrated in VLFS) in Fig. 5.15, a decreasing trend of the ratio $CW^*_{float,reg}/CW^*_{fixed,reg}$ to a value around 1 is observed for larger relative VLFS lengths L^*. This decreasing trend might be interpreted as follows: when the length of the VLFS is infinitely long, the heave motion is totally damped (see Fig. 5.6) and the same relative capture width CW^* is obtained for both fixed and floating OWC. The highest value of $CW^*_{float,reg}/CW^*_{fixed,reg}=2.58$ is achieved for $L^*=0.85$, $D^*=3.01$, $W^*=0.03$, $h^*=1.22$ and the applied relative damping $K^*=289.83$.

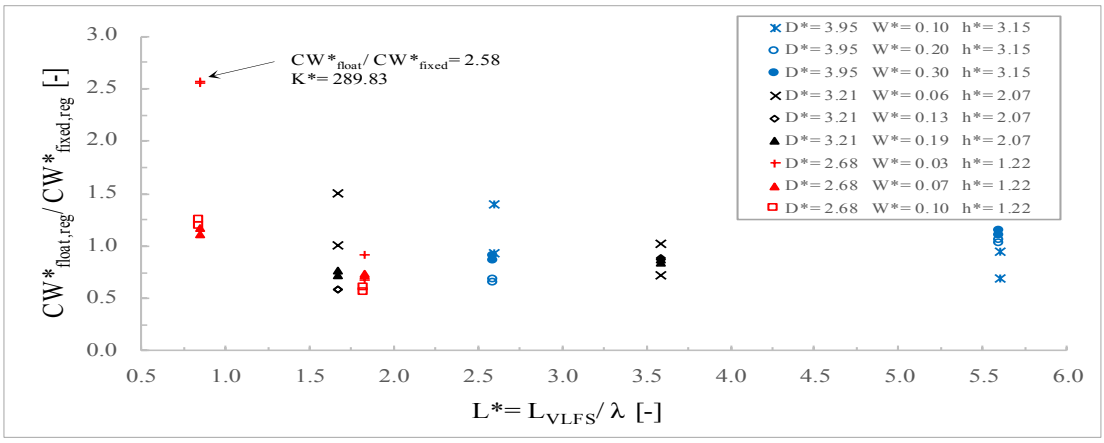

Fig. 5.15 - Comparison between $CW^*_{float,reg}$ and $CW^*_{fixed,reg}$ versus relative VLFS length L^* for all design alternatives tested for fixed OWC and VLFS-OWC models subject to regular waves (H=0.04m & kh=1.22-3.15, with k=2π/λ).

For the ratio $CW^*_{float,reg}/CW^*_{fixed,reg}$ versus relative chamber width W^* in Fig. 5.16, it is shown that an infinite increase of W^*leads to a decreasing trend of the performance ratio to a unit value.

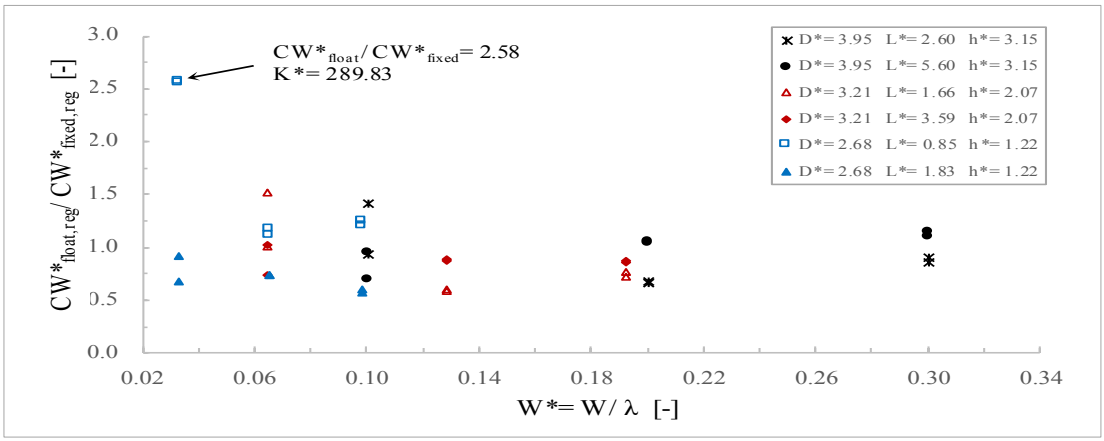

Fig. 5.16 - Comparison between $CW^*_{float,reg}$ and $CW^*_{fixed,reg}$ versus the relative chamber width W^* for all the design alternatives tested for fixed OWC and VLFS-OWC models subject to regular waves (H=0.04m & kh=1.22-3.15 with k=2π/λ).

This decreasing trend may be interpreted by considering that an infinitely large chamber width W leads to the sloshing motion within the OWC (rather than the piston motion), without producing useful energy for the PTO system (i.e., the air turbine). As stated by Sheng et al., (2012), the

sloshing motion occurs when the OWC chamber width exceeds the 1/4 – 1/5 wavelength, (i.e. for W^*>0.25-0.20).

Also, the analysis of ratio $CW^*_{float,reg}/CW^*_{fixed,reg}$ versus relative front wall draught D^* in Fig. 5.17 shows a decreasing trend of this ratio with increasing D*. Generally, for all tested relative VLFS lengths L^* and for a given relative front wall draught D^*, the relative damping K^* strongly affects the variation of $CW^*_{float,reg}/CW^*_{fixed,reg}$.

As for the relative parameters L^* and W^*, also when D^* and K^* infinitely increase, it is expected that $CW^*_{float,reg}/CW^*_{fixed,reg}$=1. This might be physically interpreted considering that infinitely high values of K^* implies a maximum air pressure inside the OWC chamber and no variation of the airflow rate. Instead, an infinite increase of D^* leads to a front wall draught equal to the water depth ($D=h$), implying a completely closed OWC chamber, so that the incident waves are fully reflected.

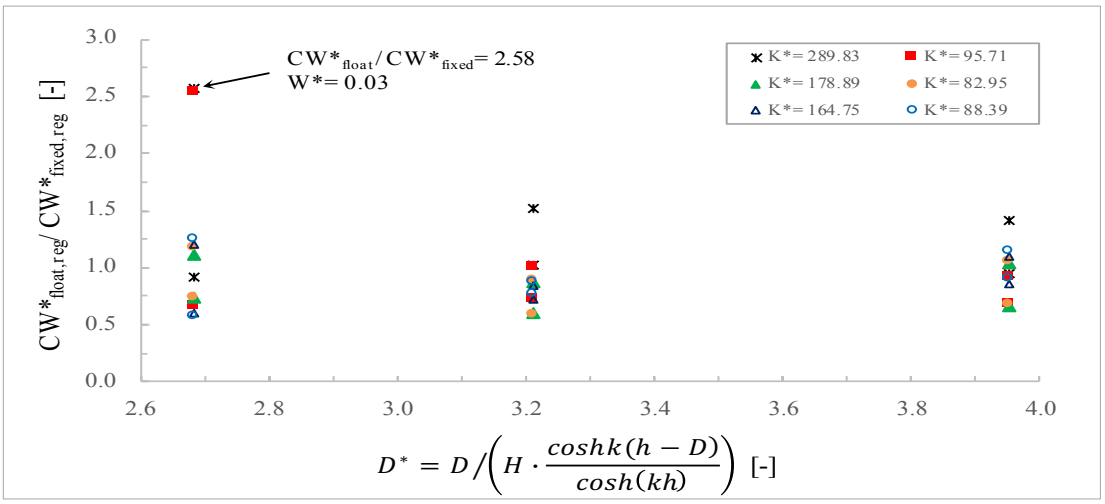

Fig. 5.17 - Comparison of $CW^*_{float,reg}$ and $CW^*_{fixed,reg}$ versus relative front wall draught D^* for all design alternatives tested for fixed OWC and VLFS-OWC models subject to regular waves (H=0.04m & kh=1.22-3.15, with $k=2\pi/\lambda$).

The performance of a fixed OWC and a floating OWC (integrated in a VLFS) in regular waves, are evaluated by comparing the ratio $CW^*_{float,reg}/CW^*_{fixed,reg}$, within the range of non-dimensional parameters tested (h^*=1.22-3.15, W^*=0.03-0.30, D^*=3.01-3.98, K^*=82.95-289.83 and L^*=0.85-5.60).

Generally, $CW^*_{float,reg}/CW^*_{fixed,reg}$, shows a trend to a unit value for an infinite increase of each of the aforementioned non-dimensional parameters. This result can be interpreted considering that, an infinite increase of relative front wall draught D implies the total reflection of the incident waves and a totally closed chamber (i.e., D=h). An infinite increase of the relative chamber width, W*, can result in the formation of sloshing-waves within the OWC chamber, without producing useful energy for the PTO system. Finally, an infinite increase of the relative VLFS length, L*, leads to a totally damped floating motion, implying the same capture width for fixed and floating OWC. As for W*, D*, L* and M*, infinitely high values of K* implies a maximum air pressure inside the OWC chamber without variation of the airflow rate.*

Although, the maximum performance of fixed OWC is 8% higher than the maximum performance achieved for the same (floating) OWC (integrated in a VLFS) (see subsections 5.1.1 & 5.2.1), the analysis of the ratio $CW^*_{float,reg}/CW^*_{fixed,reg}$ versus the relative heave motion, he shows that when the heave motion is in the order of incident wave amplitude (i.e. he*=0.79), the integration in VLFS has a positive influence, (i.e., in terms of resonance). This is the case of the OWC alternative W1D1V1% for which $CW^*_{float,reg}$=2.5$CW^*_{fixed,reg}$.*

5.5 Comparative analysis of fixed OWC vs floating OWC (integrated in VLFS) under irregular waves

As for the results obtained from the regular wave tests, the relative capture width CW^* assessed for a fixed OWC model and the same OWC model incorporated in a VLFS subject to irregular waves (respectively $CW^*_{fixed,irr}$ and $CW^*_{float,irr}$), are analysed by comparing the results of the small-scale tests in Phase I (*subsection 4.2.5*) and Phase III (*subsection 4.4.5*) and by evaluating the capture width ratio $CW^*_{float,irr}/CW^*_{fixed,irr}$.

Both models are analysed within the range of the dimensionless parameters considered for the OWC, VLFS and VLFS-OWC models tested under irregular wave conditions (Table 5-2).

Table 5-2: Range of non-dimensional parameters considered for the comparison between relative capture width assessed for fixed OWC and floating OWC in irregular waves (H_{m0}, T_p).

DESCRIPTION	DEFINITION	RANGE
Relative water depth	$h^* = k \cdot h$ (with $k=2\pi/\lambda_p$)	$1.85<h^*<2.68$
Relative OWC chamber width	$W^* = W/\lambda_p$	$0.05<W^*<0.24$
Relative OWC front wall draught	$D^* = D/\left(H_{m0} \cdot \frac{\cosh k(h-D)}{\cosh(kh)}\right)$ (with $k=2\pi/\lambda_p$)	$2.15<D^*<6.89$
Relative turbine damping	$K^* = K \cdot B \cdot W/\rho_a{}^{1/2}$	$82.95<K^*<289.83$
Relative VLFS length	$L^* = L_{VLFS}/\lambda_p$	$1.38<L^*<4.43$

Unlike to the outcomes achieved for the regular wave tests (H=0.04-0.06m & kh=1.02-3.15) (see Fig. 5.6), within the range of irregular waves tested (H_{m0}=0.02-0.04m & $1.85<h^*<2.68$), the relative heave motion he^* shows always values lower than 0.25 for all the OWC alternatives integrated in VLFS (Fig. 5.7).

For this narrow he^* range, the capture width ratio $CW^*_{float,irr}/CW^*_{fixed,irr}$ versus relative heave motion he^* (Fig. 5.18) generally shows, as expected from the results of the regular wave tests (Fig. 5.6), a relatively low variation around a unit value. However, for two OWC geometries integrated in the VLFS (W1D1V1% and W1D1V2% with H_{m0}=0.06m and kh=1.85), higher capture width ratios than those obtained for a fixed OWC ($CW^*_{float,irr}>CW^*_{fixed,irr}$) are observed.

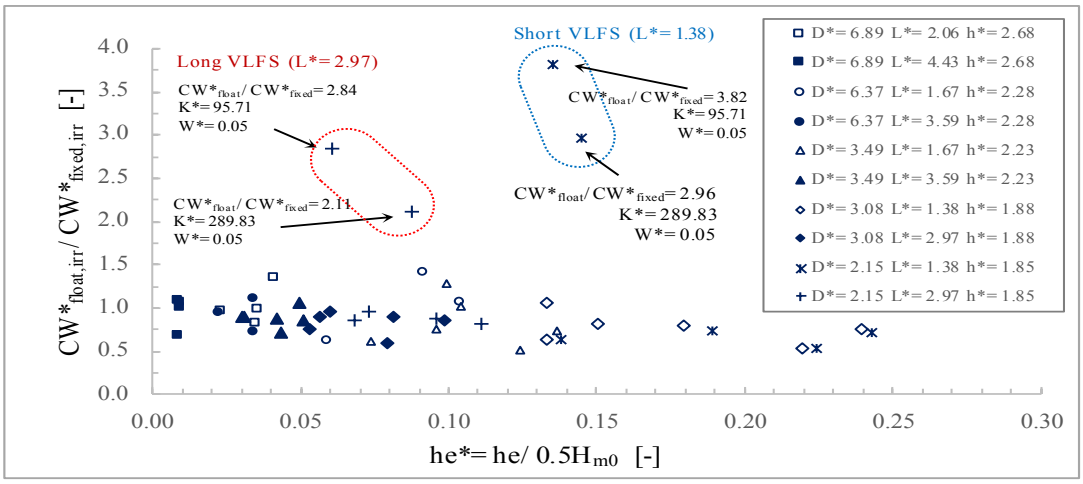

Fig. 5.18 - Comparison of capture width ratio $CW^*_{float,irr}$ and $CW^*_{fixed,irr}$ versus relative heave motion he^* for all design alternatives tested for fixed OWC and VLFS-OWC models subject to irregular waves (h^*=1.85-2.68).

For the shorter VLFS (L^*=1.38) and he^* is about 0.14 (i.e., $he=1/7a_w$, with $a_w=0.5H_{m0}$) $CW^*_{float,irr}=2.96 \cdot CW^*_{fixed,irr}$ is achieved for W1D1V1% and $CW^*_{float,irr}=3.82 \cdot CW^*_{fixed,irr}$, for W1D1V2%.

For the longer VLFS (L^*=2.97) and he* is about 0.10 (i.e., $he=1/10a_w$ with $a_w=0.5H_{m0}$) $CW^*_{float,irr}=2.11 \cdot CW^*_{fixed,irr}$ is achieved for W1D1V1% and $CW^*_{float,irr}=2.84 \cdot CW^*_{fixed,irr}$, for W1D1V2% Moreover, although $CW^*_{float,irr}/CW^*_{fixed,irr}$ shows a low variation for given he^*, it is worth to

underline the significant effect of the design parameters of the OWC (W*, D*) and the VLFS (L*) as well as of the relative damping coefficient K^* and relative water depth h^*.

As observed for the regular wave tests (Fig. 5.15 to Fig. 5.17), the capture width ratio in irregular waves $CW^*_{float,irr}/CW^*_{fixed,irr}$ shows a decreasing trend to a unit value with larger dimensionless parameters L^*, W*, M* and D* for the range of irregular waves tested (H_{m0}=0.02-0.04m & h^*=1.85-2.68) (Fig. 5.19 to Fig. 5.21).

From the analysis of $CW^*_{float,irr}/CW^*_{fixed,irr}$ versus L^*, for all design alternatives tested in both Phase I (fixed OWC) and Phase III (OWC integrated in VLFS) in Fig. 5.19, a decreasing trend of the performance ratio to a unit value for infinite values of relative VLFS lengths L^* is confirmed, which corresponds to totally damped conditions (Fig. 5.7).

The highest value of $CW^*_{float,irr}/CW^*_{fixed,irr}$=3.82 is achieved for L^*=1.38, D^*=2.15, W^*=0.05, h^*=1.85 and the applied relative damping K^*=95.71. Comparatively, for regular wave tests, the maximum value of the capture width ratio $CW^*_{float,reg}/CW^*_{fixed,reg}$=2.58 is obtained for L^*=0.85, D^*=3.01, W^*=0.03, h^*=1.22 and K^*=95.71 & 289.83 (Fig. 5.15).

Concerning the ratio $CW^*_{float,irr}/CW^*_{fixed,irr}$ versus relative chamber width W^* in Fig. 5.20, it is also shown that within the range of irregular waves tested (h^*=1.85-2.68) an increase of W* leads to a decrease to a unit value of this ratio (i.e., for W^*>0.10).

The same trend is observed for the regular waves (when W^*>0.25-0.20), (Fig. 5.16). Although the different values of W* are due to the different incident conditions, it is possible to note that generally in both cases the ratio $CW^*_{float,irr}/CW^*_{fixed,irr}$ decrease to a unit value for shorter waves.

The analysis of ratio $CW^*_{float,irr}/CW^*_{fixed,irr}$ versus relative front wall draught D^* in Fig. 5.21 shows a decreasing trend of this ratio with increasing D^*. Also in this case, an infinite increase of D^* (D=h) leads to a fully reflective OWC chamber. Moreover, as observed for the performance ratio evaluated in regular waves (Fig. 5.17), it is possible to note the relevant influence of relative damping K^* on the variation of performance ratio for given L^*, W^* and D^*.

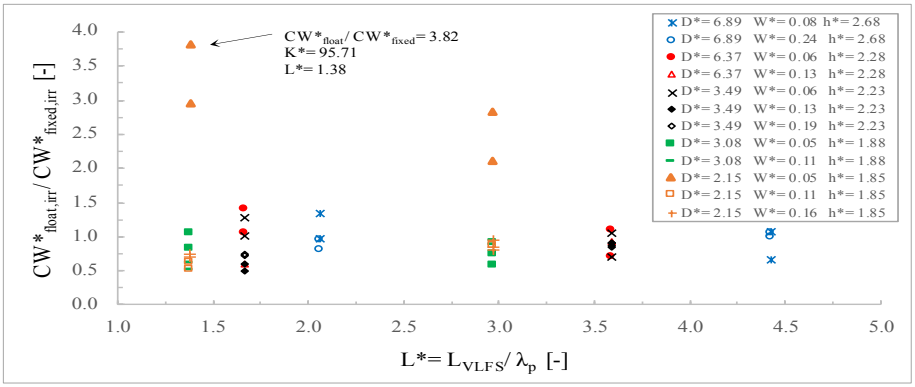

Fig. 5.19 - Comparison of $CW^*_{float,irr}$ and $CW^*_{fixed,irr}$ versus relative VLFS length L^* for all design alternatives tested for fixed OWC and VLFS-OWC models subject to irregular waves (H_{m0}=0.02-0.04m & kh=1.85-2.68, with $k=2\pi/\lambda_p$).

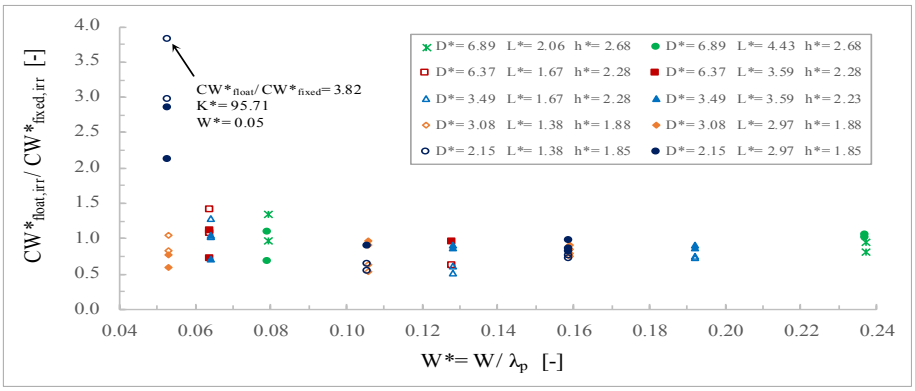

Fig. 5.20 - Comparison of $CW^*_{float,irr}$ and $CW^*_{fixed,irr}$ versus relative chamber width W^* for all design alternatives tested for fixed OWC and VLFS-OWC models subject to irregular waves (H_{m0}=0.02-0.04m & kh=1.85-2.68, with $k=2\pi/\lambda_p$).

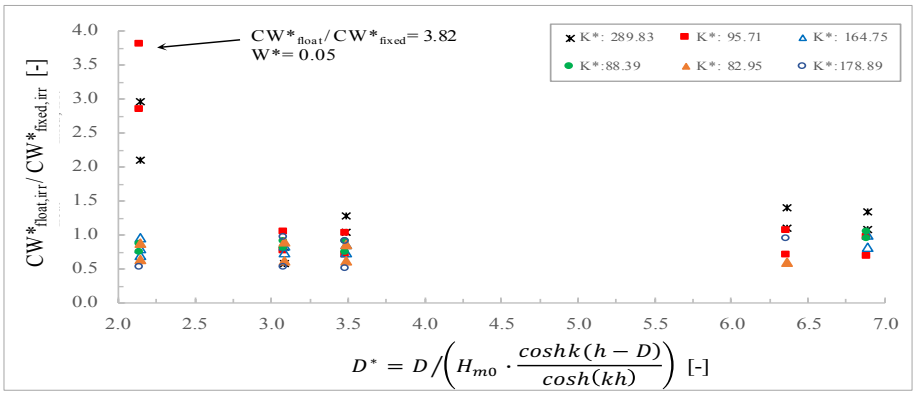

Fig. 5.21 - Comparison of $CW^*_{float,irr}$ and $CW^*_{fixed,irr}$ versus relative front wall draught D^* for all design alternatives tested for fixed OWC and VLFS-OWC models subject to irregular waves (H_{m0}=0.02-0.04m & kh=1.85-2.68, with $k=2\pi/\lambda_p$).

The comparison between the performance of fixed OWC and floating OWC, under irregular waves is conducted by analysing the ratio $CW^*_{float,irr}/CW^*_{fixed,irr}$, within the range of non-dimensional parameters tested: h=1.85-2.68, W*=0.05-0.24, D*=2.15-6.89, L*=1.38-4.43) except for K* (K*=82.95-289.83)*

The ratio $CW^*_{float,irr}/CW^*_{fixed,irr}$, shows a trend to a unit value for an infinite increase of h, W*, D* and L*. The highest value of $CW^*_{float,irr}/CW^*_{fixed,irr}$=3.82 is achieved for L*=1.38, D*=2.15, W*=0.05, h*=1.85 and the applied relative damping K*=95.71.*

For regular waves, the maximum value of the ratio $CW^*_{float,reg}/CW^*_{fixed,reg}$=2.58 is obtained for L=0.85, D*=3.01, W*=0.03, h*=1.22 and K*=95.71 & 289.83.*

As for the effect of the VLFS-OWC motion, within the range of irregular waves (H_{m0}=0.02-0.04m & 1.85<h<2.68), the relative heave motion he* is relatively low, achieving the same performance for fixed and floating OWC, except for the OWC models: W1D1V1% & W1D1V2%, which under waves with H_{m0}=0.06m & kh=1.85 show an improved performance as compared to the fixed conditions.*

Moreover, when he=1/7aw (he=0.14) and the OWC models W1D1V1% & W1D1V2% are integrated in the shorter VLFS (L*=1.38), the floating motion of the VLFS-OWC improves the performance of the device integrated (W1D1V1% and W1D1V2%), respectively of about 3 and 4 times respect to the performance in fixed conditions. When he=1/10aw (he*=0.10) and the OWC models W1D1V1% & W1D1V2% are integrated in the longer VLFS (L*=2.97), the integration of the OWC in the VLFS results in the increase of the performance respectively by about 2 and 3 times, as compared to the performance of the fixed OWC.*

5.6 Empirical formulae for the heave motion of the VLFS-OWC System

Since, as observed from the results achieved in *Sections 5.4 & 5.5,* the floating behaviour of the VLFS under the incident waves (in heave direction), plays a relevant role on the performance of the integrated OWCs, in this section two empirical formulae predicting the *relative heave motion he** of the VLFS-OWC System under regular and irregular waves, are proposed.

5.6.1 Empirical formula predicting the heave motion of the VLFS-OWC System in regular waves

Based on the analysis of the results on the VLFS-OWC models, the following formula to predict *relative heave motion, he^*_{reg}* given the wave parameters (*T, H and h*), the OWC chamber width (*W*) the turbine damping (*K*), the front wall draught (*D*) and the VLFS length (L_{VLFS}), is defined as:

$$he^*_{reg} = a\Psi^{-b} \tag{5.16}$$

The proposed formula is obtained by fitting the data from all alternatives tested for the VLFS length and the integrated OWC, under regular waves.

A non-linear regression analysis is performed to determine the numerical coefficients of the proposed formula, defined as follows: a= 0.30 and b=0.85 (Fig. 5.22) which results in a global value of the determination coefficient R^2 of about 0.96, with a Root Mean Square Error (RMSE) of

about 0.04.The input parameter Ψ is defined as the product of the following dimensionless parameters:

$$\psi = h^{*\alpha} \cdot W^{*\beta} \cdot D^{*\gamma} \cdot K^{*\delta} \cdot L^{*\varepsilon} \tag{5.17}$$

where the numerical coefficients are determined by means of an iterative regression process as follows: α=1.20, β=0.50, γ=0.40, δ=0.02 and ε=1.60.

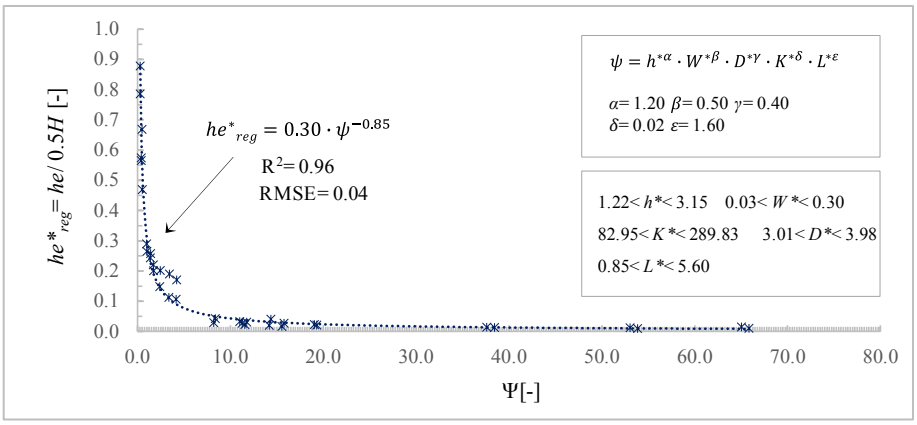

Fig. 5.22 - Relative heave motion $he^*_{reg}=he/0.5H$ of the VLFS-OWC models subject to regular waves (h^*=1.22 -3.15).

5.6.2 Empirical formula predicting the relative heave motion of the VLFS-OWC System in irregular waves

Concerning the analysis of the results on the VLFS-OWC models in irregular waves, the formula for *relative heave motion* he^*_{irr}, given the wave parameters (e.g., T_p and kh), the OWC chamber width (W), the front wall draught (D), the turbine damping (K) and the VLFS length (L_{VLFS}), is defined as follows:

$$he^*_{irr} = a\Theta^{-b} \tag{5.18}$$

A non-linear regression analysis is performed to determine the numerical coefficients of the proposed formula, defined as: a=0.96 and b=0.52. The input parameter Θ is defined as the product of the following dimensionless parameters:

$$\Theta = h^{*\alpha} \cdot W^{*\beta} \cdot D^{*\gamma} \cdot K^{*\delta} \cdot L^{*\varepsilon} \tag{5.19}$$

where, the numerical coefficients are determined by means of an iterative regression process as follows: α=6.30, β=0.01, γ=-0.10, δ=-0.35 and ε=2.40.

The empirical model proposed for relative heave motion, he^*_{irr}, (Eq. 5.18 with Θ according to Eq. 5.19) is obtained by considering the data from all alternatives tested for the VLFS length and the OWC integrated under irregular waves, resulting in a global value of the determination coefficient R^2 of about 0.91, with a Root Mean Square Error (RMSE) of about 0.02 (Fig. 5.23).

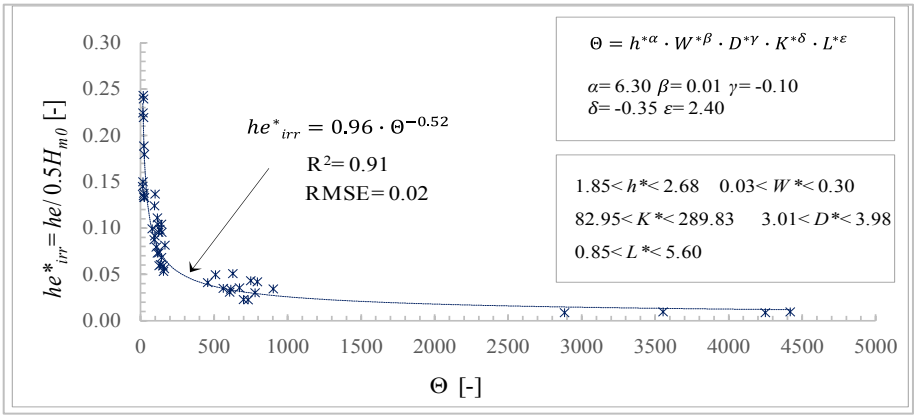

Fig. 5.23 - Empirical model for relative heave motion he^*_{irr} of VLFS-OWC models subject to irregular waves (h^*=1.85 -2.68).

5.7 Empirical formula for the performance of floating OWCs (integrated in VLFS) under regular waves

From the results achieved in s*ubsections 5.1.1 & 5.2.1* and *Section 5.3*, two empirical formulae for the prediction of *relative Capture Width, CW^*_{float}* of OWCs incorporated in a VLFS under regular waves are proposed.

The *incompressible Multi Regression Model* (MRM) proposed by Simonetti et al. (2016) for the prediction of the *relative Capture Width* for fixed OWC in regular waves ($CW^*_{fixed,reg}$) is considered as a departure basis and extended by introducing a correction factor ($CF_{float,reg}$) developed in this study (see Eq. 5.25) to account for the effect of the design parameters of the VLFS and the OWC, on the performance of the devices integrated in the VLFS under regular waves, $CW^*_{float,reg}$. Moreover, air compressibility has a relevant effect at prototype scale (see *subsection 2.2.4*), a new empirical formula for $CW^*_{float,reg}$, is obtained by applying *Correction Factors*, CF_{50}, (see Eq. 5.21) to the results of the small scale tests (Phases I & III) as suggested by Simonetti et al. (2016) on the basis of a systematic numerical parameter study and as briefly described below.

5.7.1 Incompressible Simonetti's Multi Regression Model for *Relative Capture Width* of fixed OWC in regular waves

The Simonetti's *Multi Regression Model (MRM)* is an incompressible model for the prediction of the relative Capture Width for a fixed OWC, in regular waves, obtained by fitting all the OWC design alternatives simulated by means of a CFD model (Simonetti et al., 2016) which was systematically validated with the outcomes of overall laboratory tests performed on fixed OWC in regular waves (Phase I of this study). Simonetti et al. (2016) defined the *incompressible Multi Regression Model* (*MRM*) as follows:

$$CW^*_{MRM} = \frac{f(K^* - d)}{\exp(a \cdot D^*) \cdot (1 + b \cdot (W^* - W^*_{opt})^2 \cdot c} \tag{5.20}$$

where:

- W^*, D^*, K^* are the independent variables expressed in the same dimensionless form adopted in this study and W^*_{opt} is the value of relative chamber width (about 0.12) in which the fixed OWC, simulated by the CFD model, reaches the maximum CW^*_{fixed};
- Coefficients a, b, c and d are functions of the relative water depth h^*.

Considering the results achieved with the *MRM model* and those obtained with the incompressible CFD model and the overall laboratory tests performed on fixed OWC in regular waves (Phase I of this study), an overall value of R^2=0.95 for the *MRM model* predictions with a Root Mean Square Error (RMSE) of about 0.05 was obtained (Simonetti et al., 2016).

Moreover, applying the *MRM model* to relative water depths $h^*=kh$=1.5-3.5, the agreement between the MRM model and laboratory data is still satisfactory, with a maximum error of about 0.15 (Fig. 5.24).

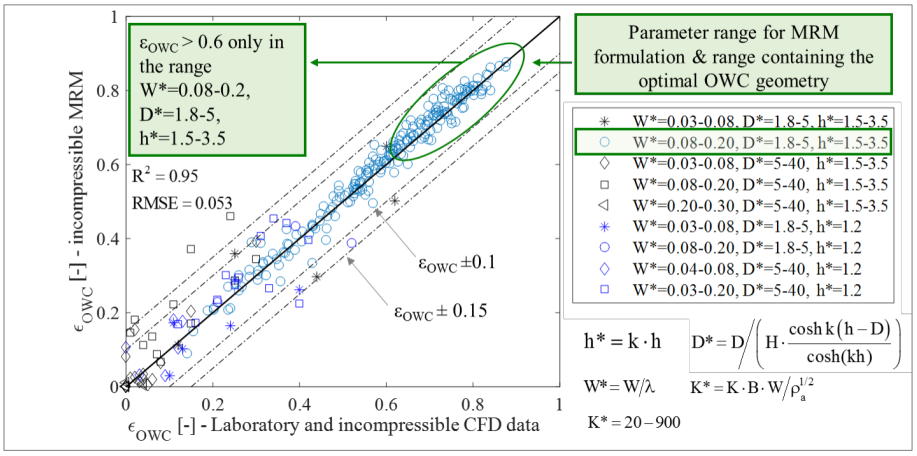

Fig. 5.24 - Scatter plot between the *incompressible MRM* prediction model and laboratory data (Phase I) of $CW^*_{fixed,reg}$ (named ε_{OWC} in figure) for different ranges of the non-dimensional parameters W^*, $D^*$and h^*(Simonetti et al., 2016).

The *incompressible MRM model* (Eq. 5.20) can predict the performance of fixed OWC in the parameter range where the highest $CW^*_{fixed,reg}$ is expected and which is related to: i) the incident wave conditions (*H, T* and *h*), ii) the OWC geometry (*W, D*) and iii) the applied damping (*K*). Since the *incompressible MRM model* was formulated by means of a regression analysis of the CFD results, it is valid within the range of dimensionless input parameters considered in Simonetti et al. (2016) study and reported in Table 5-3.

Table 5-3: Range of non-dimensional parameters in which Simonetti et al. 2016 declared the validity of the *incompressible MRM model* predicting the *relative Capture Width* for fixed OWC (CW^*_{MRM}), in regular waves (*H, T*).

DESCRIPTION	DEFINITION	RANGE
Relative water depth	$h^* = k \cdot h$ (with k=2π/λ)	$1.5<h^*<3.5$
Relative OWC chamber width	$W^* = W/\lambda$	$0.08<W^*<0.20$
Relative OWC front wall draught	$D^* = D/\left(H \cdot \frac{\cosh k(h-D)}{\cosh(kh)}\right)$ (with k=2π/λ)	$1.8<D^*<5.0$
Relative turbine damping	$K^* = K \cdot B \cdot W/{\rho_a}^{1/2}$	$20<K^*<170$

Moreover, Simonetti et al. (2016) considered the scale effects due to air compressibility, by performing a comparative analysis of the results obtained from a *compressible CFD model* at scale 1:50 and a *compressible CFD model* at scale 1:1.

The results show that air compressibility does not affect the hydrodynamics inside the OWC (i.e. variations of water surface elevation $\Delta\eta_{OWC}$) but aerodynamics (i.e., air pressure variations, Δp_{OWC}, air flow rate, Δq_{OWC} and pneumatic power output, $\Pi_{OWCfixed}$ or relative capture width, $CW^*_{fixed,reg}$[15]).

Simonetti et al. (2016) proposed *Correction Factors* (CF_{50}) for each aforementioned parameter $\chi(p_{OWC}, q_{OWC}, CW^*_{fixed})$ as the ratio between the value of χ in the 1:50 scale model and the value of χ in the simulations performed by means of CFD at prototype scale (1:1) as:

$$CF_{50} = \frac{\chi_{1:50}}{\chi_{1:1}} \tag{5.21}$$

In order to consider the variation of the air compressibility effect on the system dynamics as a function of the air pressure variation inside the OWC chamber and the characteristics of the incident waves (e.g. *T, H* and *h*), the *Correction Factor,* CF_{50}, is defined as a function of the non-dimansional pressure parameter Π^*:

$$\Pi^* = \Delta p_{OWC\ 1:50} \Big/ \left(\gamma H \frac{\cosh k(h-D)}{\cosh(kh)}\right) \tag{5.22}$$

where $\Delta p_{OWC\ 1:50}$ is the period average value of the pressure oscillation amplitude in the OWC chamber as simulated in the 1:50 scale model and scaled up to 1:1 according to Froude similarity; $\gamma=\rho g$ is the water specific weight; *k* is the incident wave number; *h* is the water depth and *D* is the draught of the OWC front wall.

The formulae for the correction factors CF_{50} as a function of parameter Π^* describing the air pressure level in the OWC chamber on Δp_{OWC}, Δp_{OWC} and $CW^*_{fixed,reg}$ to accont for air compressibility effect as proposed by Simonetti et al., (2016) are summarized in Table 5-4.

The outcomes of the comparative analysis of Simonetti et al. (2016) have shown that negleting the air compressibility results in an overestimation up to about 15% for the relative air pressure p_{OWC} and the air volume flux q_{OWC}, but less than 10% for the relative capture width $CW^*_{fixed,reg}$ (within tested range of their study Π^*=0.4-1.0).

It was also shown that the overestimation increases with increasing air pressure level in the air chamber Π^*, while the air compressibility effect becomes progressively less relevant for lower air pressure level.

[15] Since the power of the incident wave is may be considered as unaffected by the air compressibility, any variation of $\Pi_{OWCfixed}$ due to air compressibility will result in an equivalent variation of the overall relative capture width $CW^*_{fixed,reg}$.

Table 5-4: Correction Factors (CF_{50}) proposed by Simonetti et al., (2016) for the air pressure oscillation amplitude within the OWC chamber, Δp_{OWC}, the volume air flow oscillation amplitude, Δp_{OWC} and the relative Capture Width, $CW^*_{fixed,reg}$ for model scale 1:50.

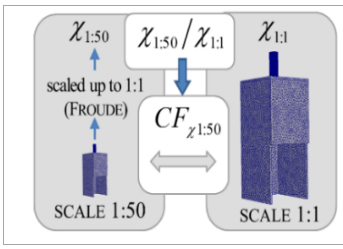

Parameter	$CF_{1:50}$	R^2
Δp_{OWC}	$0.147\Pi^{*2} + 1$	0.95
Δq_{OWC}	$0.13\Pi^{*2} + 0.11\Pi^{*} + 1$	0.97
$CW^*_{fixed,reg}$	$0.083\Pi^{*2} + 1$	0.87

5.7.2 Empirical formula predicting the performance of OWC integrated in VLFS under regular waves

Based on the outcomes achieved in *Subsections 5.1.1 & 5.2.1* and *Section 5.3*, the relation between the *relative Capture Width CW** extracted for a fixed OWC and an OWC integrated in VLFS under regular waves is proposed as follows:

$$\frac{CW^*_{float,reg}}{CW^*_{fixed,reg}} = a\,\Gamma^2 - b\,\Gamma + c \tag{5.23}$$

The polynomial fit of the proposed formula is related to the range of dimensionless parameters tested for the fixed and floating OWC (h^*=1.22-3.15, D^*=3.01-3.98, W^*=0.03-0.30, K^*= 82.95-289.83 and L^*=0.85-2.6).

A non-linear regression analysis is adopted to determine the numerical coefficients in Eq. 5.18 as follows: a=0.01, b=0.08 and c=1.00. This, results in a global value, of the determination coefficient R^2, of about 0.86 with a Root Means Square Error (RMSE) of about 0.16 (Fig. 5.25).

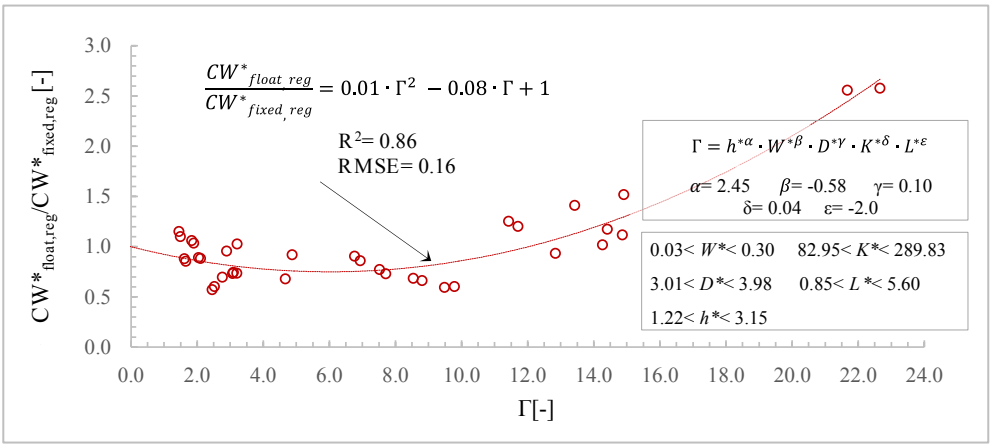

Fig. 5.25 - Relation between relative capture width ratio CW^*_{float} / CW^*_{fixed} and input parameter Γ, defined by Eq. 5.24.

The input parameter, Γ, is defined as the product of the dimensionless parameter, h^*, W^*, D^*, K^* *and* L^* as follow:

$$\Gamma = h^{*\alpha} \cdot W^{*\beta} \cdot D^{*\gamma} \cdot K^{*\delta} \cdot L^{*\varepsilon} \tag{5.24}$$

The numerical coefficients determined by means of an iterative regression process are: α=2.45, β=-0.58, γ=0.10, δ=0.04 and ε=-2.0. These are shown in Fig. 5.25, which describes relative capture width ratio $CW^*_{float,reg}/CW^*_{fixed,reg}$ as a function of input parameter Γ (Eq. 5.24).

Comparing $CW^*_{float,reg}$ predicted by Eq. 5.23 and relative capture width $CW^*_{float,reg}$ obtained from laboratory data (Phase III) for different ranges of the dimensionless parameters W^*, D^*, K^* and L^* under regular waves ($h^*=kh$=1.22-3.15), a determination coefficient R^2=0.80 and a Root Mean Square Error RMSE=0.06 are obtained (Fig. 5.26).

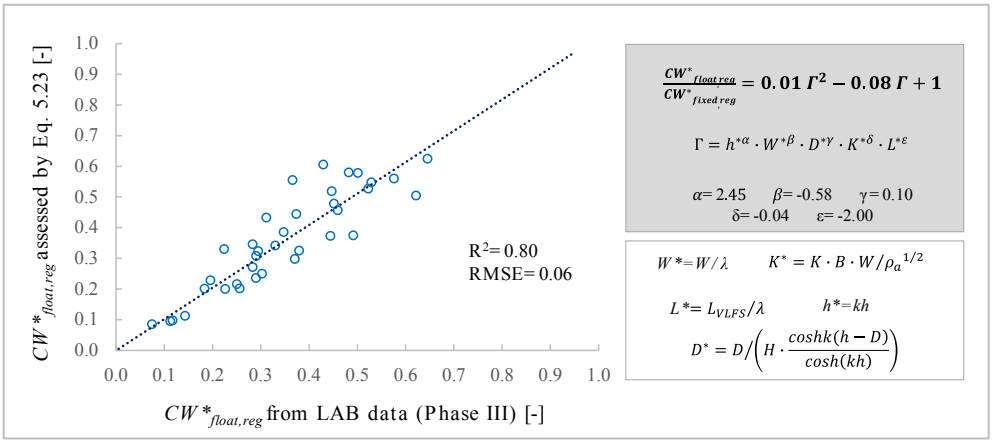

Fig. 5.26 - Scatter plot between $CW^*_{float,reg}$ predicted by Eq. 5.23 and $CW^*_{float,reg}$ obtained from laboratory data (Phase III) for different ranges of the dimensionless parameters W^*, D^*, K^* and L^* under regular waves (h^*=1.22-3.15).

The effect of the VLFS motion on the performance of a floating OWC is introduced by extending the Simonetti's *Multi Regression Model* (*MRM*) for fixed OWC in regular waves, CW^*_{MRM} (Eq. 5.20) by the following correction factor:

$$CF_{float,reg} = 0.01\,\Gamma^2 - 0.08\,\Gamma + 1 \tag{5.25}$$

Therefore, the new empirical model proposed for the prediction of the relative capture width $CW^*_{float,reg}$ for a floating OWC (integrated in VLFS) is defined by Eq. 5.26, as obtained by applying the proposed correction factor $CF_{float,reg}$ (Eq. 5.25) to Simonetti's *incompressible MRM model* (Eq. 5.20) and as illustrated in Fig. 5.28.

$$CW^*_{float,reg} = CF_{float,reg} \cdot CW^*_{MRM} \tag{5.26}$$

The relation between the laboratory results for floating OWC (Phase III) and those achieved by applying Eq. 5.26 results in an overall value of R^2=0.75, with a Root Mean Square Error (RMSE) of about 0.08 (Fig. 5.27). In this case, Simonetti's incompressible MRM model is applied to the considered range of dimensionless parameters, tested in the laboratory (Phase III), (h^*=1.22-3.15, W^*=0.03-0.30, D^*=3.01-3.98, K^*=82.95-289.83 and L^*=0.85-2.60).

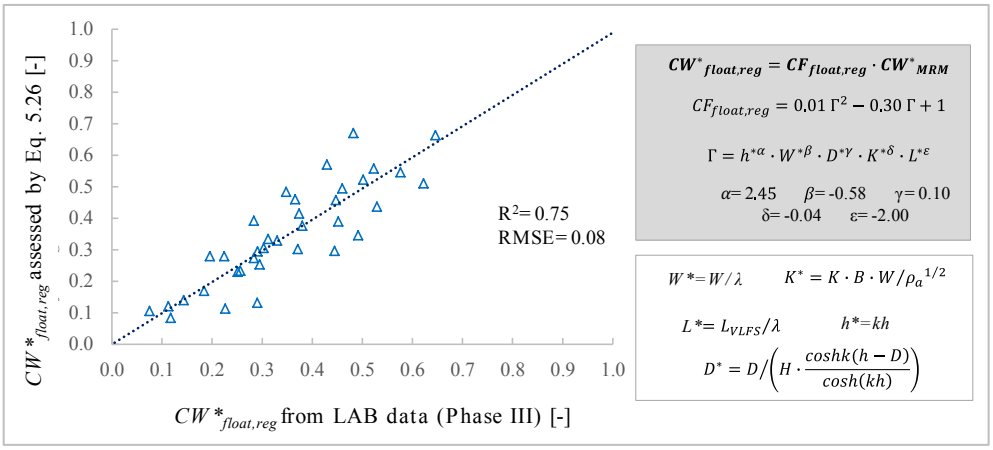

Fig. 5.27 - Scatter plot between calculated capture width $CW^*_{float,reg}$ using Eq. 5.26 and laboratory data (Phase III) of $CW^*_{float,reg}$ for different ranges of the dimensionless parameters W^*, D^*, K^* and L^* in regular waves (h^*=1.22-3.15).

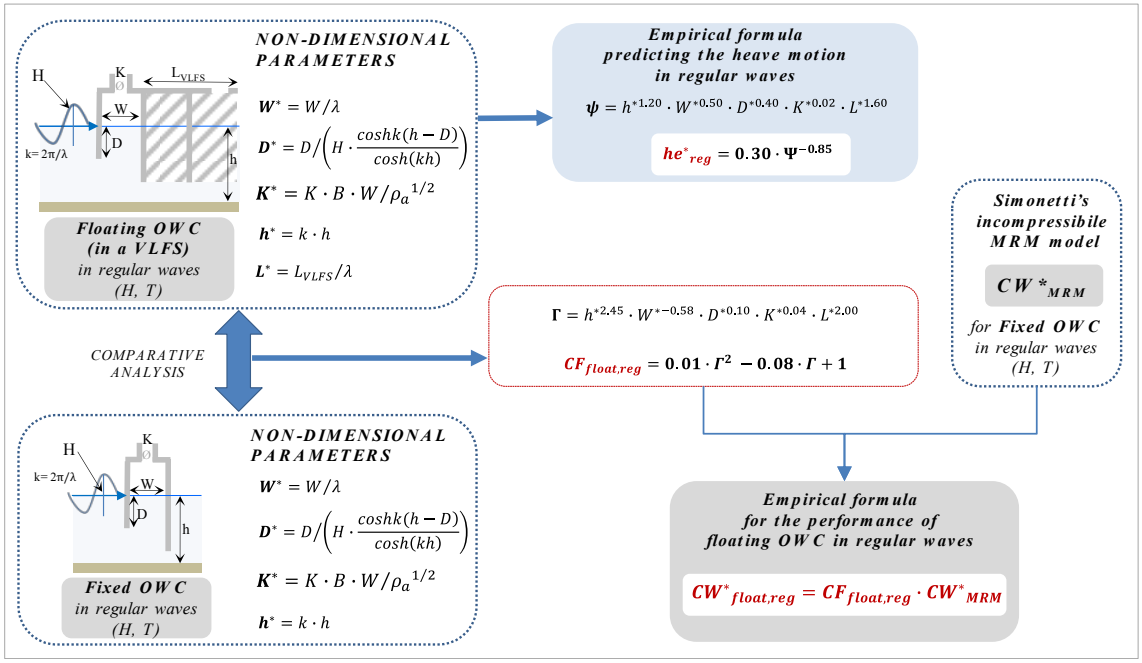

Fig. 5.28 - Procedure for the application of the proposed correction factor, $CF_{float,reg}$ to extend Simonetti's *incompressible MRM model* (Eq. 5.13) in order to obtain a prediction formula of the *relative Capture Width* $CW^*_{float,reg}$, for a floating OWC (integrated in a VLFS) in regular waves.

5.8 Empirical formulae for the performance of fixed OWC and floating OWCs (integrated in VLFS) under irregular waves

From the outcomes achieved in *Subsections 5.1.2 & 5.2.2* and *Section 5.4*, two empirical formulae aimed at estimate the *relative Capture Width* $CW^*_{float,irr}$ of a floating OWC (in a VLFS), under irregular waves are proposed.

First, a Correction Factor $CF_{fixed,irr}$, is introduced in order to extend the *incompressible MRM Model* of Simonetti et al. (2016) to irregular wave conditions. For this purpose, a comparative analysis is performed between the experimental results achieved for a fixed OWC under irregular waves (Phase I) with the outcomes of Simonetti's *incompressible MRM model* implemented for regular waves characterized by the same energy density of the irregular waves tested in the laboratory. Then, the results achieved for fixed OWC (Phase I) and for floating OWC (Phase III) in irregular waves, are compared and a new Correction Factor ($CF_{float,irr}$) is proposed.

The two aforementioned Correction Factors ($CF_{float,irr}$ and $CF_{fixed,irr}$) are applied to extend Simonetti's incompressible MRM model to a new formula for the prediction of the relative Capture Width of floating OWC in irregular waves. As for the formula proposed in *Section 5.5* for $CW^*_{float,reg}$, this new formula predicting $CW^*_{float,irr}$, could take into account the scale effects due to air compressibility through a correction of the results from small-scale model tests (Phase I & III) by means of the *Correction Factors* (CF_{50}) suggested by Simonetti et al. (2016) (see subsection 5.5.1 and Table 5-4).

The new prediction formulae might represent useful tools for the preliminary design and sizing of a VLFS-OWC system, allowing the selection of the optimal OWC design parameters, which ensure the best performance of the device in moderate wave climates.

5.8.1 Empirical formula predicting the performance of fixed OWC in irregular waves

The relation between the relative capture width $CW^*_{fixed,reg}$ of a fixed OWC in regular waves (H, T), and the relative capture width $CW^*_{fixed,irr}$, of the same fixed OWC in irregular waves (H_{m0}, T_p) is determined by comparing the response of the device (i.e. CW^*) under waves having equivalent incident wave power, Π_w (or flux of energy $\bar{\Pi}_w = \bar{E}\ C_g$).

For this purpose, it is worth to note that the distribution of wave energy of a real sea state is described by a wave spectrum over frequency. The wave spectrum is usually expressed in terms of the moments of distribution, in which, $m_0 = \int_0^\infty S_f(f)df$ is the moment of zero-order representing

the sum of the variances of individual spectral components (i.e., $m_0=a^2/2$). Then, considering the definition of the total average wave energy per unit area, $\bar{E}$ (see Eq. 2.12), the real sea state can be replaced by a single sinusoidal wave having the same energy and characterized by an equivalent wave height called *Root-Mean-Square Wave Height* (Laing et al., 1998):

$$H_{rms} = \sqrt{8E/\rho_w g} \tag{5.27}$$

in which, E represents the total energy per unit area of the sea state.

In order to have a parameter corresponding as closely as possible to the significant wave height (i.e., $H_{m0} = 4\sqrt{m_0}$), H_{rms}, can be expressed also as:

$$H_{rms} = \frac{H_{m0}}{\sqrt{2}} \tag{5.28}$$

Similar to the equivalent wave height parameter, H_{rms}, a regular wave period parameter is required with equivalent wave power to that of the irregular wave. The so-called *Energy Period Te* (or T_{m-10}), is usually adopted and can be determined by the two spectral moments (m_{-1} and m_0) as:

$$T_e = \frac{\sum_{i=1}^{N} \frac{S(f_i)}{f_i} \Delta f_i}{\sum_{i=1}^{N} S(f_i) \Delta f_i} = \frac{m_{-1}}{m_0} \tag{5.29}$$

Moreover, it is important to take into account that, when the spectral shape is unknown, the energy period must be assessed from other variables, based on the peak period, T_p (i.e. $T_e=\alpha T_p$, with α depending on the shape of the wave spectrum[16]), (Pastor & Liu, 2014).

For each irregular wave tested in Phase I on fixed OWC (see Table 4-2) equivalent height and period of a regular wave train with same incident wave power, is obtained (Table 5-5).

Table 5-5: Irregular waves simulated in the laboratory experiments and equivalent regular wave trains having the same incident wave power.

Notation	H_{m0} [m]	T_p [s]	Notation	H_{rms} [m]	T_e [s]
H1	0.025	0.9	HR1	0.018	0.9
H2	0.027	1.0	HR2	0.019	1.0
H3	0.040	1.0	HR3	0.026	1.0
H4	0.042	1.1	HR4	0.028	1.0
H5	0.061	1.1	HR5	0.040	1.1

Table 5-5 and Table 4-2 show that the regular waves tested (H01-H06) are not energetically comparable with the irregular waves, since they have different target characteristics as related to the aforementioned equivalent regular wave trains (HR1-HR5).

The approach adopted in this study, consists in comparing the outcomes from Simonetti's *incompressible MRM model* (Eq. 5.20) for fixed OWC under the equivalent regular waves HR1 to HR5 (within the range of validity of dimensionless input parameters), with the outcomes from Phase I of tests on the same fixed OWC under irregular waves H1 to H5 (Fig. 5.29):

$$\frac{CW^*_{fixed,irr}}{CW^*_{MRM}} = a \ln(\phi) + b \tag{5.30}$$

in which, the input parameter Φ is the product of the function of W^*, D^*, K^* and h^*:

$$\Phi = W^{*\alpha} \cdot D^{*\beta} \cdot K^{*\gamma} \cdot h^{*\delta} \tag{5.31}$$

A non-linear regression analysis is performed to determine the numerical coefficients in Eq. 5.31 as follows: a=0.27 and b=0.15.

The numerical coefficients in Eq. 5.31 are determined by means of an iterative regression process as: α=-3.22, β=2.97, γ=4.20 and δ=1.74.

[16] For example, $T_e=0.86T_p$ for Pierson-Moskowitz spectrum

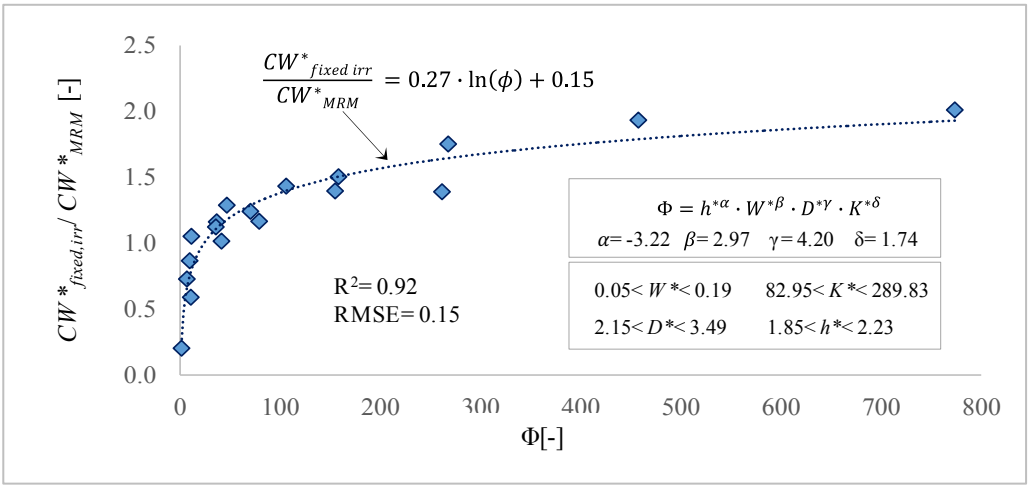

Fig. 5.29 - Capture width CW^*_{fixed} of a fixed OWC obtained from laboratory experiments with irregular waves (Phase I) and CW^*_{MRM} predicted by Simonetti's *MRM model* (Eq. 5.20) for the same fixed OWC under regular waves with equivalent energy density of the irregular waves tested, as a function of parameter Φ defined by Eq. 5.31.

The relation between the performance of fixed OWC in regular waves and the performance of the same fixed OWC in irregular waves is introduced by applying to Simonetti's *MRM model*, CW^*_{MRM} (Eq. 5.20), the following correction factor:

$$CF_{fixed,irr} = 0.27 \ln(\phi) + 0.15 \tag{5.32}$$

The proposed empirical model is determined for the range of dimensionless parameters tested for the fixed OWC (h^*=1.85-2.23, D^*=2.15-3.49, W^*=0.05-0.19, K^*= 82.95-289.83) with a global value of the determination coefficient R^2 of about 0.92, with a Root Means Square Error (RMSE) of about 0.15 (Fig. 5.30). Therefore, the new empirical formula proposed for the prediction of $CW^*_{fixed,irr}$, is defined by Eq. 5.33, obtained by applying $CF_{fixed,irr}$ to Simonetti's *incompressible MRM model* (Eq. 5.20):

$$CW^*_{fixed,irr} = CF_{fixed,irr} \cdot CW^*_{MRM} \tag{5.33}$$

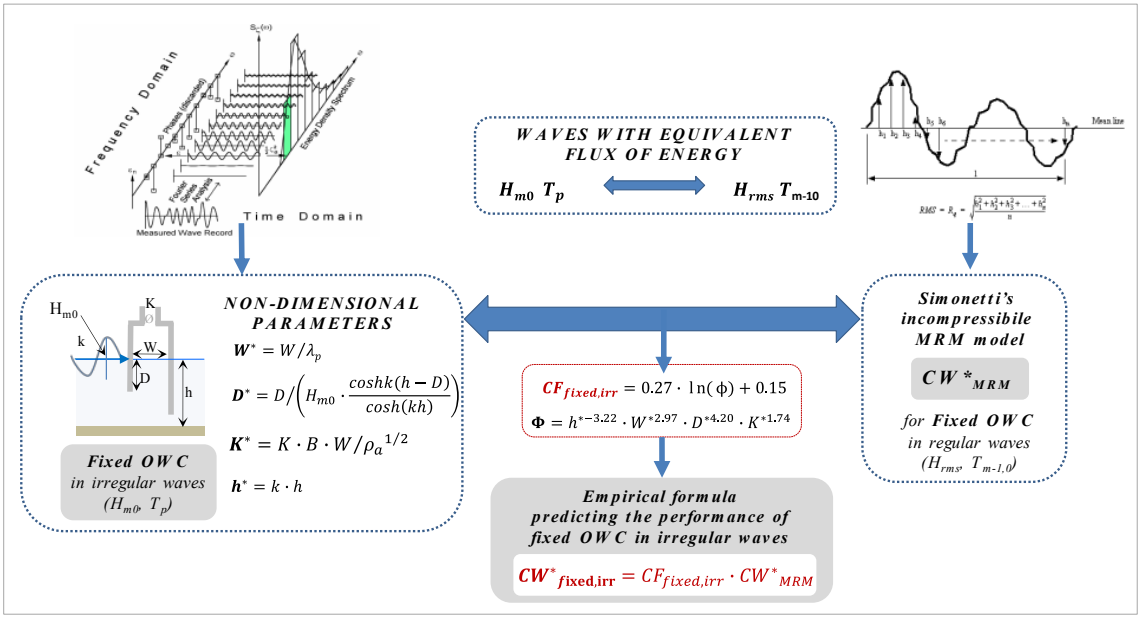

Fig. 5.30 - Procedure for the application of the proposed correction factor $CF_{fixed,irr}$ to the capture width CW^*_{MRM} from the *incompressible Simonetti's MRM model* (Eq. 5.20) for fixed OWC in regular waves in order to obtain the new formula to predict capture width $CW^*_{fixed,irr}$, for a fixed OWC in irregular waves.

The outcomes of laboratory tests for fixed OWC in irregular waves (Phase I) versus those obtained by applying $CF_{fixed,irr}$ to Simonetti's *incompressible MRM model* (Eq. 5.20) result in an overall value of determination coefficient R^2=0.91 and a Root Mean Square Error (RMSE) of about 0.15 (Fig. 5.31).

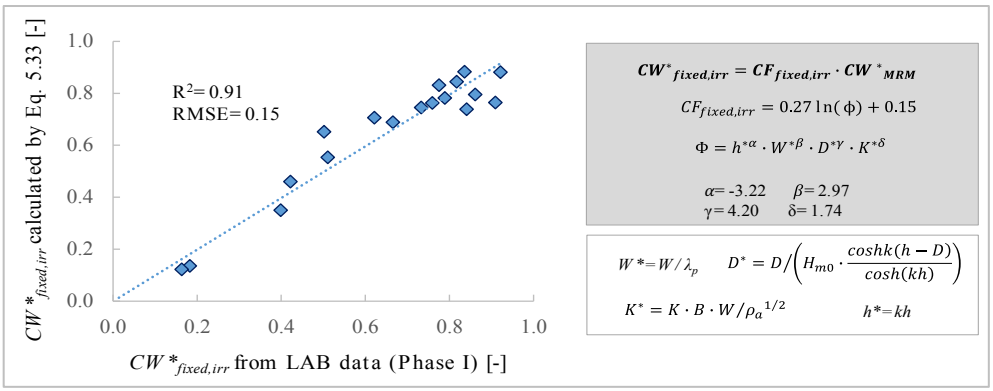

Fig. 5.31 - Scatter plot between the formula predicted by applying the Correction Factor, $CF_{fixed,irr}$ to the Simonetti's *MRM model* (Eq. 5.28) and laboratory data (Phase I) of $CW^*_{fixed,irr}$ for different ranges of the dimensionless parameters W^*, D^*, K^*, $L^*$and M^*in regular waves (h^*=1.85-2.23).

5.8.2 Empirical formula predicting the performance of OWC incorporated in a VLFS under irregular waves

From the outcomes in *Subsections 5.1.2 & 5.2.2* and *Section 5.4*, the relation between the *Relative Capture Width CW** extracted for a fixed OWC and an OWC integrated in VLFS under irregular waves is proposed as follows:

$$\frac{CW^*_{float,irr}}{CW^*_{fixed,irr}} = a\,\Omega^2 - b\,\Omega + c \tag{5.34}$$

A non-linear regression analysis is adopted to determine the numerical coefficients in Eq. 5.34 as follows: a=4.83, b=2.46 and c=1.0.

The input parameter Ω is defined as the product of the dimensionless parameters h^*, W^*, D^*, K^*, and L^*:

$$\Omega = h^{*\alpha} \cdot W^{*\beta} \cdot D^{*\gamma} \cdot K^{*\delta} \cdot L^{*\varepsilon} \tag{5.35}$$

The numerical coefficients determined by means of an iterative regression process are: α=-5.90, β=-1.95, γ=-2.00, δ =-0.10 and ε=-0.21.

For the polynomial fit of the proposed formula (Eq. 5.34 with Ω according to Eq. 5.35*)*, the experimental data obtained for the range of dimensionless parameters tested for the fixed and floating OWC (h^*=1.85-2.68, D^*=2.15-6.89, W^*=0.05-0.24, K^*= 82.95-289.83 and L^*=1.38-4.43) are considered, leading to a global value of the determination coefficient R^2 of about 0.91 with a Root Means Square Error (RMSE) of about 0.19 (Fig. 5.32).

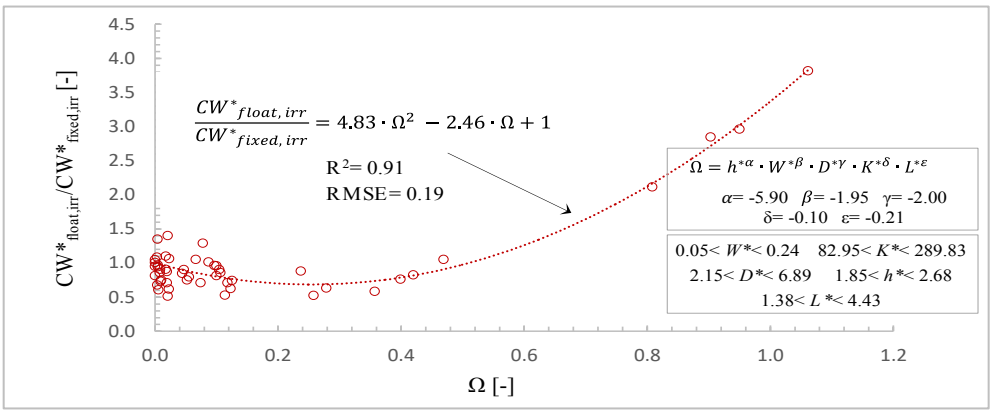

Fig. 5.32 - Empirical formula for capture width ratio $CW^*_{float,irr}/CW^*_{fixed,irr}$ as a function of parameter *Ω*, defined by Eq. 5.35.

Considering the results from the laboratory tests for floating OWC in irregular waves (Phase III) and those obtained by applying Eq. 5.34 to the experimental results on fixed OWC in irregular waves (Phase I), an overall value of R^2=0.77 and a Root Mean Square Error (RMSE) of about 0.07 are determined (Fig. 5.33).

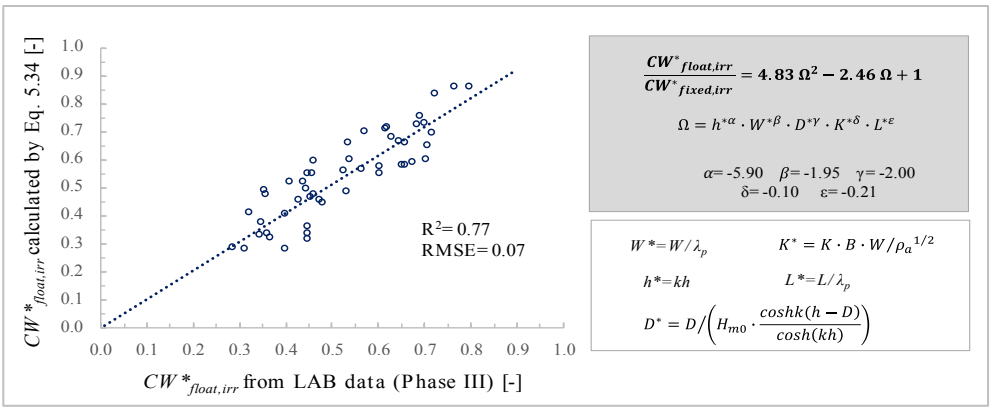

Fig. 5.33 - Scatter plot between relative capture width calculate $CW^*_{float,irr}$ using Eq. 5.34 with Ω according to Eq. 5.35 and CW^*_{float} obtained from laboratory data (Phase III) for different ranges of the dimensionless parameters W^*, D^*, $K^*$and L^*under irregular waves (h^*=1.85-2.68).

The effect of the VLFS motion on the performance of the OWC integrated in a VLFS under irregular waves is introduced by extending Simonetti's *Multi Regression Model* (*MRM*) for capture width CW^*_{MRM} of a fixed OWC in regular waves (Eq. 5.20) by means of the Correction Factor $CF_{fixed,irr}$ (Eq. 5.33) and by the following correction factor for floating OWC in irregular waves:

$$CF_{float,irr} = 4.83 \cdot \Omega^2 - 2.46 \cdot \Omega + 1 \tag{5.36}$$

Therefore, the new empirical model proposed for the prediction of the relative capture width for a floating OWC (integrated in a VLFS) in irregular waves, $CW^*_{float,irr}$, is defined as:

$$CW^*_{float,irr} = CF_{float,irr} \cdot CF_{fixed,irr} \cdot CW^*_{MRM} \tag{5.37}$$

which, is obtained applying the proposed correction factors $CF_{fixed,irr}$ (Eq. 5.33) and $CW^*_{float,irr}$ (Eq. 5.36) to Simonetti's *incompressible MRM model* (Eq. 5.20), as illustrated in Fig. 5.34.

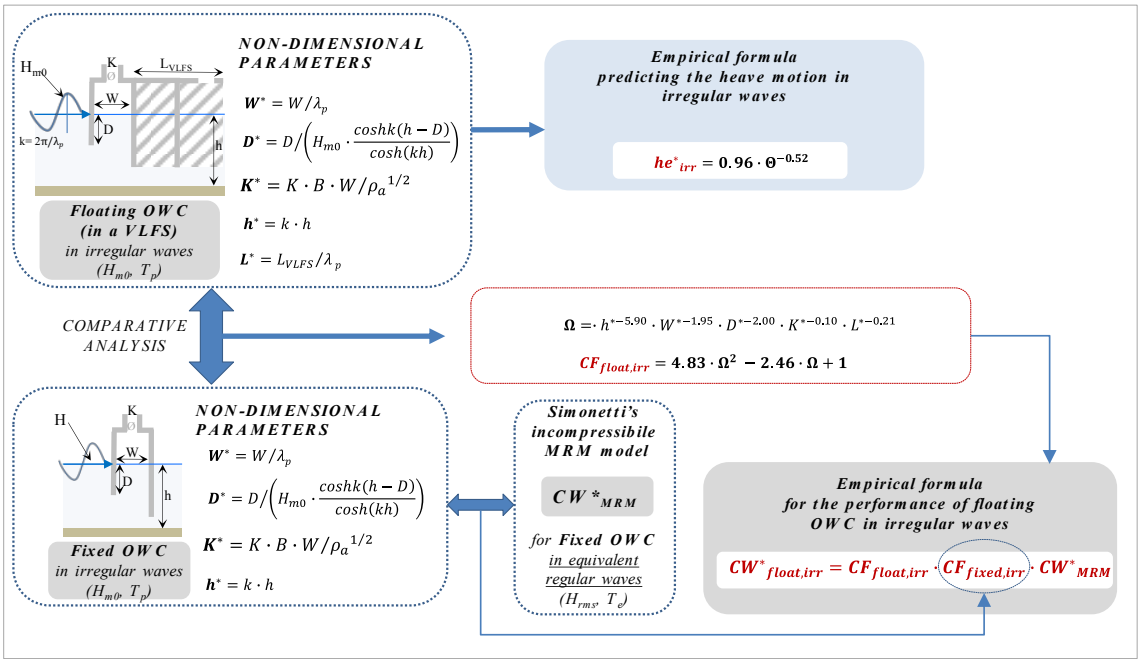

Fig. 5.34 - Procedure for the application of the proposed correction factors, $CF_{fixed,irr}$ and $CF_{float,irr}$ to *capture width* CW^*_{MRM} from the *incompressible* Simonetti's *MRM model in regular waves* (Eq.

5.20), in order to obtain the new formula (Eq. 5.37) to predict the *relative capture width* of floating OWC (integrated in a VLFS) in irregular waves, $CW^*_{float,irr}$.

The relation between the results achieved for floating OWC (Phase III) and those achieved by applying the correction factors, $CF_{flixed,irr}$ and $CF_{float,irr}$, to Simonetti's *incompressible MRM model* results in an overall value of R^2=0.72, with a Root Mean Square Error (RMSE) of about 0.08 (Fig. 5.35).

In this case, Simonetti's *incompressible MRM model* is applied to the considered range of dimensionless parameters tested in laboratory (h^*=1.85-2.68, L^*=1.38-4.43, W^*=0.05-0.24, D^*=2.15-6.89 and K^*=82.95-289.83).

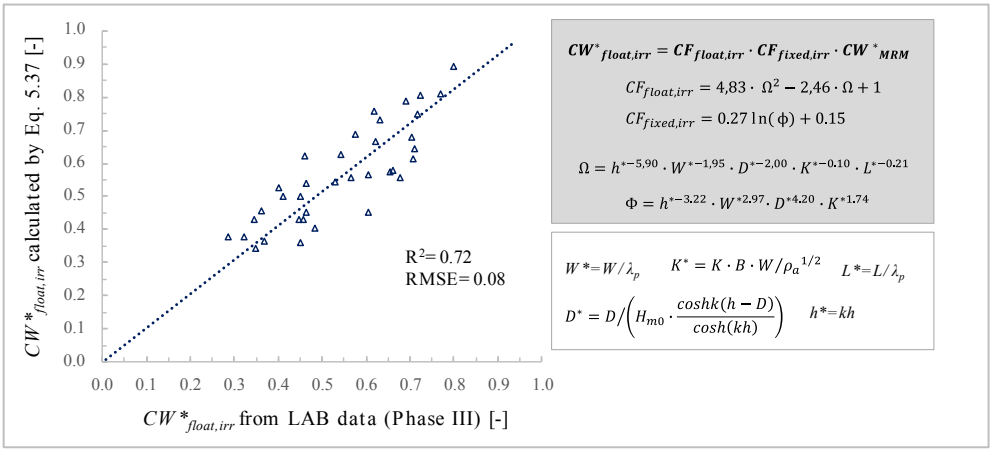

Fig. 5.35 - Scatter plot between the formula predicted by applying the correction factors, $CF_{fixed,irr}$ and $CF_{float,irr}$ to Simonetti's *incompressible MRM model* and laboratory data (Phase III) of $CW^*_{float,irr}$ for different ranges of the dimensionless parameters W^*, D^*, K^*, L^* and M^* under irregular waves (h^*=1.85-2.68).

5.9 Summary and discussion

Based on the analysis of the results achieved in the laboratory experiments on fixed OWC models (Phase I) and on OWC models integrated in the VLFS (Phase III), the dimensional analysis (*Π-theorem*) is applied to define the non-dimensional independent parameters affecting the performance of the device under both fixed and floating (integrated) conditions.

- The *relative Capture Width* of fixed OWC in regular waves ($CW^*_{fixed,reg}$) and in irregular waves ($CW^*_{fixed,irr}$) can be expressed as a function of: relative water depth h^*; chamber width W^*; front wall draught D^* and turbine damping K^*.
- The *relative Capture Width* of floating OWC (in a VLFS) in regular waves ($CW^*_{float,reg}$) and irregular waves ($CW^*_{float,irr}$) is also strongly influenced by the relative VLFS length $L^*=L_{VLFS}/\lambda$.
- The results show that increasing L^* leads to a decrease of the *relative heave motion he**, at the point closer to the leading edge of the VLFS (i.e. where the OWC is integrated). Therefore, formulae are first proposed to predict he^*_{reg}, under regular waves and he^*_{irr}, under irregular waves, given as input: wave parameters (H, T or H_{m0}, T_p); water depth h; OWC chamber width (W); damping coefficient (K) and VLFS length, (L_{VLFS}). The proposed formulae might be applied in the preliminary design of a VLFS-OWC system to assess the motion of the VLFS-OWC system for an installation site in a moderated wave climate.
- *Simonetti's MRM Model* (Simonetti et al., 2016) for fixed OWC in regular waves (CW^*_{MRM}), is extended to incident irregular waves ($CW^*_{fixed,irr}$) by means of a correction factor, ($CF_{fixed,irr}$), (Fig. 5.30). $CF_{fixed,irr}$ is obtained by comparing the response (i.e., the relative capture width CW^*) of the same fixed OWC geometry under incident waves (regular and irregular) having equivalent incident wave power. To perform this approach, each irregular wave tested (Phase I) is replaced by a single sinusoidal wave, characterized by the same incident power, (H_{rms}, T_e) and directly obtained from the wave energy spectrum. The equivalent regular waves, obtained from the irregular waves tested, suggest that the laboratory data from irregular wave tests are not energetically comparable with those from

regular wave tests (see Table 5-5 and Table 4-2). Hence, the correction factor, $CF_{fixed,irr}$ is found by relating the performance achieved for fixed OWC under the irregular waves tested, (H_{m0}=0.02-0.04m & T_p=0.9-1.1s), with the performance of the same fixed OWC predicted by *Simonetti's MRM Model,* for regular waves (H_{rms}=0.018-0.040m & T_e=0.9-1.1s) with the same incident wave power, (see Table 4-2 and Table 5-5).

- From the comparison between CW^*_{float} and $CW^*_{fixed,}$ achieved for the experiments in Phase I and Phase III, two correction factors, $CF_{float,reg}$ for regular waves and, $CF_{float,irr}$ for irregular waves, are proposed, to extend *Simonetti's MRM model,* CW^*_{MRM} (assessing the performance of fixed OWC in regular waves (Simonetti et al., 2016).
- New empirical formulae (see Fig. 5.28 and Fig. 5.34) are proposed to assess the *relative Capture Width* for floating OWCs (integrated in a VLFS) in regular waves ($CW^*_{float,reg}$) and irregular waves ($CW^*_{float,irr}$), given the following input parameters: wave height and period (H, T or H_{m0}, T_p); water depth (h); OWC design parameters (W and D); damping coefficient (K) and VLFS length (L_{VLFS}). The new formulae might be applied for the preliminary sizing of VLFS-OWC systems, allowing the selection of the optimal OWC design parameters, which ensure a better performance of the device in moderate wave climates.

Moreover, since the incompressible *Simonetti's MRM model* was developed for the following conditions: h^*=1.53-3.15, D^*=1.8-5.0, W^*=0.08-0.20 and K^*=20-170, the application of the new empirical formulae for OWC incorporated in a VLFS, should be limited to the same range of parameters. In addition, the scale effects due to air compressibility , which play an important role at prototype scale, has to be taken into account (Falcão & Henriques, 2014). To avoid an overestimation of the predicted $CW^*_{float,reg}$ and $CW^*_{float,irr}$, the correction factors (CF_{50}) as suggested in Table 5-4 by Simonetti et al. (2016), might be used to correct the results obtained at small scales (Phase I & III).

6 Concluding remarks and outlooks

6.1 General summary of the thesis

This *PhD research* aimed at studying, by means of small-scale laboratory experiments, a pontoon-type Very Large Floating Structure equipped with OWC devices (VLFS-OWC System) conceived for a hypothetical installation in a Mediterranean area characterized by a moderate wave climate (mean annual wave power of 3kW/m).

In particular, the study focused on the effect of: i) the OWC design parameters; ii) the induced damping applied by an impulse turbine (i.e., non-linear air turbine) and iii) the VLFS motions on the performance of the integrated OWC.

The experiments are carried out systematically, providing the knowledge basis for the development of empirical models for the prediction of the heave motion of the VLFS-OWC System for regular and irregular waves and tentative formulae for the prediction of the heave motion of a VLFS-OWC system and the performance of a floating OWC (integrated in a VLFS), as a supporting tool for the preliminary design of a VLFS-OWC System suitable for a moderate wave climate.

In *Chapter 2*, the current knowledge and models on VLFSs and OWC devices is reviewed and analysed and the knowledge gaps, the justifications and the implications for the objectives and methodology of this study are drawn. The available numerical and physical approaches on OWC devices and VLFS technologies are reviewed and analysed for the design and planning of the small-scale model tests.

In *Chapter 3*, a conceptual design of the VLFS-OWC System in terms of its sizing, is proposed, taking into account the technical feasibility in the hypothetical installation site (i.e., Central Tuscany area), selected according to the outcomes of Vannucchi, (2012) on the assessment of the wave energy potentials in the Mediterranean Sea and the analysis of the non-technical barriers. The representative sea state of the specific site is then considered to size the VLFS ensuring the safety conditions for possible operational staff and facilities as well as to preliminary design the OWC device to be integrated, combining the attenuation of the VLFS motions with the wave energy conversion.

In *Chapter 4*, the laboratory tests on the proposed VLFS-OWC System are described in detail and a preliminary analysis of the results is performed, with the main purpose of improving the knowledge related to the effect of design alternatives (i.e., OWC chamber width, W, OWC front wall draught, D, induced air turbine damping, K and VLFS length, L_{VLFS}) on the VLFS behaviour and the OWC performance, under regular and irregular wave trains. To address these objectives, systematically laboratory tests are carried out according to this tiered approach: i) Phase I on fixed OWC models; ii) Phase II on VLFS models without the OWCs and iii) Phase III on VLFS equipped with OWCs.

In *Chapter 5*, the dimensional analysis is performed mainly aiming at the development of prediction formulae for the floating response (i.e., heave motion) of the VLFS-OWC system, respectively in regular and irregular waves. Then, from the comparative analysis of the results achieved in Phase I (fixed OWC) and Phase III (floating OWC integrated in a VLFS) two correction

factors ($CF_{float,reg}$ & $CF_{float,irr}$) are proposed to extend the *incompressible Multi Regression Model (MRM)* proposed by Simonetti et al. (2016) for the prediction of the *relative Capture Width (CW*)* for floating OWC in regular waves and irregular waves. Both proposed prediction formulae might be useful tools for a preliminary design and sizing stage of a VLFS-OWC System, providing the assessment of the VLFS-OWC System heave motion, as well as a preliminary selection of the optimal design of the OWC to be integrated.

6.2 Summary and discussion of key results

The analysis of the results of the parameter study on the fixed OWC and the floating OWC (integrated in VLFS) leads to the following conclusions:

- The *relative Capture Width* of fixed OWC in regular and irregular waves, $CW^*_{fixed}=CW_{fixed}/B$, (where B=0.20m is the chamber length, for all the tests) is remarkably affected by the design parameters of the device (i.e., chamber width, W and front wall draught, D), the applied turbine damping K (reproduced by a vent located on the OWC top cover) and the incident wave conditions (respectively H, T for regular waves and H_{m0}, T_p for irregular waves) and water depth, h.
  - In *regular waves* ($H=0.04m$, $T=0.8\text{-}1.4s$) the maximum performance of fixed OWC ($CW^*_{fixed,reg}=0.73$) is achieved for the incident wave H=0.04m, T=1.0s (kh=2.07), when W/λ=0.13 and K=2074kg$^{1/2}$m$^{-7/2}$.
  - In *irregular waves* ($H_{m0}=0.02\text{-}0.04m$, $T_p=0.9\text{-}1.1s$) the maximum performance of a fixed OWC ($CW^*_{fixed,irr}=0.88$) is achieved for the incident wave, H_{m0}=0.04m, T_p=1.0s (kh=2.23), when W/λ=0.13 and K=2074 - 4472kg$^{1/2}$·m$^{-7/2}$.

  Generally, under both regular and irregular waves, CW^*_{fixed} shows a decreasing trend with increasing front wall draught D. Moreover, for given D, also the damping coefficient K and the incident wave frequency, significantly affect the performance of a fixed OWC.
- The *relative Capture Width* of floating OWC (integrated in a VLFS) in regular and irregular waves, $CW^*_{float}=CW_{float}/B$, is influenced by the aforementioned design parameters as for fixed OWC, but also by the length of the VLFS (L_{VLFS}) and the floating heave motion (he).
  - In *regular waves* (H=0.04m, T=0.8-1.4s) the maximum performance of floating OWC ($CW^*_{float,reg}$=0.65), occurs for the incident wave H=0.04m, T=1.0s (kh=2.07), when the heave motion is he=0.012H, W/λ=0.13, L_{VLFS}/λ=3.6, $M_{VLFS\text{-}OWC}$=233kg and K=2074kg$^{1/2}$m$^{-7/2}$.
  - In *irregular waves* ($H_{m0}=0.02\text{-}0.04m$ & $T_p=0.9\text{-}1.1s$), the maximum performance of floating OWC ($CW^*_{float,irr}$=0.80) is achieved with the incident wave, H_{m0}=0.04m, T_p=1.0s (kh=2.23), when the heave motion is he=0.05H_{m0}, W/λ=0.13, L_{VLFS}/λ=3.6, $M_{VLFS\text{-}OWC}$=227kg and K=2074kg$^{1/2}$m$^{-7/2}$.

  Generally, under both regular and irregular waves, CW^*_{float} is strongly affected by the heave motion, which in turn shows a decreasing trend with increasing length L_{VLFS} and mass $M_{VLFS\text{-}OWC}$ of the VLFS-OWC system. The different response (i.e., in terms of *Capture Width*), observed for fixed OWC and floating OWC under regular and irregular waves, can be interpreted taking into account the not comparable incident wave power, which characterizes the regular and irregular waves tested. Moreover, comparing the maximum performance achieved for fixed OWC and floating OWC in regular waves it is possible to note that, for both cases, the integration of the OWC device in the VLFS leads to a decrease of the maximum performance of about 8% (respectively, $CW^*_{fixed,reg\ max}$=0.73 & $CW^*_{float,reg\ max}$=0.65 and $CW^*_{fixed,irr\ max}$=0.88 & $CW^*_{float,irr\ max}$=0.80). This lower performance may be due to the interaction of the frequency of the heave motion of the VLFS-OWC system with the characteristic resonance frequency of the integrated OWC model.
- The comparative analysis between the results of Phase I (fixed OWC: CW^*_{fixed}) and Phase III (OWC integrated in VLFS: CW^*_{float}) in *regular waves* (H, T) is performed in the range of non-dimensional parameters (see Table 5-1): i) relative water depth, h^*=1.22-3.15; ii) relative chamber width, W^*=0.03-0.30; iii) relative front wall draught D^*=3.01-3.98; iv) relative turbine damping K^*=82.95-289.83; v) relative heave motion he^*=0.010-0.879 and vii) relative VLFS length L^*=0.85-5.60, providing the following key results:

- $CW^*_{float,reg}/CW^*_{fixed,reg}$ increases with increasing he^*, which is also affected by L^*. The maximum highest value of $CW^*_{float,reg}/CW^*_{fixed,reg}=2.58$ is obtained for L^*=0.85, D^*=3.01, W^*=0.03, h^*=1.22 and K^*=95.71 - 289.83.
- $CW^*_{float,reg}/CW^*_{fixed,reg}$ decreases towards a unit value when L^* *increases*. This can be interpreted by considering that for an infinite length of the VLFS, the heave motion is totally damped, and the same CW^* is achieved for both fixed and floating OWC.
- $CW^*_{float,reg}/CW^*_{fixed,reg}$ decreases with increasing W^* to a unit value, which can be interpreted considering the sloshing waves phenomena inside the OWC chamber when the width is much larger than the 1/4 –1/5λ (Sheng et al., 2012; Webb et al., 2005).
- $CW^*_{float,reg}/CW^*_{fixed,reg}$ reaches values of more than 2.5 for heave motions in the order of incident wave amplitude a_w (i.e. for he=0.79a_w)
- Generally, for all tested L^* and for a given D^* and W^*, the relative damping K^* has a significant effect on $CW^*_{float,reg}/CW^*_{fixed,reg}$. As observed for L^* and W^*, also an infinite increase of D^* and K^*, implies $CW^*_{float,reg}/CW^*_{fixed,reg}$=1.

- A first prediction formula (see Eq. 5.16) is proposed for regular waves to assess the relative heave motion he^*_{reg} given the wave parameters, (H, T and h), the OWC chamber width (W), the damping coefficient (K), the front wall draught (D) and the VLFS length (L_{VLFS}), (with R^2=0.96 & RMSE=0.04).
- A first correction factor (see Eq. 5.25), $CF_{float,reg}$, is proposed for regular waves in order to extend Simonetti's *incompressible Multi Regression Model (MRM)* for the performance of fixed OWC in regular waves (CW^*_{MRM}) (Simonetti et al., 2016). Then, a new empirical model for the prediction of $CW^*_{float,reg}$ (Fig. 5.28) given the wave parameters (H, T and h), the OWC design parameters (W and D), the damping coefficient (K) and the VLFS length (L_{VLFS}) is proposed (with R^2=0.86 & RMSE=0.16).
- The comparative analysis of the results of Phase I (fixed OWC: CW^*_{fixed}) and Phase III (floating OWC: CW^*_{float}) in *irregular waves* (H_{m0},T_p), is performed for the range of the following non-dimensional parameters (see Table 5-2): i) relative water depth, h^*=1.85-2.68; ii) relative chamber width, $W^*=0.05-0.24$; iii) relative front wall draught $D^*=2.15-6.89$; iv) relative turbine damping $K^*=82.95-289.83$ and vii) relative VLFS length $L^*=1.38-4.43$, providing the following key results:

  - As for the regular waves, $CW^*_{float,irr}/CW^*_{fixed,irr}$, shows a trend to a unit value for an infinite increase of each of the aforementioned non-dimensional parameters. The highest value of $CW^*_{float,irr}/CW^*_{fixed,irr}$=3.82 is achieved for L^*=1.38, D^*=2.15, W^*=0.05, h^*=1.85 and the applied relative damping K^*=95.71.
  - Due to the relatively low values of he^* obtained from the irregular waves tests, generally the ratio $CW^*_{float,irr}/CW^*_{fixed,irr}$=1 is observed, except for the OWC alternatives: W1D1V1% and W1D1V2%, which under the irregular wave H_{m0}=0.06m & kh=1.85 show an improved performance as compared to the fixed OWC conditions. In particular, when the aforementioned OWCs are integrated in the shorter VLFS (L_{VLFS}=2.60m) and he=1/7a_w, the VLFS-OWC heave motion results in an increase of the performance, respectively by about 3 times (for W1D1V1%) and 4 times (W1D1V2%) as compared to the response of the same OWCs in fixed conditions. When the OWC models W1D1V1% and W1D1V2% are integrated in the longer VLFS (L_{VLFS}=5.60m) and he=1/10a_w the integration in the VLFS results in an increase of the performance respectively by about 2 and 3 times as compared to the OWC performance in fixed conditions.

- A second prediction formula (see Eq. 5.18) is proposed for irregular waves, to assess the relative heave motion he^*_{irr}, given the wave parameters, (H_{m0}, T_p and h), the OWC chamber width (W), the damping coefficient (K), the front wall draught (D) and the VLFS length (L_{VLFS}), with R^2=0.91 & RMSE=0.02.
- A second correction factor (see Eq. 5.32), $CF_{fixed,irr}$, is proposed for irregular waves in order to extend the *incompressible Multi Regression Model (MRM)*, predicting the performance of fixed OWC in regular waves (Simonetti et al., 2016). The proposed, $CF_{fixed,irr}$, is obtained from the comparison of the response (i.e., *relative Capture Width, CW**) of the same fixed OWC device under incident regular and irregular waves, having an equivalent incident wave power (with R^2=0.92 & RMSE=0.15). Then, each irregular wave train tested in Phase

I (H_{m0}, T_p) is represented by a train of sinusoidal waves (H_{rms}, T_e), having the same incident power. The equivalent regular waves obtained confirmed that the regular and irregular wave conditions tested (regular and irregular waves) are not energetically comparable. Then, $CF_{fixed,irr}$ is obtained by relating the performance achieved for fixed OWC in irregular waves tested in Phase I with the performance of the same fixed OWC predicted by *Simonetti's MRM Model,* for regular waves with same incident wave power. (Fig. 5.34).

- A third correction factor, $CF_{float,irr}$ (see Eq. 5.36) is proposed for the prediction of the performance of floating OWC (integrated in a VLFS), under irregular waves. $CF_{float,irr}$ is obtained by comparing the performance of fixed and floating OWC under the irregular waves tested. The polynomial fit of the proposed formula (Eq. 5.34) is within the range of non-dimensional parameters tested (with R^2=0.91 & RMSE=0.19). Then, by applying the two correction factors, respectively $CF_{fixed,irr}$ and $CF_{float,irr}$ to *Simonetti's MRM model*, it is possible to obtain a new empirical formula for the prediction of performance of OWCs integrated in a VLFS, $CW^*_{float,irr}$ (see Eq.5.37), given the wave parameters (H_{m0}, T_p and h), the OWC design parameters (W and D), the damping coefficient (K) and the VLFS length (L_{VLFS}).

6.3 Outlooks

This *PhD research* has enhanced the understanding of the mutual interaction between the VLFS motion and the performance of the integrated OWC devices and developed empirical formulae for the prediction of vertical displacements of the VLFS-OWC System and a correction factor to be applied at the incompressible MRM model performed by Simonetti et al. (2016), for the preliminary assessment of the floating OWC (integrated in VLFS) performance.

Based on the knowledge gained from this PhD study, some recommendations can be drawn for future research as follows:

- The air compressibility effects, which would play an important role at prototype scale, has to be considered (Falcão & Henriques, 2014). Although the correction factors (CF_{50}) provided by Simonetti et al. (2016) proved that neglecting air compressibility in the laboratory tests may results in a limited overestimation of the *dimensionless Capture Width*, CW^* (up to 10%), overall the experimental results might be corrected.
- Since the *incompressible MRM model* for fixed OWC (Simonetti et al, 2016) should be cautiously applied in the range of: h^*=1.53-3.15, D^*=1.8-5.0, W^*=0.08-0.20 and K^*= 20-170, also the use of the empirical model for the floating OWC should be limited to the same aforementioned range. However, to extend the applicability of the model further studies are needed, possibly increasing the resolution by testing more design alternatives for both fixed and floating OWC within the range of those tested for this study (h^*=1.22-3.15, D^*=3.01-3.98, W^*=0.03-0.30 and K^*=82.95-289.83).
- This study provided useful results on the floating behaviour of the VLFS without OWC and equipped which, together with the proposed prediction formulae of the heave motion, could be used for future studies on the mitigating effect of the OWCs on the VLFS motion.

References

Anand, S. et al., 2007. Turbines for wave energy plants. In *8th International Symposium on Experimental and Computational Aerothermodynamics of Internal Flows Lyon,*. pp. 1–7.

Andrikopoulos, T., 2012. Investigation into the Hydrodynamic Response of the ogWAVE Wave Energy Converter. *National Centre for Maritime Engineering and Hydrodynamics*, pp.1–16.

Aqua-RET Project ©, 2012. Web Site.

Bearman, P.W., 1971. Corrections for the effect of ambient temperature drift on hot-wire measurements in incompressible flow DISA. , Inf. 11, pp.25–30.

Bellucci, S., 2014. *Sviluppo di un applicativo LabVIEW per taratura ed acquisizione dati da sonde a filo caldo. Master Thesis.*

Braeunig, J.P. et al., 2010. On the effect of phase transition on impact pressures due to sloshing. In *The International Society of Offshore and Polar Engineers (ISOPE)*. pp. 1–9.

Braeunig, J.P. et al., 2009. Phenomenological Study of Liquid Impacts through 2D Compressible Two-fluid Numerical Simulations. In *Nineteenth (2009) International Offshore and Polar Engineering Conference Osaka, Japan*. pp. 21–29.

Bruun, H.H., 1995. Hot-Wire Anemometry Principles and Signal Analysis. *New York, Oxford University Press Inc.*

Chenu, B. & Morris-Thomas, M. T. Thiagarajan, K.P., 2004. Some hydrodynamic characteristics of an air-cushion supported concrete gravity structure. In *15th Australasian Fluid Mechanics Conference*.

Cimbala, J.M. & Park, W.J., 1994. A direct hot-wire calibration technique to account for ambient temperature drift in incompressible flow. *Mineralium Deposita*, 29(1), pp.299–300.

Cornett, A., 2008. A global wave energy resource assessment. In *Proc. ISOPE*. pp. 1–9.

Demographia, 2012. Demographia World Urban Areas. In *Demographia World Urban Areas: 8th Annual Edition*. pp. 1–173.

Drew, B., Plummer, A.R. & Sahinkaya, M.N., 2009. A review of wave energy converter technology. *Proceedings of the Institution of Mechanical Engineers, Part A: Journal of Power and Energy*, 223(8), pp.887–902.

Endo, H., 2000. The behavior of a VLFS and an airplane during takeoff/landing run in wave condition. *Marine Structures*, 13, p.477–491.

Endo, H. & Yago, K., 1999. Time history response of a large floating structure subjected to dynamic load. *Journal of the Society of Naval Architects of Japan*, 186, pp.369–376.

Evans, D. V, 1978. The Oscillating Water Column Wave-energy Device. , (April), pp.423–433.

Evans, D. V., 1982. Wave-power absorption by systems of oscillating surface pressure distributions. *Journal of Fluid Mechanics*, 114(1), p.481.

Evans, D.V. & Porter, R., 1995. Hydrodynamic characteristics of an oscillating water column device. *Applied Ocean Research*, 17(3), pp.155–164.

Falcão, A.F. de. O., 2004. First-Generation Wave Power Plants: Current Status and R&D Requirements. *Journal of Offshore Mechanics and Arctic Engineering*, 126(4), pp.384–388.

Falcão, A.F. de. O., 2013. Modeling of Wave Energy Conversion: " internal report of the Wave Energy Specialization. *Section of the EUREC Master, February-May, IST Lisbon*.

Falcão, A.F. de. O., 2000. The shoreline OWC wave power plant at the Azores. In *Proc. 4th European Wave Energy Conference.* Aalborg, Denmark.

Falcão, A.F. de. O., 2010. Wave energy utilization: A review of the technologies. *Renewable and Sustainable Energy Reviews*, 14(3), pp.899–918.

Falcão, A.F. de. O. & Gato, L.M.C., 2012. *Air turbines*,

Falcão, A.F. de. O. & Henriques, J.C.C., 2014. Model-prototype similarity of oscillating-water-column wave energy converters. *International Journal of Marine Energy*, 6, pp.18–34.

Falcão, A.F. de. O. & Justino, P.A.P., 1999. OWC wave energy devices with air flow control. *Ocean Engineering*, 26, pp.1275–1295.

Forestier, J.M. et al., 2007. Value and validation of small scale physical model tests of floating wave energy converters. In *7th European Wave and Tidal Energy Conference, Porto, Portugal*.

Fu, S. et al., 2007. Hydroelastic analysis of flexible floating interconnected structures. *Ocean Engineering*, 34(11–12), pp.1516–1531.

Goda, Y. & Suzuki, Y., 1995. Estimation of incident and reflected waves in regular wave experiments. *Ocean Engineering*, 22(1), pp.77–86.

Gomes, M.N. et al., 2012. Two-Dimensional geometric optimization of an Oscillating Water Column Converter. *Engenharia Térmica (Thermal Engineering)*, 11, pp.30–36.

Gomes, R.P.F. et al., 2012. Testing of a small-scale floating OWC model in a wave flume. *International Conference on Ocean Energy*, (1982), pp.1–7.

Grotmaack, R., 2003. Small rigid floating bodies under the influence of water waves. *Research Letters in the Information and Mathematical Sciences*, 5, pp.143–155.

He, F., Huang, Z. & Law, A.W.-K., 2013. An experimental study of a floating breakwater with asymmetric pneumatic chambers for wave energy extraction. *Applied Energy*, 106, pp.222–231.

He, F., Huang, Z. & Wing-Keung Law, A., 2012. Hydrodynamic performance of a rectangular floating breakwater with and without pneumatic chambers: An experimental study. *Ocean Engineering*, 51, pp.16–27.

Heath, T., Whittaker, T.J.T. & Boake, C.B., 2000. The design, construction and operation of the LIMPET wave energy converter (Islay, Scotland). In *Proc. 4th European Wave Energy Conference.* Aalborg, Denmark.

Hong, D.C. & Hong, S.Y., 2007. Hydroelastic responses and drift forces of a very-long floating structure equipped with a pin-connected oscillating-water-column breakwater system. *Ocean Engineering*, 34(5–6), pp.696–708.

Hong, D.C., Hong, S.Y. & Hong, S.W., 2006. Reduction of hydroelastic responses of a very-long floating structure by a floating oscillating-water-column breakwater system. *Ocean Engineering*, 33(5–6), pp.610–634.

Hong, S.Y. & Kyoung, J.H., 2007. Effects of Location and Shape of OWC-Chamber on the Hydroelastic Response of VLFS. In *Proceedings of the 7th International Offshore and Polar Engineering Conference*. Lisbon, Portugal, pp. 434–438.

Hong S. Y., Kim B. W., K.J.H., 2009. Numerical and Experimental Study on Coupled Hydroelastic Behavior of VLFS and OWC Chamber. In *5th International Conference on Hydroelasticity in Marine Technology*. Southampton, UK, pp. 303–312.

Hughes, S., 1993. *Introduction. In S. Hughes, Physical Models and Laboratory Techniques in Coastal Engineering. World Scientific.*,

Ikoma T., Maeda H., Masuda K., R.C.-K., 2003. Effects of the Air-Chambers on the Hydroelastic Response Reduction. In *Proceedings of International Symposium on Ocean Space Utilization Technology.* Tokyo, Japan., pp. 180–188.

Iturrioz, A. et al., 2014. Time-domain modeling of a fixed detached oscillating water column towards a floating multi-chamber device. *Ocean Engineering*, 76, pp.65–74. Available at: http://dx.doi.org/10.1016/j.oceaneng.2013.11.023.

Iturrioz, A. et al., 2015. Validation of OpenFOAM® for Oscillating Water Column three-dimensional modeling. *Ocean Engineering*, 107, pp.222–236.

Kamath, A., Bihs, H. & Arntsen, Ø.A., 2015. Numerical investigations of the hydrodynamics of an oscillating water column device. *Ocean Engineering*, 102, pp.40–50.

van Kessel, J.L.F., 2010. *Aircushion Supported Mega-Floaters*. Delft University of Technology & SBM Gusto.

Kim, B.W. et al., 2005. Investigation on Wave Reduction Performances of Floating Hinge-Linked Breakwater. *Young*, (October).

Kim, J. & Zi, G., 2011. Development of Design Charts for Very Large Floating Structures. In *Twenty-first (2011) International Offshore and Polar Engineering Conference Maui, Hawaii, USA*.

Kolman, R., 2012. New land in the water: economically and socially, land reclamation pays. *Terra et Aqua*, Number 128, pp.3–8.

Kyoung J. H., H.S.Y., 2008. Localized Finite Element Method on Hydroelastic Responses of OWC-Embedded VLFS. In *ASME Paper No.OMAE2008-57995*.

Laing, A.K. et al., 1998. *Guide to wave analysis and forecasting*,

Lee, C. & Newman, J.N., 2000. Wave effects on large floating structures with air cushions. *Marine Structures*, 13, pp.315–330.

Lewis, A., Gilbaud, T. & Holmes, B., 2003. Modelling the Backward Bent Duct Device-B2D2, a comparison between physical and numerical models. In *5th European Wave Energy Conference, Cork, Ireland, 17-20th*.

Li, R., Shu, Z. & Wang, Z., 2003. A Numerical and Experimental Study on the Hydroelastic Behavior of the Box-Typed Very Large Floating Structure in Waves. In *30th International Offshore and Polar Engineering Conference*. Honolulu, Hawaii, USA, May, pp. 25–30.

Lopez, I. et al., 2012. Turbine—chamber coupling in an OWC Wave Energy Converter. *Civil Engineering*, pp.1–7.

López, I., Castro, A. & Iglesias, G., 2015. Hydrodynamic performance of an oscillating water column wave energy converter by means of particle imaging velocimetry. *Energy*, 83, pp.89–103.

López, I. & Iglesias, G., 2014. Efficiency of OWC wave energy converters: A virtual laboratory. *Applied Ocean Research*, 44, pp.63–70.

Lovas, S., Mei, C.C. & Liu, Y., 2010. Oscillating water column at a coastal corner for wave power extraction. *Applied Ocean Research*, 32(3), pp.267–283.

Luo, Y. et al., 2014. Numerical simulation of a heave-only floating OWC (oscillating water column) device. *Energy*, 76, pp.799–806.

Maeda, H. et al., 1985. Fundamental Research on Oscillating Water Column Wave Power Absorbers. *ASME, Journal of Energy Resources Technology*, 107, pp.81–86.

Maeda, H. et al., 2000. Hydro-elastic response reduction system of a very large floating structure with wave energy absorption devices. *OCEANS 2000 MTS/IEEE Conference and Exhibition*, 1(1), pp.527–531.

Malmo, O. & Reitan, A., 1986. Development of the Kværner multi-resonant OWC. *D. V. Evans and A. F. de O. Falcão, editors, Hydrodynamics of Ocean Wave Energy Utilization. Berlin: Springer-Verlag*.

Martinelli, L., Pezzutto, P. & Ruol, P., 2013. Experimentally Based Model to Size the Geometry of a New OWC Device, with Reference to the Mediterranean Sea Wave Environment. *Energies*, 6(9), pp.4696–4720.

McCormick, M., 1981. Ocean Wave Energy Conversion. *John Wiley & Sons, New York*.

Morris-Thomas, M., Irvin, R.J. & Thiagarajan, K.P., 2007. An Investigation Into the Hydrodynamic Efficiency of an Oscillating Water Column. *Journal of Offshore Mechanics and Arctic Engineering*, 129(4), p.273.

Ning, D.Z. et al., 2016. An experimental investigation of hydrodynamics of a fixed OWC Wave Energy Converter. *Applied Energy*, 168, pp.636–648.

Ohkawa, Y., 2000. Various mega-float model experiments on elastic behavior in waves. In *74th General Meeting of the Ship Research Institute*. pp. 291–294.

Ohmatsu, S., 1999. Numerical calculation method of hydroelastic response of a pontoon-type VLFS close to a breakwater. In *3rd International Workshop on Very Large Floating Structure*. pp. 22–24.

Ohmatsu, S., 1998. Numerical calculation of hydroelastic behavior of VLFS in time domain. In *Proceedings of the Second International Conference on Hydroelasticity in Marine Technology, Fukuoka, Japan.* pp. 89–97.

Ohmatsu, S., 2005. Overview: Research on wave loading and responses of VLFS. *Marine Structures*, 18(2), pp.149–168.

Ohta, H., Torii, T., Hayashi, N., Watanabe, E., Utsunomiya, T., Sekita, K., & Sunahara, S., 1999. Effect of attachment of a horizontal/vertical plate on the wave response of a VLFS. In *3rd international workshop on very large floating structure*. University of Hawaii at Manao Honolulu, HI., p. (Vol. 1) 256-274.

Ohta, M. et al., 2002. A Study on Progress in Antiwave Performance of Mega-Float. , 3.

Pastor, J. & Liu, Y., 2014. Retracted: "Wave Energy Resource Analysis for Use in Wave Energy Conversion" [ASME Journal of Offshore Mechanics and Arctic Engineering, 137 (1), p. 011903]. *Journal of Offshore Mechanics and Arctic Engineering*, 137(1), p.11903.

Payne, G.S., 2008. Guidance for the experimental tank testing of wave energy converters. , pp.1–44.

Pernice, R., 2009. Japanese urban artificial islands: an overview of projects and schemes for marine cities during 1960s–1990s. *J. Arch. Plann (Trans of AIJ), 74 (642)*, pp.1847–1855.

Pinkster, J.A., 1997. The Effect of Air-Cushions Under Floating Offshore Structures. In *Conference on the Behavior of Offshore Structure*. Delf, The Netherlands, pp. 143–158.

Price, A. A. E., Dent, C. J., & Wallace, A.R. (2009)., 2009. On the capture width of wave energy converters. Applied Ocean Research, 31(4), 251-259. *Applied Ocean Research*, 31(4), pp.251–259.

Pullen, T. et al., 2007. EurOtop, European Overtopping Manual - Wave overtopping of sea defences and related structures: assessment manual. , (August).

Robinson, R.W., 1982. *The Effects of Geometric-Wave Field Interactions on the Performance of Oscillating Water Column Wave Energy Convertors", PhD Thesis, Queens University, Belfast*.

Sarmento, A.J.N.A., 1993. Model test optimization of an OWC. *International Journal of Offshore and Polar Engineering*, 3, pp.66–72.

Sarmento, A.J.N.A., 1992. Wave flume experiments on two-dimensional oscillating water column wave energy devices. *Experiments in Fluids*, 12(4–5), pp.286–292.

Sheng, W., Lewis, T. & Alcorn, R., 2012. On wave energy extraction of oscillating water column device. *International Conference on Ocean Energy*, (iii), pp.1–9.

Shigemitsu, H., Ogata, T., Kobayashi, H., Inoue, K.-I., Fukuoka, T., Takaoki, T., 2001. Feasibility Study of Reducing Wave Load on Pontoon-Type Mega-Float Structure. In *ASME Paper No. OMAE2001/OSU-5011*.

Shuku, M. et al., 2001. Overview of Mega-Float and its utilization. Mitsubishi Heavy Industries Technical Review. , 38(2), pp.39–46.

Simonetti, I. et al., 2015. Numerical Modelling of Fixed Oscillating Water Column Wave Energy Conversion Devices: Toward Geometry Hydraulic Optimization. (pp. V009T09A031-V009T09A031). *ASME 2015 34th International Conference on Ocean, Offshore and Arctic Engineering American Society of Mechanical Engineers.*, pp.1–10.

Simonetti, I., 2016. *Optimization of Oscillating Water Column Wave Energy Converters in Moderate Wave Climate*. University of Braunschweig & University of Florence.

Simonetti, I., Cappietti, L. & Oumeraci, H., 2016. *Site-specific parameter optimization of the OWC geometry and of turbine induced damping (Internal report 6)*,

SNAJ - Society of Naval Architects of Japan, 1997. Chapter 9, Experimental Technique, Seizando. In *Mega-Float offshore structure*. pp. 303–342.

Suroso, A., 2005. The original OWC system was modified by installing a reflector for increasing the efficiency performance of the model . , (19), pp.84–94.

Suzuki, H., 2005. Overview of Megafloat: Concept, design criteria, analysis, and design. *Marine Structures*, 18(2), pp.111–132.

Suzuki, H. et al., 2006. Very large floating structures. In *16th International ship and offshore congress*. Southamppton, UK, pp. 391–442.

Suzuki, H. & Yoshida, K., 1996. Design flow and strategy for safety of very large floating structure, VLFS'96, Hayama, Japan. In *Proceedings of international workshop on very large floating structures, VLFS'96*. Hayama, Japan., pp. 21–27.

Sykes, R.K., Lewis, A.W. & Thomas, G.P., 2009. A hydrodynamic study of a floating circular OWC. , pp.618–627.

Takao, M. & Setoguchi, T., 2012. Air turbines for wave energy conversion. *International Journal of Rotating Machinery*, 2012.

The Carbon Trust, 2005. *Marine Energy Challenge Oscillating Water Column Wave Energy Converter Evaluation Report*,

Thiagarajan, K. P. T. & Morris-Thomas, M., 2006. Wave-Induced Motions of an Air Cushion in Shallow Water. In *Ocean Eng*. pp. 143–1160.

Thorimbert, Y., 2014. *Water wave interaction with an Oscillating Water Column Wave-Energy Converter: experimental validation of lattice Boltzmann numerical simulations, Marinet internal report, User-Project: LBM4OWC.*,

Torre-Enciso, Y. et al., 2009. Mutriku Wave Power Plant : from the thinking out to the reality. In *Proceedings of the 8th European Wave and Tidal Energy Conference*. Uppsala, Sweden, pp. 319–329.

Tsubogo, T., 1997. A basic investigation on deflection wave propagation and strength of Very Large Floating Structures. (The 2nd report). *Journal of the Society of Naval Architects of Japan*, 182, pp.381–390.

Utsunomiya, T., Watanabe, E., Nakamura, N., 2001. Analysis of Drift Force on VLFS by the Near-field Approach. In *Proceedings of the 11th International Offshore and Polar Engineering Conference*. Stavanger, Norway., pp. 217–221.

Vannucchi, V., 2012. *Wave energy harvesting in the Mediterranean Sea*. Florence University.

Vannucchi, V., Cappietti, L. & Falcão, A.F. de. O., 2012. Estimation of the offshore wave energy potential of the Mediterranean Sea and propagation toward a nearshore area. *Icoe*, pp.1–5.

VSL International LTD., 1992. Floating Concrete Structures Examples From Practice. , (July), pp.1–24.

Wang, C.M. et al., 2010a. Literature Review of Methods for Mitigating Hydroelastic Response of VLFS Under Wave Action. *Applied Mechanics Reviews*, 63(3), p.30802.

Wang, C.M. et al., 2010b. Literature Review of Methods for Mitigating Hydroelastic Response of VLFS Under Wave Action. *Applied Mechanics Reviews*, 63(3), p.30802.

Wang, C.M. & Wang, B.T., 2015. *Large Floating Structures : Technological Advances* C. M. Wang & B. T. Wang, eds., Singapore.

Wang, C.M., Watanabe, E. & Utsunomiya, T., 2008. *Very Large Floating Structures*,

Watanabe, E., Wang, C.. M., et al., 2004. Very Large Floating Structures: applications, analysis and design. *Centre for Offshore Research and Engineering National University of Singapore*, pp.1–30.

Watanabe, E., Utsunomiya, T. & Wang, C.M., 2004. Hydroelastic analysis of pontoon-type VLFS: A literature survey. *Engineering Structures*, 26(2), pp.245–256.

Watanabe E., Utsunomiya T., Ohta H., H.N., 2003. Wave Response Analysis of VLFS With an Attached Submerged Plate: Verification With 2-D Model and Some 3-D Numerical Examples. In *International Symposium on Ocean Space Utilization Technology, National Maritime Research Institute, Tokyo, Japan*. pp. 157–164.

Watts, K.C. et al., 1985. Non Linear Analysis of a Non-Vertical Walled OWC Ocean Wave Energy Converter. In *5th Offshore Mechanics and Arctic Engineering Symposium*. Dallas, Texas.

Webb, I., Seaman, C., Jackson, G., 2005. *The Carbon Trust - Oscillating Water Column Wave Energy Converter Evaluation Report*,

Weber, J., 2007. Representation of non-linear aero-thermodynamic effects during small scale physical modelling of OWC WECs. In *Proceedings of the 7th European Wave and Tidal Energy Conference.*

Whittaker, T.J.T. & McPeake, F.A., 1986. Design optimization of axi-symmetric tail tube buoys. *D. V. Evans and A. F. de O. Falcão, editors. Hydrodynamics of Ocean Wave Energy Utilization. Berlin: Springer-Verlag*.

Yeung, R.W., 1981. Added mass and damping of a vertical cylinder in finite-depth waters. *Applied Ocean Research*, 3(3), pp.119–133.

Zhang, Y., Zou, Q.P. & Greaves, D., 2012a. Air water two-phase flow modeling of hydrodynamic performance of an oscillating water column device. *Renewable Energy*, 41, pp.159–170.

Zhang, Y., Zou, Q.P. & Greaves, D., 2012b. Air-water two-phase flow modelling of hydrodynamic performance of an oscillating water column device. *Renewable Energy*, 41, pp.159–170.

Annex A: Calibration curves for each pressure transducer

Calibration curve for pressure transducer PT-1

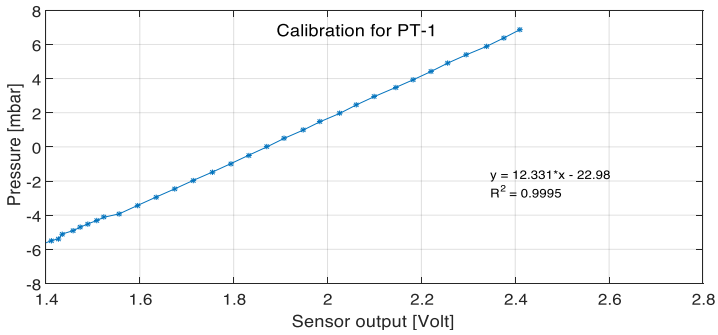

Calibration curve for pressure transducer PT-2

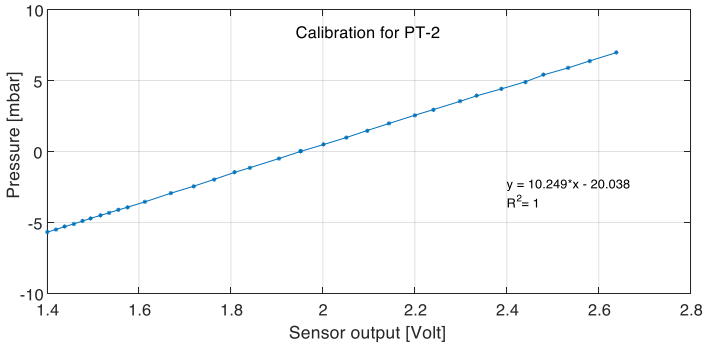

Calibration curve for pressure transducer PT-3

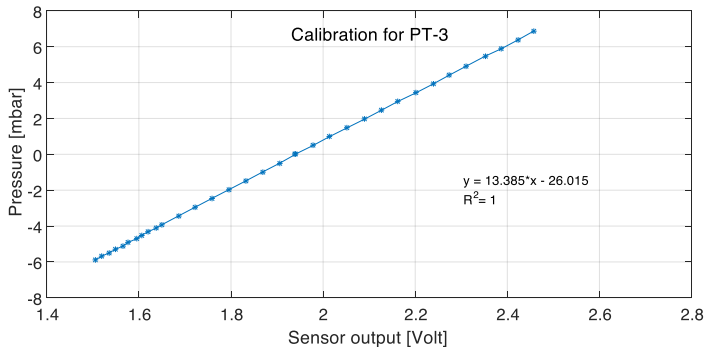

Calibration curve for pressure transducer PT-4

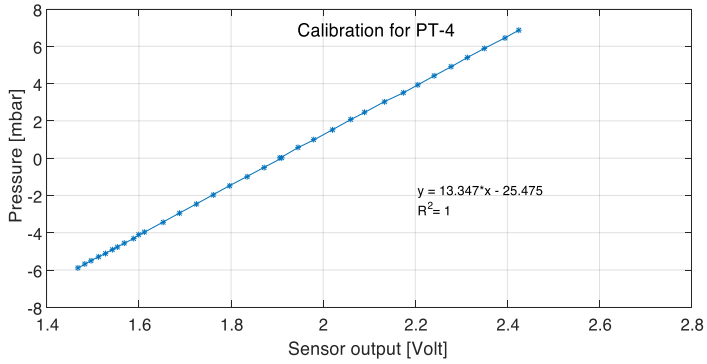

Calibration curve for pressure transducer PT-5
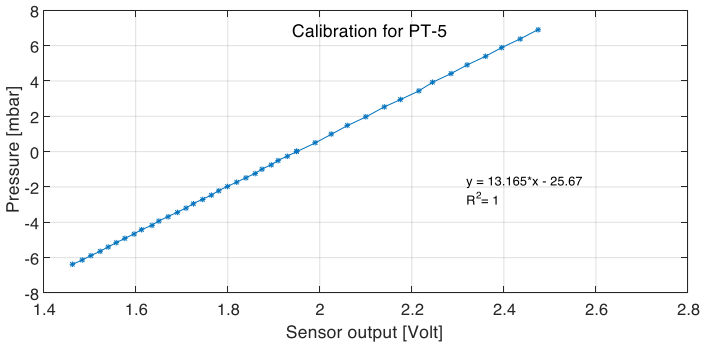

Calibration curve for pressure transducer PT-6
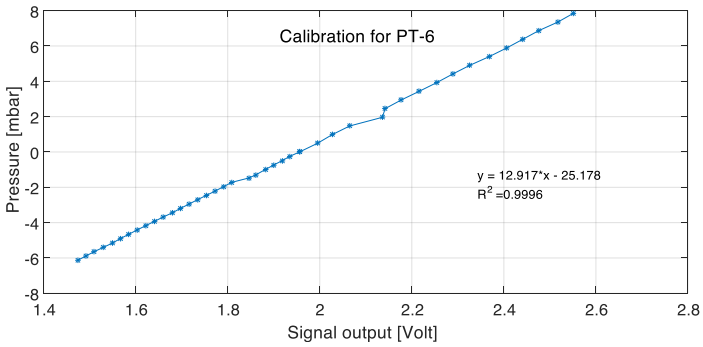

Calibration curve for pressure transducer PT-7
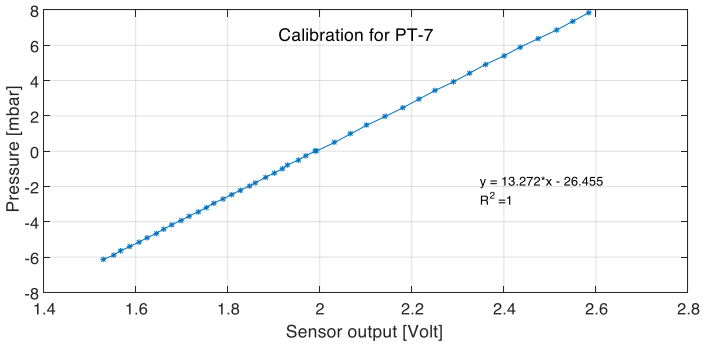

Annex B: Calibration curves for each hot wire anemometer

Calibration curve for the hot wire anemometer HW-1

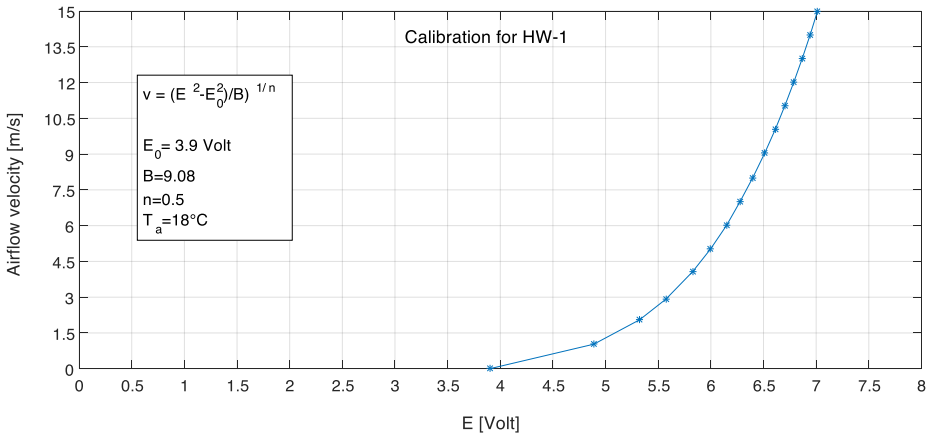

Calibration curve for the hot wire anemometer HW-2

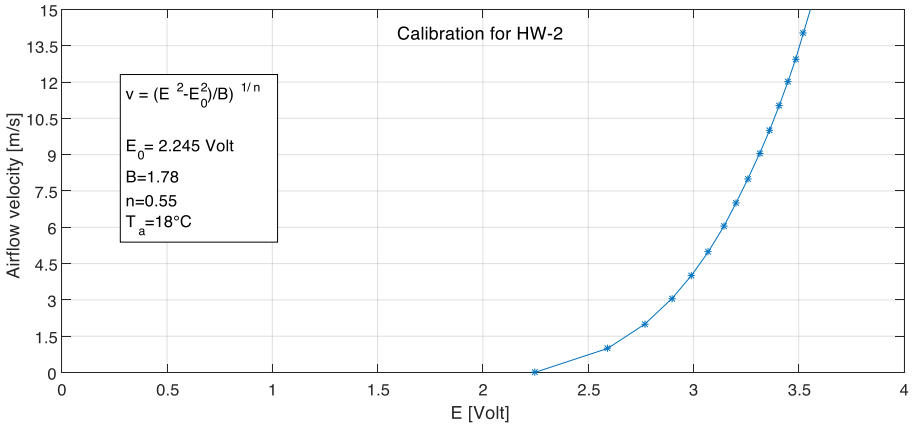
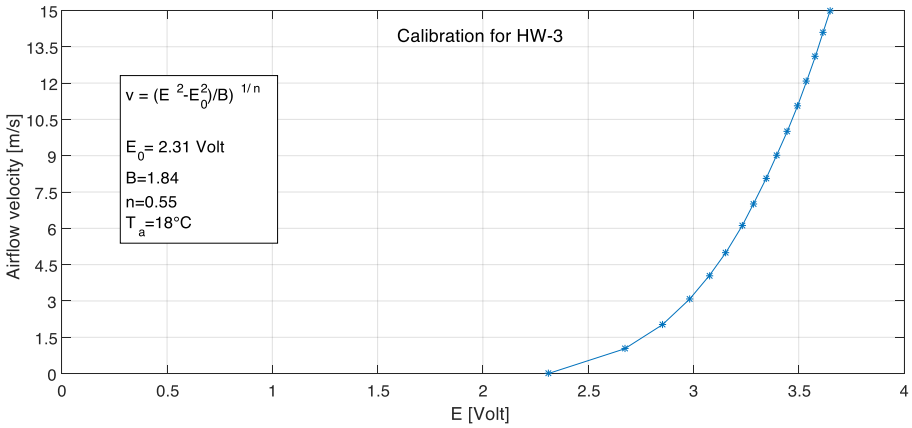
Calibration curve for the hot wire anemometer HW-3